UNIVERSITÀ DI PARMA

UNIVERSITÀ DEGLI STUDI DI PARMA

DOTTORATO DI RICERCA IN

Scienze del Farmaco, delle Biomolecole e dei Prodotti per la Salute

CICLO XXXIII

"Complex between *S. aureus* hemophore and human hemoglobin as a target for novel antimicrobial agents: from complex characterization to compounds identification"

Coordinatore:

Chiar.mo Prof. Marco Mor

Tutore:

Chiar.ma Prof.ssa Barbara Campanini

Dottorando:

Omar De Bei

Anni Accademici 2017/2018 – 2019/2020

The thesis contains unpublished results and results that have been published in the following paper:

Gianquinto E., Moscetti I., **De Bei O.**, Campanini B., Marchetti M., Luque F. J., Cannistraro S., Ronda L., Bizzarri A. R., Spyrakis F., Bettati S.; Interaction of human hemoglobin and semi-hemoglobins with the Staphylococcus aureus hemophore IsdB: a kinetic and mechanistic insight; Scientific Report, 9(1); 18629; 2019

Omar De Bei performed part of his experiments in the following laboratories:

- ID09 WHITE BEAM STATION beamline of the European Synchrotron Radiation Facility (Grenoble) funded by the same facility.

  Collaborator: Dr. Matteo Levantino.

  Project: Investigating the heme extraction mechanism of hemophores with time-resolved WAXS.

  Period: 17th-24th July 2018

- Department of Biochemistry, University of Cambridge, as part of an EMBO short term fellowship.

  Supervisor: Prof. Ben Luisi.

  Project: Cryo-EM structure of the complex between bacterial hemophore IsdB and human hemoglobin.

  Period: July-December 2019

Surface Plasmon Resonance experiments were performed in collaboration with Prof. Salvatore Cannistraro (Università della Tuscia).

Potential inhibitors were identified by structure-based virtual screening and molecular docking by Prof.ssa Francesca Spyrakis (Università di Torino), and purchased from commercial suppliers (Enamine Ltd., Specs, and Vitas-M Laboratory, Ltd.). Omar De Bei validated the activity. The identified hit compounds were analyzed by Saturation-Transfer Difference - Nuclear Magnetic Resonance, performed by Prof.ssa Serena Faggiano (Università di Parma), to confirm their specific binding to hemoglobin.

Table of contents

Abstract

Nowadays and in the coming decades antimicrobial resistance will be among the most serious health threats. It is expected that, in 2050, more people will die from superbugs than currently die from cancer. Methicillin-resistant *Staphylococcus aureus* (MRSA) is one of the most dangerous multi-drug resistant bacteria worldwide and it is included as a high priority in the Global Priority Pathogens List drafted by the World Health Organization (WHO) in 2017.

The *S. aureus* pathogenesis of the human infections has been shown to be reliant on the acquisition of iron. However, the human body has developed a "nutritional immunity" that controls iron trafficking with the aim of alleviating the toxicity of free iron and restraining microbial growth. To overcome the human nutritional immunity, *S. aureus* has developed the Iron-regulated Surface Determinant (Isd) system aimed at iron retrieval based on hemoglobin (Hb) binding. In the Isd system, IsdB and IsdH are the proteins in charge of binding Hb to extract heme. These proteins present a typical modular organization with two or three NEAr Transporter (NEAT) domains exposed on the outer surface of the bacterial cell, which act in concert to bind, extract and transfer heme from Hb to downstream Isd proteins. In this scenario, IsdB but not IsdH has been found essential for *S. aureus* pathogenesis and included in the list of principal virulence factors of the bacterium. Antibodies and vaccines directed against IsdB have been demonstrated to protect against *S. aureus* infections. These experimental evidences and the MRSA threat make IsdB-Hb protein-protein interaction (PPI) a suitable target to develop new antimicrobial agents. The interference with PPIs poses new opportunities and challenges for the development of innovative therapeutics, but requires an in-depth knowledge of the structural and functional details of protein complexes.

This project focused on the biochemical and biophysical characterization of the complex between human Hb and IsdB and the screening of the first set of molecules aimed to interfere with this PPI.

During the project, the conditions for expression and purification of IsdB as recombinant protein in *Escherichia coli* were optimized. Moreover, two variants of the hemophore (presenting either Y165A or Y440A substitutions) were designed and the mutated constructs were expressed and purified based on the protocol optimized for the wild-type (WT) protein.

The Y165A mutant has a reduced affinity for Hb and it was exploited to increase the sensitivity of the screening assay for molecules aimed to interfere with IsdB-Hb complex formation, whilst the substitution of the tyrosine 440 with an alanine has resulted in an hemophore impaired in heme extraction. Human oxyhemoglobin (oxyHb) was purified from blood of non-smoking donors and several forms of the protein were prepared, including methemoglobin (metHb), carboxyhemoglobin (COHb), and semihemoglobins (semiHbs). Purified/prepared proteins were used to provide more insight into the mode of action of IsdB. Microscopic kinetic constants for IsdB-Hb complex formation were defined for the first time by Surface Plasmon Resonance (SPR), while heme extraction was followed using visible spectroscopy. These experiments were repeated employing semiHbs, which are Hb derivatives that bind heme only on α- or β-chain, while the other subunit is heme free, to assess preferential binding and heme extraction of IsdB from either α- or β-Hb chains.

Furthermore, the stoichiometric ratio and the oligomeric state of IsdB complexes with ligated forms of Hb (namely, oxyHb and COHb) or metHb were defined using visible spectroscopy and Size-Exclusion Chromatography – Multi-Angle Light Scattering (SEC-MALS).

The low-resolution structure of IsdB isolated or in complex with metHb was determined using small-angle X-ray scattering (SAXS). Cryogenic electron microscopy (cryo-EM) was employed to obtain high-resolution structural insight on IsdB-COHb and IsdB-metHb complexes, and define the structural determinants of complex formation and heme extraction. The biochemical and biophysical characterization allowed to obtain a complete model for IsdB-metHb complex formation and heme extraction, which was still missing and severely hampered the exploitation of the complex for the identification of PPI inhibitors.

Finally, inhibitors of IsdB-Hb interaction were tested in our laboratory for the first time. For this purpose, an Enzyme-Linked ImmunoSorbent Assay (ELISA) was developed for inhibitors testing that has high-throughput screening capabilities. Potential inhibitors were selected by Prof.ssa Spyrakis' group (Università di Torino) based on the *in silico* screening of online libraries, and evaluated using the ELISA. Eight hit compounds have been identified and further tests are ongoing to confirm their activity.

Abbreviations

COHb	Carboxyhemoglobin
Cryo-EM	Cryogenic Electron Microscopy
FL-IsdB	Full-Length-IsdB
Fur	Ferric uptake regulator
Hb	Hemoglobin
hHb	Human Hemoglobin
Hp	Haptoglobin
Isd	Iron-regulated Surface Determinant
$IsdB^{N1LN2}$	The central and functional region of IsdB
$IsdB^{Y165A}$	$IsdB^{N1LN2}$ variant with Y165 substituted with an alanine
$IsdB^{Y440A}$	$IsdB^{N1LN2}$ variant with Y440 substituted with an alanine
metHb	Methemoglobin
MRSA	Methicillin-resistant Staphylococcus aureus
MSCRAMM	Microbial Surface Component Recognizing Adhesive Matrix Molecules
MSSA	Methicillin-sensitive Staphylococcus aureus
NEAT	NEAr Transporter
NMR	Nuclear Magnetic Resonance
oxyHb	Oxyhemoglobin
PPI	Protein-Protein Interaction
RBC	Red Blood Cell
SAXS	Small-Angle X-ray Scattering
SEC	Size-Exclusion Chromatography
SEC-MALS	Size-Exclusion Chromatography – Multi-Angle Light Scattering
SemiHb	Semihemoglobin
SPA	Single Particle Analysis
SPR	Surface Plasmon Resonance
STD-NMR	Saturation-Transfer Difference - Nuclear Magnetic Resonance
WHO	World Health Organization
WT	Wild-Type

Acknowledgements

First and foremost, I would like to thank my supervisor and mentor Prof.ssa Barbara Campanini for her knowledge, support, encouragement, and helpful discussion throughout my scientific growth path. I would also acknowledge Prof. Luca Ronda, Prof. Stefano Bettati, Prof. Andrea Mozzarelli, Dr. Matteo Levantino, Prof.ssa Francesca Spyrakis, and Prof.ssa Serena Faggiano for their valuable time, suggestions, and sharing their experiences.

I would acknowledge Prof. Ben Luisi for giving me the opportunity to learn and work in his laboratory during my secondment.

Thank you, Mery, for teaching me so many things, and for sharing every challenge and every success.

My thanks also to Eleonora, Francesco, Giulia, and all the past and present members of the "Lab Mozz": wonderful people that helped me throughout my time as a Ph.D. student.

Finally, to Letizia and my family: I will never be able to adequately express how much I need to thank you for always believing in me and for giving me the energy to overcome every hurdle.

Introduction

1 *STAPHYLOCOCCUS AUREUS*

S. aureus is among the first bacterial pathogens to be identified [1,2], and it belongs to Staphylococcaceae, a family of Gram-positive cocci. The word "Staphylococcus" is composed by "staphyle" and "coccus". The first term derives from the Greek word for a bunch of grapes and describes the ability of these bacteria to grow in grape-like clusters. "Coccus" simply means grain or berry [3]. The specific epithet "*aureus*" has been assigned for the golden-yellow pigment that characterizes the colonies, which has been historically associated with the more pathogenic strains of *Staphylococcus* [4]. Recently, Liu and co-workers [5] confirmed the antioxidant activity of the carotenoid pigments responsible for the colour, unraveling their contribution to *S. aureus* pathogenesis as virulence factors. Along with the color, the identification of pathogenic strains is carried out with a coagulase test [6,7], where the presence of the so-called staphylocoagulases is assessed. These bacterial enzymes interact with prothrombin and activate the host coagulation cascade leading to the encapsulation of staphylococcal communities and subsequent abscess development [8]. This mechanism promotes the infection persistence and the evasion from the host immune system thus is considered a virulence strategy of the bacterium. Therefore, staphylococcal strains that result positive to the coagulase test are usually the more pathogenic and threatening.

1.1 Infections by *S. aureus* and virulence factors

S. aureus is one of our most common bacterial residents, and it is estimated to colonize the anterior nares of more than 20% of the population [9,10]. However, it can give life-threatening diseases, among which bacteremia, infective endocarditis, skin and soft tissue infections, and osteoarticular infections [11]. The bacterium becomes particularly pathogenic when it manages to breach the sites of initial colonization enabling its access to contiguous tissues and the bloodstream [12].

The effectiveness of *S. aureus* pathogenicity is strictly related to the wide range of virulence factors that have been developed by the bacterium [12,13]. The major roles of these effectors range between immune evasion, nutrient acquisition, cytolytic activity, and host adhesion. Due to their importance, complex regulatory mechanisms have been evolved to ensure the expression of these factors only when necessary [14].

The following sub-sections and Figure 1 have the aim of describing the most prevalent groups of virulence factors, whereas the complete list of these factors is presented at http://www.mgc.ac.cn/cgi-bin/VFs/genus.cgi?Genus=Staphylococcus.

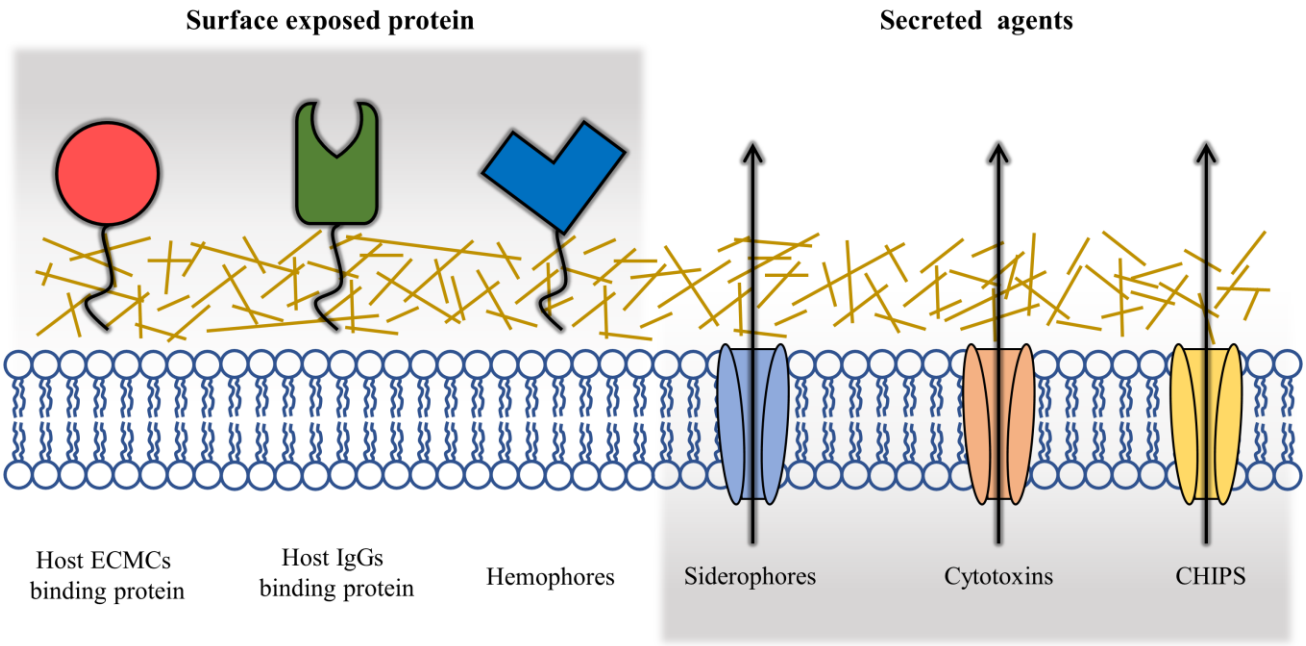

Figure 1: Schematic representation of virulence factors of S. aureus divided in surface exposed proteins and secreted agents. Abbreviations: extracellular matrix component (ECMC), Immunoglobulin G (IgG), and chemotaxis inhibitory protein of staphylococci (CHIPS).

1.1.1 Microbial Surface Component Recognizing Adhesive Matrix Molecules (MSCRAMMs)

The term MSCRAMM identifies a family of surface proteins that interact with the host extracellular matrix component (ECMC - such as fibrinogen, fibronectin, and collagen) enabling bacterial colonization of the host and subversion of host immune system [15]. Recently, the definition of MSCRAMM has been extended including all surface proteins made of two adjacent Immunoglobulin G-like subdomains [16,17]. Interestingly, most of the proteins belonging to this class seem to be naturally selected to have more than one function, and this is probably due to the limited number of surface proteins that may be expressed by the bacterium [17,18]. Examples are clumping factors or collagen-binding proteins that bind fibrinogen and collagen, respectively [17].

1.1.2 Iron uptake

S. aureus, like many other bacterial pathogens, needs iron for its survival [19–21]. This metal plays a key role in many catalytic processes, such as DNA, RNA, and amino acids synthesis, electron transport, and peroxide reduction. The sequestration of iron, implemented by humans and many other vertebrates, has a significant antimicrobial activity and is part of the so-called nutritional immunity [22,23] (see section 2.2 for details). To overcome this limitation, *S. aureus* has developed two sophisticated classes of molecular effectors, siderophores and hemophores, that allow to retrieve inorganic and heme-bound iron, respectively [24–26]. Hb is the principal target of hemophores, but it is normally secured inside red blood cells (RBC), thus, to increase the availability of free Hb *S. aureus* secerns hemolysins [27]. They are pore forming proteins that cause lysis of RBC. Hemolysins are important *S. aureus* virulence factors as well. Moreover, iron and heme may be released by macrophages and neutrophils to trigger the production of several microbicidal oxidants in the so-called oxidative burst. In such circumstances, iron acquisition systems directly reduce the concentration of these harmful molecules thus shielding the pathogen from the host immune system attack [28]. Iron acquisition and protection against oxidative damage are essential for *S. aureus* survival and thus for its pathogenesis, turning into virulence factors the molecular effectors involved in these systems [18,29,30].

1.1.3 Immune evasion

The last type of virulence factor includes both surface exposed protein and secreted macromolecules that directly engage host effectors enrolled within its immune response.

Staphylococcal protein A (SpA) is present on the bacterial surface, and its presence is correlated with the opsonophagocytosis failure and the B-cell death [31]. To exert its function SpA binds the Fc region of antibody and the Fab regions of the B-cell receptor. Together with SpA, cytotoxins and chemotaxis inhibitory protein of staphylococci (CHIPS) are the two principal secreted virulence factors aimed to immune evasion. Leukocidins are examples of cytolytic toxins, and fulfill their role creating pores onto the cell membrane of leukocytes [32], while CHIPS can specifically inhibit neutrophils and monocytes to block the immune system response [33].

1.2 The staphylococcal resistance to antibiotics

Before the advent of antibiotics, the fatality rate of *S. aureus* bacteremia was greater than 80% [34], remarking the unquestionable pathogenicity of this bacterium. Ironically, *S. aureus* is a valid target for every antibiotic developed so far, but its well-known ability to become resistant makes it immune to the majority of them [35]. This ability is strictly related to two main factors: its presence in the host as an asymptomatic resident [9,10] and its powerful horizontal and vertical gene transfer ability [35,36].

Just a few years after penicillin launch, in the early 1940s, the first resistant strains of *S. aureus* were identified [37,38], which based their resistance mechanism on penicillinase activity [39]. To overcome the resistance, methicillin, a penicillin cognate antibiotic insensitive to the bacterial enzyme, has been developed in 1960 [40]. Sadly, the year after the first MRSA was identified [41]. Thereafter, many MRSA strains have been isolated. The complete history of the resistance evolution has recently been reviewed by Lakhundi and Zhang [42].

In the beginning, methicillin-resistant strains were isolated only in the nosocomial environment [43], thus they have been referred to as hospital-associated MRSA. There was probably a link between the propensity of *S. aureus* to incorporate external genes into the genome and the need for large use of antibiotics within medical procedures. But then, in the early 1990s, new MRSA strains were identified amongst healthy people [44].

Nowadays, MRSA has acquired a dramatic relevance since it is becoming more and more resistant to the arsenal of antibiotics currently in use. Updated calculations in the United States reported nearly twenty-thousands of deaths related to MRSA infections [45], and, in general, it has been estimated that by 2050 antibiotic-resistant bacteria will kill more patients than cancer [46].

Notably, MRSA has been listed as one of the "ESKAPE pathogens" in 2008 [47], as a "serious threat" in the Centers for Disease Control and Prevention assessment of antibacterial resistance threats in 2013 [48], and as a "high priority" in the global priority list of antibiotic-resistant bacteria by the WHO in 2017 [49]. In short, the major health threat caused by antibiotic-resistant strains of *S. aureus* makes it imperative to better understand how the bacterium infects the human host.

2 HUMAN IMMUNE DEFENCE AGAINST *S. AUREUS*

Different mechanisms have evolved in living organisms to help them tackling the invasion by bacterial pathogens that, taken together, compose the immune response. Generally, it is possible to identify an innate and an adaptive immunity. The first is mainly non-specific against the invader, whereas the latter has specifically evolved against a single pathogen [50]. In this scenario, cellular immunity (e.g., neutrophils and T-helper cells) takes part in both innate and adaptive responses, and it has been designated as having a major role in the response against *S. aureus* [51]. While the entire immune system plays a key role in the defense against *S. aureus*, the description of the complex mechanisms of adaptive immunity is beyond the scope of this thesis, which will focus on a specific form of the innate immunity, called nutritional immunity.

2.1 The first host shield: innate immunity

S. aureus is routinely colonizing the human skin and mucosa; however, its threatening pathogenesis starts when it gains access to underlying tissues and the bloodstream. The first defensive line deployed to avoid bacterial invasion consist of anatomical and physiological barriers, the main ones are an intact skin, a mucociliary clearance system, the strongly acidic stomach medium, and the presence of bacteriolytic enzymes in the major glandular secretions [52,53]. A set of Toll-like receptors (TLRs) act together with these barriers as a reinforcement with the final aim of allowing local colonization but avoiding systemic invasion. TLRs are transmembrane proteins mainly expressed by macrophages and dendritic cells that specifically recognize diverse microbial epitopes (e.g., TLRs1/2/6 selectively detect pathogen lipoproteins) to identify intruders and trigger the appropriate adaptive immune response [54]. If these boundaries are broken, bacteria will proceed in its pathogenesis. At this stage, pattern recognition receptors (PRRs) become essential to detect the invader and activate a large number of defense processes, which include opsonization, activation of complement and coagulation cascades, phagocytosis, activation of pro-inflammatory signalling pathways, and induction of apoptosis [55]. Along with the immune response to bacterial infection, the host has evolved sophisticated systems that withdraw free iron, and other transition metals, in a

process called “nutritional immunity” that starve bacteria of elements that are essential for their fitness and virulence. [22].

2.2 Nutritional immunity

2.2.1 Iron: a double-edged sword

Iron is a vital nutrient for almost all forms of life. Its electron configuration allows the formation of stable ferrous (Fe(II)) or ferric (Fe(III)) ions, and thus it is utilized in many biochemical and biological processes for a wide range of electron transfer reactions within a broad electrochemical potential (−500 / +500 mV) [56]. The same chemical properties are responsible for the generation of reactive oxygen species (ROS) that may damage biological macromolecules. This subsection is aimed to present both these crucial aspects of this essential trace element.

The Biosphere is characterized by the presence of a rich variety of nutrients that have allowed the development of life. Among these nutrients, iron is one of the most plentiful atoms, and it is the most abundant transition metal in the human body [57,58].

In biological systems, two major iron pools exist: hemic and non-hemic iron. Heme is a multifunctional prosthetic group largely used in biological processes, whereas non-hemic iron is found alone as an inorganic cofactor, or in iron-sulfur (Fe-S) clusters [59,60]. Either way, its ability in cycling between Fe(II) and Fe(III) is its distinctive feature. Notably, the free form of ferric iron at neutral pH forms highly insoluble amorphous hydroxides (solubility limit of 10^{-18} M) [61], and needs to bind to proteins or hydrophilic chelators to be biologically available.

On one hand, members of oxidoreductase, oxygenase, and dehydrogenase enzyme families base on non-hemic iron their catalytic activity [62–64]. Fe-S clusters are key components in the respiratory electron chain inside ferredoxin, but also important in iron storage or the regulation of gene expression and enzyme activity [60]. On the other hand, heme finds a central role in cellular metabolism when it is bound to cytochromes [65,66], it is essential for many catalases and nitric oxide synthases [67,68], and is involved in gas sensing, microRNA processing, and cellular differentiation [69–71]. Lastly, Hb and myoglobin (Mb) rely on heme to bind oxygen [72].

Heme is a macrocyclic molecule (Figure 2) composed of a protoporphyrin IX molecule and an iron atom in its core. Within the heme, iron is coordinated by four pyrrole nitrogens. Since octahedral coordination geometry is preferred by both Fe(II) and Fe(III) [73], besides the former four chemical interactions, the hemic-iron establishes two more coordination bonds. These additional bonds allow the embedding of the heme molecule inside heme-binding proteins and its capacity to bind different ligands. When the heme is bound to a protein, the axial coordination bonds are either established with two amino acid residues (e.g., hexacoordination) or one amino acid residue and one small molecule (e.g., pentacoordination). Typical amino acids that form coordination bonds with heme are histidine, tyrosine, methionine, or cysteine, while principal ligands of the cofactor are oxygen, carbon monoxide, nitric oxide, and cyanide [74].

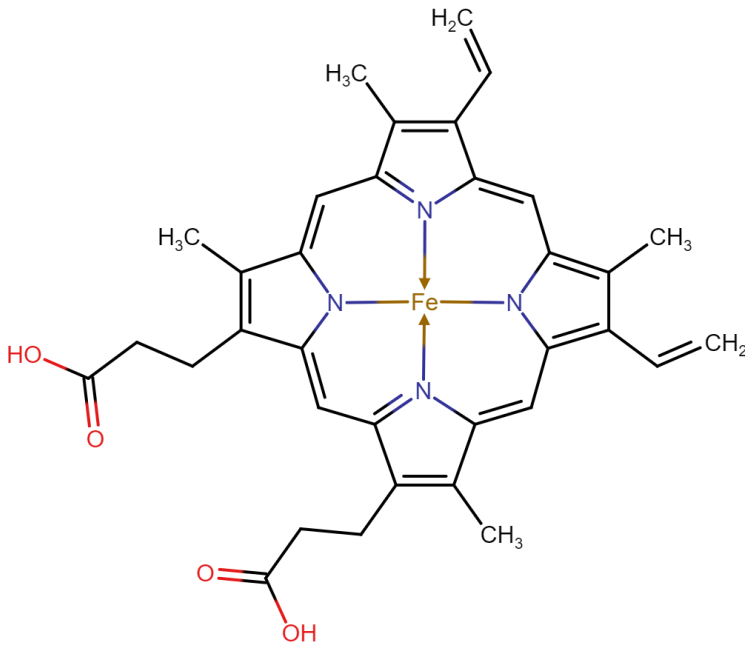

Figure 2: Heme molecule. Chemicalize was used for molecule representation, August 2020, https://chemicalize.com/, developed by ChemAxon.

As previously stated, together with its indispensable role in several biological processes, iron in the low micromolar range, both in the hemic and in the non-hemic forms, results in highly toxic species [75].

One of the main reasons why iron gets dangerous is the ability to react with oxygen leading to the formation of ROS. The catalyzed processes are well described by two chemical reactions, proposed by Fenton in 1894, and by Haber and Weiss in 1974 [76,77].

$$H_2O_2 + Fe(II) \rightarrow Fe(III) + OH^- + OH^{\cdot}$$

$$Fe(III) + O_2^{\cdot -} \rightarrow Fe(II) + O_2$$

In this respect, the presence of too high concentration of iron in a biological milieu determines the accumulation of large amounts of ROS. The latter are chemical species containing oxygen and presenting highly reactive unpaired valence electrons or unstable bonds. They can be neutral molecules (e.g., hydrogen peroxide), ions (e.g., superoxide anion), or radicals (e.g., hydroxyl radicals) and they are particularly harmful due to their ability in reacting/damaging biomolecules (proteins, lipids, and nucleic acids), altering protein biosynthesis of proteins, and leading to a general impairment of cell proliferation [78,79].

Notably, oxidative stress linked to the presence of ROS has been associated with carcinogenesis, atherosclerosis, and diabetes and neurodegenerative disorders insurgence in mammals [80–82].

2.2.2 Iron homeostasis in human: the core of the immunity

The overall amount of iron in the human body is estimated to range between 3 and 5 grams [57,83], and 70-80% of this metal is found within the heme molecule [83,84], which is principally bound to Hb and Mb to support the distribution of oxygen to peripheral tissue and aerobic metabolism [85]. Since free iron forms highly insoluble oxides under oxidizing conditions, the remaining part of the human pool is managed by iron-binding proteins that capture it in a biologically useful form [86].

Owing to the reactivity of both non-hemic and hemic forms of iron and the lack of regulated pathways for its excretion [87], its bioavailability is strictly limited within the human body, thus requiring meticulous homeostasis. This careful control will also restrict the access to iron to *S. aureus* and many other pathogens, resulting in the so-called nutritional immunity [22], i.e., the process by which limitation of metal bioavailability leads to reduced bacterial

colonization, hence it is an antimicrobial strategy. The definition of the nutritional immunity has been extended including the mechanisms by which the host also controls the local concentration of manganese, zinc, and other transition metal, thus resulting in more extensive metal starvation of pathogens [58]. The following sub-sections and Figure 3 are meant to explain the mechanisms underlying the regulation of free and heme-bound iron concentrations.

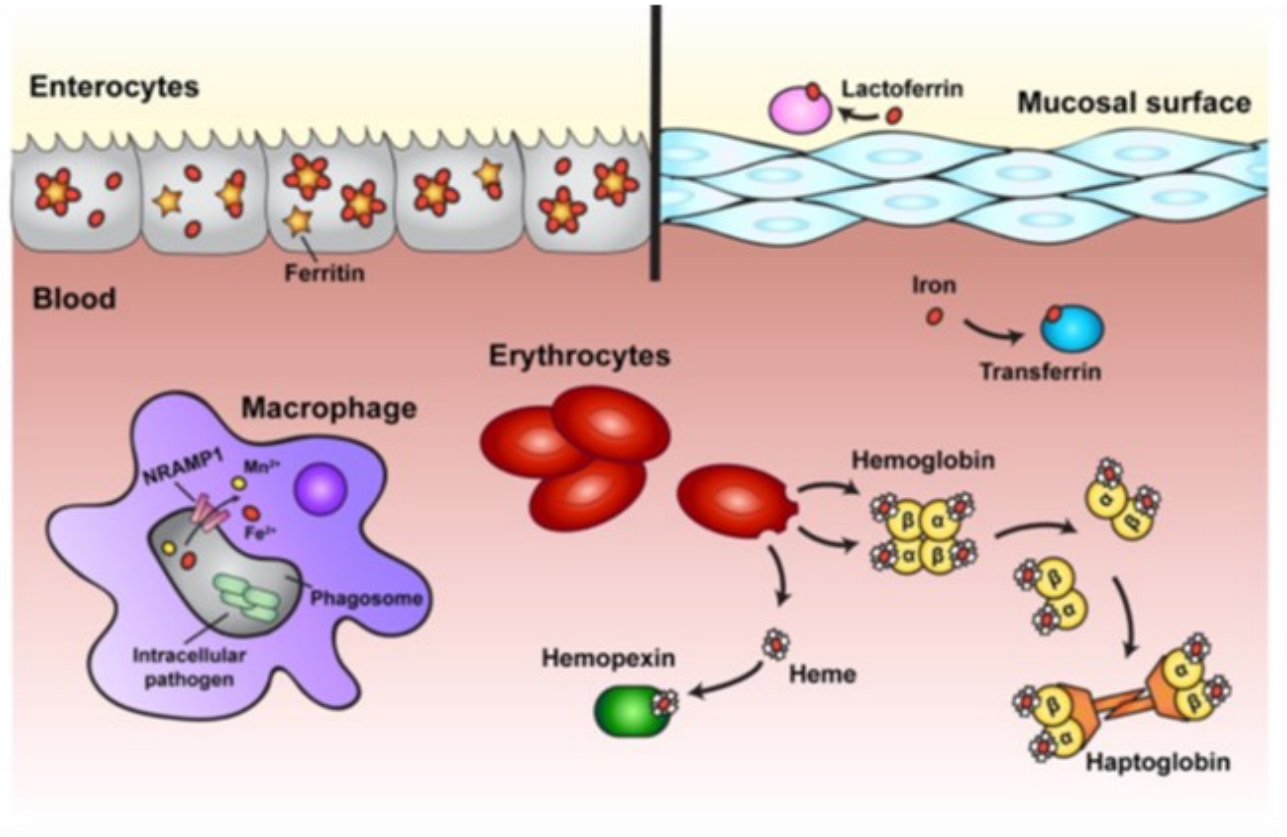

Figure 3: Overview of nutritional immunity systems [88].

Non-hemic iron. In mammals, free iron is virtually absent. Its concentration is estimated to be less than 10^{-20} M [89], even lower than its solubility limit of 10^{-18} M. Since the concentration of iron needed by bacteria is around 10^{-6} M [90], such a low concentration has an antibacterial activity, and it is the most striking example of nutritional immunity.

Before discussing the host effectors that lower the free iron concentration, it is important to emphasize that the 70-80% of iron is complexed within the heme molecule, thus non-hemic iron is only the 20-30% of the entire human pool. To manage this latter portion, several host iron-binding proteins are engaged, and the main are ferritin [91], transferrin (Tf) [92], and lactoferrin (Lf) [93]. Other than limiting the iron availability, these three proteins ensure the

metal transport and storage throughout the entire organism, preventing the iron-mediated oxidative damage. In addition to iron-binding proteins, a small portion of non-hemic iron is sequestered inside iron-dependent enzymes and Fe-S clusters [94].

The iron-binding proteins have different localization within the organism, ferritin is physiologically located inside cells, whereas Tf and Lf carry out their functions extracellularly (vide infra). More exactly, ferritin manages almost all the non-hemic iron (up to 30% of the entire host pool) [87], whereas the Tf family (which includes both serum Tf and Lf) carries approximately 0.1% of non-hemic iron [87,95].

By storing the great majority of non-hemic iron, ferritin, plays a key role in iron metabolism [96]. Sequestering this transition metal, ferritin exerts the dual functions of iron detoxification and iron reserve, which render the protein essential and thus ubiquitously distributed among most living species. Ferritin is a heteropolymeric protein that carries up to 4500 iron ions inside its hollow shell structure [96]. It is principally found in enterocytes, but also in erythroblasts, hepatocytes, and macrophages [97]. Iron is imported inside the cells where ferritin is localized by a specialized divalent metal transporter 1 (DMT1) [98], also known as natural resistance-associated macrophage protein 2 (Nramp2) [99,100]. Once inside the cell, iron is incorporated by ferritin in the crystalline form, which is principally composed of ferrihydrite and phosphate ions [96].

The transport of the non-hemic iron throughout the organism is carried out by serum Tf [101]. This protein retrieves metal absorbed from the gut and released from lysed cells. The major player allowing Tf binding to dietary iron is ferroportin (Fpn), a membrane protein that is responsible for the release of this metal on the basal side of enterocytes [97]. Fpn is also present on the membrane of hepatocytes, where it enables the deployment of the stored iron. Interestingly, Fpn expression on enterocytes and hepatocytes is mutually regulated, suggesting the strict involvement of both in iron homeostasis [102,103]. Lastly, Fpn is located on macrophages, which are the second major storage site of inorganic iron in the body [94] and where Fpn is expected to play a similar role as on the hepatocytes. Interestingly, regulation of Fpn expression has a direct role in nutritional immunity. The other way around, most of the Tf-bound iron is utilized by the erythropoietic process, where it is incorporated in the heme molecule and thus in Hb [87]. One of the key properties of Tf is its particularly high affinity for iron, the estimated K_D is in the order of 10^{-20} M or even lower [89,104,105]. The large

affinity and its molar excess against free non-hemic iron (only 30% of Tf is saturated in physiological condition) ensure the virtual absence of the free metal within the organism [106]. To deliver the iron, Tf interacts with a dedicated receptor (TfR1) exposed by cells in need [107]. Once the complex between transferrin and its receptor is formed, the cellular uptake of iron begins, following the so-called Tf cycle [107]. The key steps of this cycle are the receptor-mediated recognition of iron-bound Tf, the internalization of the latter inside dedicated endosomes, and the pH-dependent release of iron within these intracellular organelles. Once liberated from Tf, the iron is pumped from the endosome into the cytosol through DMT1 [108]. Finally, apo-Tf is transported back outside the cell.

Lf belongs to the Tf family and it is in charge of chelating iron in tears, breast milk, seminal fluid, and saliva [105], but it is also secreted by neutrophils during infection and/or inflammation processes [109]. The affinity of Lf for iron is similar to that of Tf (K_D lower than 10^{-20}), but its distinctive ability in preserving the affinity for iron in very acidic conditions (down to pH 3) is necessary for ensuring its activity in infection/inflammation sites [105,109,110]. Furthermore, Lf shows a direct bactericidal effect through its proteolytic activity [89,104], likely following a serine protease mechanism of action. Particularly attractive for the focus of the thesis is the study performed by Clarke and co-worker who reported an impairment in antimicrobial activity of Lf on *S. aureus* in the presence of either PMSF (a directed inhibitor of serine proteases) or IsdA, the staphylococcal hemophore [111]. Interestingly, Lf is one of the most abundant antistaphylococcal polypeptides in human nasal secretions, and its proteolytic activity could underpin its role [111].

When bacterial pathogens infect the host, the iron homeostasis becomes even more complicated and nutritional immunity needs to be strengthened. Some of the proteins involved in nutritional immunity form the so-called “acute-phase proteins”, proteins whose expression is modulated, usually increased, during the first stages of infection. The first problem can arise from the uptake of iron by macrophages through DMT1, aimed at the metal storage needed for the oxidative burst, and the presence of intracellular bacterial pathogens into the phagosomes, which could instead benefit from the increased iron concentration in their colonization site. To achieve iron starvation of these bacteria, the specialized natural resistance-associated macrophage protein 1 (NRAMP1) forces iron out the compartment [107]. Moreover, various excellent tricks have been developed by extracellular bacterial pathogens to obtain iron when

it is limited by host nutritional immunity. Among them, siderophores are small molecules that bind non-hemic iron with an extraordinary affinity. Siderophores are secreted by bacteria and then retrieved when they have bound iron (vide infra). To overcome this bacterial assault, the expression of Tf is stimulated [112]. Moreover, a specialized set of proteins called siderocalins (or neutrophil gelatinase-associated lipocalin - NGAL) are secreted by neutrophils and bind bacterial siderophores (both in iron-free and iron-bound form) with high affinity making them no longer available to bacterial retrieval [113,114].

A more sophisticated system to iron starve pathogenic bacteria relies on hepcidin, a small peptide hormone, that is mainly expressed by hepatocytes [97]. Its expression in the liver is repressed by hypoxia and active erythropoiesis, while it is promoted by reduced concentrations of plasmatic iron [115,116]. This hormone plays a fundamental role in regulating cellular iron efflux, by interacting with Fpn [97] which is the major player in iron absorption and mobilization from storage sites [102,103]. Hepcidin directly interacts with Fpn, and once formed, the hepcidin-Fpn complex is prompted to its internalization and degradation [103]. Thus, the release of hepcidin leads to reduced absorption of iron in the bowel and limited unloading of iron storages.

Hemic iron. Most human iron is in the hemic form [83,117], again the vast majority of hemic iron is bound by Hb [85,87,94]. The fact that Hb is secured inside erythrocytes prevents direct access to this iron source by bacterial pathogens. However, hemolysis occurs physiologically as well as under some pathological conditions, e.g., *S. aureus* produces specialized hemolysins to get access to hemic iron [118]. To avoid oxidative damage and bacterial access to hemic-iron, two essential proteins have evolved: haptoglobin (Hp) and hemopexin (HPX) [119–121]. Whenever Hb leaks from erythrocytes, it undergoes processes that increase its toxicity. The physiological tetramer tends to dimerize, due to its dilution into the bloodstream, and heme is prone to oxidation and it can also be lost [122]. Hp binds Hb dimer with an extremely high affinity (K_D lower than 10^{-12} M) [123,124] and ensures the Hb clearance from the vascular compartment [125]. Hp stabilizes Hb and promotes the recognition of the Hb-Hp complex by the macrophage scavenger receptor CD163 [126]. Hb-Hp complex is internalized, Hb is degraded inside lysosomes and heme is disassembled by a specific oxygenase (HO-1) to release iron and bilirubin [127]. Hp is both a physiologically present and an acute-phase

protein, and it is mainly produced by the liver. Under normal conditions, the plasma concentration of Hp ranges between 0.5 and 3 g/L, which is sufficient for Hb clearance during moderate hemolysis. However, Hp expression is markedly induced (up to 5-fold) by the presence of interleukin-6 (IL-6), IL-1, and other cytokines produced in response to infection and inflammation [125,128]. IL-6 and other ILs also induce the expression of the CD163 receptor and HO-1 [129,130]. Remarkably, two different Hp variants have been identified in humans (Hp-1 and Hp-2), and these result in three distinct phenotypes: Hp1-1, Hp1-2, and Hp2-2. The main differences between them are the quaternary structure, the affinity for Hb, and the binding to the CD163 receptor [123,131]. Among Hp phenotypes, Hp2-2 has a decreased affinity for Hb and thus correlates with a more serious oxidative damage due to a reduced plasmatic Hb clearance. Patients expressing Hp2-2 have worse infections outcome and high vascular risk [132], hinting at the importance of Hp in iron homeostasis.

In addition to free Hb, which could lose heme before being caught by Hp, other hemoproteins cause the release of the prosthetic group into the bloodstream. Under physiological conditions, free heme is aspecifically trapped by the ubiquitous albumin, which has a reasonable affinity for it (around 10^{-8} M), and then relocated to the HPX, which has a high affinity for heme (K_D lower than 10^{-12} M) [133]. Under active infection conditions the concentration of free heme may increase resulting in the HPX overexpression, which is an acute-phase glycoprotein, and its expression is directly related to IL-6 and other ILs [134,135]. Similarly to Hp, heme-binding HPX is recognized by CD91 receptors on hepatocytes [136], where the heme is degraded by specific heme oxygenase and the iron is recycled [121].

3 *S. AUREUS* STRATEGIES FOR IRON ACQUISITION FROM HUMANS

In the former section, it has been presented the essentiality of iron, in both hemic and non-hemic forms, to enable many vital functions in almost every form of life. During the infection, bacterial pathogens are confined inside the host, which tries to sequester iron to starve the intruders. The present section is aimed at introducing the molecular mechanisms developed by *S. aureus* to face human nutritional immunity. Since iron acquisition seems to be fundamental for *S. aureus* growth during colonization, most of these strategies have been indicated as virulence factors, and thus as a potential target for antimicrobial agents (Figure 4).

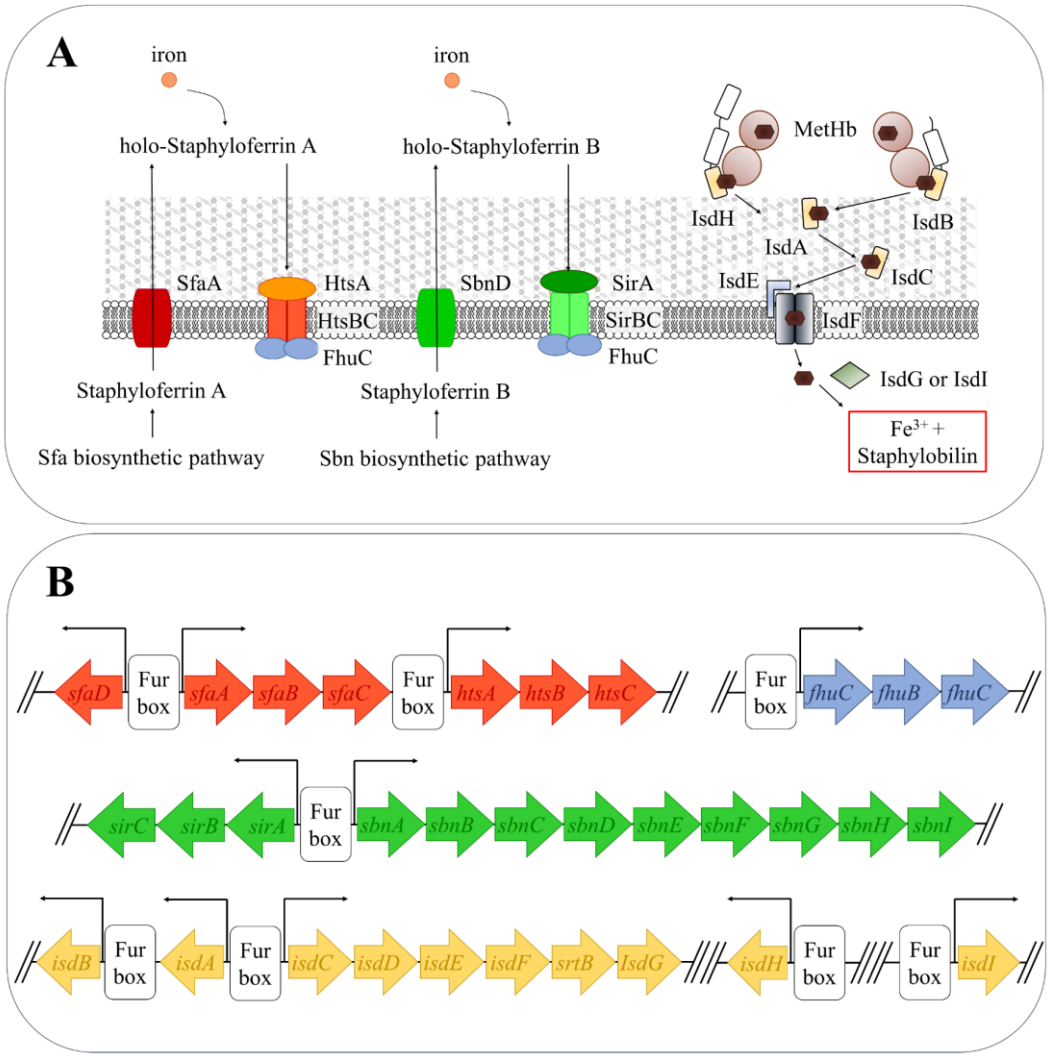

Figure 4: A model of the S. aureus iron acquisition pathways, adapted from [20]. (A) Schematic representation of proteins employed for iron acquisition. (B) Genetic loci involved in S. aureus iron acquisition.

3.1 Regulation of iron uptake

The progress in staphylococcal infection usually involves the formation of purulent abscess, which has been described to proceed in four stages [137]**.** In the first stage, the bacteria strive to survive in the bloodstream and start to disseminate to peripheral tissues. In the second stage, staphylococcal cells reach tissues where the abscess will form. Stage three involves the formation of a large mass of invading pathogens. Finally, the mature abscess in stage four undergoes rupture of his boundaries leading to bacterial dissemination aimed to the formation of new infection sites. In the context of the second stage, essential nutrients are needed. Among them, iron is one of the most difficult to retrieve due to the nutritional immunity deployed by the host. To face the problem, *S. aureus* can alter its protein expression profile by exploiting the activity of the ferric uptake regulator (Fur) [110].

Fur is a transcription factor present in almost all Gram-positive and Gram-negative bacteria, where it principally acts as a repressor exploiting Fe(II) as a corepressor providing optimized management of both intracellular and extracellular concentration of iron. Notably, the virulence of pathogenic bacteria has been demonstrated to be directly related to the presence of Fur [138]. In this respect, *S. aureus* is not an exception and the expression of almost all the proteins enrolled by this bacterium for the iron uptake is regulated by Fur [110,139–144]. The transcriptional modulation is achieved by Fur recognition of a specific target sequence, the so-called “Fur box”, that overlaps the RNA polymerase binding site. Fe(II) acts as a corepressor and the formation of the complex with Fur enables the binding of the latter to the specific DNA sequence. Notably, the Fur affinity for iron is in the low micromolar range, and the holo-form of the repressor presents a nanomolar affinity for the DNA. Conversely, Fur mutants defective for the iron-binding do not recognize and associate with their related DNA sequence [145]. Therefore, a decrease in iron concentration within bacterial cells involves Fur release from the DNA, after the Fur-Fe(II) complex dissociation, and results in the transcription of the controlled genes [142]. Besides the iron acquisition, Fur is responsible for switching on genes coding virulence factors, which strengthen the staphylococcal ability to survive within the host environment [14], suggesting that Fur plays a pivotal role in many aspects of infection establishment [146,147]. A good example is the expression of KatA, which is a catalase that manages oxidative stress, and its transcription is directly controlled by Fur [148]. Differently from the ordinary mechanism of action, Johnson and co-workers [149] reported that expression

of the Eap/Emp system, involved in biofilm formation, is iron-independently regulated by Fur. Furthermore, Fur cooperates with different other transcription factors (i.e., Agr, Sae, and Rot): a good example is the transcriptional regulation of IsdA and IsdB, which is controlled by both Fur and Sae [147]. The last important effect of Fur transcriptional control is probably achieved through an sRNA-dependent modulation [150,151] and results in the down-regulation of the TCA cycle, this latter machinery involves many iron-containing enzymes and its deactivation indirectly reduces iron demands. Suppressing biological pathways that leads to a reduced iron demand is known as the "iron-sparing" response, which has been found in *S. aureus* and many other bacteria [152–155]. Notably, the simultaneous upregulation of fermentative metabolism, that compensates the energetic needs of the bacterium, leads to the production of lactate. The latter is exported outside the bacterial cell where it lowers the pH. A lower pH increases iron bioavailability due to the increase of Fe(III) solubility and the decrease in the affinity of Tf for iron [110].

3.2 Non-hemic iron capture

Iron deprivation leads bacteria to secrete siderophores, which are secondary metabolites able to form soluble Fe(III) complexes to scavenge free ferric iron from the environment, even if it is present in a very low concentration [156]. Notably, also fungi and plants produce siderophores [157], but they will not be discussed here. The high affinity and the great selectivity for ferric iron are the essential properties that characterize siderophores [157]. Within the human host, the incredibly low K_D of these scavengers (up to 10^{-52} M [158,159]) allows bacteria to directly compete with Tf family proteins for iron [20,88], or to solubilize the ferric hydroxides precipitates. At the same time, the higher selectivity for ferric iron (which is achieved through the presence of hard negatively charged electron donors in the binding site [160]) enables the exclusive uptake of iron from the environment and the control of the metal reactivity, by reducing the redox potential and thus hampering the harmful Fe(III)-Fe(II) cycle [61]. Within the bacterial genera, many types of siderophores have been identified. The main classification is based on the functional groups involved in iron coordination, thus allowing to separate three principal classes of siderophores: catecholates, hydroxamates, and (α-hydroxy)carboxylates. In addition to these, 'mixed type' siderophores carrying

hydrophenyloxazolone, α-aminocarboxylates, and α-hydroxyimidazole groups are also present but in lower amounts [157,159,161,162].

3.2.1 *S. aureus* siderophores

The two principal *S. aureus* siderophores are staphyloferrin A (SA) [163,164] and staphyloferrin B (SB) [165,166], which are both characterized by carboxylate iron-chelating groups. SA and SB allow *S. aureus* to face iron starvation by accessing the sources of inorganic iron in the extracellular media of the colonized host. Interestingly, these two siderophores seem to have specific roles in different types of infection: SA generally spreads beyond the site of colonization when secreted, while SB seems to act locally [167]. Additionally, SB seems to mainly support virulence being produced only by the most invasive strains of *S. aureus*, while SA is produced constitutively [168]. These recent findings disclose a sophisticated regulation of siderophore usage by *S. aureus* under different conditions. Notably, the presence of at least one of the two siderophores is essential for *S. aureus* growth and colonization in iron-depleted media [169], revealing their importance as virulence factors [167,170].

The proteins involved in the biosynthesis and secretion of SA are coded by the *sfa* gene cluster (Figure 4), which is under the control of Fur and thus is up-regulated under iron starvation [171,172]. Subsequently, the iron-bound SA is imported by the heme transport system (HtsABC) [173]. Although the name is misleading, it has been confirmed that the lipoprotein receptor HtsA forms a tight complex with SA (with a dissociation constant in the low nanomolar range) [171,173,174] and the HtsBC dimer forms an integral membrane permease that ensures the siderophore uptake [171]. Contrarily to the dedicated systems described so far, SA shares with SB a non-specific ATPase FhuC that allows ATP-dependent siderophore transport [171,175]. The gene coding for FhuC is part of the ferric hydroxamate uptake operon (*fhuCBG*), which will be further discussed below. Once the Fe-siderophore complex is inside the cell, the iron needs to be recovered, and the most likely mechanism adopted by *S. aureus* is the reduction of ferric iron, which is demonstrated by the need of the bacterium for NrtA, a nitroreductase, to correctly utilize SA-iron [176]. The negative redox potential of ferric iron is the basis of siderophore affinity and selectivity, and the reduction of the metal severely impairs the siderophore binding ability by decreasing the thermodynamic stability and increasing the

kinetics of ligand exchange [157,160]. Notably, the reductive retrieval of iron allows the full recovery of active siderophores ready for another uptake cycle.

SB is synthesized and exported by the SbnA-I protein system (Figure 4), which is encoded in the Fur regulated *sbn* locus [177]. As well as SA, the iron-SB complex is actively imported inside the bacterial cell thanks to the so-called staphylococcal iron-regulated transporter complex (SirABC), which is an ABC transporter [178] that relies on the non-specific FhuC ATPase to generate the energy needed. Subsequently, iron is accessed from the complex with SB by a mechanism that is yet to be fully elucidated. Although reductive release is a convincing mechanism for Fe(III)-SA complex, any viable theory for iron recovery from the complex with SB has not been identified [176].

SA and SB are the most studied and characterized *S. aureus* siderophores, but a few cognate iron scavengers have been studied over the years. The first is aureochelin, which has been identified by Courcol and co-workers [179], but its structure is not known, and its actual existence is still debated [140]. The second is called staphylobactin [162], and only recently a newly identified iron-regulated gene cluster was proposed to be responsible for its production. Lastly, a well-characterized dipositive cation scavenger produced by *S. aureus* is called Staphylopine (StP) and, besides binding and importing ferrous iron, it ensures the uptake of copper, nickel, cobalt, and zinc as well.
in addition to those directly produced, *S. aureus* is well known for its ability in making maximum use of biological resources in its environment, and so it is for the exploitation of siderophores produced by bacterial cohabiters (xenosiderophores). This ability allows *S. aureus* to reduce the metabolic cost for siderophore biosynthesis without reducing the iron acquisition, thus resulting in a huge advantage in the competition within the bacterial community. To import xenosiderophores, *S. aureus* has developed two different membrane permease systems, FhuBCDG and SstABCD, that allow the uptake of hydroxamate and catecholate xenosiderophores, respectively [170,180]. Once internalized, the bacterium needs to release the iron from the complex with siderophore. The process by which *S. aureus* recovers the scavenged iron is still not confirmed even for endogenous siderophores, and the problem is reflected on exogenous siderophores.

3.3 Heme: the *S. aureus* preferred iron source

In the presence of both hemic and non-hemic iron, the first one is the preferred source of the essential trace element by *S. aureus*, and the shortage of heme results in an impairment of the bacterial virulence [174,181–183]. Such preference is possibly related to more efficient systems for iron sourcing, but it is surely related to the great abundance of hemic iron within the human body (up to 70%). A key pathway for heme acquisition is the Isd system that ensures the extracellular extraction of the heme from Hb and its transport inside the cell, where it is utilized [19,139]. Interestingly, the same Isd system includes two heme oxygenases (IsdG and IsdI) that catalyze the iron release from the protoporphyrin group, however, the bacterium seems to be able to directly exploit the intact molecule as a prosthetic group ("heme hijacking hypothesis") [174,184], for example for the biosynthesis of cytochromes. Since this latter mechanism helps bacteria in saving metabolic energy, it could partially explain why heme is the preferred source, especially under iron-starvation. Likewise, the enrolment of cell-wall anchored hemophores, typical effectors of the Isd system, provides a more cost-effective strategy with respect to the production of siderophores, which can diffuse away from the site of colonization or be stealth by other bacterial cohabiters [185].

As Hb resides inside erythrocytes, *S. aureus* (just like many other bacteria) produces hemolysins to gain access to the human oxygen carrier. The expression of α-toxin (Hla), which is mainly responsible for hemolysis, is promoted by Fur under iron starvation, supporting the relationship between this pore-forming protein and the bacterial response to nutritional immunity [146]. A good validation of the efficiency of this mechanism is the ability of *S. aureus* to grow when erythrocytes are present as a sole iron source [181].

Although most of the human pool of heme is bound to Hb, also cytochromes, hemopexin, and Mb bind the prosthetic group and are potential targets for *S. aureus*. As a matter of fact, cytochromes are eventually too difficult to access by the bacterium inside mitochondria and hemopexin seems to not support *S. aureus* growth [181]. Contrarily, Mb could be a potential target for the bacterium due to its similarity to Hb, and, even if a definitive mechanism is still missing, the fact that *S. aureus* is able to effectively colonize the Mb-rich myocytes surely supports its potential role as heme source [118,186].

3.4 *S. aureus* iron homeostasis

As already discussed in section 2.2.2, an iron surplus within the cell becomes highly toxic for most organisms, and *S. aureus* is no exception. Differently from humans, this bacterium can excrete or store the superfluous nutrients. In this sense, it is important to differentiate between hemic and non-hemic iron. The excess of the first is managed by the heme sensor system (HssRS), a bicomponent system that detects heme excess and upregulates the expression of the heme-regulated transporter (HrtAB). The latter is an efflux pump that is responsible for the heme detoxification [187–190]. Otherwise, the prosthetic group is degraded to release iron by specific heme oxygenase (i.e. IsdG-I) [144]. Then, inorganic iron is carefully handled by the system described above. A different way of heme degradation has been related to the Fep system [143,191]. This is a Fur-regulated tricomponent protein network (FepABC) that binds heme outside the cell, reduces iron to bring it out the protoporphyrin ring, and internalizes the metal. The role of this system is still debated, but it has been proposed to reduce the extracellular concentration of hemic iron limiting the oxidative burst [143]. Finally, the presence of heme has been correlated to the transcriptional repression of the SB biosynthesis [192,193]. This observation uncovers the intricate mechanism by which the bacterium limits further non-hemic iron uptake when hemic iron is already exceeding. By contrast, non-hemic iron is stored by bacteria if it is not needed as a building block. For this purpose, *S. aureus* expresses the ferritin FtnA, which has a high degree of identity to other bacterial and eukaryotic ferritins, and allows the storage of large amounts of non-hemic iron. *S. aureus* also prevents oxidative damage due to the temporary iron overflow by producing hydroperoxide scavenger (AhpC) and a DNA protecting effector (MrgA). FtnA, AhpC, and MrgA are orchestrated by peroxide-responsive repressor (PerR), which works closely with Fur and ensures the protection of *S. aureus* from iron-related oxidative stress [194–196].

4 THE Isd SYSTEM

Heme is the preferred iron source of *S. aureus*, which acquires the prosthetic group from metHb [181]. The latter is the most abundant form of the protein free in the bloodstream, which is the only available to the bacteria, and it carries the hemic iron in the oxidized state. Following the oxygen carrier release from erythrocytes by hemolysins, the Isd system, which is composed of nine proteins (IsdA-I), is responsible for heme acquisition and it fulfils this task through four main steps: extraction from Hb, transfer across the cell wall, internalization, and degradation [19,137,139,174,184,197–206]. The expression of the genes encoding for Isd proteins is iron-regulated by a Fur box present upstream of each *Isd* operon (Figure 4), thus allowing the bacteria to face the iron shortage inside the host [19,142,182,207,208].

4.1 Stages 1 and 2: heme extraction and transport through the cell-wall

The first two stages of the Isd pathway are carried out by four cell-wall anchored proteins that are also called hemophores (meaning heme carriers) [209]. IsdB and IsdH are two surface-exposed Hb receptors, whereas IsdA and IsdC are partially and entirely embedded into the cell-wall envelope, respectively (Figure 4). These four proteins are covalently anchored to peptidoglycan by two sortases, the bacterial ubiquitous sortase A (SrtA) and the Isd-specific sortase B (SrtB) [20,181,202,210–214]. SrtA recognizes a defined molecular pattern at the C-terminus of IsdB, IsdH, and IsdA, composed of a hydrophobic domain and an LPXTG motif [207,215], and links the hemophores to immature peptidoglycan through a transpeptidation reaction [216]. Similarly, IsdC is attached to the cell-wall by SrtB, which recognizes a different binding motif, NPQTN [141]. The SrtB gene is located within the *Isd* locus (Figure 4) and it is controlled by a Fur box, similarly to all the other genes [139].

4.1.1 The heme relay system

The extraction process starts with the metHb capture onto the bacterial cell-wall, experimentally demonstrated by Torres and co-workers [181] that reported the binding of Hb to the *S. aureus* surface. At this level, two cell-wall anchored Hb receptors, IsdB and IsdH, bind the human oxygen carrier and subsequently extract the heme [139,217–219]. The holo-form, which refers to the heme-bound form, of the two Hb receptors passes unidirectionally

the prosthetic group to IsdA [203,204,220]. IsdA selectively transfers the heme to IsdC [203,221,222], which in turn passes it to the dedicated membrane transporter, IsdE [203,206]. Since the staphylococcal cell-wall is approximately 30-100 nm thick [212], the simple heme transfer from the environment that involves sequentially IsdB or IsdH, IsdA, and IsdC may not be enough to reach the cellular membrane, but the presence of multiple copies of the same hemophore (IsdA or IsdC) dipped into the cell wall and the ability of IsdA and IsdC to self-transferring the heme might allow the efficient transport of cofactor through the peptidoglycan layer [223].

The biochemical characterization of the pathway by which *S. aureus* extracts the heme and transports it through the cell-wall has been studied since its discovery. *In vitro* studies reported a relay system mechanism by observing that heme transfer from metHb to IsdA and from IsdB to IsdC were promoted by a catalytical concentration of IsdB and IsdA, respectively [198,204,224]. Moreover, the heme transfer between hemophores does not need energy input and the driving force for the process is simply the increase in the affinity of the hemophores for the cofactor moving from the outside to the cellular membrane [221,223,225,226]. The same transfer is supported by the ability of hemophores to form ultra-weak complexes which induce a transient structural distortion of the binding pocket of the heme donor and guide the cofactor out of it [205,223]. In the final step, an ultra-weak interaction allows IsdC to transfer heme to the membrane-anchored IsdE [223]. The similar affinity of IsdC and IsdE for heme [202] make the heme transfer "thermodynamically paralyzed" *in vitro* [204,206], however, the following internalization of IsdE-bound heme, which involves an ABC transporter, is expected to pull the IsdC-IsdE transfer process.

4.1.2 NEAT domain

Hemophores are modular proteins that possess one or more NEAT domains, which are composed of approximately 125 amino acids and are characterized by a conserved immunoglobulin-like eight-strands β-sandwich fold despite a variable degree of sequence identity (Table 1) [20,225,227–231]. Two principal types of this domain have been identified, which are referred to as "Hb-binding" and "heme-binding" domains, respectively.

Table 1: NEAT sequence identity (S. aureus, strain MW2) calculated using the Align tool in UniProtKB [232]. IsdB-NEAT1 (or IsdB^{N1}) / IsdH^{N2} and IsdB^{N2} / IsdH^{N3} pairs share a very high sequence identity, but also IsdB^{N1} / IsdH^{N1} and IsdH^{N1} and IsdH^{N2} are similar. Apart from the above-mentioned, NEATs generally share a 20% identity or lower. Similarities between "Hb-binding" or "heme-binding" domains are highlighted in yellow and orange, respectively.

	IsdA	**IsdB^{N1}**	**IsdB^{N2}**	**IsdC**	**IsdH^{N1}**	**IsdH^{N2}**	**IsdH^{N3}**
IsdA	100	22	21.1	20.9	21.7	17.3	21
IsdB^{N1}	22	100	11.7	21.3	44.5	64.6	13.1
IsdB^{N2}	21.1	11.7	100	22.6	14.5	13.3	57.6
IsdC	20.9	21.3	22.6	100	17.9	21	16.5
IsdH^{N1}	21.7	44.5	14.5	17.9	100	48.4	11.6
IsdH^{N2}	17.3	64.6	13.3	21	48.4	100	16.1
IsdH^{N3}	21	13.1	57.6	16.5	11.6	16.1	100

On one hand, the "Hb-binding" domain enables the tight interaction with the oxygen carrier of the two surface-exposed receptors IsdB and IsdH, which display one (IsdB^{N1}) [233] and two (IsdH^{N1} and IsdH^{N2}) [220,234] of these domains, respectively. The reason why the two receptors present a different number of Hb-binding domains is still debated, but the ability of IsdH to bind and extract heme also from the Hp-Hb complex could explain this difference [235]. Importantly, the presence of this functional domain is essential for enhancing the subsequent heme extraction even if it is not directly involved in the interaction with the cofactor [233]. The entire sequence of the "Hb-binding" domain has been intensively studied to identify the key residues responsible for the Hb affinity [233,234,236–241]. Notably, a "Hb binding region" has been identified on IsdB^{N1}, IsdH^{N1}, and IsdH^{N2} and it is characterized by the presence of a disordered coil (loop 2) in the apo-form that folds in an α-helix upon binding [233,242]. This region is fundamental for the formation of the complex with Hb, by interacting with A and E helix of the human protein [224,236,237,239,243]; the hydrophobic nature of the amino acid residues that compose this portion is supposed to be essential for the protein reorganization [233,237,244]. Interestingly the same region seems to enable IsdH^{N1} to bind Hp [234]. Within this polypeptide moiety, a specific sequence of key residues has been recognized and called "Hb-binding motif" (Figure 5), and the substitution of amino acids composing this

region results in the impairment of the complex formation [234,237–239]. IsdB^{N1} and IsdH^{N2} share an identical Hb-binding motif, whereas the presence of some differences in corresponding IsdH^{N1} sequence results in the selective binding to Hb α-chains of the latter.

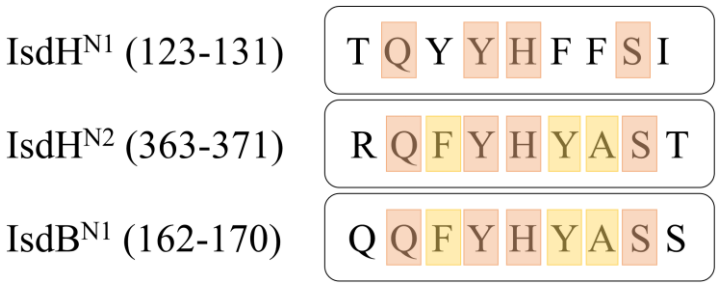

Figure 5: Alignment of the Hb binding motifs from IsdH and IsdB.

On the other hand, the "heme-binding" NEAT domain is responsible for the direct interaction with the cofactor [219,229,234,245]. This domain is present in IsdB^{N2}, IsdH^{N3}, IsdA, and IsdC. The first two hemophores exploit this domain for extracting heme from Hb and transferring it to IsdA and IsdC. These latter are not directly interacting with Hb and thus utilize the NEAT domain to simply receive and pass the cofactor to other hemophore. The principal structural features of "heme-binding" NEAT domains are the dedicated hydrophobic heme pocket, formed by 6-stranded antiparallel β-sheets and a 3_{10}-helix "lip" that faces the binding site. Within this cleft, a flat surface that accommodates the protoporphyrin ring is formed by residues in β7 and β8 strands, moreover, on the β8 strand a conserved amino acid pattern, the heme-binding motif, is composed of two tyrosines spaced out by three variable residues (YxxxY) [225,233,239]. The first of the two Tyr directly coordinates the ferric iron through its phenol ring, whereas the second one supports this interaction with the cofactor by establishing a hydrogen bond with the first tyrosine and a π-stacking interaction with the porphyrin ring [88,220,222,225,228,229,246–251]. Interestingly, IsdA, IsdH, and IsdC are known to form penta-coordinates interaction with hemic-iron through the mentioned Tyr residue [228,239,248,252,253], whereas a methionine residue has been identified on IsdB to serve as additional axial ligand resulting in the unique Tyr-Met hexa-coordination architecture with heme [225]. Despite the uniqueness of this geometry of interaction, no differences between IsdB and IsdH were pointed out in extracting the heme from Hb or passing it to the other hemophores. Surely, the identification of functional differences between the two Hb

receptors could help in deciphering the timeless enigma concerning the reason for the redundancy of *S. aureus* Hb receptors.

As anticipated, the first task assigned to the "heme-binding" NEAT domain of IsdB and IsdH is the extraction of the cofactor from Hb. Even if several structures have been deposited, many muteins have been studied, and various molecular dynamics studies have been performed [224,225,239–241,243,250], the precise mechanism that allows the removal of the prosthetic group from the human oxygen carrier is not completely understood. However, the heme-binding motif, and particularly IsdB-Tyr440 or IsdH-Tyr642 and IsdB-Tyr444 or IsdH-Tyr646, were suggested to play a key role in heme extraction as well as by directly interacting with the cofactor when it is still bound to Hb. Equally, amino acids from IsdB-Tyr353 or IsdH-Phe555 to IsdB-Val367 or IsdH-Val569 are reported to engage Hb and promote heme extraction.

The funnelling of extracted heme through the cell-wall relies on formation by heme-binding NEAT domains of a PPI that has been described as a "handclasp" complex (Figure 6) [205], which increases the heme transfer kinetics, compared to the spontaneous hemin release and re-uptake, from IsdB to IsdA and from IsdA to IsdC by 87,000 and 70,000 times, respectively [204,221,226]. Within this ultra-weak protein complex (K_D in the millimolar range), hemophores interact in a stereochemical specific manner by juxtaposing their 3_{10}-helices and β7/ β8 strands [205,223], probably driving some conformational changes that promotes the transfer, even if the molecular dynamics of interacting hemophores reveals no big changes in 3D structure during the process [199]. Moreover, it has been proposed that the heme coordinating tyrosines of both the donor and the acceptor domains interact temporarily with the iron, unraveling that the formation of the complex relies on the presence of the heme, also referred to as the complex activation [199,205,222].

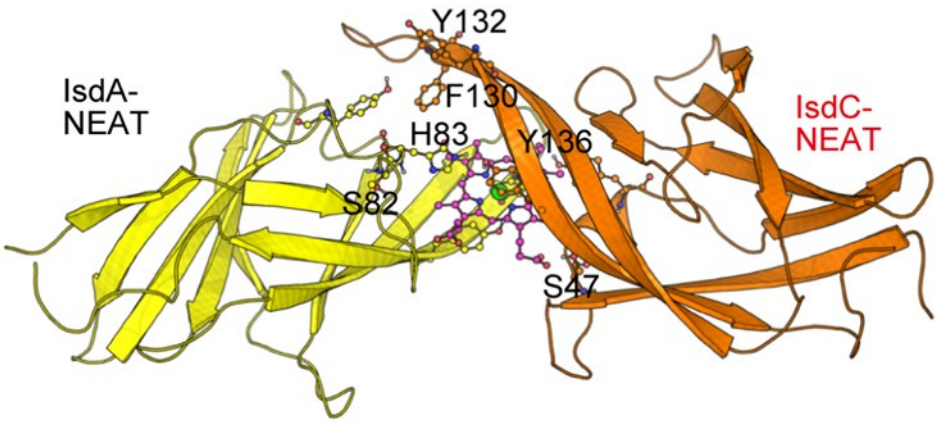

Figure 6: The "handclasp" complex between IsdA and IsdC [199].

As already mentioned, the heme passage proceeds along an increasing affinity gradient, which is principally influenced by the different amino acid sequence of the loop 1 and physical length of the β7/β8 loop of the hemophore [226,250]. In this scenario, the presence of negatively charged residues near the coordinating tyrosine of $IsdH^{N3}$ has a detrimental influence on heme-binding affinity [247], whereas the particularly extended IsdC β7/β8 loop, which results more flexible than the one of the cognate proteins, increases the affinity for the heme and is essential for the selective binding of IsdC to IsdE [223,241]. Although many studies have characterized the IsdA-IsdC complex, only the colocalization of IsdB and IsdA onto the cell-wall supports their engagement finalized to heme internalization [182].

4.2 Stage 3: heme internalization

S. aureus expresses a multi-domains ABC membrane transporter, which is presumably composed of three proteins IsdD, IsdE, and IsdF [139,202] to pump heme into the cytoplasm, Although the role of the membrane-anchored IsdD is still unknown and no known homologs of this protein have been found in other Gram-positive bacteria [88,251], it is supposed to be an Isd system component because it binds heme and the gene coding for this protein is part of the Isd locus [202]. Notably, its expression is up-regulated in MRSA under iron-starvation [254], and it has been supposed that IsdD might provide energy through the ATP hydrolysis [20] but, since the protein did not result essential in IsdEF functionality, it is possible to speculate that it could act as a periplasmic heme reservoir or as a heme sensor that regulates the heme uptake through the IsdEF transporter avoiding the bacterial iron poisoning [187].

Conversely, the energy required for the transport could be provided by the multifunctional FhuC [175]. The second protein of the ABC transporter is IsdE, a class III periplasmic heme-binding protein [255–257] that coordinates the heme in the hexacoordinated form through the interaction with a histidine residue, position 229, and a methionine residue, position 78, both of which ensure the selectivity of the heme transfer from IsdC (and not from IsdA) to this membrane-anchored lipoprotein [199,206,258,259]. Despite the clear presence of the two residues bound to the hemic iron in the electron density map within the crystallographic dataset, only the His229 is essential for the bacterial acquisition of the cofactor *in vitro* [223] and *in vivo* [259]. Furthermore, although IsdE is known to selectively form a complex with IsdC to complete the heme transfer, neither H229 nor M79 are involved in this interaction [206,223,258,260]. Lastly, the IsdE-bound heme is transferred to IsdF, the ABC permease that concludes the internalization of the prosthetic group [202,259].

4.3 Stage 4: heme degradation

Once heme is pumped inside the cytoplasm, it may be reused directly or degraded to release inorganic iron. In the latter case, two dedicated heme oxygenases (HO) are involved (IsdG and IsdI) that catalyze the heme degradation by opening the macrocyclic ring and releasing the essential trace element [261]. IsdG and IsdI are paralogs that differ from typical bacterial HOs and indistinctly cleave the porphyrin ring at the β- or δ-meso carbons by producing iron, formaldehyde and two distinct staphylobilins. The latter are different from the commonly produced bilirubin (Figure 7A), which is the result of the porphyrin scission on the α-meso carbon [262,263]. The different cleavage position derives from a completely new ferredoxin-like homodimeric structure that characterize the two staphylococcal HOs [264], which also results in a novel heme binding mode (Figure 7B) [262,265] and this conformation might result in enhanced activity of the two enzymes compared to the canonical HOs, suggesting an evolutionary adaptation of these microbial proteins to a unique environment [264]. Since the discovery by Skaar and co-workers of the two *S. aureus* heme degrading enzymes [261], other IsdG homologs have been discovered and characterized in Gram-positive bacteria [181,266,267] leading to the formation of the new "IsdG-family" of HOs. Moreover, this enzyme family shares the need for an NADPH-dependent reductase, IruO in *S. aureus*, to catalyze the heme degradation at the maximum rate [268].

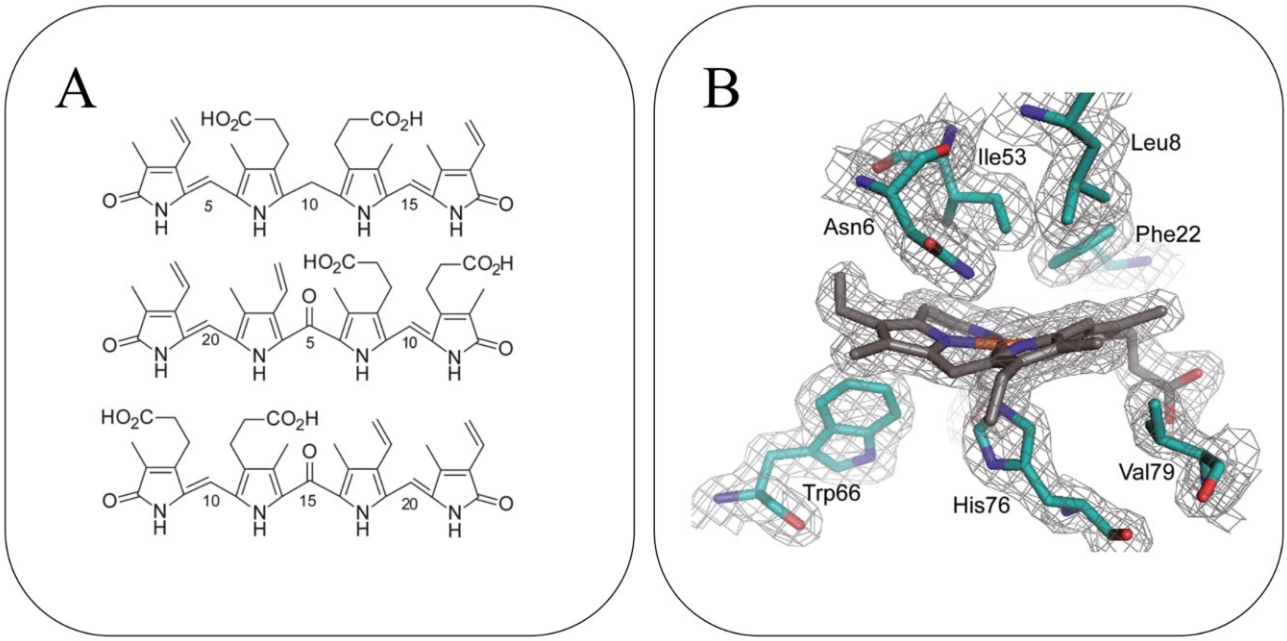

Figure 7: (A) Heme degradation products, from the top down bilirubin, 5-oxo-δ-bilirubin, and 15-oxo-δ-bilirubin [262]. (B) High-resolution structure of IsdI bound to heme [262].

As well as the other Isd proteins, IsdG and IsdI expression is transcriptionally regulated by Fur and the presence of both is required for the full virulence of *S. aureus* [144,208]. However, the intracellular presence of heme seems to play a crucial role, in fact, only the heme-bound form of IsdG is stable whereas the apo-form is readily degraded [208]. Moreover, IsdI appears to be over-expressed within infected tissue during abscess formation [269]. Therefore, it has been hypothesized that the two HOs are differentially regulated both transcriptionally and post-transcriptionally [208].

4.4 Other roles of the surface-exposed proteins

Being exposed outside the *S. aureus* envelope the hemophores, already described for funnelling heme through the cell-wall, have been also identified for their "side" activities. Although many of these duties have been specifically assigned to a single hemophore, other processes are still hard to characterize and thus are shared by different Isd proteins. Obviously, proteins exported outside the cellular membrane represent the principal "pathways to pathogenesis" [270], and, generally, each cell-wall anchored protein interacts with multiple host proteins, and a single host protein is bound by many surface proteins of the bacteria [18,36,271]. In this scenario, IsdA is responsible for binding a variety of host proteins (such as

fibronectin, fibrinogen, transferrin, fetuin, involucrin, loricrin, cytokeratin K10, and asialofetuin) promoting the adherence to epithelial and kidney cells [202,217,272–276], and the protection from the protease activity of lactoferrin [111] and the antimicrobial activity of skin fatty acids [111]. Moreover, it cooperates with IsdB in building resistance against neutrophil killing attacks [277]. IsdB is also known to binds fibronectin, integrins, and vitronectin [16,278–282] allowing interaction and internalization inside human cells, but also causing platelets aggregation. Lastly, IsdH seems to have a role in evading phagocytosis by promoting rapid conversion of C3b to C3d, thus impairing the efficient activation of the complement [283]. Differently to the other cell-wall anchored isd proteins, IsdC resides inside the cell-wall and thus it has limited access to the environment. However, its inactivation, like the one of IsdD, results in a down-regulation of IsdE, IsdF, and IsdG expression, unraveling a possible role in gene regulation within the heme acquisition system [202].

Since MSCRAMMs are described as proteins exposed outside bacterial envelope that interact with host extracellular matrix component, enable the subversion of the host immune system, and present two or more IgG-like subdomains, it is possible to speculate that IsdB, but also IsdA and IsdH, could be categorized in this bacterial protein family, increasing interest in their inhibition. To support this view, IsdB and IsdH present, like many other MSCRAMMs, the YSIRK-GS motif in their N-terminal moieties [211] that result in a preferential distribution of these Hb receptors next to the septal ring during cell division [182]. In this scenario, two scientific works list IsdA, IsdB, and IsdH as MSCRAMMs, but a further validation of this classification is probably needed [284,285].

4.5 The Isd system within the antimicrobial therapy

4.5.1 Direct inhibition of heme acquisition

Because iron is an essential trace element, the bacterium needs it to grow and colonize the host, especially during infection when the host nutritional immunity attempts to iron-starve the invaders. Under such circumstances, the Isd system plays a pivotal role as it is the principal system employed for iron acquisition. As a result, cell-wall anchored proteins and HOs belonging to this pathway have been consistently indicated as virulence factors

[137,181,208,219,220,236,238,286–289]. Even if the interference with these virulence factors is a promising antimicrobial approach, it is still little explored, leaving open the opportunity for the development of novel antimicrobial agents with the potential to remedy the antibiotic resistance crisis.

The effects of the Isd proteins' deletion on the bacterial viability are summarised here briefly. Starting from the Isd cell-wall anchored proteins (IsdA, IsdB, IsdC, and IsdH), their importance in *S. aureus* fitness is indicated by the reduced ability of SrtA and SrtB mutants to bind Hb and to grow when heme is the sole iron source, together with the high attenuation of these mutants in a murine abscess model [181,202,207,287,290–292]. However, since SrtA is a ubiquitous sortase, it is hard to distinguish between the effect on the cell-wall attachment of Isd proteins from that on other effectors that are substrates for this enzyme. Notably, IsdB and IsdA appear crucial in the first stages of infection supporting colonization and abscess development [137,174,287,293,294], and their transcription relies on Sae, like many other virulence factors [147]. On one hand, the inactivation of IsdB , contrarily to IsdH deletion, causes severe impairment in bacterial colonization and virulence [20,181,182,225,238,247,294], unraveling its potential essentiality during infection, which is also confirmed by the observation of a 40-fold increase in this hemophore expression by MRSA under iron-starvation [254]. On the other hand, IsdA mutants present growth defects when heme is the sole iron source [248], but the genetic deletion of IsdA results in an IsdC overexpression that allows bacteria to partially compensate IsdA absence [202], suggesting that the reported role of IsdA in virulence is probably related to its secondary functions. Lastly, inactivation of either IsdC or SrtB results in a *S. aureus* strain only partially compromised in abscess formation [202,287]. Moving to the other Isd proteins, the IsdE mutants appear limited in hemic iron acquisition [177], whereas the growth of bacteria lacking IsdF is markedly compromised, but not suppressed [174,202]. Finally, IsdG and IsdI inactivation both lead to *S. aureus* iron-starvation and increases the bacterial risk of heme poisoning [189,208,295], and their uniqueness in respect to human heme oxygenases would allow to selectively target these enzymes reducing possible side effects.

To conclude, the inhibition of heme acquisition usually leads to impaired growth and pathogenesis, but rarely to bacterial killing. The resulting antiinfective activity of these inhibitors, unlike the usually desirable feature of most antibiotics that kill unselectively all microbes, could exert a reduced selective pressure toward the development of bacterial

resistance [139,296], which is of special importance considering the high rate of resistance development registered for *S. aureus*.

4.5.2 Biopharmaceuticals

The Isd proteins have been proposed for many years as potential targets for antibodies and vaccine development to face the MRSA threat [36,285,297–299]. The ability of this bacterium in establishing new mechanisms of resistance to newly marketed antimicrobial agents would motivate the choice of developing biopharmaceutical drugs as an alternative therapeutic approach, since the latter is characterized by a very low resistance rate. Moreover, the Isd proteins exposed on the staphylococcal cell-wall are known to have further functions besides heme acquisition, which render them essential throughout different stages of infections and thus constantly produced by almost all the *S. aureus* strains, including MRSA and MSSA [36]. Indeed, IsdB has been indicated as the more immunogenic protein of the Isd pathway and, in some cases, of the entire *S. aureus* proteome [299], however selectively targeting this hemophore did not lead to any good results driving recent work to focus on more than one target, either selecting within the same Isd system or looking for other staphylococcal virulence factors. Another crucial point in the development of biopharmaceuticals is their ability in inducing the opsonophagocytic activity by specific antibodies or the complement, which ensures *S. aureus* efficient clearance and killing [300,301]. In this scenario, the V710 Merck vaccine has been the greatest failure in exploiting the Isd system for vaccines development. In fact, V710 was based on active immunization against a single target, IsdB, and its 2b/3 phase was terminated due to safety concerns and low efficacy [302,303]. Recently, a multicomplex composed of SpA, anti-IsdB antibody, IsdB, Hb, and Hp has been discovered to mediate *S. aureus* internalization and survival inside macrophages [304], succeeding to explain the safety problems of the V710 vaccine.

Despite the great effort in developing biopharmaceuticals to counteract the *S. aureus* infection by targeting the Isd proteins (current state-of-the-art is summarized in Table 2), no vaccine or antibodies have been commercialized so far [51,284,301,305–308]. On one side, developing antibodies against Isd proteins interestingly resulted in macromolecular systems that can actively inhibit heme acquisition besides their roles as a tracking point for the humoral immune response of the host [293]. On the other side, vaccines should be considered according to

different levels of protective efficacy, and, even if the prevention of the pathogenesis is the major goal, also reducing the severity and mortality of the staphylococcal infection might be an important result for the upcoming research studies [51,306]. In this scenario, the little differences in virulence between pathogenic and human resident *S. aureus* and the ability to naturally accept/tolerate the bacterial colonization within the nasal cavities imply the role of adaptive host immunity in controlling the outcome of bacterial colonisation [306]. This type of adaptation might inspire the development of efficacious biopharmaceuticals, as demonstrated by the efficacy of human serum samples taken from children with invasive *S. aureus* infections to protect mice against the bacterial challenge [309].

Table 2: State-of-the-art development of biopharmaceuticals targeting Isd system. Abbreviations: serine-aspartate repeat-containing protein D and E (SdrD-E), hemolysins alpha and gamma (Hla-g), clumping factor A (ClfA), staphylococcal enterotoxin B (SEB), staphylococcal protein A (SpA), and manganese transport protein C (MntC).

Type	Target	Activity	Reference
Vaccine	IsdA and IsdH	Protection against nasal carriage in cotton rat model	[310]
	IsdB	(Merck V710) Protection of mice against lethal *S. aureus* infection. Stimulation of anti-IsdB antibodies in rhesus macaques. Positive immune response in human (Phase I)	[311,312]
	IsdA, IsdB, SdrD and SdrE	Induction of opsonophagocytic antibodies and protection of mice against lethal challenge with diverse *S. aureus* strains	[313]
	Hlg, ClfA and IsdB	Enhanced phagocytosis in vitro, reduction in bacterial load in mice spleen, and protection of mice in the intraperitoneal challenge	[314,315]
	IsdB and ClfA	Induction of antibody response through opsonophagocytic killing (OPK) activity, and Th1/Th17-skewed cellular immune response	[270]
	Hla, SEB, SpA, $IsdB^{N2}$ and MntC	Consistent protection in lethal sepsis and pneumonia mouse model, induction of comprehensive cellular and humoral immune responses.	[316]
Antibody	IsdB	Murine monoclonal antibodies (mAbs) presenting partial OPK activity and efficacy in murine challenge models	[317]
	IsdB	Human mAbs with an elevated OPK activity in vitro and protection of rats in lethal sepsis model	[300,318]
	IsdA and IsdB	Protection against abscess formation and lethal challenge through the inhibition of heme acquisition	[293]
	IsdB	Antibodies involved in the adaptive immune system, which recognize the iron acquisition determinant with the aim of directly inhibiting its function.	[319,320]
	IsdA	Human mAbs that inhibit heme acquisition and exert Fc-mediated protective effects in vivo. Characterization of a panel of IsdH and cross-reactive Isd human mAbs	[309]

5 IsdB and IsdH, the two Hb receptors

IsdB and IsdH are the two isofunctional proteins used by *S. aureus* to bind Hb and extract the heme, which is then handled by the other proteins of the Isd pathway. Although many studies have been carried out, the differential role played by the two receptors is still ambiguous. In this context, Jenkins and co-workers reported for the first time that a specific MRSA strain selectively overexpressed IsdB during infection whereas an MSSA strain overexpressed IsdH under the same conditions [321]. On the contrary, in 2018 IsdH was found to be expressed by an MRSA whereas IsdB was not [322]. In any case, IsdH is encoded by a gene that is not part of the locus including *isdA*, *isdB*, and *isdC* (Figure 4), and its presence seems to be dispensable for the bacterium survival [181,204,219]. Conversely, IsdB showed a great variety of "side activities" and it is considered the principal virulence factor of *S. aureus*.

Interestingly, IsdH presents an extra Hb-binding NEAT domain compared to IsdB (Figure 8), which is referred to as NEAT1 and is proposed to increase the affinity of the hemophore for Hb [235], but, besides this, IsdB (composed of NEAT1, and NEAT2) and its homologous IsdH counterpart (composed of NEAT2, and NEAT3) share most of the biochemical properties. Based on the latter evidence and considering that this section aims to present the biochemical and structural characterization of the interaction between these two hemophores with Hb and the subsequent heme extraction, the scientific results on IsdB and IsdH has been joined to build a more complete description of the system.

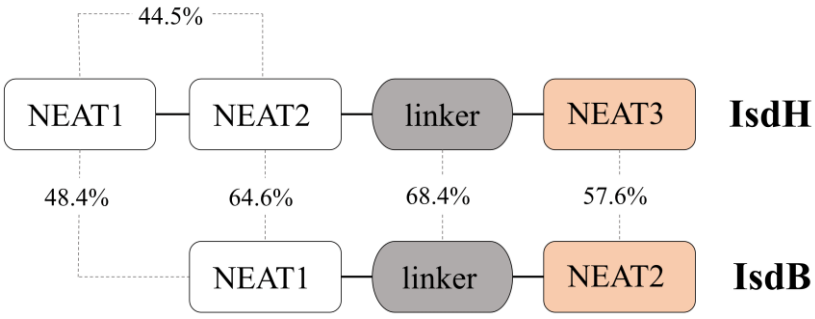

Figure 8: Sequence identity of IsdH and IsdB domains.

5.1 Hb, the human oxygen carrier

Hb is physiologically contained inside the RBC, where it exists as a tetramer of α and β globins (homodimer – $\alpha_2\beta_2$ - of heterodimer - αβ) and each subunit (also known as chain) binds one heme molecule with iron in the ferrous state [323]. α-Hb chains are composed of 141 amino acid residues that form seven helices connected by short loops, while β-Hb chains consist of 146 amino acid residues that form eight helices. Figure 9 and 10 represent the wiring diagrams of α- and β-Hb chains, together with the traditional naming scheme of Hb. The latter is used throughout all the thesis when referring to Hb amino acid residues.

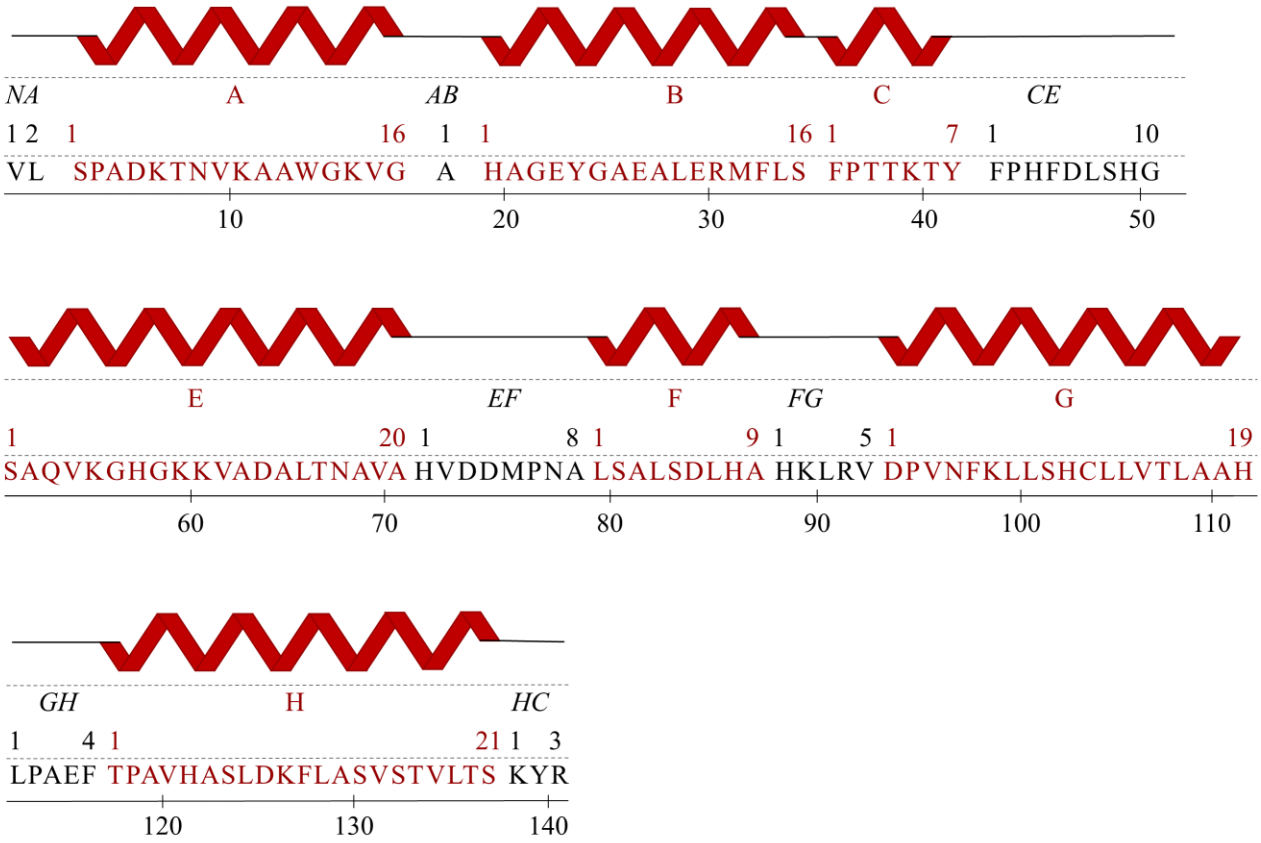

Figure 9: Schematic representation of α-Hb. From the top down the image reports the wiring diagram, the traditional naming scheme (composed of the name of loops – black – and helices – red – names, and the associated residues numbering), the amino acid sequence, and the progressive numbering scheme of residues.

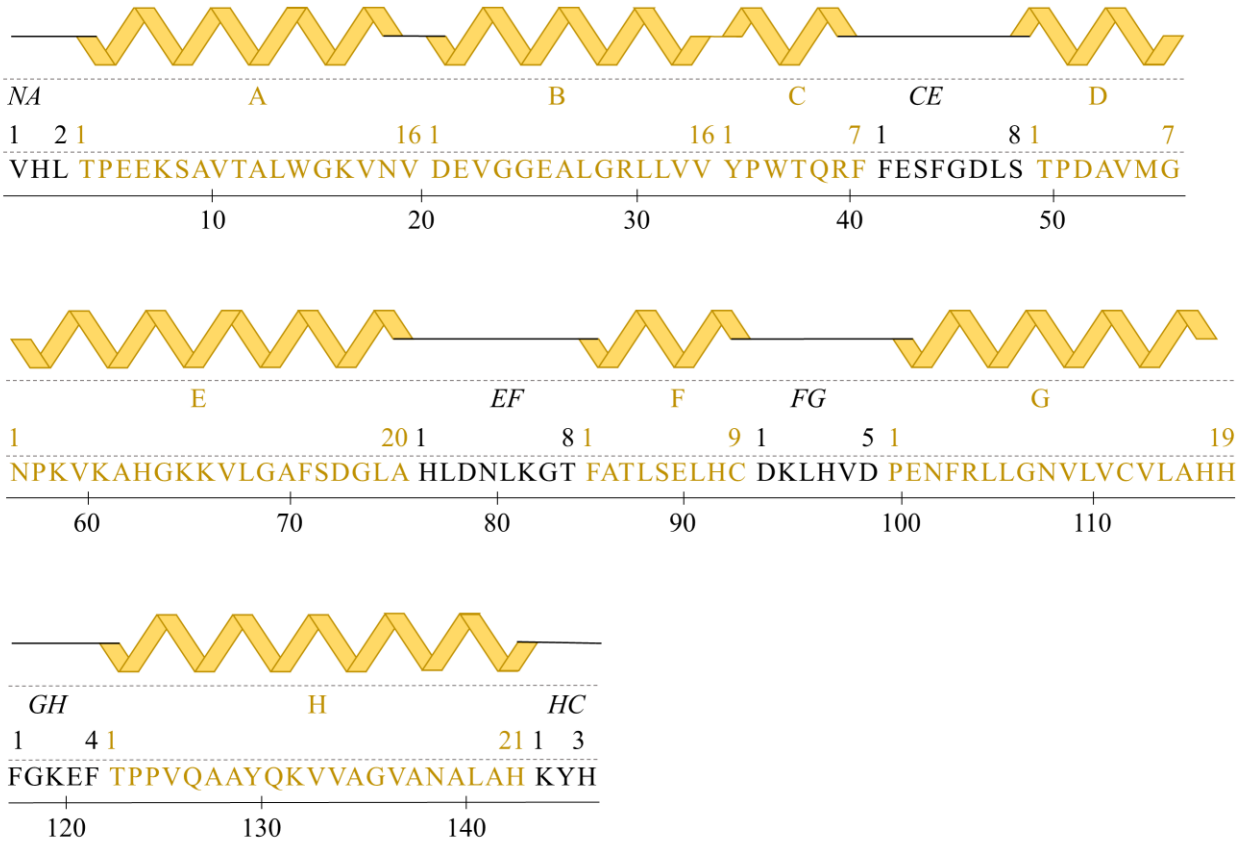

Figure 10: Schematic representation of β-Hb. From the top down the image reports the wiring diagram, the traditional naming scheme (composed of the name of loops – black – and helices – yellow – names, and the associated residues numbering), the amino acid sequence, and the progressive numbering scheme of residues.

Each erythrocyte contains approximately 280 million molecules of Hb and thus over 1 billion atoms of iron [324], which makes it the major source of the metal inside the organism. Moreover, confinement of this large amount of protein inside RBCs leads to a concentration close to 2 mM [74], which is essential for keeping the protein in its tetrameric state (the calculated K_D (dimer-tetramer) is reported to be in the low micromolar range [325,326]) and, together with the reductive systems present inside the RBCs, the iron in its ferrous state. Notably, only the reduced form of Hb is capable of binding oxygen and the quaternary structure is essential in preserving the positive cooperativity of the Hb-oxygen interaction, which underlies the optimal acquisition of the gas inside the lungs and release in the tissues.

However, Hb could be found free in the bloodstream due to the physiological RBCs turnover or to the hemolysins-mediated lysis of RBCs [327]. In this milieu, protein concentration is drastically reduced (μM range [219]) and the aforesaid reductive systems are lost causing

protein dimerization and heme oxidation [328]. The resulting metHb, as already been mentioned in section 4, is the only Hb form available to pathogens and, interestingly, IsdB and IsdH can bind both reduced and oxidized forms of Hb but they only extract ferric heme [220,224], supporting a natural adaptation of the hemophore for its physiological ligand. Notably, many *in vitro* studies utilized COHb or oxyHb to prevent heme extraction and evaluate the pure binding of the hemophores to the globin chains [198,225,235,238,244]. Furthermore, solid scientific findings support the existence of an evolutionary pressure exerted by human Hb on IsdB which could enable the pathogen to better colonize the human host. In fact, *in vitro* studies reported a greater affinity of IsdB for human Hb (hHb) over the murine protein, and the preference of many *S. aureus* strains for hHb as a sole iron source compared to the Hb from other mammals, as baboon, horse, pig, rat, cow, or rabbit. Lastly, mice expressing hHb are more efficiently colonized by *S. aureus*, although this ability is abolished in ΔIsdB bacteria [294]. At the same time, a phylogenetic analysis reported the rapid co-evolution of Hb and the two hemophores, IsdB and IsdH, unraveling a fascinating molecular arms race that drives high mutation rates of the surface hotspots on Hb that are sites for interaction with IsdB/IsdH. On the other hand, this has put a selective pressure on hemophores to preserve their ability to selectively interact with Hb [296,329].

As already outlined in section 2.2.2.2, Hp is an acute-phase protein that is enrolled to limit the concentration of free metHb in the bloodstream and thus the oxidative damage related to the latter. The tight Hp-Hb complex has been demonstrated to stabilize Hb dimer and reduce the heme release [330], possibly playing an active role in nutritional immunity. Both IsdB and IsdH can efficiently bind Hp-Hb complex [219,224,234,237,238,244,245], but only IsdH appeared able to extract a very limited quantity of heme from the Hp-Hb complex [235], which could support *S. aureus* growth when the Hp-bound metHb is the sole iron source. Moreover, when IsdH binds Hb-Hp complex, its NEAT1 has been demonstrated to inhibit the binding by the CD163 receptor, avoiding macrophages clearance [235]. Notably, a recent study demonstrated the ability of the acute phase protein in reversing the IsdH heme extraction, thus disclosing the Hp inhibitory activity also against IsdH [243].

5.2 The IsdB/IsdH complex with metHb

Since the discovery of the Isd system, many biochemical and biophysical techniques have been applied to characterize the behaviour of the two *S. aureus* Hb receptors through their interaction with metHb. The IsdB/IsdH complex with metHb is indicated as the first step in staphylococcal hemic-iron acquisition, which is generally considered the preferred strategy for this metal retrieval by the bacterium (vide infra). IsdB/IsdH are exposed outside the cell-wall and are thus able to directly interact with free Hb within the colonization site. The initial formation of the complex between the hemophore and the human oxygen carrier is followed by the extraction of the cofactor. The latter is then passed to the following proteins of the Isd system to complete the pathway for heme acquisition. The current subsection will focus on the aspects relevant for the results of this thesis, including many aspects that still deserve further investigation as complex stoichiometry, kinetics of heme extraction and a proper structural characterization.

Up to this point of the thesis, IsdB and IsdH activity has been assigned only to the Hb-binding ($IsdB^{N1}$ and $IsdH^{N2}$) and heme-binding ($IsdB^{N2}$ and $IsdH^{N3}$) domains, however, it is well-known that these functional NEAT domains are connected by a 3-helix linker, which is essential for their coordinated activity [198,233]. A 70% amino acid sequence identity is shared by IsdB and IsdH linker domains [233], and the substitution of this domain with a poly-GS peptide leads to the impairment of IsdH heme extraction [197,200,242]. Notably, the structure of the linker appears rigid and does not change upon complex formation [200,224,237,239], whereas the C-terminal peptide of the Hb-binding domain acts as a hinge region to correctly direct the multidomain composed of the linker and the heme-binding domain in the close proximity to the heme-binding pocket of Hb [200,233,241]. The first role assigned to this 3-helix bundle was to finely space out the two functional domains onto the Hb surface, but recent high-resolution details have disclosed a direct interaction of the linker domain with the heme-binding pocket of Hb, which appeared essential for the heme extraction [241,243]. Isothermal titration calorimetry [198,224,240], surface plasmon resonance [219,234], nuclear magnetic resonance (NMR) [197,233], and size-exclusion chromatography (SEC) [236,331] have been applied to investigate the affinity and the stoichiometry of IsdB/IsdH binding to either Hb or heme. Briefly, IsdB and IsdH displayed high affinity for Hb (in the nanomolar range) and a decent affinity for free heme (in the micromolar range),

however, if the ability of the heme-binding NEAT domain of interacting with a single heme molecule is now clear, the selectivity of Hb-binding NEAT domain for α- or β-chain of Hb is still debated [224,233,236,240,332] thus leaving the right stoichiometric ratio in doubt. To answer this last question, speculations have been made during the kinetic study for heme extraction characterization, but the more convincing model could be extrapolated from the high-resolution structure of the complex (vide infra).

The kinetics of heme extraction have been mainly evaluated by visible spectroscopy, often coupled with a stopped-flow apparatus, that exploits the distinctive and well-studied capacity of heme to absorb visible light in an environment-dependent fashion, resulting in a clear peak transition when it moves from Hb to the hemophore (Figure 11). The kinetic constants for heme extraction were mainly calculated at 406 nm, the wavelength of maximum absorbance for metHb.

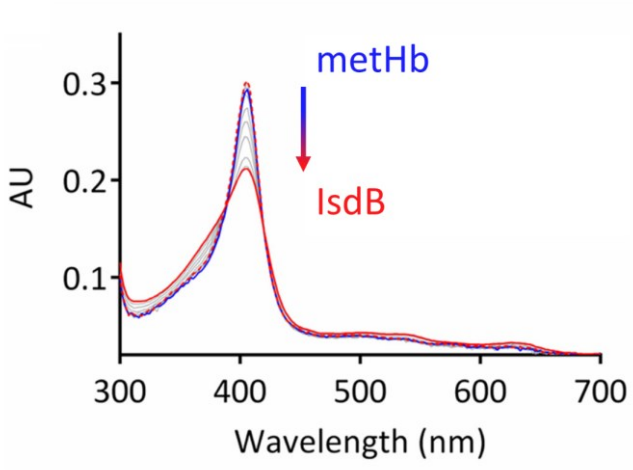

Figure 11: Time-resolved spectra of IsdB-mediated heme extraction process from metHb. The metHb spectrum (in blue) undergoes a transition when IsdB is added that ends with heme bound to the hemophore (in red). Red dashed and grey lines are intermediate steps of heme extraction (adapted from [224]).

The spectroscopic transition is evident but the kinetic model to be applied varies over the studies. A simple mono-exponential process has often been applied [204,233,332] resulting in observed rate constants ranging from 0.04 to 0.3 s^{-1}. A single exponential process coupled with a complete heme extraction from Hb, was suggested to indicate an efficient heme extraction from both α- and β-chains [332]. However, more recent scientific works reported the need of a more complicated kinetic model to properly fit the extraction process followed spectroscopically at 406 nm. A bi-exponential fit resulted in k_1 = 0.85 s^{-1} and k_2 = 0.099 s^{-1}

observed rate constants [200]. Whereas a kinetic model including four different exponential curves was proposed by Bowden and co-workers [224]. The results from the fit were not reliable, thus the authors decided to study the extraction process at 428 nm, where a mono-exponential fit resulted in an observed rate constant comparable with published work (e.g., k_{obs} = 0.35 s^{-1}).

Interestingly most of the kinetic studies were conducted at room temperature and the observed rate constants turned out to be roughly comparable regardless of the model used. However, Pishchany and co-workers [238] performed experiments at 4 °C. A bi-exponential fitted data, but calculated observed rate constants were found to be reduced by one-order of magnitude, indicating that the extraction process is significantly dependent by the temperature.

Although the dynamics of complex formation and heme extraction are still debated, the more reliable model is given below for IsdH, which should be also valid for IsdB. The model has been defined using a recombinant IsdH construct modified to selectively bind Hb α-chains [240].

$$\mathrm{Hb[hemin]} + {}^{\alpha}\mathrm{IsdH} \underset{k_{-1}}{\overset{k_1}{\rightleftharpoons}} \mathrm{Hb[hemin]}{:}{}^{\alpha}\mathrm{IsdH} \xrightarrow{k_{trans}} \mathrm{Hb}{:}{}^{\alpha}\mathrm{IsdH[hemin]}$$

Within this model, the complex between IsdH and metHb is formed first and the subsequent extraction results irreversible [240]. The study allowed to calculate for the first time the microscopic constants for IsdB-Hb encounter, k_1 = 2.8 x10^7 M^{-1} s^{-1} and k_{-1} = 2.4 x10^3 s^{-1}. Moreover, the calculated k_{trans} is 0.54 s^{-1} which is in line with the heme extraction rate already calculated by all the kinetic studies published over the years, making this model even more reliable.

The three-dimensional structure of the full-length protein has never been solved for IsdH nor for IsdB. On the other hand, different structures have been deposited of the complex with Hb, only one involving IsdB. The complete list of structures deposited in PDB is reported in Table 3.

Table 3: Summary table of all published high-resolution structure of IsdB and IsdH.

IsdB			
Separated domains			
2MOQ	$IsdB^{N1}$	NMR	[233]
3RTL	Holo-$IsdB^{N2}$	1.45 Å	[225]
3RUR	SelMet-$IsdB^{N2}$	1.7 Å	[225]
Bound to other ligands			
5D1Q	$IsdB^{N2}$ bound to D2-06	3.2 Å	[319]
5D1X	$IsdB^{N2}$ bound to D4-30	3.2 Å	[319]
5D1Z	$IsdB^{N2}$ bound to D4-10	3.2 Å	[319]
Complex with con Hb			
5VMM	$IsdB^{N1N2}$-Hb	3.6 Å	[224]
IsdH			
Separated domains			
2H3K	$IsdH^{N1}$	NMR	[244]
2Z6F	Holo-$IsdH^{N3}$	1.90 Å	[229]
2E7D	$IsdH^{N3}$	2.20 Å	[229]
3QUH	$IsdH^{N3}$[MnPP]	2.70 Å	[220]
3QUG	$IsdH^{N3}$[GaPP]	1.70 Å	[220]
3VTM	$IsdH^{N3}$[InPP]	2.8 Å	[333]
3VUA	$IsdH^{N3}$	1.85 Å	[333]
2LHR	$IsdH^{linker}$	NMR	[197]
Complex with Hb			
3SZK	$IsdH^{N1}$-metHb	3.01 Å	[236]
4IJ2	$IsdH^{N2N3,Y642A}$-Hb	4.24 Å	[237]
4XS0	α$IsdH^{N2N3,Y642A}$-Hb	2.55 Å	[239]
3OVU	$IsdH^{N1}$-metHb-ASHSP	2.83 Å	[334]
3S48	$IsdH^{N1}$-αHb	3.05 Å	[334]
4FC3	$IsdH^{N2}$:metHb	2.26 Å	[334]
4WJG	$IsdH^{N1}$-Hb-Hp	3.1 Å	[335]
6TB2	$IsdH^{N2N3,Y642A}$-Hb-Hp	2.9 Å	[243]

The first clear evidence that came from the published crystal structures is the ability of the hemophore to bind both α- and β-chains within the complex. However, Dickson and co-workers pointed out that steric factors could interfere with the simultaneous binding of IsdH to all four globin subunits within the Hb tetramer, thus giving a plausible explanation on the inconsistent data on complex stoichiometry *in vitro*, which could be affected by the oligomeric state of Hb.

Most of the crystallographic structures present the hemophore bound preferentially to the α-chains. In fact, in the IsdB-Hb complex [224] the hemophore bound to the β-chains underwent a proteolytic event after heme extraction, whereas the IsdH bound to Hb [239] was recombinantly modified to selectively bind the α-chains. Only a low-resolution structure of Hb with an IsdH extraction defective mutant [237] or the IsdH complex with Hp:Hb complex [243] show the interaction of the intact hemophore with β-chains, thus limiting the analysis of the mechanism underlying the heme extraction from this subunit.

Looking at the interaction of the hemophore with the α-chain, the disruption of the F helix of the globin appears evident [224,239] and it could be at the basis of the heme displacement out of its binding pocket. This conclusion is supported by the physiological reverse process, e.g., the heme insertion into the Hb binding pocket during the protein synthesis, which passes through the unfolding of the F helix as well [336,337].

A molecular dynamic (MD) study in 2017 investigated the heme extraction by $IsdH^{N3}$ from α-chain of Hb through a steered simulation [250]. The study revealed that heme moves about 15 Å to reach the hemophore binding pocket, and it needs to make a 180-degree rotation along its way from Hb to IsdH. In this scenario, NEAT2 has the role to keep tight the IsdH-metHb complex, whereas NEAT3 domain only weakly interacts with Hb to better adapt its position during heme rotation. MD simulation also suggested the principal driving forces of the process, which are (1) the hydrophobicity of IsdH binding pocket and (2) the presence of a tyrosine residue (Y646) that pulls the heme out the Hb binding pocket first and then supports the interaction between heme and the iron-coordinating tyrosine (Y642). Instead, the limiting step of the heme extraction has been proposed to be the exit of heme from the Hb binding pocket.

So far, it remains unclear how and when Hb dissociates from the complex after the heme extraction in order not to "clog" the extraction/transfer system. In fact, the extracted heme from Hb needs to be passed to IsdA and the Hb receptor needs to regenerate in order to behave as

expected in the relay mechanism proposed for IsdB/IsdH [204]. One potential mechanism is the dissociation of Hb from IsdB/IsdH once the receptor has transferred heme to the recipient protein IsdA [204]. Alternatively, IsdA can compete with apo-Hb for the binding to IsdB/IsdH when heme extraction is completed. Either way, contrarily to what has been published on IsdA/IsdC/IsdE, the formation of a complex between IsdB/IsdH and IsdA was never reported and more effort must be made to better understand the basis of this key process.

Aim of the thesis

The aim of the thesis was the biochemical and biophysical characterization of the complex between IsdB and human Hb, and to validate the activity of *in silico* selected molecules in interfering with IsdB-Hb complex formation.

Therefore, the following activities were carried out:

- ✓ Preparation of the expression construct and optimization of the purification conditions for a truncated, soluble form of IsdB that contains all the functional domains (NEAT1, linker and NEAT2) and lacks the N- and C-terminal domains ($IsdB^{N1LN2}$);
- ✓ Site-directed mutagenesis, expression and purification of IsdB variants presenting Y165A ($IsdB^{Y165A}$) or Y440A ($IsdB^{Y440A}$) single-point mutations. $IsdB^{Y165A}$ was reported to have reduced affinity for Hb: it was principally used in the screening assay to increase its sensitivity for the first, potentially weak, sets of inhibitors. $IsdB^{Y440A}$ was expected to be impaired in heme extraction because Tyr440 coordinates the cofactor in holo-IsdB high-resolution structure, and is directly interacting with Hb in IsdB-Hb complex structure: it was used to capture an intermediate step between IsdB-Hb complex formation and heme extraction;
- ✓ Purification of human oxyHb from blood of non-smoking donors and preparation of several Hb forms, including metHb, COHb, and semiHbs. IsdB efficiently binds OxyHb and COHb but it does not extract the heme: the reduced, ligated forms of Hbs were thus used to study, both kinetically and structurally, the first step of IsdB-Hb complex formation that precedes heme extraction. SemiHbs are derivatives of Hb that bind heme only on either α- or β-chain, while the other chain is heme free: they were used to assess if IsdB preferentially binds and extracts heme from one specific Hb chain. MetHb is the prevalent form of free Hb in the bloodstream, IsdB binds and extract heme from it and, indeed, it was used to study the heme extraction process;
- ✓ Determination of microscopic and macroscopic kinetic constants for IsdB-Hb complex formation and identification of the rate-limiting step for heme extraction using SPR and visible spectroscopy;
- ✓ Determination of stoichiometric ratio of IsdB-Hb complexes using different Hb forms and IsdB variants by exploiting visible spectroscopy and SEC-MALS techniques;

- ✓ Determination of low and high-resolution structures of IsdB-Hb complexes by X-ray scattering and cryo-EM with the aim to better characterize the molecular details of PPI and to provide and improved structural model for future *in silico* screening campaigns aimed to find PPI inhibitors;
- ✓ Development of an ELISA as a screening platform for potential inhibitors of IsdB-Hb PPI;
- ✓ Screening of *in silico* selected molecules aimed to interfere with IsdB-Hb complex formation.

Chapter I – protein preparation

1 Objectives

The project required the use of *S. aureus* IsdB and hHb. Expression systems and purification conditions were designed and optimized for $IsdB^{N1LN2}$, which corresponds to the central and functional region of IsdB and was used in most of the scientific publications covering the biochemical characterization of the hemophore [198,224,233] (Figure 12). The construct was cloned in-frame with a StrepTag®II that was exploited not only for protein purification but also to immobilize IsdB on 96-well plates for ELISA and gold chips for SPR. Together with IsdB, the expression and purification of full-length-IsdB (FL-IsdB) was designed and set-up. FL-IsdB construct includes the entire amino acid sequence, only lacking the propeptide and signal peptide portions. Propeptide is not present in the mature protein because it is removed *in vivo* by sortase to anchor the protein to the cell-wall, thus it was not considered for the heterologous expression [270]. Similarly, signal peptide was not included because it is removed *in vivo* by a dedicated signal peptidase [270].

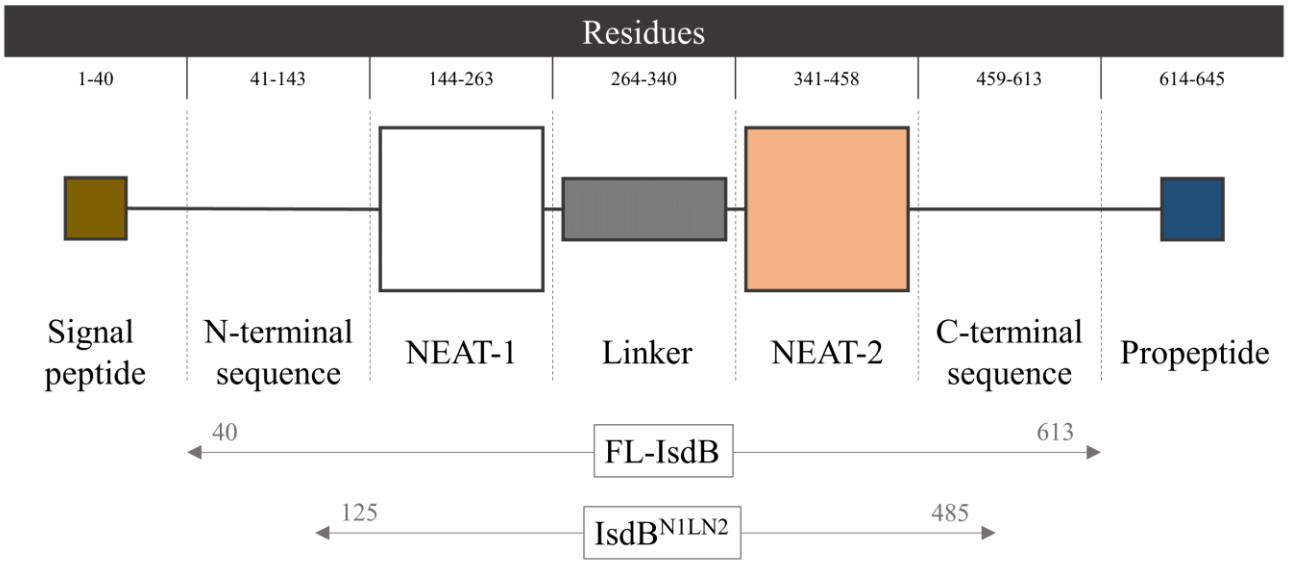

Figure 12: Schematic representation of IsdB sequence with its functional domains and of the FL-IsdB and $IsdB^{N1LN2}$ recombinant constructs.

The biochemical characterization of IsdB was supported by the preparation and exploitation of two variants of the hemophore where either tyrosine 165 or tyrosine 440 were replaced by an alanine residue.

IsdB carrying the Y165A mutation was reported to be extremely impaired in Hb binding [238], while mutation on Y440 was expected to hamper the heme extraction step [224].

The purification protocol for human Hb from RBCs was already available in the laboratory and was used with minor modifications [338]. A published protocol [339] was used to prepare semiHbs. SemiHbs are Hb derivatives where only α- or β-Hb subunit binds heme, while the other subunit is heme free, and they were used to assess if IsdB preferentially extracts heme from either α- or β-subunits, as previously suggested by indirect evidence [198,240].

2 Materials and Methods

All reagents, if not otherwise specified, were obtained from Sigma Aldrich (St. Louis, MO, USA) at the best commercial quality available, and used as-received. Tris (2-carboxyethyl) phosphine (TCEP) was purchased from Apollo Scientific (Stockport, UK).

2.1 Growing media

Luria-Bertani (LB) broth contained:

- 10 g/L tryptone;
- 10 g/L NaCl;
- 5 g/L yeast extract.

LB agar plates were prepared from LB with the addition of 15 g/L agar.

M9 minimal broth contained:

- 1x M9 salts (33.9g/L Na_2HPO_4, 15g/L KH_2PO_4, 3.5g/L NaCl, 5g/L NH_4Cl);
- 11 mg/L $CaCl_2$;
- 240 mg/L $MgSO_4$;
- M9 was supplemented with 0.4% glucose.

2.2 Expression system for IsdB and its variants

IsdB^{N1LN2}. The gene coding for the central and functional region of IsdB, residues 125-485, was optimized for expression in *E. coli* and generated by total gene synthesis (GeneArt) based on *S. aureus* MW2 chromosomal DNA (UniProt entry: Q8NX66). Restriction sites BsaI on both 5' and 3' ends were added to the sequence to allow the subcloning of the designed gene into the final expression vector, pASK-IBA3plus (IBA Lifesciences). Synthetic IsdB^{N1LN2} construct was cloned in vector pMK (a standard GeneArt delivery vector). This plasmid was transformed by electroporation in E. coli XL1blue competent cells, where it was in vivo amplified and consequently extracted and purified by miniprep (GenElute™ Plasmid Miniprep Kit, Sigma Aldrich). Subsequently, pMK::IsdB^{N1LN2} and pASK-IBA3plus (IBA Lifesciences) were digested with BsaI in CutSmart buffer (New England Biolabs) and the digestion products were separated on 1% agarose gel and extracted using NucleoSpin™ (Macherey Nagel

Bioanalysis). For the ligation, vector and insert were mixed in the molar ratio 1:15 and ligated by T4 ligase (New England Biolabs) during overnight incubation at 15 °C. Resulting pASK-IBA3plus::IsdB^{N1LN2} plasmid was electroporated in *E. coli* XL1blue cells, where it was *in vivo* amplified and consequently extracted and purified (GenElute™ Plasmid Miniprep Kit, Sigma Aldrich). The sequence of the new construct was confirmed by sequencing reaction (Microsynth Seqlab GmbH). New expression plasmid was electroporated in *E. coli* BL21(DE3) cells for protein overexpression and purification.

IsdB variants. IsdB^{Y165A} and isdB^{Y440A} variants were prepared with an optimized QuickChange™ site-directed mutagenesis [340], where the use of partially overlapping primers significantly enhanced amplification efficiency by (1) reducing primer dimerization and (2) permitting the newly synthesized DNA to be used as the template in subsequent amplification cycles. Designed primers are listed in Table 4. Briefly, pASK-IBA3plus::IsdB^{N1LN2} plasmid was extracted and purified from E. coli XL1blue cells by miniprep (GenElute™ Plasmid Miniprep Kit, Sigma Aldrich). In the following stage, PCRs were carried out to obtain the constructs coding for IsdB^{Y165A} or IsdB^{Y440A} mutants. Mutated plasmids were electroporated in *E. coli* XL1blue cells, where they were *in vivo* amplified and consequently extracted and purified (GenElute™ Plasmid Miniprep Kit, Sigma Aldrich). Mutations were verified by sequencing reaction (Microsynth Seqlab GmbH), and expression plasmids carrying the desired mutations were electroporated in *E. coli* BL21(DE3) cells for protein overexpression and purification.

FL-IsdB. The construct coding for mature protein FL-IsdB, residues 40-613, was optimized for expression in *E. coli* by and generated by total gene synthesis (GeneArt) based on *S. aureus* MW2 chromosomal DNA (UniProt entry: Q8NX66). Restriction sites NdeI (5’ end) and XhoI (3’ end) were added to the sequence to allow the subcloning of the designed gene into the definitive expression vector, pET28a. Synthetic FL-IsdB construct was cloned in vector pMA-T (a standard GeneArt delivery vector). The subcloning protocol was adapted from the one used for pASK-IBA3plus::IsdB^{N1LN2} preparation. Purified pMA-T::FL-IsdB and pET28a::hSR (already present in the laboratory) plasmids were digested with NdeI in CutSmart buffer (New England Biolabs). Partially cleaved plasmids were digested with XhoI in Buffer R (Thermo

Fisher Scientific) to finally obtain the vector (pET28a) and the insert (FL-IsdB). This last two DNA fragments were separated on 1% agarose gel and extracted with NucleoSpin™ (Macherey Nagel Bioanalysis). For the ligation, vector and insert were mixed in the molar ratio 1:4 and ligated by T4 ligase (USB®) during overnight incubation at 20 °C. The sequence of the new construct was confirmed by sequencing reaction (Microsynth Seqlab GmbH), and the expression plasmid was electroporated in *E. coli* BL21(DE3) cells for protein overexpression and purification.

FL-IsdB variants. Since proteolytic events were demonstrated to involve the C-terminal part of the FL-IsdB (vide infra), the mutagenesis for obtaining FL-IsdB *604L (FL-IsdB^{*604L}) variant was designed. The mutation is intended to remove the stop codon at the C-terminus of the protein allowing the transcription of a double-HisTag construct at both N- and C-term. In fact, FL-IsdB is subcloned into a pET28a expression plasmid which presents the sequence for N- and C-term HisTags. During the design of FL-IsdB construct, the C-terminal HisTag was bypassed because not essential, in fact, N-terminal HisTag is often enough for satisfactory protein purification. Moreover, N-terminal HisTag is removable by the cleavage with thrombin, while C-terminal HisTag is not. FL-IsdB^{*604L} variant was prepared in a similar way to IsdB^{N1LN2} variants and using the primers in Table 4. The optimized QuickChange™ site-directed mutagenesis [340] protocol was used as already described. Mutation was verified by sequencing reaction (Microsynth Seqlab GmbH), and expression plasmids carrying the mutation was electroporated in *E. coli* TUNER™ BL21(DE3) cells for protein overexpression and purification.

Table 4: Primers for QuickChange™ site-directed mutagenesis. Overlapping sequences are indicated with bold letter, while mutated nucleotides are red.

Variant	Mutation	Primers	
IsdB^{Y165A}	TAT > GCA	For	5'-**CACCCAGC**AGTTTGCACATTAT-3'
		Rev	3'-TTTTTTTCCTACC**GTGGGTCG**-5'
IsdB^{Y440A}	TAT > GCA	For	5'-**ATGCAGATG**GCCAGTATCATG-3'
		Rev	3'-ACTTTTGGTAGC**TACGTCTAC**-5'
FL-IsdB^{*604L}	TAA > TTA	For	5'-**CAGACCGCT**AGCTTACTCGAG-3'
		Rev	3'-TTTTCGGACGGC**GTCTGGCGA**-5'

2.3 Protein overexpression

IsdB^{N1LN2} and its variants in LB broth. *E. coli* BL21(DE3) cells transformed with pASK-IBA3plus::IsdB^{N1LN2}, or the plasmids coding for IsdB^{Y165A} or IsdB^{Y440A} mutants, were plated on LB agar with 100 µg/mL ampicillin and grown overnight at 37 °C. A single colony was inoculated in 10 mL of LB broth with 100 ng/mL ampicillin and grown overnight at 37 °C and 250 RPM. Overnight culture was diluted 1:100 in LB broth with 100 µg/mL ampicillin. Cells were grown at 37 °C and 250 RPM until the midlog phase (OD600 = 0.5 – 0.6), which usually took less than 4 hours, and induced with 0.2 µg/mL anhydrotetracycline (AHT). Induction was performed for 20 hours at 20 °C. Cells were removed from the broth by centrifugation (5,000 RPM, 10 minutes), washed once with PBS and frozen at -80 °C in aliquots corresponding to 250 mL of culture.

IsdB^{N1LN2} in M9 minimal medium. *E. coli* BL21(DE3) cells transformed with pASK-IBA3plus::IsdB^{N1LN2} were plated on LB agar with 100 µg/mL ampicillin and grown overnight at 37 °C. A single colony was inoculated in 10mL of LB broth with 100 ng/mL ampicillin and grown overnight at 37 °C and 250 RPM. Overnight culture was diluted 1:100 in M9 minimal medium with 100 µg/mL ampicillin. Cells were grown at 37 °C and 250 RPM until the midlog phase (OD600 = 0.5 – 0.6), which usually took 5 hours, and induced with 0.2 µg/mL AHT. Induction was performed for 3 hours at 37 °C. Cells were removed from the broth by centrifugation (5,000 RPM, 10 minutes), washed once with PBS and frozen at -80 °C in aliquots corresponding to 500mL of culture.

Screening conditions for IsdB^{N1LN2} overexpression. *E. coli* BL21(DE3) cells transformed with pASK-IBA3plus::IsdB^{N1LN2} were plated on LB agar with 100 µg/mL ampicillin and grown overnight at 37 °C. A single colony was inoculated in 10mL of LB broth with 100 ng/mL ampicillin and grown overnight at 37 °C and 250 RPM. Overnight culture was diluted 1:100 in either 5 mL of LB broth or M9 minimal medium with 100 µg/mL ampicillin. Cells were grown at 37 °C and 250 RPM until the midlog phase (OD600 = 0.5 – 0.6) and induced with 2-200 ng/mL AHT. Inductions were performed either for 3 hours at 37 °C or for 20 hours at 20 °C. Cells were removed from the broth by centrifugation (5,000 RPM, 10 minutes), washed once with PBS and frozen at -80 °C in aliquots.

FL-IsdB in LB broth. *E. coli* BL21(DE3) cells transformed with pET28a::FL-IsdB were plated on LB agar with 50 µg/mL kanamycin and grown overnight at 37 °C. A single colony was inoculated in 10 mL of LB broth with 50 µg/mL kanamycin and 1% glucose and grown overnight at 37 °C and 250 RPM. Overnight culture was diluted 1:100 in LB broth with 50 µg/mL kanamycin and 1% glucose. Cells were grown at 37 °C and 250 RPM until the midlog phase (OD600 = 0.5 – 0.6) and induced with 1 mM isopropyl-D-thiogalactopyranoside (IPTG). Induction was performed for 20 hours at 20 °C. Cells were removed from the broth by centrifugation (5,000 RPM, 10 minutes), washed once with PBS and frozen at -80 °C in aliquots corresponding to 500 mL of culture.

2.4 Protein purification

IsdB^{N1LN2} and its variants. The protein purification protocol was identical for protein overexpressed both in LB broth and M9 minimal medium and started by resuspension of cell pellet in 25 mL of buffer W (100 mM Tris pH 8, 150 mM NaCl, 1 mM EDTA) in presence of 1 mg/mL lysozyme, 0.2 mM PMSF, 0.2 mM benzamidine and 1.5 µM pepstatin A. Cells lysis was completed by sonication, approximately three 1 minute-cycles (10s ON/30s OFF) at 30% amplitude ensured the almost complete protein recovery. Cell debris was removed by centrifugation, 1 hour at 4 °C and 16,000 xg. The pH of the supernatant was adjusted to more than 8 before loading the solution on preequilibrated column, packed with Strep-Tactin® XT resin (IBA Lifesciences). Protein was eluted with Buffer BXT (50 mM biotin in Buffer W). A final SEC step using a HiLoad 16/600 Superdex 75 prep grade column was necessary to separate the IsdB^{N1LN2} monomer from the dimer. Under these conditions, dimeric form of IsdB^{N1LN2} eluted in the void volume, well separated from the monomer. The final protein preparation was over 95% pure. IsdB^{N1LN2} concentration was calculated by using extinction coefficient ε(280 nm) = 47790 M^{-1} cm^{-1} and molecular weight = 43190 g/mol, or ε(280 nm) = 46300 M^{-1} cm^{-1} and molecular weight = 43100 g/mol for IsdB^{Y165A} and IsdB^{Y440A} variants.

Since IsdB^{N1LN2} partially acquired heme from *E. coli* during overexpression, the amount of holo-IsdB^{N1LN2} in the preparation was estimated by calculating the heme concentration with the ε(405 nm) = 90500 M^{-1} cm^{-1} (estimated in this work) and following the equation:

$$\%holo - IsdB = \frac{\left({OD_{405}}/{\varepsilon_{405}}\right)}{\left({OD_{280}}/{\varepsilon_{280}}\right)} \times 100$$

Optimization of overexpression conditions for IsdB^{N1LN2}. Protein purification was started by resuspension of cell pellet in 2.5 mL of buffer W (100 mM Tris pH 8, 150 mM NaCl, 1 mM EDTA) in presence of 1 mg/mL lysozyme, 0.2 mM PMSF, 0.2 mM benzamidine and 1.5 µM pepstatin A. Cells lysis was achieved through sonication, approximately three rounds of 1 minute (10s ON/30s OFF) at 30% amplitude ensured the almost complete protein recovery. Cell debris was removed by centrifugation, 1 hour at 4 °C and 16,000 xg. The pH of the supernatant was adjusted to more than 8 before loading the solution onto a pre-equilibrated Strep-Tactin® XT spin column (IBA Lifesciences), 500 µL at a time. The lysate was passed through the small layer of resin by centrifugation (30s at 700 xg). This process was repeated four times to pass all the lysate through the resin. Flow-through was discarded each time. The spin column was washed four times with 100 µl of buffer W before the elution. Protein was eluted with 150 µL of Buffer BXT (50 mM biotin in Buffer W) in two steps: (1) 30s at 700 xg and (2) 15s at 16,000 xg. Protein concentration was calculated by using extinction coefficient ε(280 nm) = 47790 M^{-1} cm^{-1}. Approximately 5 µg of purified protein were analyzed by native PAGE to assess the relative proportion of monomer and dimer.

FL-IsdB. Protein purification was started by resuspension of cell pellet in 25mL of lysis buffer (50 mM Tris pH 8, 150 mM NaCl) in presence of 1 mg/mL lysozyme, 0.2 mM PMSF, 0.2 mM benzamidine and 1.5 µM pepstatin A. Cells lysis was achieved through sonication, approximately four rounds of 1 minute (5s ON/55s OFF) at 30% amplitude ensured the almost complete protein recovery. Cell debris was removed by centrifugation, 1 hour at 4 °C and 16,000 xg. The pH of the supernatant was adjusted to more than 7.5 before loading the solution on preequilibrated column packed of TALON® Superflow™ resin (GE Healthcare).

Subsequently, washing buffer (20 mM imidazole in lysis buffer) was used to remove non-specific binding proteins from the resin before eluting FL-IsdB with elution buffer (500 mM imidazole in lysis buffer). Thrombin (Sigma Aldrich) was added to the protein solution to cleave the HisTag, 5 µL of the protease per mg of purified protein were added as suggested by the seller. HisTag-FL-IsdB concentration was calculated by using extinction coefficient ε(280 nm) = 43780 M^{-1} cm^{-1} and molecular weight = 67230 g/mol. The digestion was completed overnight at room temperature. The resulting solution was concentrated with an Amicon Stirred Cell (Millipore) using a 30 kDa cut-off membrane, this step was also intended to remove HisTag from the solution. Final concentration of FL-IsdB was calculated by using extinction coefficient ε(280nm) = 43780 M^{-1} cm^{-1} and molecular weight = 65400 g/mol.

Human Hb. Human Hb A was purified from outdated blood obtained from a local blood transfusion center. Only Hb from non-smoking donors was purified, as described previously [341,342]. Briefly, red blood cells (RBC) were washed in saline solution and then lysed under hypotonic conditions (e.g., adding 7 volumes of Buffer Hb1 - 10 mM HEPES pH 6.9, 1 mM EDTA). The supernatant containing the oxyHb was separated from cell debris by centrifugation, 1 hour at 4 °C and 23,000 xg, and dialyzed against Buffer Hb1. The resulting solution was layered on a 100 X 5 cm CM-Sephadex C-50 column. Soluble RBC components were separated from Hb using a linear gradient from 0 to 80% of buffer Hb2 (10 mM HEPES pH 8.6, 1 mM EDTA), while Hb was eluted using a linear gradient from 80 to 85% of buffer Hb2. The purified protein was dialyzed against the storage buffer (10 mM HEPES pH 7.2, 1 mM EDTA), aliquoted, flash-frozen in liquid nitrogen and stored at −80 °C until further use. The concentration and the oxidation state of purified oxyHb was determined by UV-visible absorption spectroscopy by exploiting tabulated molar extinction coefficients for heme-characteristic absorption peaks [343].

2.5 Preparation of various Hb forms

MetHb. MetHb was obtained by oxidizing oxyHb in the presence of 5 mM potassium ferricyanide (Fluka). OxyHb was incubated for 10 minutes at room temperature in the presence of the oxidizing agent, the latter was removed on a Sephadex G-25 desalting column. MetHb concentrations was calculated spectroscopically by using the extinction coefficient at 406 nm determined in this thesis.

COHb. COHb was prepared by keeping oxyHb in a sealed glass chamber where a stream of pure carbon monoxide was passing over the solution. The reaction was carried out at 4 °C in the dark for 10 minutes by gently shaking the sample chamber to increase the diffusion of the gas into the solution and thus the ligand exchange. The completion of the reaction was confirmed by absorption spectroscopy by using tabulated molar extinction coefficients for heme-characteristic absorption peaks [343].

SemiHbs. SemiHbs are derivatives of human Hb which carry the heme on only α- or β-chains, while the complementary chain is heme-free, and they were prepared as described previously [339] mixing apo-Hb with isolated α- and β-subunits. First, apo-Hb (the heme-free form, where heme is totally removed from both α- and β-subunits) was prepared as previously described [344]. Briefly, metHb is added to an equal volume of butanone in a separatory funnel at 4 °C and the pH was adjusted to 2.5 with 1 M HCI under vigorous stirring. After standing 1 min at 4 °C, the aqueous phase was separated from the organic layer. Acidic solution was intended to denature Hb resulting in the heme loss, with the latter moving into the organic solvent. The extraction was repeated three times on the recovered aqueous phase. The resulting solution was exhaustively dialyzed against distilled water to remove butanone, then against 0.2 M phosphate buffer pH 7.0, and finally against the buffer used for semiHb preparation (0.1 M phosphate pH 7, 150 mM NaCl, 1 mM EDTA).

The preparation of separated α and β subunits in their native state was carried out by following the method of Bucci and Fronticelli [345]. Briefly, COHb was mixed with p-chloromercuribenzoate (CMB) in 20 mM potassium phosphate pH 7 at the ratio Hb : CMB of 1:8. Ionic strength was brought to 0.1 with potassium chloride and the pH was adjusted to pH 6, then reaction was completed overnight at 4 °C. CMB was intended to bind thiol group on

both α- and β-Hb subunits forcing Hb monomerization. The resulting solution was equilibrated in 10 mM potassium phosphate pH 5.8 and loaded on a CM-Sephadex column. The elution of separated Hb subunits was achieved with a pH gradient, β-Hb chains eluted at pH 6.4 while α-Hb chains eluted at pH higher than 7.4. After the separation, CMB was removed from Hb subunits by adding cysteine at 50-molar excess with respect to the number of thiol groups to be regenerated. Finally, protein solutions were exchanged in the buffer needed for semiHb preparation (0.1 M potassium phosphate pH 7, 150 mM NaCl, 1 mM EDTA). Semi(α)Hbs, the form presenting the prosthetic group bound only to the α-Hb subunit, were prepared by mixing apo-Hb with isolated α-chains in the carboxy form in 0.1 M potassium phosphate pH 7, 0.15 M NaCl, and 1 mM EDTA. The reaction was completed in 65 h at 4 °C. A final SEC step using a GE HiLoad 16/600 Superdex 75 prep grade column (separation range 3 – 70 kDa) allowed to separate intermediate compounds (including apo-Hb monomer and tetramer, but also unreacted species such as isolated chains of holo-Hb), and thus isolating the desired final product. Semi(β)Hbs were prepared by mixing apo-Hb with separated β-Hb subunits, and following the same protocol as semi(α)Hbs.

2.6 Fast Protein Liquid Chromatography (FPLC)

All chromatographic runs were performed at 4 °C using an AKTA Prime Liquid Chromatography System (GE Healthcare) equipped with a single wavelength UV detector (280 nm) and a conductivity meter.

Affinity chromatography.

- XK 16/200 column (GE Healthcare), packed in house with 3 mL Strep-Tactin® XT resin (IBA Lifesciences), was exploited for affinity purification of StrepTag®II-IsdB^{N1LN2} and its variants.
- XK 16/200 column (GE Healthcare), packed in house with 10 mL TALON® Superflow™ resin (GE Healthcare), was exploited for affinity purification of FL-IsdB and its variants.

SEC. SEC experiments were performed for both preparative and analytical purposes.

- HiLoad 16/600 Superdex 75 pg prepacked column (GE Healthcare), separating range 3-70 kDa, was principally used as a preparative column. The column was cleaned every five purification processes and calibrated with blue dextran (void volume), conalbumin (75 kDa), ovalbumin (43 kDa), carbonic anhydrase (29 kDa), myoglobin (17 kDa) to validate its separation performance.
- XK 16/300 column (GE Healthcare) packed in-house with 48 mL of a BioSepra Ultrogel AcA 44 resin, separating range 10-130 kDa, was exploited for analytical purposes. A sample volume of 0.5 mL was usually applied to the columns. The column was calibrated with blue dextran (void volume), alcohol dehydrogenases (140 kDa), conalbumin (75 kDa), ovalbumin (43 kDa), and carbonic anhydrase (29 kDa).

To estimate the area under the curve of chromatographic runs, the elution profile was deconvoluted into multiple gaussians (Fityk software [346]).

Determination of the dissociation constant for the tetramer-dimer equilibrium of oxy- and metHb. The tetramer-dimer dissociation equilibrium of both oxyHb and metHb was assessed using SEC on the HiLoad 16/600 Superdex 75 column (GE Healthcare) in 0.1 M Tris/HCl pH 8, 0.15 M NaCl, 1 mM EDTA. 500 µL of Hb samples in the oxy and met forms were injected on the column at different concentrations (from 0.2 to 40 µM). Dilution factors after elution were calculated according to [326].

2.7 UV-visible absorption spectroscopy

Proteins UV-visible absorption spectra were recorded on an Agilent Cary 4000 spectrophotometer equipped with a temperature-controlled cell-holder. Hellma™ Far UV Quartz Cuvettes (1 cm pathlength) were used unless otherwise indicated.

Molar extinction coefficients of metHb in different buffers. The estimation of the molar extinction coefficient of metHb at 406 nm was carried out in buffer W (100 mM Tris/HCl pH 8, 150 mM NaCl, 1 mM EDTA) and binding buffer (25 mM Tris/HCl pH 7.6, 140 mM NaCl, 2 mM EDTA). The entire analysis was performed in a sample chamber that consisted of a 2-mm optical path length cuvette fused to a 25-ml open-top threaded reservoir, where a screw

cap with fittings for inlet and outlet gas lines can be mounted. The UV-visible spectrum (240-750 nm) of oxyHb was recorded before proceeding with Hb deoxygenation. To obtain deoxygenated Hb (deoxyHb) a flow of helium was continuously passed over the Hb solution. During Hb deoxygenation, the sample chamber was thermostated at 20 °C in a shaking bath. The completion of the reaction was confirmed by UV-visible absorption spectroscopy. Finally, deoxyHb was oxidized by adding 2 µL of 250 mM potassium ferricyanide. The final spectrum of metHb form was acquired. OxyHb and deoxyHb UV-visible spectra are independent from the buffer pH and were used to precisely calculate the Hb concentration inside the cuvette before the heme oxidation that led to metHb formation.

Molar extinction coefficient of holo-IsdB^{N1LN2}. IsdB^{N1LN2} was mixed with an equimolar amount of hemin (Fluka Analytical) during overnight incubation at 4 °C on the rotary mixer. Denatured proteins and heme aggregates were removed by centrifugation, 30 minutes at 4 °C and 16,000 xg. The heme content of holo-IsdB^{N1LN2} was determined with the pyridine hemochromagen assay [347]. Pyridine hemochromagen is the hexacoordinated form of heme, where the axial positions are occupied by two pyridine molecules. Briefly, protein solution was mixed with NaOH (final concentration, C_f = 0.1 M), which caused the protein denaturation, pyridine (C_f = 20%), which formed the hemochromagen by coordinating the freed heme from the protein, and potassium ferricyanide (C_f = 0.5 mM), which ensured the heme oxidation. The spectrum of the oxidized hemochromagen was recorded before adding a few grains of solid dithionite to the cuvette, which immediately reduced hemic-iron. The spectrum of the reduced form of hemochromagen was recorded and the tabulated ε(557 nm) = 32 M^{-1} cm^{-1} was used to calculate the concentration of the prosthetic group.

2.8 PolyAcrylamide Gel Electrophoresis (PAGE)

Sodium Dodecyl Sulphate PAGE (SDS-PAGE). The electrophoretic runs of protein samples in denaturing conditions were performed on 0.75 mm freshly casted mini gels, which were prepared following the recipes in Table 5 and were composed of two different gel layers (stacking and separating gel). Standard 12% gel was used for any purpose, while 15% gel was exploited to separate α- and β-Hb chains. Mini gels were run in a Bio-Rad Mini-PROTEAN

Tetra Vertical Electrophoresis Cell powered by Bio-Rad PowerPac™ Basic Power Supply set at 200V. Precision Plus Protein™ Unstained Protein Standards (Bio-Rad) was used as a molecular weight marker. After electrophoretic run, the gel was incubated 10-15 minutes in Coomassie staining solution. Subsequently several destaining steps were performed up to the desired visualization of protein bands.

*Table 5: Recipes for SDS-PAGE. * Volume necessary to prepare a 0.75mm Bio-Rad Mini-PROTEAN gel.*

Stacking gel* (acrylamide/bis, 4% final)	Volume (µL)
Acrylamide/bis, 30% 29:1	400
0.5 M Tris/HCl pH 6.8	750
Water	1730
SDS, 10%	30
APS, 10%	20
TEMED	6
Separating gel* (acrylamide/bis, 12% final)	**Volume (µL)**
Acrylamide/bis, 30% 29:1	1992
0.5 M Tris/HCl pH 6.8	1250
Water	1662
SDS, 10%	50
APS, 10%	40
TEMED	8
Separating gel* (acrylamide/bis, 15% final)	**Volume (µL)**
Acrylamide/bis, 30% 29:1	2500
0.5 M Tris/HCl pH 6.8	1250
Water	1160
SDS, 10%	50
APS, 10%	40
TEMED	8

Sample buffer 4X	Volume (mL)
0.5 M Tris/HCl pH 6.8	2
SDS, 10%	4
β-mercaptoethanol	0.4
Bromophenol blue 0.5%	0.8
Glycerol, 100%	2.8
Running solution 10X	**Grams in 500 mL**
Tris base	15.1
SDS	0.5
Glycine	72.1
Coomassie Staining solution	**Volume (mL)**
Coomassie Blue	2.5 g
Glacial acetic acid	100
Ethanol	200
Water	700
Coomassie Staining solution	**Volume (mL)**
Glacial acetic acid	100
Ethanol	200
Water	700

Native PAGE. The optimized protocol uses 1 mm freshly casted continuous mini gel, which was prepared following the recipes reported in Table 6. The protocol was adapted from the method proposed by McLellan [348].

*Table 6: Recipes for native PAGE. * The pH of the solution does not need to be adjusted.*

Separating gel solution for a single 1 mm gel	
Acrylamide/Bis-acrylamide (29:1), 30%	2.25 mL
Water	3.75 mL
Running buffer 5X (14.64 g/L imidazole and 41.71 g/L HEPES)	1.5 mL
APS 10%	100 µL
TEMED	12 µL
Sample buffer 3X	
Running buffer, 5X	1 mL
Glycerol, 50%	2 mL
Malachite green solution, 1%	0.2 µL
Running buffer 5X*	
Imidazole	14.64 g/L
HEPES	41.71 g/L

Approximately 5 µg of sample, diluted in 20 µL of sample buffer 1X, were usually analyzed, with smaller samples giving the best resolution. Internal running buffer was freshly diluted from the 5X solution for every electrophoretic run, whereas the external buffer was reused. Both buffers were cooled down before the use by keeping them at 4 °C overnight. Mini gels were run in a Bio-Rad Mini-PROTEAN Tetra Vertical Electrophoresis Cell located into an ice bath to keep temperature below 10 °C throughout all the electrophoretic run and powered by Bio-Rad PowerPac™ Basic Power Supply. The electrophoretic run was divided into three steps to maintain the voltage below 200 V: (1) 10 minutes at 20 mA, (2) 10 minutes at 15 mA, and (3) 330 minutes at 11 mA. Purified monomeric and dimeric $IsdB^{N1LN2}$ were used as internal markers. After electrophoretic run, the gel was incubated 10-15 minutes in Coomassie staining solution. Subsequently several destaining steps were performed up to the desired visualization of protein bands.

Densitometry of the stained gels was used to quantify the relative composition of protein bands corresponding to monomeric and dimeric $IsdB^{N1LN2}$ populations within the same lane. Gels were imaged with a ChemiDoc MP imaging system (Bio-Rad©) and densitometric analysis was performed on Image Lab™ software (Bio-Rad©).

3 Results and Discussion

3.1 IsdB^{N1LN2} overexpression and purification

E. coli BL21 (DE3) cells transformed with pASK-IBA3plus::IsdB^{N1LN2} expression plasmid were used for the hemophore overexpression and purification. Overexpression and affinity chromatography step resulted in a fast and high-yield purification (up to 150 mg of protein form 1 L of bacterial culture), moreover final purity was higher than 95% (Figure 13).

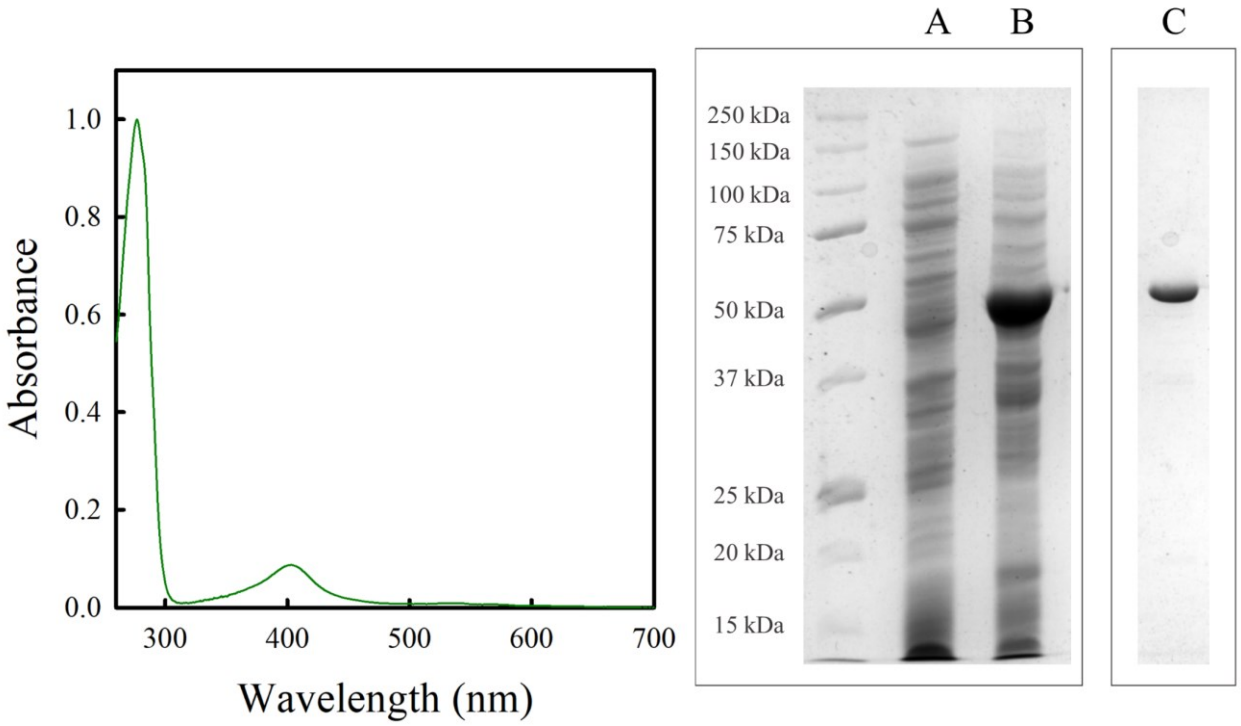

Figure 13: Purification of IsdB^{N1LN2}. On the left, UV-visible absorption spectrum of the purified IsdB^{N1LN2} stock solution in buffer W. The amount of holo-IsdB^{N1LN2} was calculated to be lower than 5%. On the right, SDS-PAGE analysis of IsdB^{N1LN2} overexpression and purification. (A) Noninduced cells, (B) induced cells, (C) purified IsdB^{N1LN2}.

However, SEC on purified protein preparation indicated the presence of two different species of the hemophore in solution, one having a molecular weight twice as the other (Figure 14). The chromatograms were obtained with three distinct rounds of overexpression and purification. Even if the relative amount of low- and high-molecular weight fractions varied among different preparations, it was not possible to directly attribute this result to a specific growth parameter.

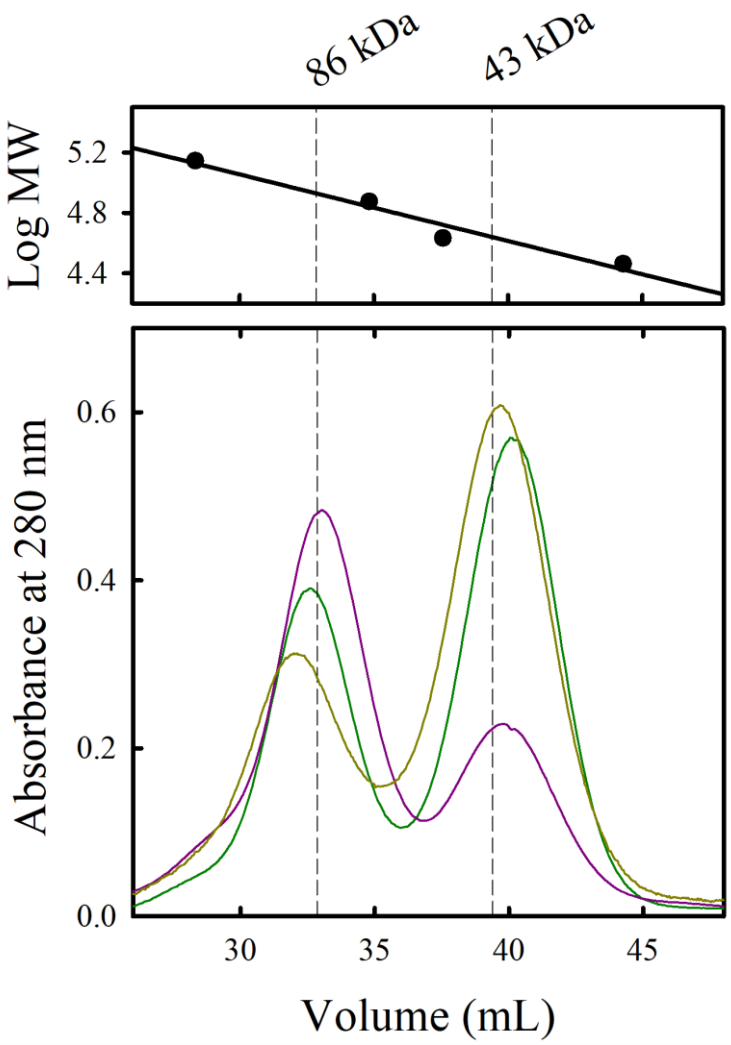

Figure 14: SEC of three different IsdB^{N1LN2} preparations on BioSepra Ultrogel AcA 44 resin. The upper plot reports the calibration curve, while the lower plot shows the three chromatograms (run 1 in yellow, run 2 in purple, and run 3 in green). Dashed lines indicate the molecular weight of IsdB^{N1LN2} monomer and dimer in both plots.

However, a link between the dimer formation and the heterologous expression in *E. coli* was found by exploring different overexpression conditions (vide infra). Electrophoresis under denaturing conditions confirmed that both the high- and low-molecular weight forms were IsdB^{N1LN2}, suggesting that the high-molecular weight population was formed by a dimer of IsdB^{N1LN2} that dissociates under denaturing conditions (Figure 15).

This observation was supported by the good correspondence of the SEC calculated molecular weight and the theoretical one, calculated with ProtParam based on the sequence of the recombinant construct (Table 7).

Table 7: Calculated molecular weight of monomeric and dimeric IsdB^{N1LN2} compared with estimated molecular weights of species separated from purified IsdB^{N1LN2} samples on BioSepra Ultrogel AcA 44 resin.

	Peak 1 – molecular weight (Da)	Peak 2 – molecular weight (Da)
Calculated	86,380	43,190
Run 1 (yellow)	93,510	41,950
Run 2 (dark pink)	84,710	41,480
Run 3 (dark green)	88,690	40,350

The spectroscopic analysis of the two populations revealed that the Soret band had a higher relative intensity for monomeric IsdB^{N1LN2} compared to that of dimeric fraction, suggesting a reduced ability of the latter in binding heme in *E. coli* during heterologous overexpression (Figure 17).

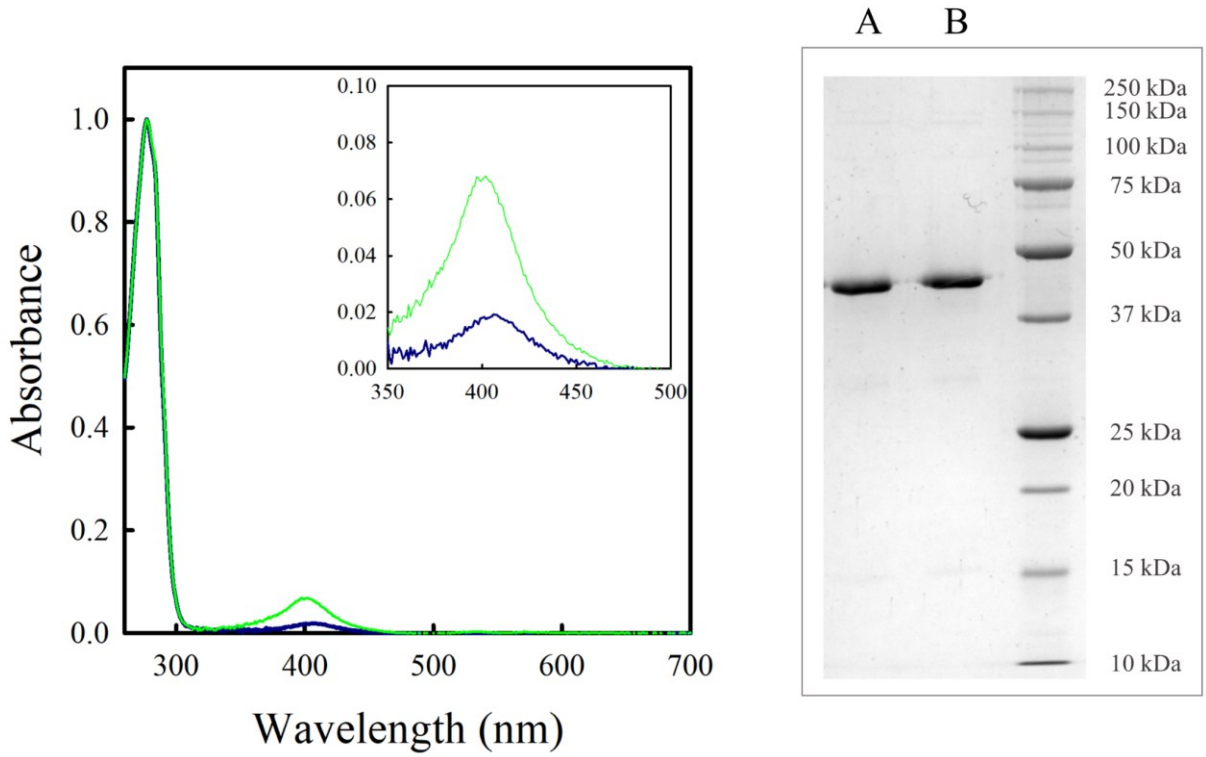

Figure 15: Characterization of monomeric and dimeric IsdB^{N1LN2}. On the left: UV-visible absorption spectra of monomeric (green) and dimeric (dark blue) IsdB^{N1LN2}, heme content was lower than 5% for monomeric IsdB^{N1LN2} and lower than 1% for dimeric IsdB^{N1LN2}. Inset: visible region of monomeric and dimeric IsdB^{N1LN2} spectra. On the right: SDS-PAGE analysis of (A) monomeric and (B) dimeric IsdB^{N1LN2}.

Monomeric and dimeric fractions of IsdB^{N1LN2} were successfully separated using a HiLoad 16/600 Superdex 75 prep grade column, which allowed to increase the rate of the separation step, and characterized independently. All the experiments performed in the thesis were conducted on the monomeric IsdB^{N1LN2} purified after the overexpression in LB medium.
Since the presence of dimeric IsdB^{N1LN2} has never been reported in literature, it was separated and tested independently to achieve further insights on this unexpected protein organization, results of these analyses are presented in Chapter II. Notably, the dimer appeared not to be in equilibrium with the monomer (e.g., only chemical denaturation and subsequent refolding allowed to recover the monomeric protein), which has enabled to easily characterize the two populations separately. The relative intensity of Soret peak compared to the absorbance at 280 nm was comparable throughout all the protein preparations after Strep-Tactin® XT affinity purification, regardless of the relative composition in monomeric/dimeric fractions. This finding suggested that the hemophore always acquired the same total amount of heme during overexpression, that was limited by the ability of *E. coli* cells to produce the cofactor. However, since dimeric fraction turned out to be less contaminated with heme, the preparations where the proportion of dimeric IsdB^{N1LN2} was higher resulted in highly contaminated monomeric IsdB^{N1LN2} (heme content >5%) which were considered not suitable for further analysis. This last problem made the optimized overexpression conditions inconvenient, therefore alternative protocols were tested with the aim of finding a way for limiting the dimer formation.

3.2 Native PAGE for the separation of IsdB^{N1LN2} monomer and dimer

To characterize the relative content of monomeric and dimeric fractions of different purified protein preparations and to speed-up the search for optimal expression/purification conditions, a native PAGE protocol was optimized. The rationale was that the two protein populations present the same charge to mass ratio, but they move differently through the gel matrix due to their different size. The selection of running buffer and polyacrylamide gel composition was based on the work published in 1982 by McLellan [348] and the ProtParam calculated isoelectric point of IsdB^{N1LN2}, which is approximately 8.9. The histidine-MES (pH 6.1) and imidazole-HEPES (pH 7.5) ions pairs were tested, and the latter was chosen for the satisfactory separation of IsdB^{N1LN2} monomer and dimer bands.

To certify the analytical performance of the developed native PAGE protocol, the method was compared with a preparative SEC run onto the HiLoad 16/600 Superdex 75 prep grade column (GE Healthcare). The same sample was analyzed with both techniques and the monomer-dimer ratio calculated, resulting in a comparable result (Figure 16 and Table 8).

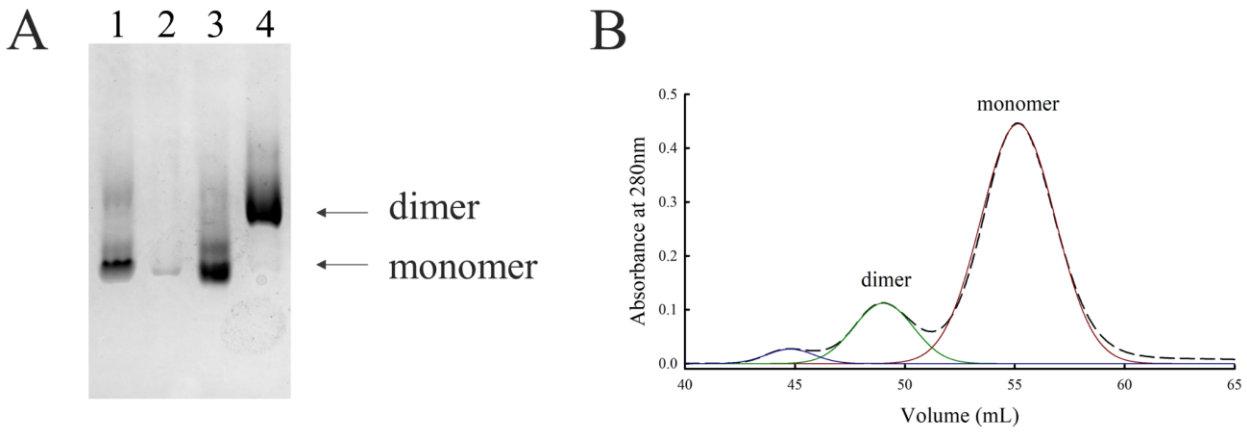

Figure 16: Comparison between the performance of native PAGE and SEC analysis in the separation and relative quantification of monomeric and dimeric fractions of IsdB^{N1LN2}. (A) Native PAGE was loaded with: lane 1 - 5 µg of the IsdB^{N1LN2} on Strep-Tactin® XT column, lane 2 - 1 µg of the IsdB^{N1LN2} on Strep-Tactin® XT column, lane 3 - monomeric IsdB^{N1LN2}, and lane 4 - dimeric IsdB^{N1LN2}. (B) Deconvolution of elution profile performed using Fityk software. The plot shows the three extrapolated components (blue, green, and red) compared with the experimental track (dashed line).

Table 8: Comparison between native PAGE and SEC results (Figure 16). % values for native PAGE were calculated through densitometric analysis, while SEC relative values were calculated based on the chromatogram deconvolution.

	% of monomer	% of dimer
Native PAGE	79	21
SEC	82	18

Since native PAGE showed reliable outputs, it was used as a fast method for assessing relative monomer-dimer composition of different overexpression conditions.

3.3 Optimization of IsdB^{N1LN2} overexpression to reduce dimeric fraction

Since dimeric IsdB^{N1LN2} is an undesirable contaminant for the biochemical characterization of the IsdB-Hb complex formation, as detailed in Chapter II, different overexpression conditions were tested to find the one that minimized its formation. Overexpression in 5 mL of liquid culture and purification on Strep-Tactin® XT spin columns allowed to test several different conditions.

The tested conditions are the following:

(1) liquid nutrient media:
   a. LB;
   b. M9 minimal medium;

(2) concentrations of the inducer AHT:
   a. 2 ng/mL;
   b. 20 ng/mL;
   c. 200 ng/mL;

(3) temperature and duration of expression:
   a. 3 hours at 37 °C;
   b. 20 hours at 20 °C.

In Figure 17 the native PAGE of IsdB^{N1LN2} obtained under the above-mentioned conditions and purified on spin-columns is shown. Overexpression with 200 ng/mL AHT in M9 minimal medium at 37 °C for 3h was identified as the best condition to limit the formation of dimeric IsdB^{N1LN2} and to cut down on heme contamination of purified hemophore. In fact, also the overexpression condition in LB at 37 °C for 3 hours appeared good to limit dimer formation, but the bacterial growth in minimal medium was also expected to limit the production of heme inside the cells, with subsequent reduction of the cofactor acquisition by the hemophore during overexpression.

The comparison, through densitometric analysis of the gel, between the new selected condition in lane A with the initial overexpression condition in lane C revealed that the fraction of dimeric IsdB^{N1LN2} for expression in LB (50%) was decreased to less than 20% in M9.

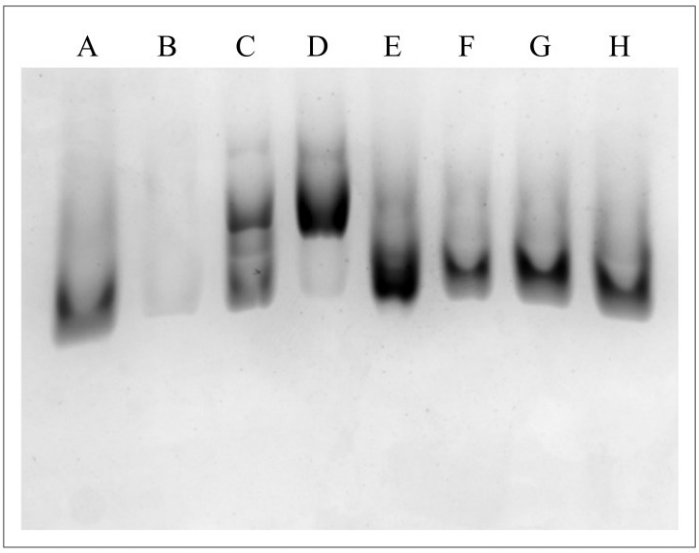

Figure 17: Native PAGE analysis of different IsdB^{N1LN2} overexpression conditions. (A) 200 ng/mL AHT in M9 minimal medium at 37 °C for 3 hours, (B) 200 ng/mL AHT in M9 minimal medium at 20 °C for 20 hours, (C) 200 ng/mL AHT in LB broth at 20 °C for 20 hours, (D) internal marker for dimer IsdB^{N1LN2} , (E) internal marker for monomeric IsdB^{N1LN2}, (F) 2 ng/mL AHT in LB broth at 37 °C for 3 hours, (G) 20 ng/mL AHT in LB broth at 37 °C for 3 hours, and (H) 200 ng/mL AHT in LB broth at 37 °C for 3 hours.

3.4 IsdB^{N1LN2} overexpression and purification in M9 minimal medium

After the optimization, *E. coli* BL21 (DE3) cells transformed with pASK-IBA3plus::IsdB^{N1LN2} were used for the hemophore overexpression in M9 minimal medium and purification (Figure 18). Compared to the LB broth, the amount of overexpressed protein was lower, but the total yield of the purification was satisfactory as well. In fact, 40 mg of monomeric IsdB^{N1LN2} were purified form 1 L of bacterial culture, with the final purity higher than 95% and the amount of holo-IsdB^{N1LN2} lower than 1%. Moreover, monomeric fraction consistently resulted higher than 85% of the total amount of purified protein, confirming the results obtained during the optimization trials.

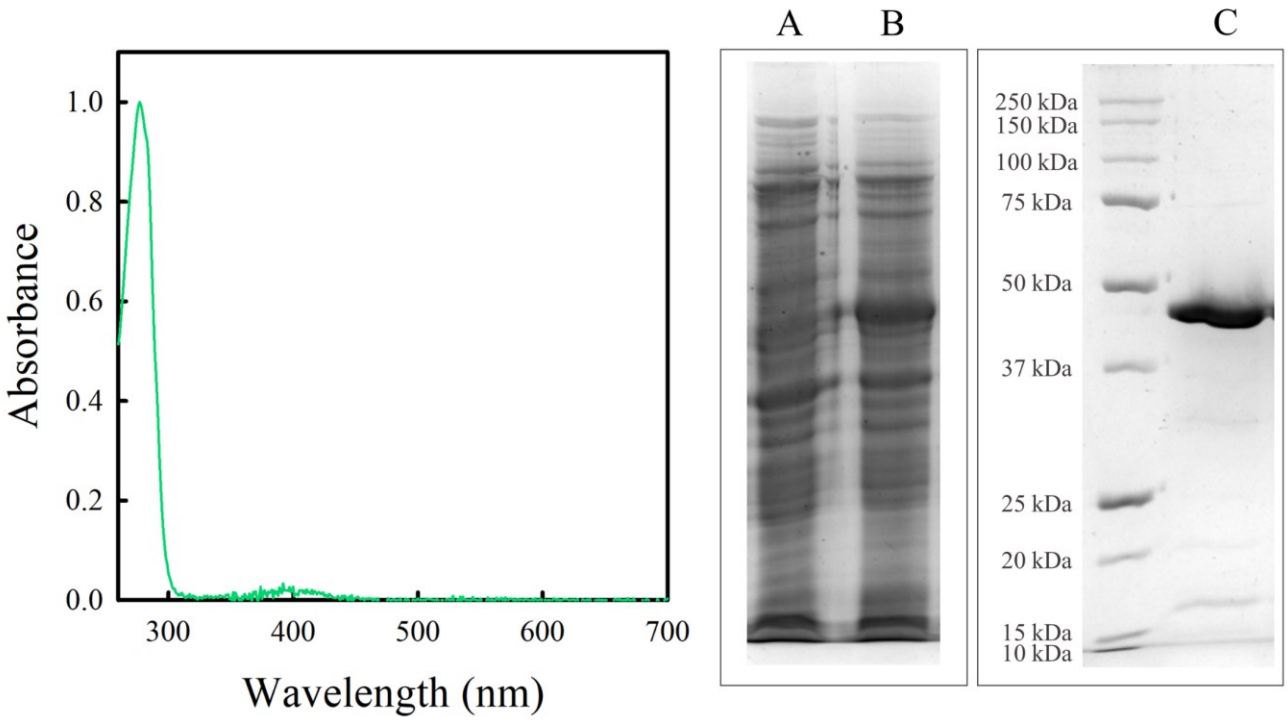

Figure 18: IsdB^{N1LN2} overexpression in M9 minimal medium and purification. On the left, UV-visible absorption spectrum, the amount of holo-IsdB^{N1LN2} was calculated to be lower than 1%. On the right, SDS-PAGE analysis of (A) non-induced cells, (B) induced cells, and (C) purified IsdB^{N1LN2}.

3.5 Expression and purification of IsdB^{N1LN2} variants.

Mutated plasmids for the heterologous expression of IsdB^{Y165A} and IsdB^{Y440A} were prepared with a modified protocol based on the QuickChange™ site-directed mutagenesis. Sequencing reactions confirmed the successful insertion of mutations (Figure 19).

E. coli cells transformed with pASK-IBA3plus::IsdB^{Y165A} or pASK-IBA3plus::IsdB^{Y440A} were used for the overexpression in LB broth and purification of the two IsdB^{N1LN2} variants (Figure 20). The yield of purification was similar to that of the WT protein (namely 100 mg of each mutant were purified from 1 L of bacterial culture) and the purity of the preparations was satisfactory (higher than 95%). Also, IsdB^{N1LN2} variants both presented monomeric and dimeric fractions, which were separated using a HiLoad 16/600 Superdex 75 prep grade column. Notably, mutants were prepared in the initial part of the work when the expression in M9 minimal medium was not optimized yet. The high yield of purification and the limited amount of protein needed for the experiments presented in this thesis did not make it necessary to purify further mutants. However, future expression of these proteins will be carried out with the optimized protocol in M9 for IsdB^{N1LN2}.

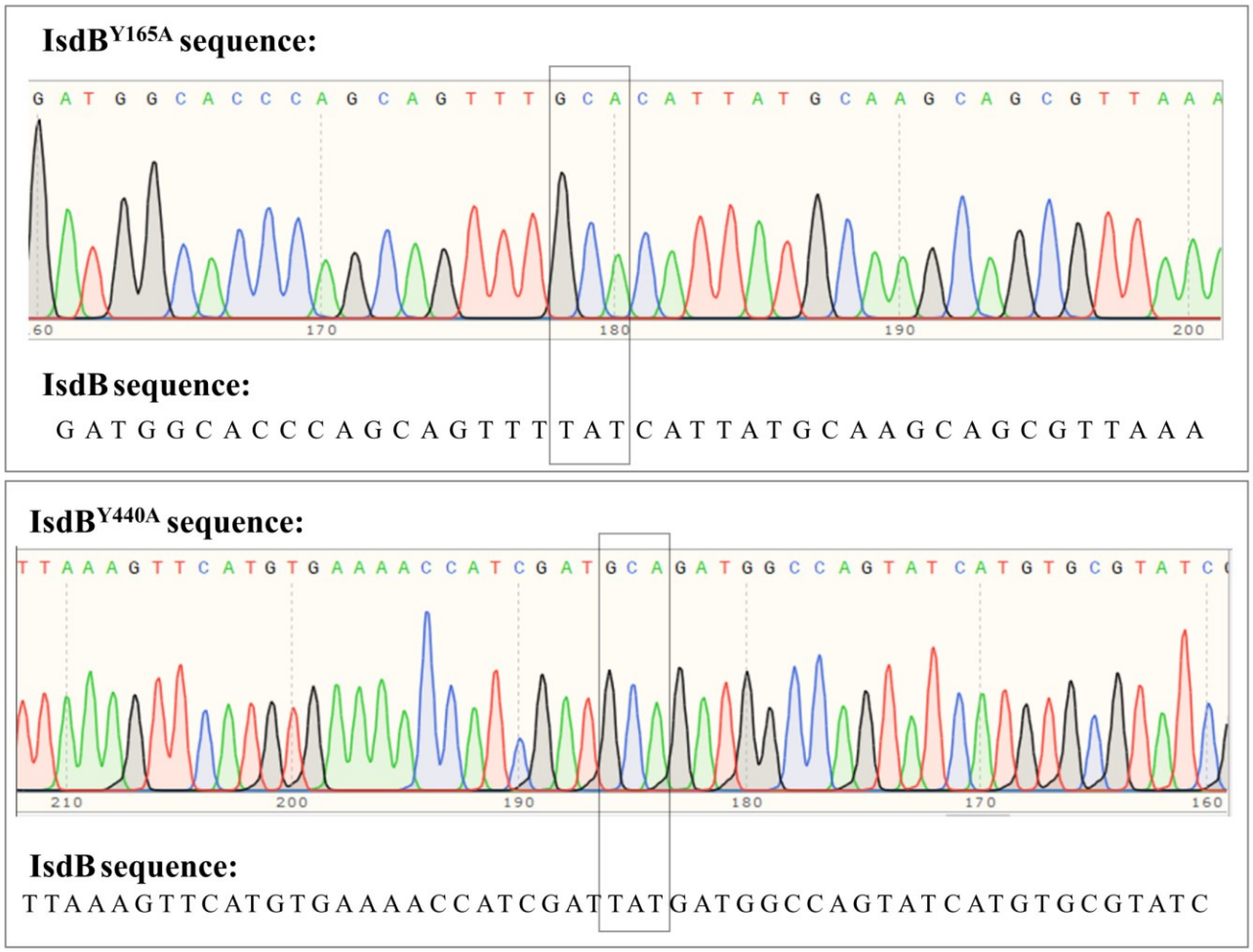

Figure 19: Results of sequencing reactions. On the top, comparison between sequencing results for IsdB^{Y165A} mutant and WT IsdB sequence. On the bottom, comparison between sequencing results for IsdB^{Y440A} and WT IsdB sequence.

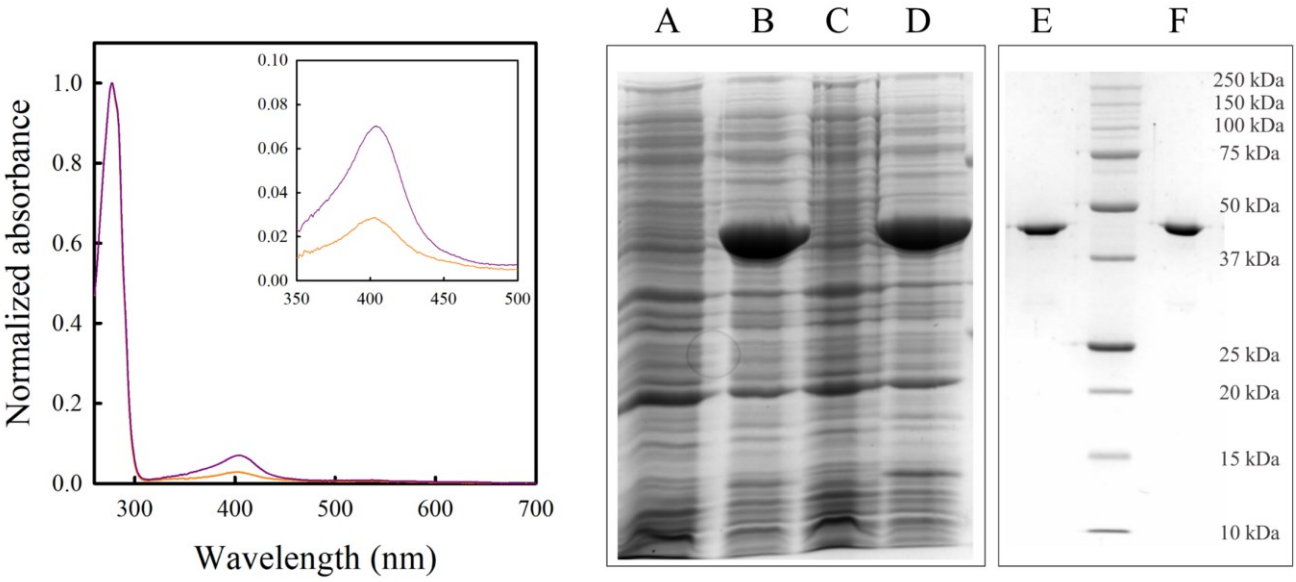

Figure 20: Overexpression and purification of IsdB^{Y165A} and IsdB^{Y440A} variants. On the left, UV-visible absorption spectra of the mutants. The amount of holo-form was lower than 4% and 2% for IsdB^{Y165A} and IsdB^{Y440A}, respectively. Inset: visible region of IsdB^{N1LN2} mutants spectra. On the left, SDS-PAGE analysis of (A) IsdB^{Y165A} noninduced cells, (B) IsdB^{Y165A} induced cells, (C) IsdB^{Y440A} noninduced cells, (D) IsdB^{Y440A} induced cells, (E) purified IsdB^{Y165A}, and (F) purified IsdB^{Y440A}.

Hb purification

OxyHb was purified from 25 mL of RBC. The purification protocol allowed to isolate 1.1 gram of pure oxyHb (more than 99% pure), with a metHb fraction lower than 1% (Figure 21). Since IsdB efficiently binds reduced ligated form of Hb but does not extract the heme from it, oxyHb (together with COHb) was employed to study IsdB-Hb complex encounter. Therefore, it was an important goal to produce a fully reduced oxyHb and metHb was considered an undesirable contaminant for the analysis.

The Hb Q bands region (500-650 nm) is highly sensitive to the oxidation state of the iron center of Hb, and the presence of metHb in solution is expected to determine both the formation of the characteristic peak at 630 nm and the variation of the oxyHb Q bands relative intensity. The UV-visible spectrum of oxyHb, in Figure 21, does not show the peak centred at 630 nm and the intensity of peaks at 415 nm, 541 nm and 575 nm was in good agreement with tabulated extinction coefficients [343].

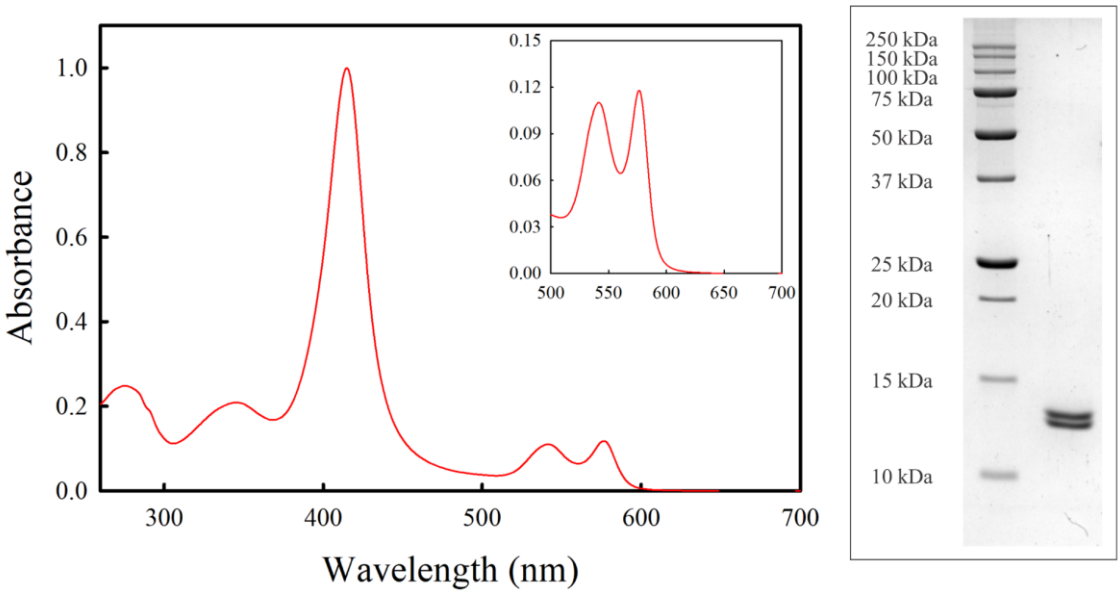

Figure 21: OxyHb purification. On the left, oxyHb UV-visible absorption spectrum; inset: Q bands region. On the right, SDS-PAGE analysis of purified Hb.

3.6 Preparation of COHb

COHb was prepared from oxyHb and it was used for the preparation of semiHbs and for cryo-EM analysis of IsdB-COHb complex. This reduced, ligated form of Hb is known to be less prone to autoxidation compared to oxyHb [349] and thus it was selected to avoid the formation of metHb. The protein, produced using a published protocol [350], presented the typical peaks of ligated-Hb (Figure 22). The concentration of the protein was calculated with tabulated molar extinction coefficients (ε(419 nm) = 191 mM^{-1} cm^{-1} [343]).

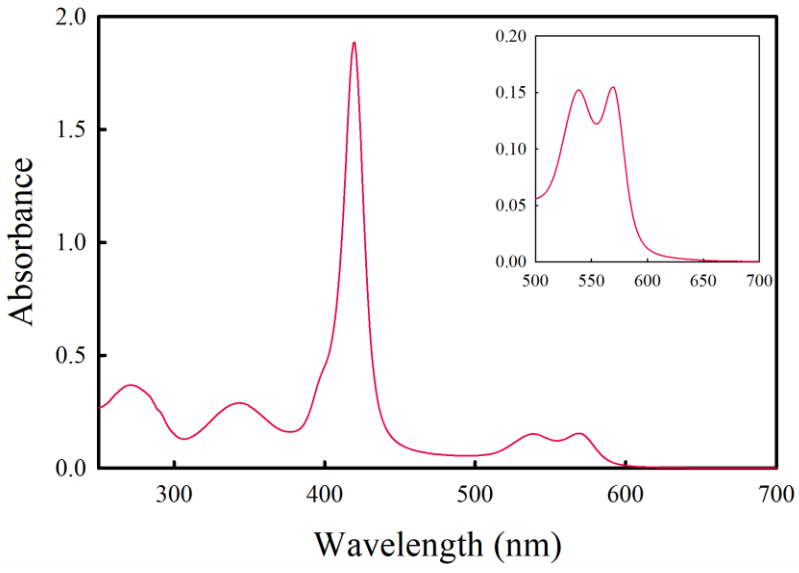

Figure 22: UV-visible absorption spectrum of COHb; inset: Q bands region.

3.7 Preparation of semiHbs

SemiHbs were prepared by following a published protocol. Figure 23 shows the final chromatograms for the separation of the desired products. The yield of semiHb reconstruction was satisfactory for both semi(α)Hb and semi(β)Hb and the estimated molecular weight corresponded to an Hb dimer, confirming that these Hb derivatives fold in dimers in solution, as already reported [351,352]. Notably, the retention time of both semiHbs, which fold into dimers in solution, was not in perfect agreement with the one estimated through the calibration curve. However, Hb is well-known to elute as a smaller molecule [326]. Moreover, in Figure 23, UV-visible absorption spectra of both semi(α)metHb and semi(β)metHb compared to native metHb showed the 406 nm/280 nm ratio reduced by half, as expected for a protein which is half-saturated with the cofactor.

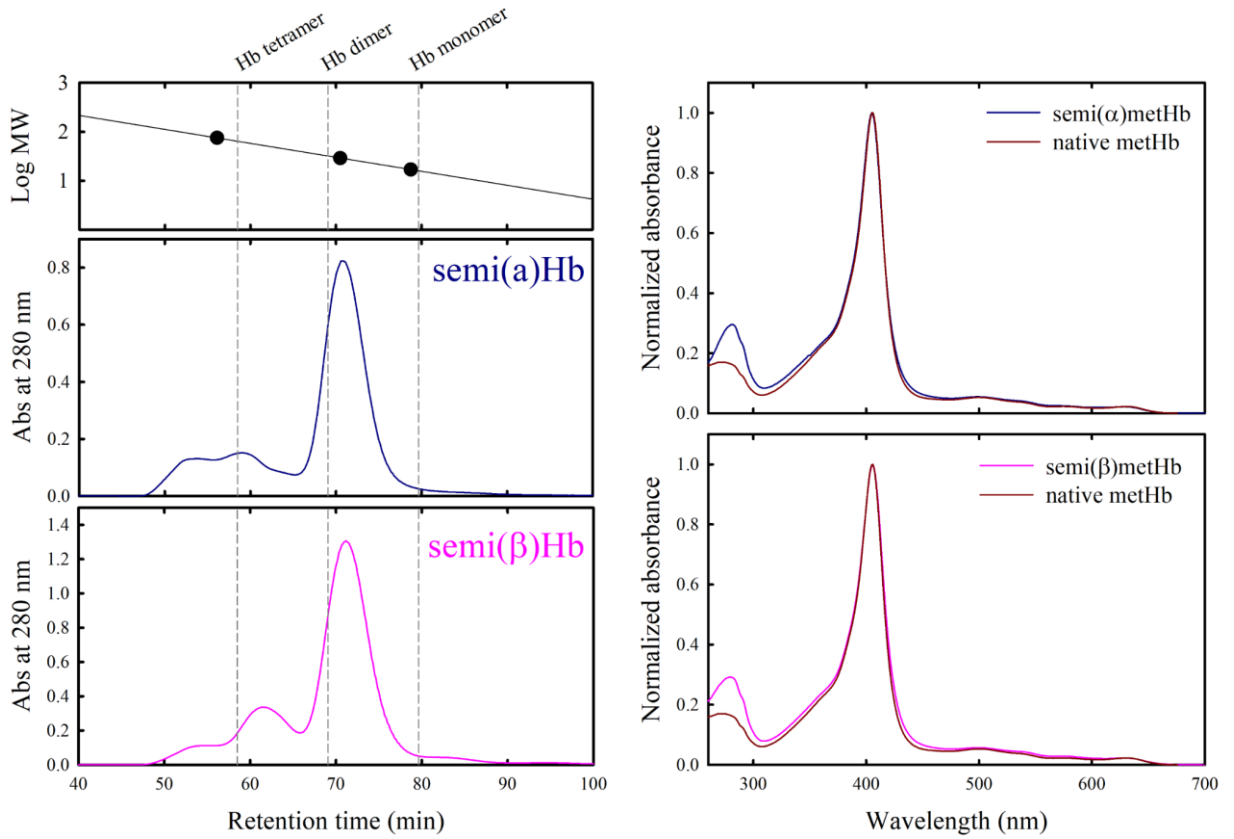

Figure 23: Preparation of semiHbs. On the left, final SEC to separate semi(α)Hb (dark blue) and semi(β)Hb (pink) from intermediate reaction components or protein aggregates. On the top of the chromatograms, the calibration curve is reported, which was obtained by using conalbumin (75 kDa), ovalbumin (43 kDa), and carbonic anhydrase (29kDa). Dashed lines, from left to right, correspond to 64 kDa (Hb tetramer), 32 kDa (Hb dimer), and 16 kDa (Hb monomer). On the right, UV-visible absorption spectra of semi(α)metHb (dark blue) and semi(β)metHb (pink) compared to the native metHb spectrum (dark red).

3.8 Molar extinction coefficient of metHb in different buffers.

Buffer W (0.1 M Tris/HCl pH 8, 0.15 M NaCl, and 1 mM EDTA) was the buffer used throughout all the biochemical characterization of IsdB-metHb interaction, while binding buffer (0.25 M Tris/HCl pH 7.6, 0.14 NaCl , and 2 mM EDTA) was used for the ELISA. Since the spectroscopic properties of metHb changes based on the pH of the solution, molar extinction coefficients of metHb at 406 nm in these two buffers were calculated with the aim of precisely estimating metHb concentration when needed (Figure 24).

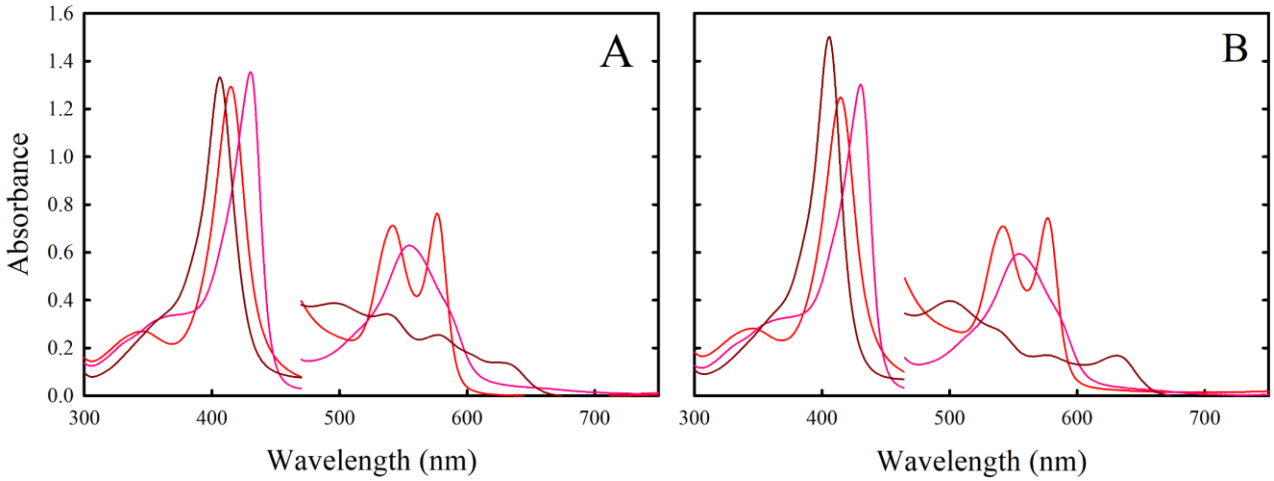

Figure 24: Estimation of metHb molar extinction coefficients. (A) OxyHb - red, deoxyHb – magenta, and metHb – brown spectra in buffer W. (B) OxyHb - red, deoxyHb – magenta, and metHb – brown spectra in binding buffer. Absorption values from 465 to 750 nm are multiplied by a factor 5 to improve visualization of Hb Q bands.

Starting from oxyHb and passing through deoxyHb allowed to precisely calculate the concentration of Hb in the cuvette, in fact the extinction coefficients for these two forms of Hb are published in [343] and do not depend on pH. Calculated concentration allowed to precisely calculate ε(406 nm) for metHb in the same solution (Table 9). It is interesting to notice that ε(406 nm) was increased by 15% when pH decreased by 0.4 units, making essential the determination of the right extinction coefficient for metHb each time the working pH changes.

Table 9: Molar extinction coefficients of oxidized heme bound to Hb in different buffer conditions.

	ε(406 nm) (M^{-1} cm^{-1})
MetHb in buffer W	130,000
MetHb in binding buffer	150,000

3.9 Determination of the dissociation constant for the tetramer-dimer equilibrium of oxy- and metHb.

The dissociation constant for dimer-tetramer equilibrium ($K_D(2,4)$) was demonstrated to vary mainly with ionic strength, pH and temperature [325]. A published protocol was repeated by exploiting SEC with the aim of defining the $K_D(2,4)$ of oxyHb and metHb in the experimental buffer that has been used to perform most of the experiments of the thesis, e.g., buffer W (0.1 M Tris/HCl pH 8, 0.15 M NaCl, 1 mM EDTA). The results reported in Figure 25, which were fitted with an isothermal equation, allowed to calculate a dissociation constant of 0.25 µM and 0.52 µM for oxyHb and metHb, respectively.

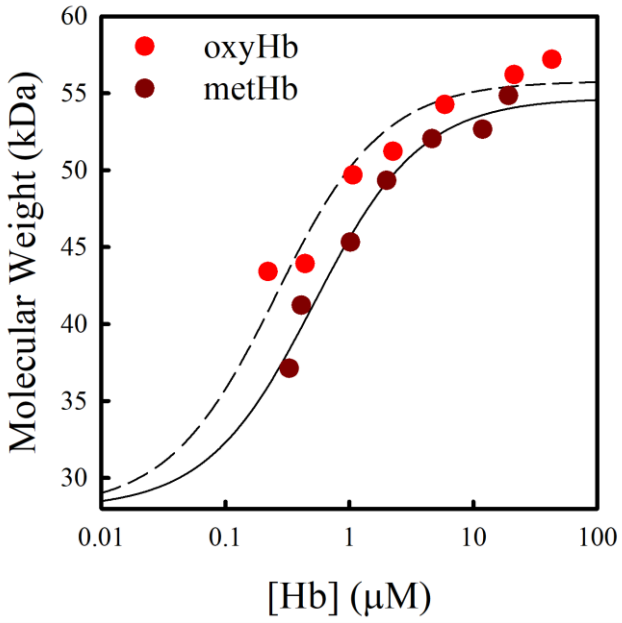

Figure 25: Dependence of oxyHb (red) and metHb (dark red) molecular weights on globin concentration. Dashed and solid lines are the fitting of oxyHb and metHb data, respectively.

3.10 Holo-IsdB^{N1LN2}: heme extinction coefficient.

The molar extinction coefficient of heme bound to IsdB has never been published, making it difficult to assess whether the protein reaches full saturation upon interaction with heme and/or Hb. O/N incubation of 11 µM IsdB^{N1LN2} mixed with an equimolar amount of heme resulted in a significant increase in the intensity of the absorption bands in the visible region of the UV-visible spectrum (Figure 26A). Pyridine hemochromagen assay (Figure 26B) allowed to calculate the concentration of heme bound by IsdB^{N1LN2}, 8.3 µM and thus the extinction

coefficient at 405 nm, ε(405 nm)= 90500 M^{-1} cm^{-1}. Moreover, overnight incubation of $IsdB^{N1LN2}$ with equimolar concentration of heme does not lead to the complete saturation of the hemophore, with only 75% of the hemophore saturated.

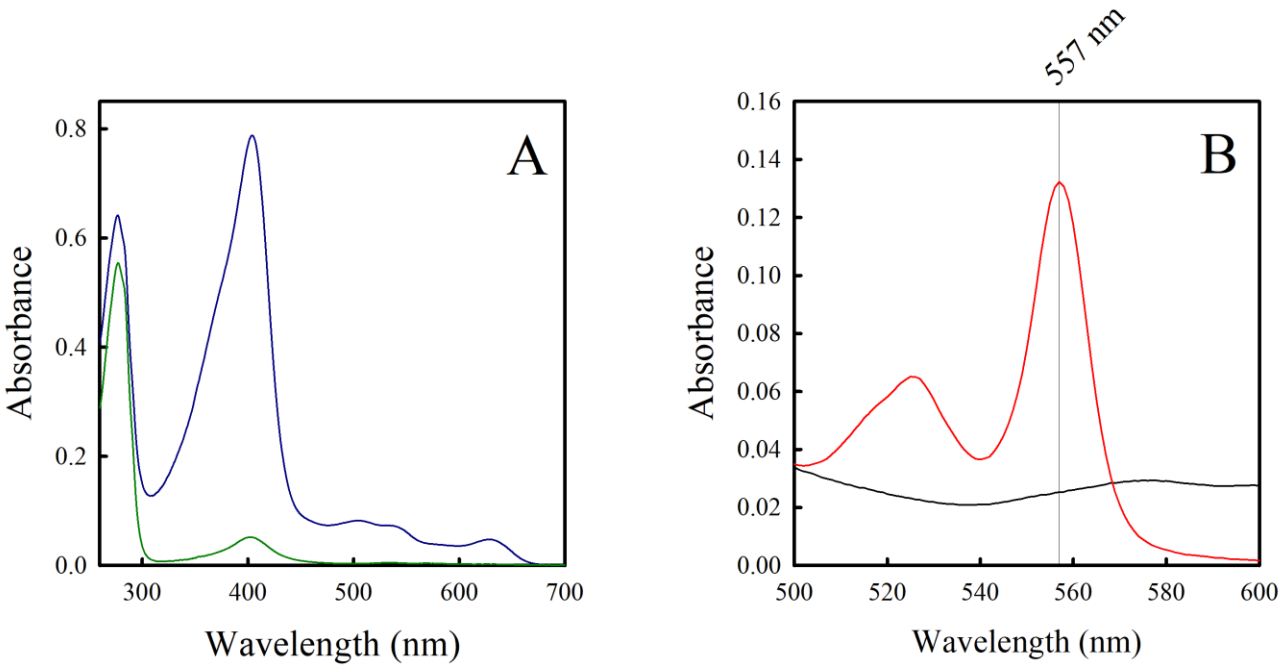

Figure 26: Estimation of the extinction coefficient of $IsdB^{N1LN2}$-bound heme. (A) Comparison of $IsdB^{N1LN2}$ spectra before (green) and after (dark blue) overnight incubation with hemin. (B) Pyridine hemochromagen assay, absorption spectra of oxidized (black) and reduced (red) forms of pyridine hemochromagen.

The molar extinction coefficient for heme bound to $IsdB^{N1LN2}$ was principally used throughout the thesis for the estimation of holo-$IsdB^{N1LN2}$ in purified protein pool.

3.11 FL-IsdB overexpression and purification

Sequencing reaction of pET28a::FL-IsdB was carried out to confirm the correctness of the new construct, and the resulting nucleotide sequence was aligned to the designed construct sequence confirming the absence of mutations. FL-IsdB overexpression was carried out as indicated in the methodologies section and the result was satisfactory (Figure 27). The purification gave a good yield of 25 mg of protein from 1 L of bacterial culture.

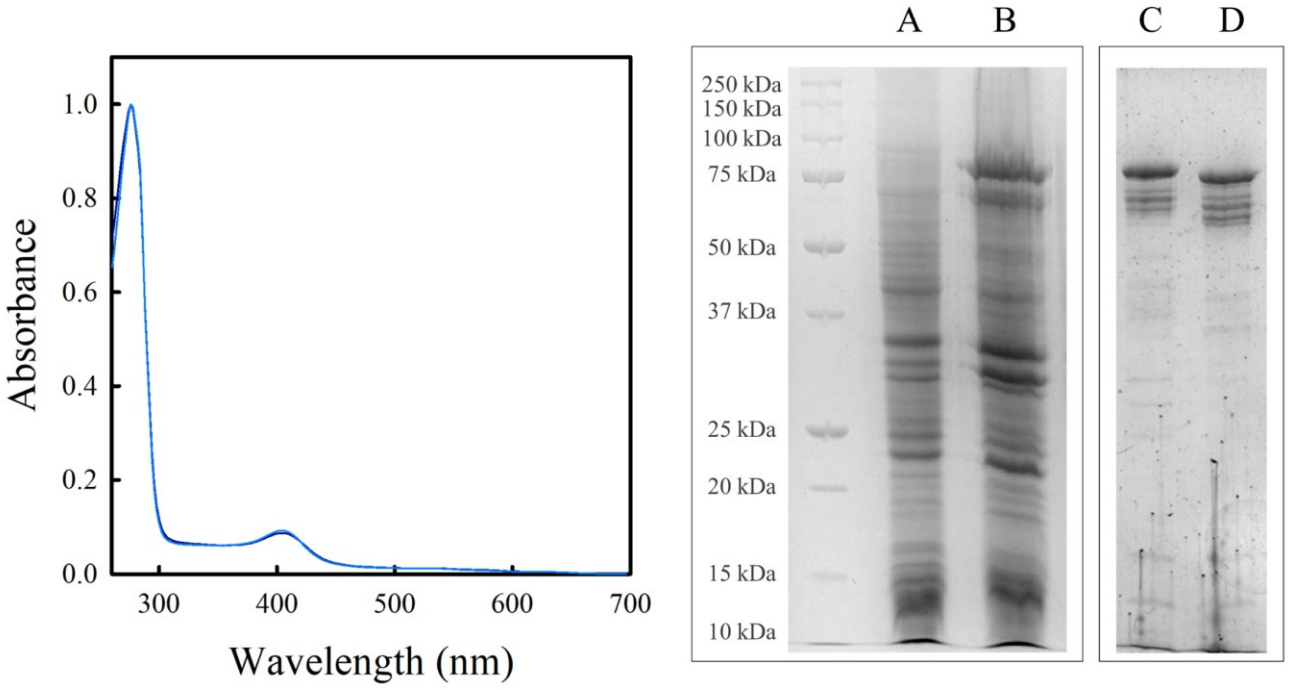

Figure 27: Overexpression and purification of FL-IsdB. On the left, UV-visible spectra of HisTag-FL-IsdB (dark blue) and FL-IsdB (light blue) after the thrombin reaction. On the right, SDS-PAGE analysis of FL-IsdB overexpression and purification. (A) Not induced cells, (B) induced cells, (C) purified HisTag-FL-IsdB, and (D) FL-IsdB after digestion with thrombin.

However, the presence of multiple low molecular weight bands was observed (lanes C and D, Figure 27). The pattern moved toward low molecular weight after thrombin digestion indicating that the entire protein pattern was composed of FL-IsdB fragments. Incomplete protein synthesis was identified as the principal cause of the presence of protein fractions. Proteolytic events during the purification were excluded because most of the protein bands were also visible in the lane corresponding to induced cells (lane B). Incomplete protein synthesis causes the deletion of the C-terminal part of the protein, while the N-terminus is retained, allowing purification of the fragments by IMAC together with the FL protein.

To solve the problem, the mutagenesis for obtaining FL-IsdB^{*604L} variant was carried out.

The presence of the mutation was verified by sequencing reaction (Figure 28).

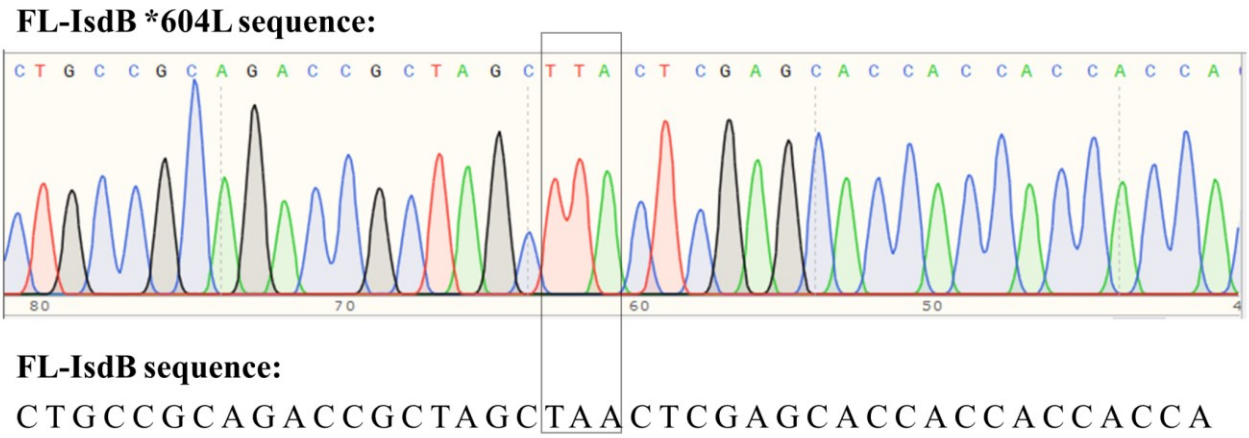

Figure 28: Comparison between sequencing results and the sequence of the WT IsdB.

pET28a::FL-IsdB^{*604L} was electroporated in *E. coli* TUNER™ BL21 (DE3) cells for protein overexpression. The purification of the new construct will include two affinity chromatographic steps on TALON® Superflow™ resin. In the first, all contaminant proteins present in the crude cell extract are removed. N-term HisTag removal through thrombin cleavage before the second chromatographic step is expected to separate the intact FL-IsdB (which binds the resin through the C-terminal HisTag) from the truncated forms that do not carry the C-terminal tag. Although the new protocol was optimized and ready for protein overexpression and purification, the project aimed at the characterization of FL-IsdB stopped because of COVID-19 pandemic, as well as its use in the determination of the three-dimensional structure of IsdB-Hb complex by cryo-EM.

Chapter II – interaction between IsdB and Hb: a structural and dynamic investigation

1 Objectives

Critical to *S. aureus* growth is the ability to scavenge iron from metHb, to this aim the bacterium produces a sophisticated set of hemophores. Among these, IsdB is in charge of binding Hb and extracting the heme, the first step in iron acquisition.

Despite significant advances in the knowledge of IsdB, mechanistic and structural data about IsdB alone and in complex with Hb is still missing or incomplete. In order to provide a deeper insight into the function of IsdB, biochemical and biophysical techniques were combined to study the kinetics of complex formation with Hb and the structure in solution. Better knowledge of the molecular details of IsdB-Hb PPI will pave the way to the identification of PPI inhibitors as new antimicrobial agents.

The main open questions that we addressed involve the kinetics of IsdB-Hb complex formation and heme extraction, the exact stoichiometry of the complex, and the existence of preferences for heme extraction from either α- or β-Hb chains. Furthermore, no high-resolution structure of WT IsdB in complex with Hb was available, except for one, low-resolution, structure that traps an intermediate in the heme extraction process and contains protein fragments generated by proteolysis during crystallization. Differently from previous work published on this topic, we addressed these structural and functional aspects using different forms of Hb (i.e., oxyHb, COHb, metHb and semiHbs) and IsdB variants ($IsdB^{N1LN2}$, $IsdB^{Y165A}$, $IsdB^{Y440A}$) that underwent a full characterization under the same conditions. Data were thus comparable and allowed to obtain a comprehensive picture of the structural and dynamic details of complex formation and heme extraction. SPR was exploited to calculate the microscopic kinetic constants for complex formation and to define the rate limiting step of the process. The work was carried out within a collaboration with Prof. S. Cannistraro, Università della Tuscia. UV-visible spectrophotometry allowed to evaluate the kinetics of heme extraction and the complex stoichiometry. The latter was confirmed using SEC-MALS, which combines the resolving power of chromatography with the accuracy in estimating molecular masses of light scattering technique. SEC-MALS experiments were carried out during a PhD secondment at the University of Cambridge under the supervision of Prof. Ben Luisi. Finally, the long-standing need for further structural insights on IsdB isolated in solution or within the complex was addressed exploiting either low- or high-resolution techniques. In particular, SAXS (in

collaboration with Dr. M. Levantino, ESRF, Grenoble) and cryo-EM (performed at the cryo-EM facility of the Department of Biochemistry, University of Cambridge, during a PhD secondment under the supervision of Prof. Ben Luisi) were employed to address the structural characterization of the complex under conditions that mostly resemble those encountered in solution and likely prevent the artifacts observed in the crystal.

2 Materials and Methods

All reagents, if not otherwise specified, were obtained from Sigma Aldrich (St. Louis, MO, USA) at the best commercial quality available, and used as-received.

Experiments were carried out in Buffer W (0.1 M Tris/HCl pH 8, 0.15 M NaCl, 1 mM EDTA), unless otherwise stated.

2.1 Visible absorption spectroscopy for equilibrium and kinetic characterization of heme extraction

Spectroscopical characterization of heme extraction was carried out using a Cary 4000 spectrophotometer (Agilent). Heme extraction was already reported to cause a significant variation of visible absorption spectrum due to the different environment and coordination state of the cofactor upon transfer from metHb to IsdB [224]. Absorption spectra (350-700 nm) of Hb and $IsdB^{N1LN2}$ were recorded before and after mixing the two proteins at 20 °C. With the aim of removing artefacts due to sample dilution and protein contribution, a double chamber cuvette was used (Figure 29, each chamber has a 4.375 mm pathlength). The two chambers were separately filled with Hb and $IsdB^{N1LN2}$ solutions, at 3 and 15 µM concentration, respectively, and the acquired spectrum was the sum of the two proteins spectra. The solutions were then mixed by inverting the cuvette leading to proteins interaction and thus the heme extraction. Heme-transfer rate was evaluated at 406 nm, which is the wavelength of maximum absorbance for metHb and it has already been used in many papers to study heme extraction kinetic [224,233,238,332]. The decrease in absorption signal was followed over time after mixing the solution into the double chamber cuvette. Once the reaction was finished, a final spectrum of the protein complex was recorded. Identical volumes were used to fill the cuvette, therefore the final concentration of the analyzed sample was diluted by a factor of two, resulting in 1.5 µM Hb (heme concentration) and 7.5 µM $IsdB^{N1LN2}$.

Figure 29: Double-cell cuvette.

The kinetic study was performed on the same sample used to record the static absorption spectra. The extraction kinetics was fitted with a modified bi-exponential decay equation:

$$y = y_0 + ae^{(-b(x+x_0))} + ce^{(-d(x+x_0))}$$

Where y is the absorbance at 406 nm, a and c are the amplitude of the exponential phases observed, and b and d are the corresponding observed rate constants. y_0 is the absorbance value at infinite times and x_0 is an offset introduced to consider the manual mixing time.

2.2 Visible absorption spectroscopy for determination of stoichiometric ratio

The stoichiometric ratio of IsdB-metHb complex was assessed by following the decrease of absorbance at 406 nm in the presence of 5 µM MetHb (heme concentration) and increasing concentrations of $IsdB^{N1LN2}$ in the range of 0.3–40 µM. The complex formation between metHb and IsdB was expected to result in the heme extraction, and thus a signal decrease at 406 nm. Once all the metHb molecules available to form the complex were bound by the hemophore no further heme extraction was possible and the absorption at 406 nm stabilizes, allowing to identify the relative concentration of IsdB and metHb and thus the stoichiometric ratio. The experiment was performed using a Cary 4000 spectrophotometer (Varian), with the cell holder maintained at 20 °C with a circulating water bath, and a Hellma™ Far UV Quartz Micro Cuvette (1 cm pathlength). The absorption spectrum was recorded in the 350–700 nm range 10 minutes after each addition of hemophore to allow the heme extraction process to be concluded. The spectra were then subtracted of the contribution of $IsdB^{N1LN2}$ in the visible

range (due to the presence of a small portion of heme-saturated hemophore in the purified pool) and corrected for the dilution factor.

2.3 SPR

SPR measurements were performed using a Biacore X100 (GE Healthcare) at 25 °C according to the method reported [338]. Briefly, C-terminal StrepTag®II on $IsdB^{N1LN2}$ was exploited to immobilize it onto a CM5 sensor chip surface (GE Healthcare) previously functionalized with StrepMAB-Immo™ antibodies (IBA Lifesciences). Subsequently, five sequential increasing concentrations of Hb (0.1-1 µM) were fluxed over the chip functionalized with $IsdB^{N1LN2}$, and each of them was followed by a dissociation step obtained by fluxing the experimental buffer. A final dissociation step, after the five injections, was performed to lead the complete dissociation of Hb. The kinetic parameters were extracted from SPR data through the BiaEvaluation software 2.1 (GE Healthcare) by using the kinetic models presented in the Results section. Goodness of the fits was evaluated by X^2 value and residual plots.

2.4 SEC-MALS

Determination of absolute molar masses of proteins was carried out by SEC-MALS. Single proteins and their complexes (100 µL at 1 g/L concentration) were loaded onto a Superdex™ 200 10/300 Increase GL SEC column (GE Healthcare) at 0.5 mL/min using an AKTA Purifier (GE Healthcare). All protein solutions were centrifuged 30 minutes at 17,200 rpm (4 °C) before loading, and complex solutions were allowed to react 15 minutes before centrifugation. Estimation of protein concentration was carried out using a NanoDrop® ND-1000 UV-visible Spectrophotometer (Thermo Scientific).

Along with SEC-MALS analysis, chromatograms were acquired and analyzed using UNICORN software (GE Healthcare) by recording the absorption signal at two different wavelengths, 280 nm for detecting the elution of aromatic residues of all the proteins and 406 nm, for metHb, or 419 nm, for COHb, to follow the elution of heme-bound to the proteins at the wavelength of maximum absorption. Signals were exploited to extrapolate information about complex stoichiometry and heme extraction process. Absorption signals in the visible

range were smoothed by applying Savitzky-Golay filters in MatLab®; Figure 30 shows the comparison of the signal before and after the filter application to demonstrate the absence of artifacts in the result.

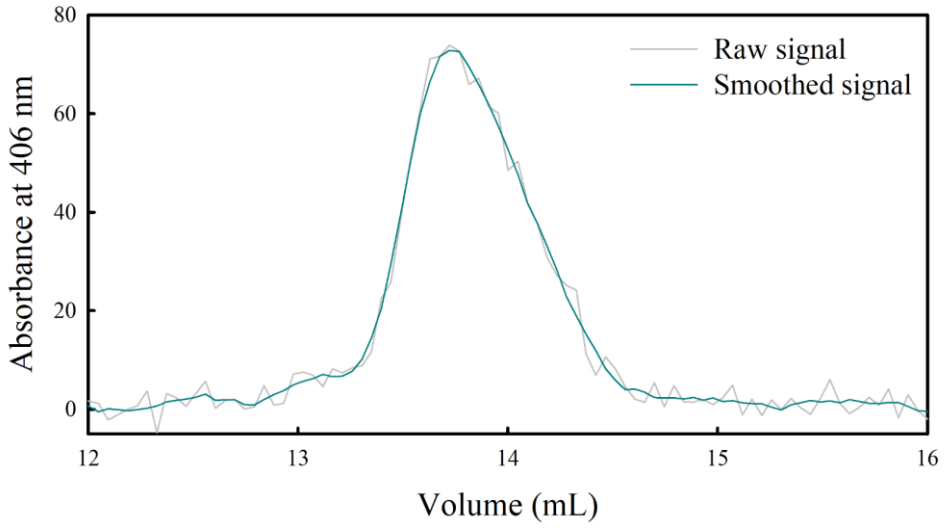

Figure 30: Effect of Savitzky-Golay filters on raw SEC data.

To separate contributions of co-eluting proteins, the chromatograms were deconvoluted into single or multiple gaussians (Fityk software [346]).

The solution eluted from the SEC column was analyzed with an online DAWN HELEOS II MALS detector (Wyatt Technology), followed by an Optilab T-rEX differential refractometer (Wyatt Technology) at 25 °C. The light scattering cell was illuminated by a 664 nm polarized laser source, and scattered light by the sample was detected by eight fixed angle detectors. Absolute and differential refractive indexes were calculated using a 658 nm LED light source. Data collection and analysis was performed using ASTRA 6 software (Wyatt Technology). The entire system was preconditioned with the experimental buffer and bovine serum albumin was used as a standard to confirm the system performance. On-line calculation of standard Zimm Plot [353], using a dn/dc value of 0.1850 mL/g, on eluted peaks from SEC column allowed to precisely estimate the molecular masses of separated samples.

2.5 SEC

SEC analysis were performed with different FPLC systems and chromatographic columns:

- To further investigate the results of SEC-MALS experiments, an AKTA pure (GE Healthcare) working at 4 °C was combined with a Superdex™ 200 10/300 Increase GL column (GE Healthcare), by keeping experimental parameters comparable with SEC-MALS analysis. Chromatograms were acquired and analyzed using UNICORN software (GE Healthcare) by recording the absorption signal at two different wavelengths, 280 nm for detecting the elution of aromatic residues of all the proteins and 406 nm, for metHb, or 419 nm, for COHb, to follow the elution of heme-bound to the proteins at the wavelength of maximum absorption.
- Investigation of dimeric form of $IsdB^{N1LN2}$ was performed using XK 16/300 column (GE Healthcare) packed in-house with 48 mL of a BioSepra Ultrogel AcA 44 resin connected to an AKTA prime (GE Healthcare). The column was calibrated with blue dextran (void volume), alcohol dehydrogenases (140 kDa), conalbumin (75 kDa), ovalbumin (43 kDa), and carbonic anhydrase (29 kDa).

2.6 SAXS

SAXS was exploited for the structural characterization of IsdB-metHb complex, but also to investigate the structural properties of the single components involved. Proteins were used at a concentration ranging from 3 g/L to 12 g/L in buffer W (0.1 M Tris/HCl pH 8, 0.15 M NaCl, 1 mM EDTA). SAXS data were collected at the BM29 BIOSAXS beamline of the European Synchrotron Radiation Facility (Grenoble), in collaboration with Dr. Matteo Levantino, who performed the data reduction. The radius of gyration (R_g) was calculated using PRIMUS [354]. *Ab initio* shape reconstruction was performed using DAMMIF web interface of ATSAS online [355]. Within the online procedure, the DAMAVER suite [356] were implemented to improve the refinement and identify possible outlier shapes generated by DAMMIF. The high-resolution structures used for fitting the generated shapes were differently derived:

- Since the 3D structure of isolated IsdB has never been published before, it was extracted from 5VMM pdb structure [224], which was the only IsdB-Hb complex model published at that time;

- PDB 3P5Q was used to obtain the high-resolution structure of metHb;
- The structural model of the IsdB-metHb complex was created *ad hoc* (courtesy of Spyrakis' group, Università di Torino). It was based on the only published high-resolution structure of the IsdB-Hb complex (PDB 5VMM [224]), and then modelled to obtain the complex formed by an Hb dimer with two IsdB molecules, one for each Hb subunit. The sequence of the hemophore in the model was modified to add the StrepTag® II, which was not present in the published structure.

The simple fit of 3D structures inside the shapes was done with UCSF Chimera [357].

2.7 Cryo-EM: samples preparation, data-collection, processing, and model refinement

Complexes of the hemophore have been prepared for structural studies using two different oxidation forms of Hb to separately analyse the key steps of the interaction: initial binding and the heme extraction event. Since IsdB cannot extract the heme from the ligated forms of Hb, the simple bi-molecular encounter complex has been captured by mixing the hemophore with carbon monoxide Hb. The complex between IsdB and metHb, which is the oxidised, ferric form of Hb, should represent the complex after heme transfer has taken place, in which the iron-histidine bond is severed.

The purification of the proteins and the preparation of the two different forms of Hb are described in the Chapter I. $IsdB^{N1LN2}$ was mixed with metHb in a 1-to-1 stoichiometric ratio (e.g., one $IsdB^{N1LN2}$ molecule for each Hb chain) to reach a final concentration of 2 g/L, whereas the complex with COHb was prepared at 8 g/L concentration by mixing the hemophore with Hb in a 1-to-2 stoichiometric ratio. The different proportion between $IsdB^{N1LN2}$ and Hb in the two complexes was chosen based on the PPI results discussed in the Results section of this chapter. Samples were prepared in 10 mM HEPES buffer (pH 7.3) to reduce the electron density of the background for cryo-EM data collection, and the zwitterionic detergent CHAPSO was added immediately before plunge freezing to a final concentration of 8 mM to overcome preferred orientation of the particles in the vitreous ice. Three microliters of both the complex solutions were applied onto glow-discharged 300-mesh R1.2/1.3 UltrAuFoil grids, and then blotted for 3 s before rapidly cryocooling them in liquid ethane. For

blotting and freezing the grids, a Vitrobot Mark IV (Thermo Fisher Scientific) device was used, and the sample chamber was kept at 4 °C and 99% humidity.

A Talos Arctica cryo-electron microscope (Thermo Fisher Scientific) operating at 200 kV was used to evaluate the quality of the vitrified specimens. For the high-resolution study, both IsdB^{N1LN2}-metHb and IsdB^{N1LN2}-COHb complexes were imaged in a Titan Krios cryo-electron microscope (Thermo Fisher Scientific) at 300 kV, with a Gatan K3 direct electron detector working in super-resolution mode at the calibrated magnification of ×130,000, yielding a pixel size of 0.326 Å. Micrographs were recorded by EPU software (Thermo Fisher Scientific) in movie mode, where each image was composed of 40 individual frames with an exposure time of 1.1 s and a dose rate of 15.3 electrons per second per Å^2. The IsdB^{N1LN2}-metHb and IsdB^{N1LN2}-COHb complex datasets resulted in a total of 3050 and 2852 movie stacks, with a defocus range of −0.8/−2.8 μm and -1.0/-3.1 μm, respectively.

The IsdB^{N1LN2}-COHb complex was analyzed on-the-fly using WARP [358] to identify 460,000 particles, which were processed using cryoSPARC to classify 2D and 3D classes and refine particle orientation parameters [359]. The maps were modified for interpretation using the *auto_sharpen* and *resolve_cryo_em* tools of the Phenix package by imposing C2 symmetry [360].

The single particle analysis (SPA) of the IsdB^{N1LN2}-metHb complex was carried out using RELION [361]. All micrographs were motion-corrected using MOTIONCOR2 implemented in RELION and the contrast transfer function (CTF) was estimated using Kai Zhang's GCTF [362]. Particles were found using the auto-picking option in RELION, resulting in roughly 300,000 extracted particles, which were screened through multiple rounds of 2D and 3D classification to find the best set. The final refinement was run after the CFTRefine and Bayesian Polishing jobs in RELION with a final selection of roughly 100,000 particles.

Cryo-EM data processing yielded 2.90 Å and 5.80 Å maps for the IsdB^{N1LN2}-COHb and IsdB^{N1LN2}-metHb complexes, respectively. These resolutions for the final maps were estimated by the 0.143 criterion of FSC curve (Figure 31).

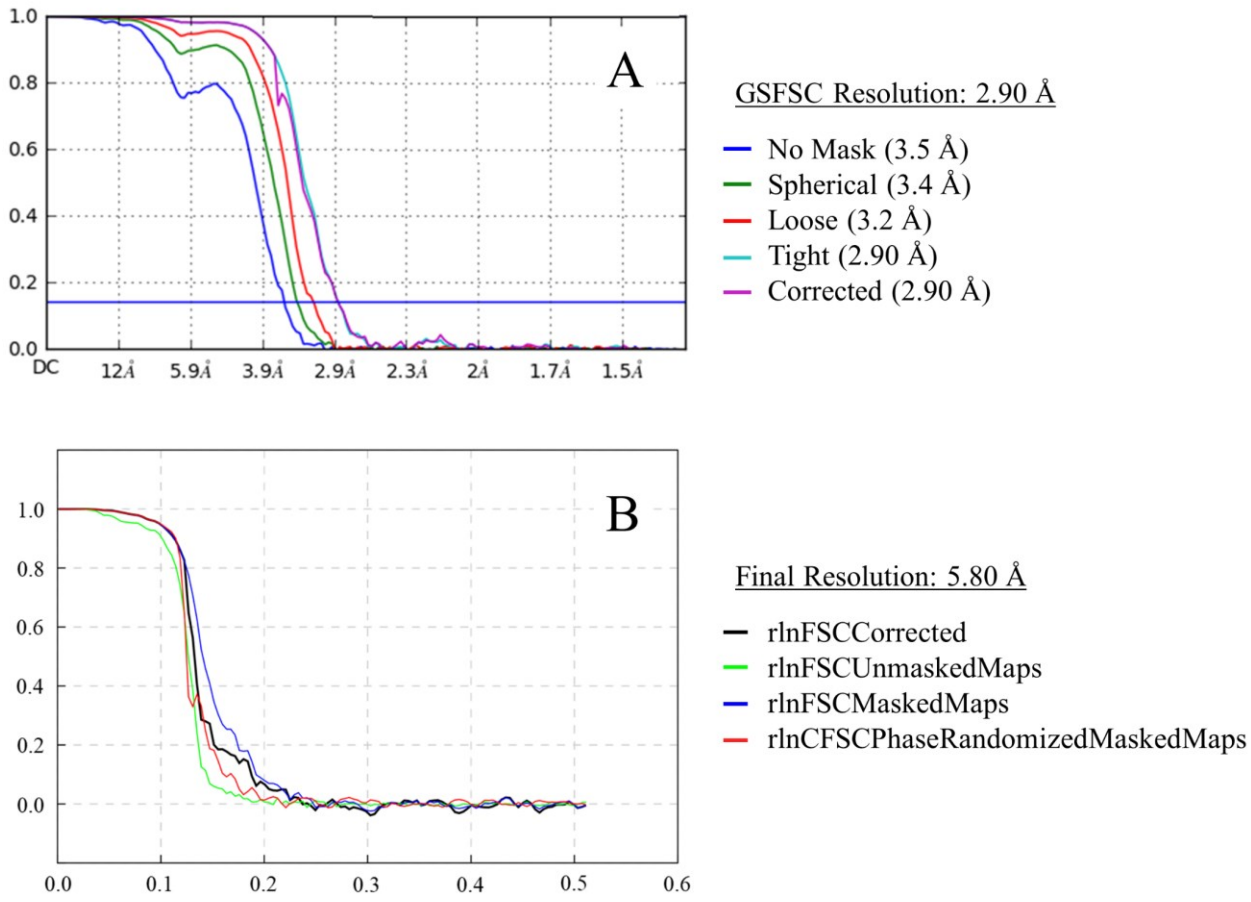

Figure 31: FSC plot for the final resolution estimation. Gold-standard FSC curves indicate a final resolution of 2.90 Å for IsdB^{N1LN2}-COHb complex dataset (A), and 5.80 Å for the IsdB^{N1LN2}-metHb complex dataset (B).

The atomic model of IsdB^{N1LN2}-COHb complex was prepared by Prof. Luisi by manually adjusting and refining in Coot [363] a starting model made by the Spyrakis' group (Università di Torino) based on the crystal structure of the proteolyzed hemophore bound to the βHb chains with an incomplete Hb structure (PDB: 5VMM). The IsdB^{N1LN2}-metHb model was prepared by modifying the high-resolution crystal structure of metHb (PDB: 3P5Q), using IsdB bound to the α-Hb chain in the 5VMM PDB with a terminal StrepTag®II added.

The map density of the IsdB^{N1LN2}-metHb complex was not sufficiently detailed to accurately derive the position of the protein residues within the complex. Therefore, the same *ad hoc* model generated for SAXS analysis (courtesy of Spyrakis' group, Università di Torino) has been fitted to map by using Namdinator [364]. The model represented the complex formed by an Hb dimer with two IsdB molecules, one for each Hb subunit. Refinement through

Namdinator requires the removal of protein ligands, thus the resulting atomic model is missing the heme molecules.

Atomic models were compared with published high-resolution structures principally using UCSF Chimera [357] and EMBL-EBI PDBePISA [365].

2.8 Chemical denaturation with guanidinium hydrochloride (GndHCl).

$IsdB^{N1LN2}$ was denatured in 1.4 M GndHCl. The protein sample at 10 µM concentration was incubated one hour at room temperature in the presence of GndHCl. Then, it was extensively dialyzed overnight at 4 °C to remove the denaturing agent. The protein sample was expected to refold during the overnight dialysis. The denaturation process was followed by fluorescence spectroscopy exploiting the different emission spectra of tryptophan residues in the folded and unfolded protein. The sample was diluted five times to perform the measurement. Emission spectra were collected at 20 °C upon excitations at 298 ($slit_{ex/em}$ = 4/5) using a FS5 Spectrofluorometer (Edinburgh Instruments Ltd.).

3 Results and Discussion

3.1 Characterization of IsdB mode of action: kinetic and mechanistic insights

3.1.1 Characterization of the heme extraction process by visible absorption spectroscopy

As already reported in literature, IsdB heme extraction from metHb (likely the dominant form interacting with the hemophore under *in vivo* infection conditions) can be followed spectroscopically, as the main absorption peak of the cofactor (the Soret peak at 406 nm) changes shape and intensity upon transfer from metHb to IsdB [198,224,238]. When a 5-fold excess $IsdB^{N1LN2}$ was mixed with metHb a rapid decrease in absorbance at 406 nm was observed (Figure 32), confirming that the purified hemophore was efficiently extracting heme from metHb. The visible spectrum after heme extraction showed a decrease and a blue-shift of the Soret peak (from 406 nm to 405 nm) and a signal increase at 380 nm. These two spectral variations are the spectroscopic signature of the heme transfer from metHb to IsdB. Fitting of the kinetic trace with a bi-exponential equation gave an observed kinetic rate constant (k_{obs}) for the main fast phase (attributed to heme transfer) of 0.2 s^{-1} (Table 10), in very good agreement with published data collected under similar conditions [198,240].

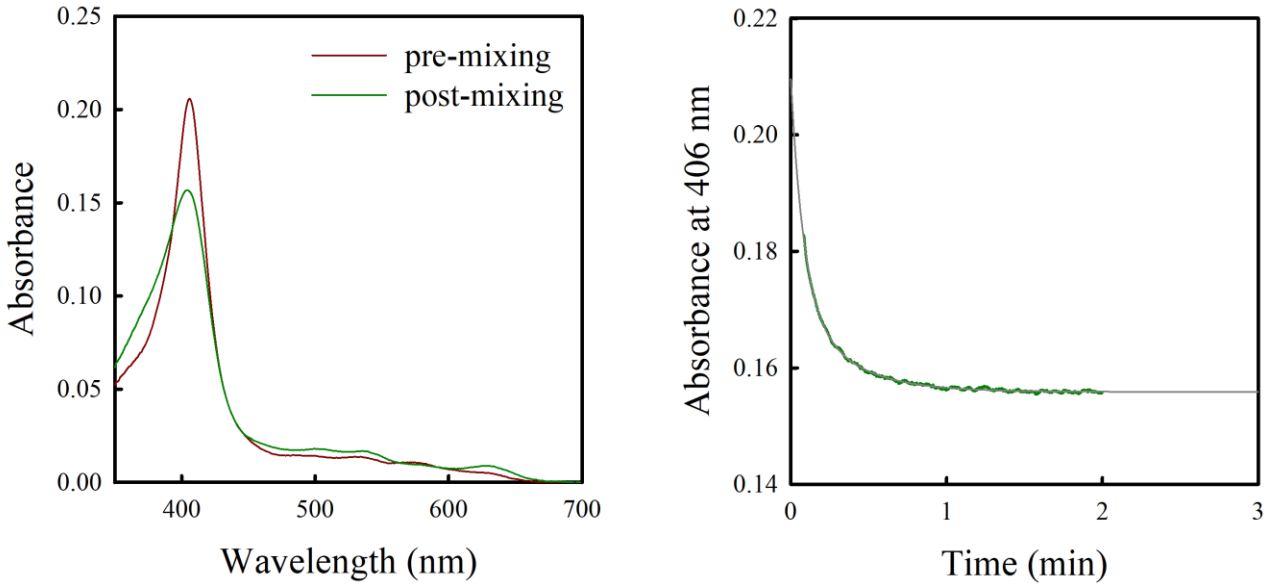

Figure 32: Spectroscopic characterization of heme extraction of IsdB^{N1LN2} from metHb. Plot on the left represents the spectral variation due to the transfer of the cofactor, whereas plot on the right depicts the kinetics of heme extraction process, fitting with a bi-exponential decay is shown with black line.

Table 10: Observed rate constants and relative amplitudes obtained by fitting single-wavelength UV-visible kinetics with the modified bi-exponential equation.

	$k_{1,obs}$ (s^{-1})	% Amp_1	$k_{2,obs}$ (s^{-1})	% Amp_2
IsdB^{N1LN2}-metHb	0.204 ± 0.004	63	0.0526 ± 0.0007	37
IsdB^{N1LN2}-semi(α)metHb	0.289 ± 0.003	76	0.0385 ± 0.0003	24
IsdB^{N1LN2}-semi(β)metHb	0.296 ± 0.002	74	0.0365 ± 0.0002	26
IsdB^{Y165A}-metHb	0.043 ± 0.001	43	0.0036 ± 0.0001	57
IsdB^{Y440A}-metHb	0.211 ± 0.002	89	0.0112 ± 0.0002	11

The same experiment was repeated mixing IsdB^{N1LN2} with semi(α) and semi(β)metHb (Figure 33). Spectroscopic changes comparable with those registered with native Hb were observed. Notably, also the observed heme transfer rates were very similar, suggesting that the hemophore can extract the heme with comparable efficiency from α and β subunits.

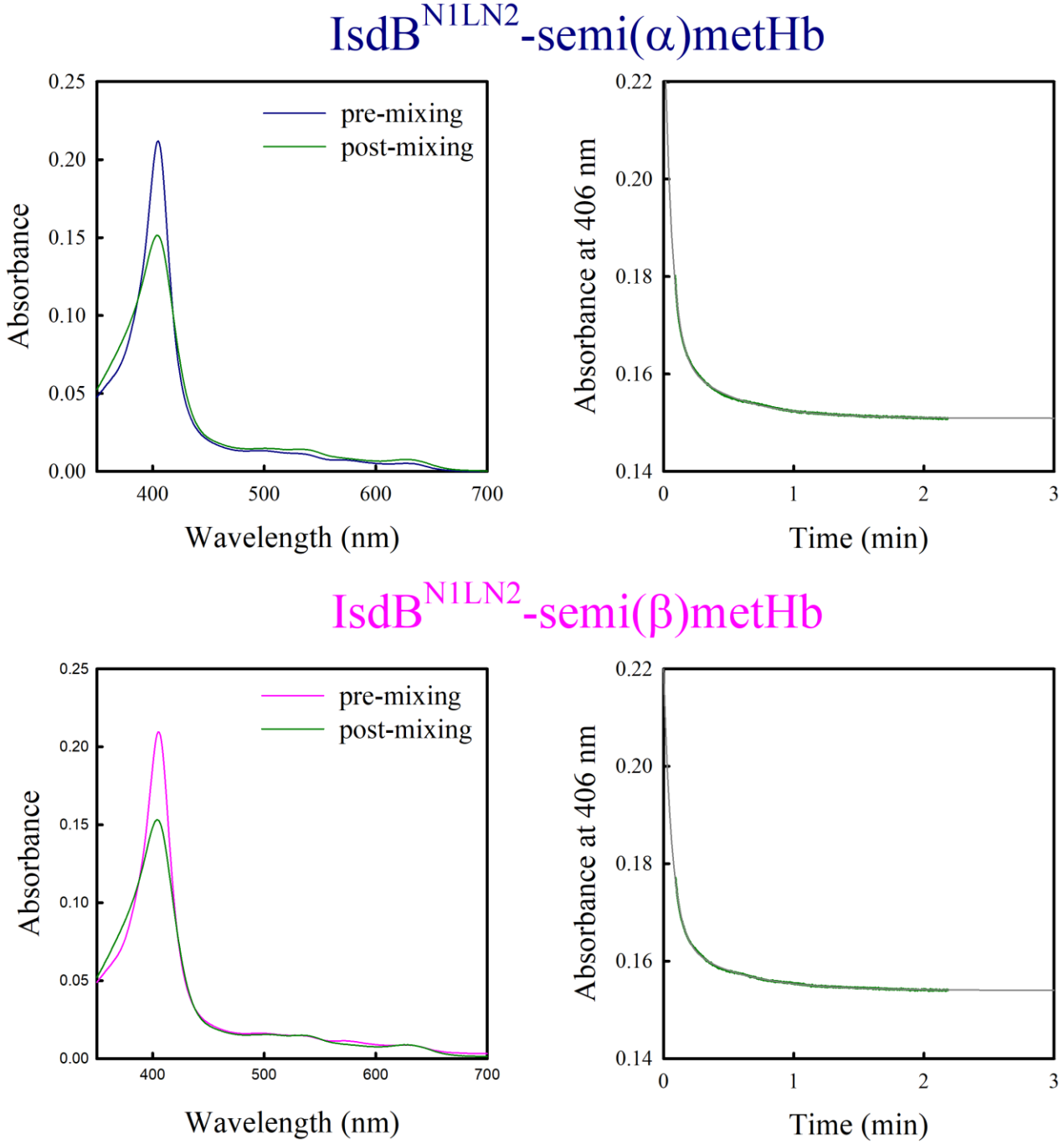

Figure 33: Spectroscopic characterization of heme extraction of IsdB^{N1LN2} from semi(α)metHb, and semi(β)metHb. Plots on the left represent the spectral variation due to the transfer of the cofactor, whereas plots on the right depict the kinetics of heme extraction process, fittings with a bi-exponential decay are shown with black line.

Differently, when IsdB^{N1LN2} was added to a solution of reduced ligated Hb (both oxyHb and COHb), the spectrum does not change (Figure 34) indicating that the hemophore was not able to extract the cofactor from these Hb forms, which agrees with literature data [198,224].

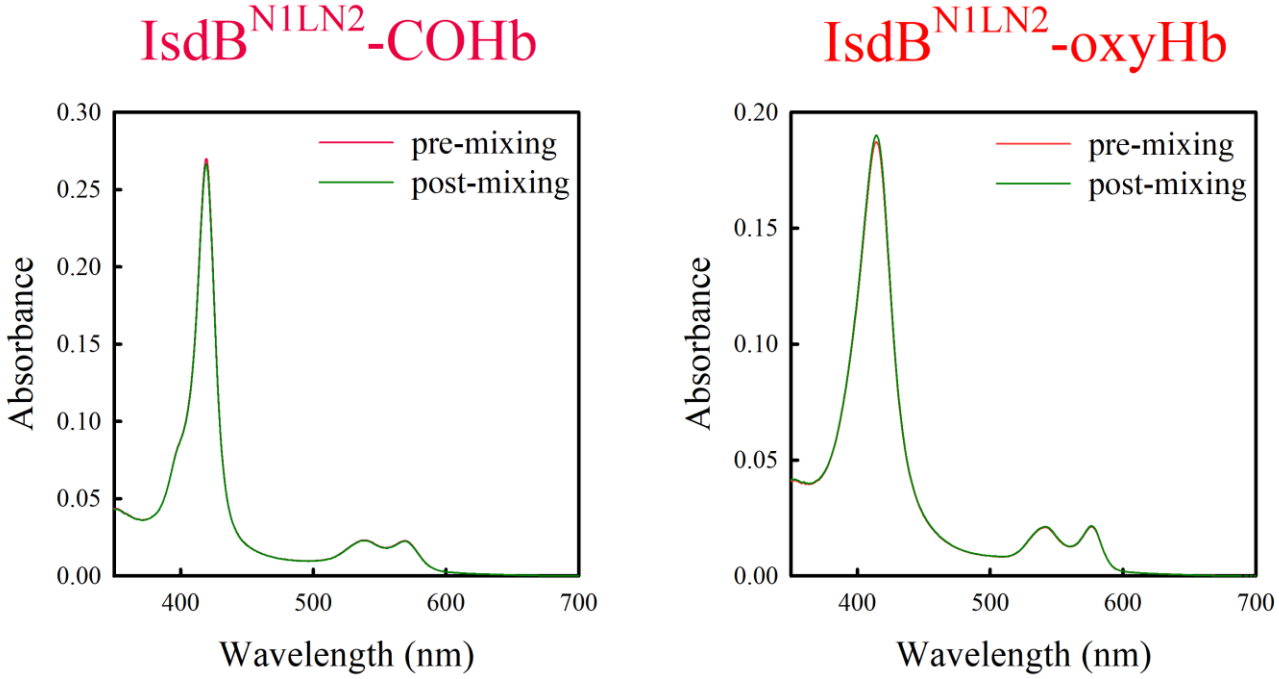

Figure 34: Spectroscopic characterization of IsdB^{N1LN2} interaction with either COHb (on the left) or oxyHb (on the right). Since no spectra changes were observed the kinetics of heme extraction was not measurable.

Finally, IsdB^{N1LN2} mutants were tested. The reaction between metHb and IsdB^{Y165A} resulted in a similar spectral change compared to IsdB^{N1LN2}, however the heme extraction rate of the mutant was significantly affected by the mutation, resulting in 5-fold decrease of the fast k_{obs} (Figure 35). The Y165A mutation was reported to impair IsdB affinity for Hb [238], therefore a reduced rate in heme transfer could reflect a reduced rate of complex formation. Differently, when IsdB^{Y440A} was mixed with metHb, it caused a red shift in the absorption spectrum of heme, suggesting that the final microenvironment was different from that experienced with IsdB^{N1LN2}. The final spectrum was centred at 410 nm (Figure 35). Tyrosine 440 is coordinating heme in holo-IsdB 3D structure [225], is interacting with proximal histidine of Hb in the IsdB-Hb complex structure [224], and is directly interacting with heme propionate in IsdB^{N1LN2}-COHb complex solved in this thesis (vide infra). Therefore, the differences observed in the kinetics possibly reflect a partial heme extraction process that cannot proceed to completion because of the mutation.

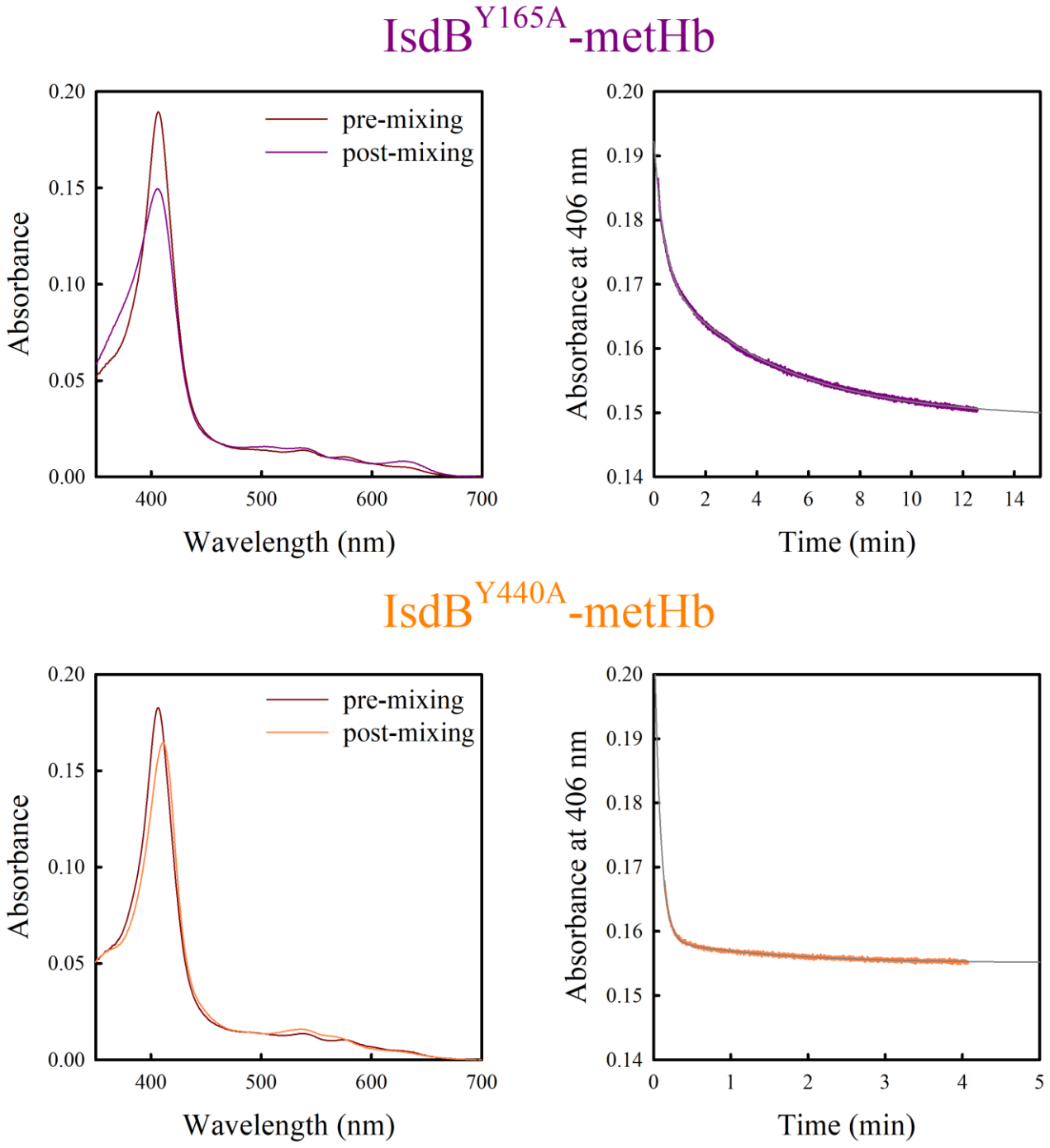

Figure 35: Spectroscopic characterization of heme extraction of IsdB^{N1LN2} variants from metHb. Plots on the left represent the spectral variation due to the transfer of the cofactor, whereas plots on the right depict the kinetics of heme extraction process, fittings with a bi-exponential decay are shown with black line.

3.1.2 Determination of stoichiometry of IsdB-Hb complex by absorption spectroscopy

Since the published stoichiometries of IsdB-Hb complex were not fully consistent [198,224], the spectral variation observed as a result of heme extraction was used to extrapolate the stoichiometric ratio of IsdB-metHb complex. With this aim, the reduction of the metHb

absorbance at 406 nm following the addition of increasing concentrations of IsdB^{N1LN2} was studied (Figure 36). The signal progressively decreased until the stoichiometric ratio was reached, after which addition of further IsdB^{N1LN2} did not lead to any further signal decrease. The calculated stoichiometric ratio was close to 1, meaning that each Hb monomer binds one IsdB^{N1LN2} molecule. This result confirmed that IsdB binds both α- and β-chain of Hb, as already suggested by the kinetic study.

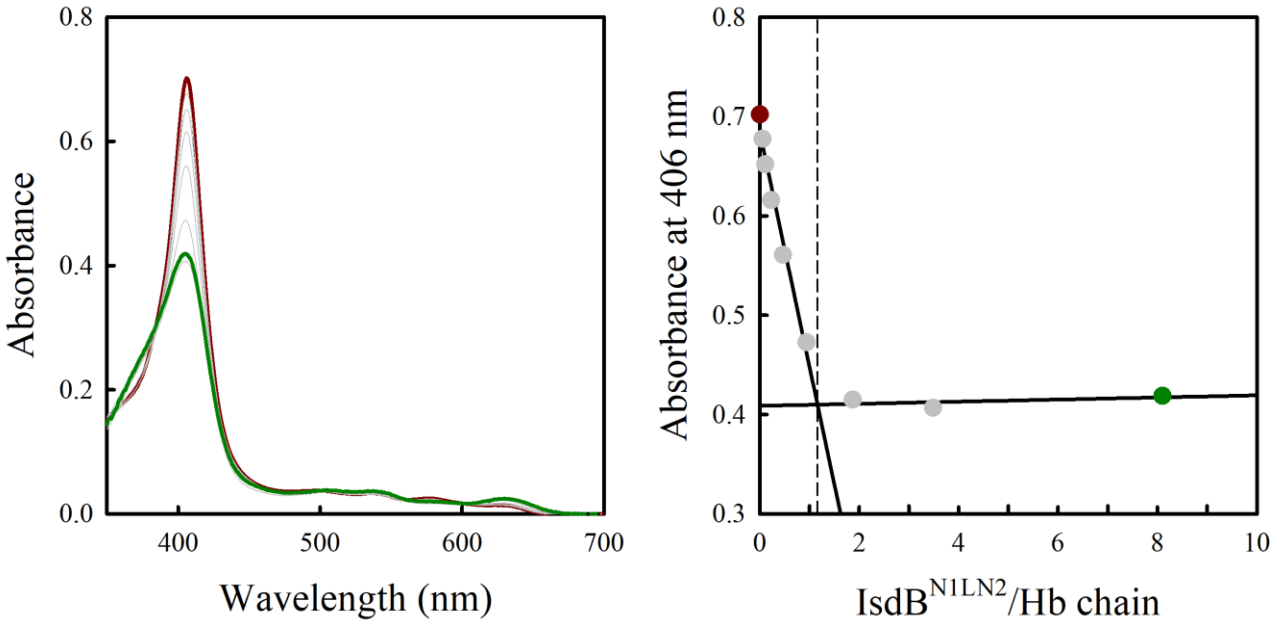

Figure 36: Stoichiometric titration of metHb with IsdB^{N1LN2}. On the left, visible absorption spectra of 5.4 µM metHb in the absence (dark red) or the presence of increasing concentrations of IsdB^{N1LN2} (grey). The final spectrum of the titration is in dark green. On the right, dependence of the absorbance at 406 nm on IsdB^{N1LN2}/metHb ratio. Dashed vertical line indicates the stoichiometric ratio, which is 1.16.

3.1.3 Determination of microscopic kinetic constants and dissociation constants for IsdB-Hb complex formation

Visible spectroscopy and SPR were combined to obtain key information on the kinetics of complex formation and on the role of key residues in the heme transfer process. SPR experiments were performed on both IsdB^{N1LN2} and IsdB^{Y440A} and different forms of Hbs (oxyHb, metHb and semiHbs) under the same experimental conditions with the aim of defining the simplest kinetic model and determine the microscopic rate constants for the individual steps.

The selection of kinetic steps to define the simplest model was based on literature data on IsdH [240]. The resulting model was:

$$IsdB + metHb \rightleftharpoons IsdB\text{-}metHb \rightarrow holo\text{-}IsdB\text{-}apo\text{-}Hb \rightleftharpoons holo\text{-}IsdB + apo\text{-}Hb$$

In this model, the complex formation between IsdB and metHb is followed by the irreversible heme extraction by the hemophore. The resulting holo-IsdB-apo-Hb complex is then expected to dissociate. The heme transfer step was considered irreversible on the basis of published data on IsdH [240] and the extensive protein unfolding occurring on Hb upon heme transfer (vide infra). With the aim of isolating the first reversible step of the model, the kinetics of IsdB-oxyHb complex formation was studied. In fact, the spectroscopic characterization confirmed the inability of the hemophore in heme-extraction from oxyHb (Figure 34). The expected kinetic model for IsdB-oxyHb encounter complex formation was:

$$IsdB + oxyHb \rightleftharpoons IsdB\text{-}oxyHb$$

The interaction between IsdB and oxyHb was also intended to be the simplest model, and thus the most favourable to start (Figure 37A). The sensorgram was obtained by injecting increasing concentrations of oxyHb (ranging from 0.01 to 1 μM) on a $IsdB^{N1LN2}$-functionalized chip, where the immobilization was obtained exploiting the StrepTag®II at the C-terminus of the hemophore.

This setup was chosen since it closely mimics the physiological conditions where complex formation takes place, i.e. IsdB is attached on the surface of the bacterium by anchoring its C-terminus to the bacterial cell wall. Experimental data were fitted using a 1:1 model to extract the kinetic parameters for the PPI, the results are reported in Table 11. Fitting to a two-state model with either a reversible or irreversible second step does not improve the fitting significantly (data not shown). In the following step, the interaction between $IsdB^{N1LN2}$ and semiHbs was studied to get further insight on possible preferences of the hemophore in binding to either α or β chains of Hb. This observation has critical consequences not only on the mechanistic description of complex formation, but also on the design of PPI inhibitors tackling the complex stability. Figure 37B and 37C show the sensorgrams corresponding to the injection of five increasing concentrations of semi(α) or semi(β)oxyHb over the chip functionalized with $IsdB^{N1LN2}$. The 1:1 model gave a good description of experimental data, and calculated kinetics constants are summarized in Table 11. Notably, microscopic constants

and calculated K_D resulted very similar when the two forms of semiHbs were used, witnessing the absence of selectivity for binding to either α- or β-chain of Hb. The interaction between $IsdB^{N1LN2}$ and metHb or (semi)metHbs was studied with the same single-cycle kinetics SPR approach described for the oxyHbs. Figure 37D, 37E, and 37F present the sensorgrams obtained by injecting five increasing concentrations of metHb or (semi)metHbs over the $IsdB^{N1LN2}$ functionalized chip. The sensorgrams were best fitted by using a two-state irreversible model. The first, reversible step corresponded to the encounter complex formation, while the second, irreversible, step was assumed to include the heme transfer and the dissociation of apo-Hb from holo-IsdB. The resulting parameters are reported in Table 11. Complex formation and dissociation were significantly faster when the oxidized forms of Hb were used. Despite the difference in microscopic kinetic constants, the dissociation constants for oxyHb and metHb were comparable. The same procedure was applied to study the interaction between $IsdB^{Y440A}$ and Hb. 1:1 and two-steps irreversible models were used to analyse the complex formation with oxy and metHb, respectively. Sensorgrams are shown in Figure 37E and 37F, while calculated constants are summarized in Table 11. The kinetic parameters calculated for oxyHb binding to $IsdB^{Y440A}$ are very similar to those obtained for $IsdB^{N1LN2}$, demonstrating that the mutation does not affect the complex formation. The substitution of Y440 with an alanine residue was indeed intended to impair heme extraction.
As a matter of fact, despite the K_D similar to that calculated for $IsdB^{N1LN2}$-metHb complex formation, $k_{on,1}$ and $k_{off,1}$ were significantly reduced in the variant. Therefore, a clear difference between WT and mutated IsdB interacting with metHb was detected, but it was not possible to get further insights on it based on SPR data analysis. Finally, the interaction between $IsdB^{Y165A}$ and oxy- or metHb was investigated. The response signal of $IsdB^{Y165A}$-functionalized chips was strongly reduced, especially at the higher concentrations of Hb used, witnessing a reduced ability of this mutant to bind both oxyHb and metHb. Notably, Y165A mutation was demonstrated to impair affinity for Hb *in vitro* and *in vivo* [238,294], thus our results further support the role played by this residue in complex formation.

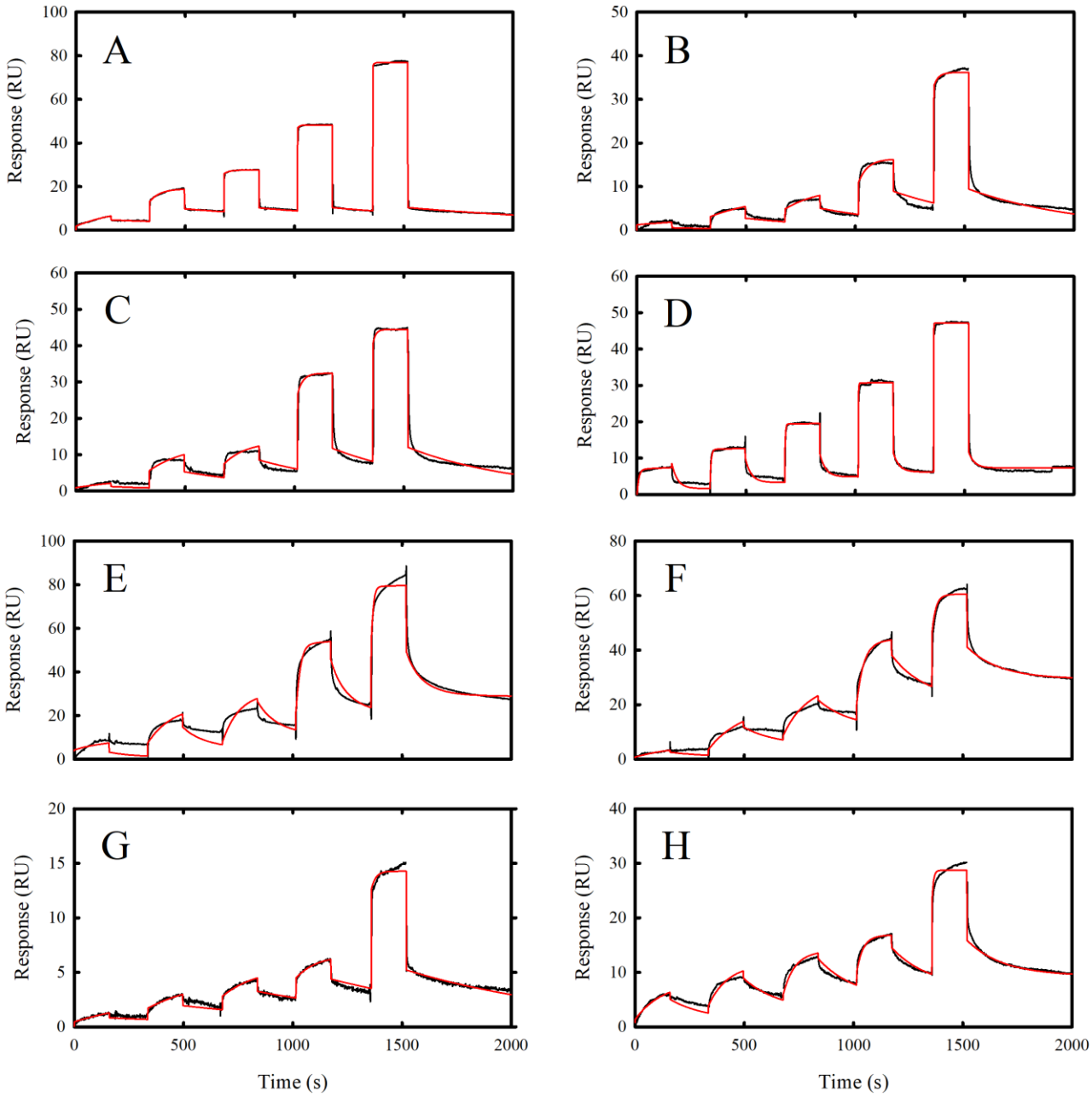

Figure 37: SPR sensorgrams (black curves) of the response (Resonance Units, RU) versus time of the single-cycle kinetics performed by injecting five increasing concentrations (0.01, 0.05, 0.1, 0.5, 1 μM) of Hb over the IsdB^{N1LN2}-functionalized chip. The red curves are the fitting with either a 1:1 or a two-state irreversible binding model. Fitting parameters are reported in Table 11. (A) IsdB^{N1LN2}-oxyHb (1:1) (B) IsdB^{N1LN2}-semi(α)oxyHb (1:1) (C) IsdB^{N1LN2}-semi(β)oxyHb (1:1) (D) IsdB^{N1LN2}-metHb (two-state irreversible) (E) IsdB^{N1LN2}-semi(α)metHb (two-state irreversible) (F) IsdB^{N1LN2}-semi(β)metHb (two-state irreversible) (G) IsdB^{Y440A}-oxyHb (1:1) (H) IsdB^{Y440A}-metHb (two-state irreversible). Adapted from [338].

Table 11: Microscopic kinetic constants and dissociation constants calculated by SPR.

	$k_{on,1}$ / $k_{off,1}$ (10^3 $M^{-1}s^{-1}$) / (10^{-3} s^{-1})	$k_{on,2}$ (10^{-3} s^{-1})	K_D (nM)	R_{max}	X^2
$IsdB^{N1LN2}$-oxyHb	8.1 ± 0.1 / 0.83 ± 0.02	n.d.	102 ± 3	10.43	0.27
$IsdB^{N1LN2}$-semi(α)oxyHb	44 ± 1 / 1.93 ± 0.05	n.d.	44 ± 2	9.85	1.22
$IsdB^{N1LN2}$-semi(β)oxyHb	77 ± 2 / 2.0 ± 0.1	n.d.	26 ± 1	12.35	2.85
$IsdB^{N1LN2}$-metHb	530 ± 40 / 37 ± 1	1.21 ± 0.03	70 ± 6	11.8	1.09
$IsdB^{N1LN2}$-semi(α)metHb	130 ± 10 / 14 ± 1	1.51 ± 0.03	108 ± 11	52	10.90
$IsdB^{N1LN2}$-semi(β)metHb	54 ± 2 / 4.9 ± 0.2	1.21 ± 0.03	91 ± 5	42.7	3.36
$IsdB^{Y440A}$-oxyHb	9.7 ± 0.1 / 1.2 ± 0.1	n.d.	124 ± 10	5.3	0.12
$IsdB^{Y440A}$-metHb	53 ± 1 / 5.1 ± 0.2	0.97 ± 0.02	96 ± 4	16.6	0.94

In conclusion, gathering up data from SPR and UV-visible spectroscopy regarding IsdB-metHb interaction, it is possible to define the following kinetic model:

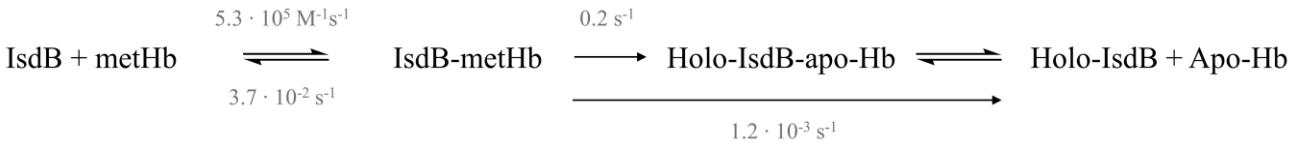

3.1.4 Stoichiometry and oligomeric state of IsdB-Hb complexes in diluted solutions

$IsdB^{N1LN2}$ and metHb were analyzed separately or mixed in 1:1 stoichiometric ratio. Figure 38 shows the results of SEC-MALS analysis. All three samples eluted as a single principal peak, suggesting that loaded solutions were monodisperse.

The calculated molecular weight for $IsdB^{N1LN2}$ was 42.2 kDa, which is close to the one expected based on amino acid sequence (43.2 kDa). MetHb eluted as a single peak with a molecular weight of 38.5 kDa, which is consistent with a dimer-tetramer equilibrium (32-64 kDa). Indeed, the dissociation constant for this equilibrium calculated in the same buffer at 4

°C was 0.5 μM (vide infra). The sample loaded onto the column was 1 g/L (60 μM heme) and was diluted on the column by a factor of 10 (final concentration 6 μM), therefore it was expected to elute principally as a tetramer. However, since SEC-MALS experiments were performed at 25 °C and K_D (dimer-tetramer) significantly increases when temperature rises [325] then the observed equilibrium is plausible. Finally, the elution of a single peak when the mixture of $IsdB^{N1LN2}$ and metHb was loaded confirmed the stoichiometric ratio used for preparing the sample, one IsdB for each single Hb chain (namely 1:1 ratio). Moreover, the possible complexes that follow the identified stoichiometric ratio are formed by one $IsdB^{N1LN2}$ molecule bound to a single Hb chain (59 kDa), two $IsdB^{N1LN2}$ molecules bound to an Hb dimer (118 kDa), or four $IsdB^{N1LN2}$ molecules bound to an Hb tetramer (236 kDa). The estimated molecular weight of 47.7 kDa supported the presence of the smallest complex in solution, and even if Hb monomerization usually occurs at extremely low concentration (K_D in the pM range [366]) the extraction of the heme as a result of IsdB binding could have led to the destabilization of the Hb dimer, as already proposed by an ESI-MS experiment on IsdH [197]. Apparently, no dissociation of the holo- $IsdB^{N1LN2}$-apo-Hb complex takes place under the SEC-MALS experimental conditions.

To evaluate the impact of the ligation state of heme bound to Hb on complex formation with IsdB, SEC-MALS analysis was performed both on oxyHb and COHb and their complexes with the hemophore (Figure 39). OxyHb and COHb showed a similar behaviour both isolated in solution and within the complex with $IsdB^{N1LN2}$. When isolated in solution oxy- and COHb eluted as single peaks with a molecular weight of 47.8 and 46.2 kDa, respectively. As already discussed for metHb, the calculated molecular weight was attributable to the dimer-tetramer equilibrium. The eluted protein was approximately 6 μM and the K_D (dimer-tetramer) for oxyHb was calculated to be 0.25 μM in the experimental buffer used for SEC-MALS at 4 °C. Once more, the higher temperature at which the SEC-MALS experiments was conducted could have caused the increase of the dissociation constant and thus shifted the equilibrium toward the dimeric species. Notably, the molecular weight of the ligated forms of Hb is significantly higher than the metHb one, suggesting a higher prevalence of tetramer in solution, which is in good agreement with the lower K_D (dimer-tetramer) of reduced Hb form compared to the oxidized form.

Complexes of IsdB^{N1LN2} with oxyHb and COHb resulted in two, partially unresolved peaks, the molecular weight of the particles in the first peak was estimated to be approximately 57 kDa, whereas the one for the protein eluted in the second peak was 48 kDa. The observed heterogeneity revealed that the stoichiometric ratio used (namely one IsdB^{N1LN2} molecule for each Hb subunit) was not correct and lead to a mixture of species. Indeed, the low-molecular weight species likely corresponds to free IsdB^{N1LN2}.

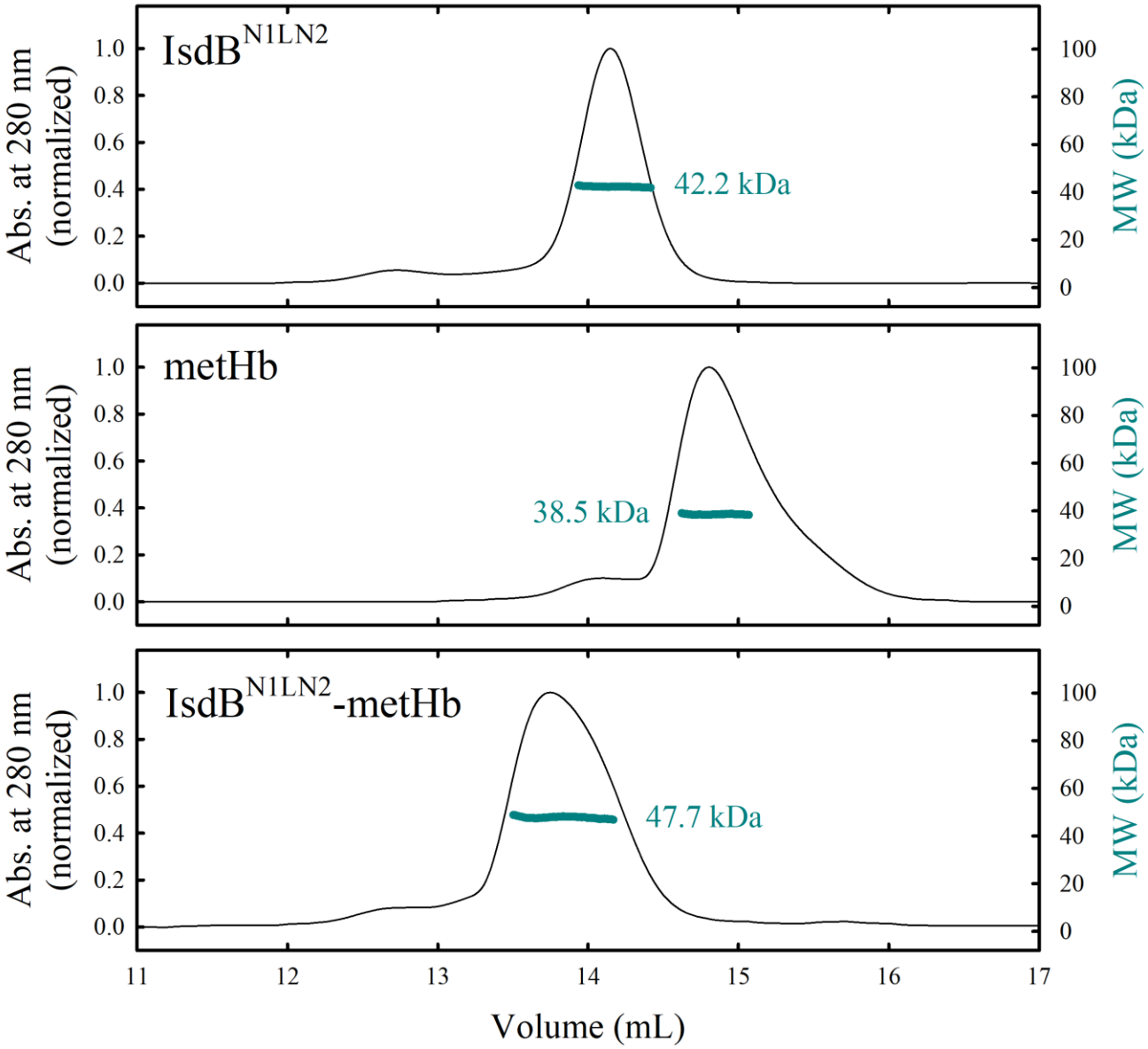

Figure 38: SEC-MALS analysis on IsdB^{N1LN2}, metHb, and IsdB^{N1LN2}-metHb. Black line represents the UV absorption signal, and dark cyan dots depict the molecular mass estimation across the eluted peak.

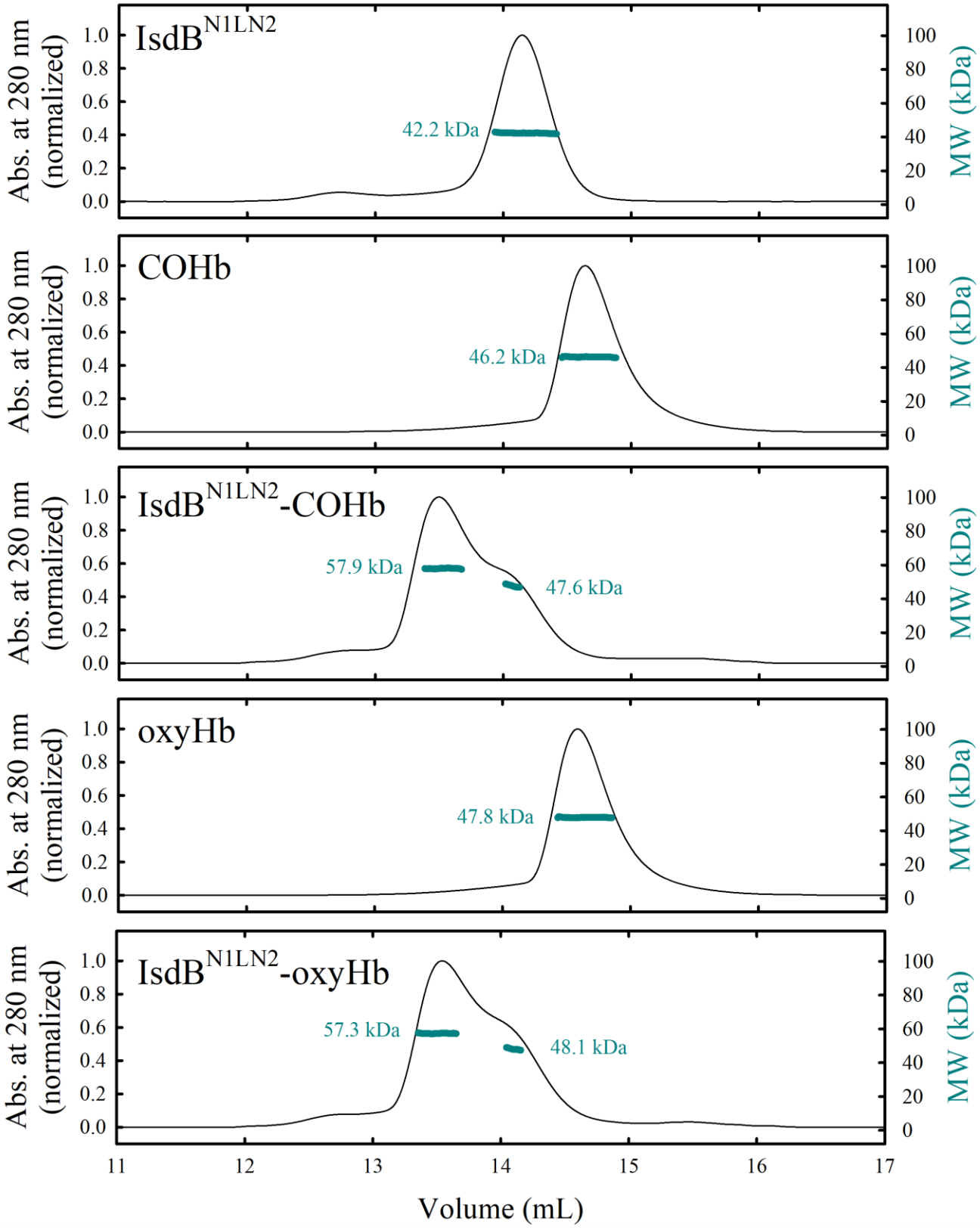

Figure 39: SEC-MALS analysis of IsdB^{N1LN2}, COHb, IsdB^{N1LN2}-COHb complex, oxyHb, and IsdB^{N1LN2}-oxyHb complex. Black line represents the UV absorption signal, and dark cyan dots depict the molecular mass estimation across the eluted peak.

The attribution of peaks to molecular species was further supported by measuring the absorption signal in the visible range where heme absorbs. This signal was recorded with the second absorption detector mounted on the AKTA purifier used for SEC-MALS analysis while experiments were ongoing, thus allowing to evaluate the presence of heme in the eluting sample. Finally, the deconvolution of chromatographic peaks with one or multiple Gaussian curves allowed to identify the peaks of the different species that were present in solution (Figure 40 and 41).

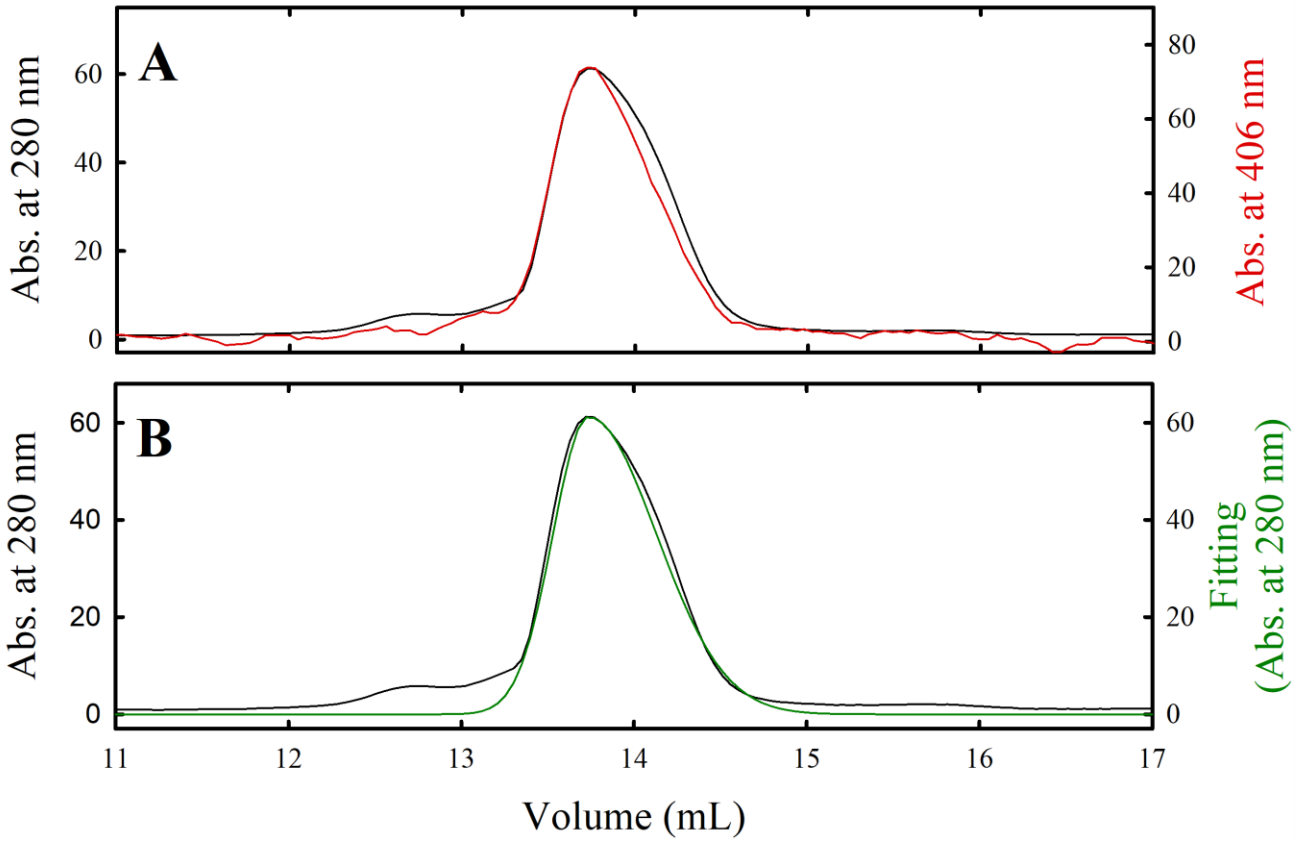

Figure 40: Elution profile of IsdB^{N1LN2}-metHb complex measured at 280 nm, overlaid (A) with the elution profile measured at 406 nm and (B) with the simulated elution profile obtained from Fityk fitting.

The 280 nm and 406 nm peaks corresponding to IsdB^{N1LN2}-metHb complex were essentially comparable, and fitting of the signal at 280 nm resulted in a single component. Together, these results suggested that the only species in solution was the protein complex, which was binding the full amount of heme in solution.

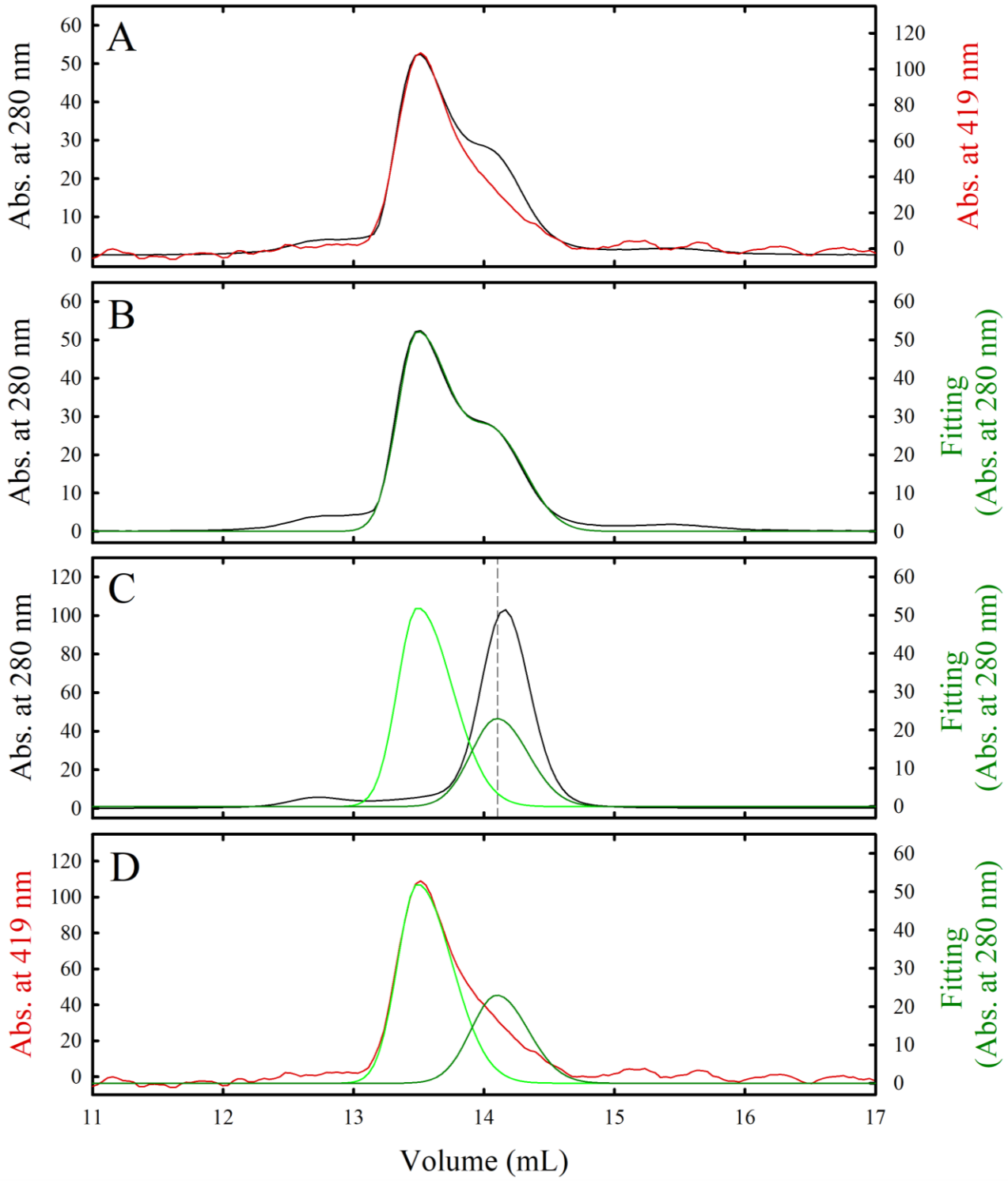

Figure 41: Elution profile of IsdB^{N1LN2}-COHb complex measured at 280 nm, in comparison with (A) the elution profile measured at 419 nm, and (B) the simulated elution profile obtained from Fityk fitting. The resulting component from the fitting (light and dark green) are compared with (C) IsdB^{N1LN2} elution profile at 280 nm, and (D) IsdB^{N1LN2}-COHb complex signal at 419 nm.

The elution profile of the heme-containing component as monitored at 419 nm does not completely overlap with the elution profile at 280 nm of $IsdB^{N1LN2}$-COHb complex (Figure 41). The peak that absorbs in the visible region corresponds to a single component that overlaps with the higher molecular weight species and binds the whole amount of heme. The lower molecular weight species does not contain heme. The deconvolution of the peak at 280 nm identified two peaks. The first resulted comparable with the elution profile of the complex recorded at 419 nm, while the second was in good agreement with the peak corresponding to $IsdB^{N1LN2}$ free in solution. Therefore, the most likely arrangement of the complex was one $IsdB^{N1LN2}$ bound to each Hb dimer (1:2 ratio). Since the whole amount of heme was found to elute with the peak corresponding to the complex, the result confirmed that the hemophore was not able to extract the cofactor. The two possible complexes following the calculated stoichiometric ratio were either one $IsdB^{N1LN2}$ bound to a Hb dimer (75 kDa), or two $IsdB^{N1LN2}$ molecules bound to a Hb tetramer (150 kDa). The molecular weight for the complex calculated by SEC-MALS analysis (58 kDa) mainly supported the presence of the smallest complex.
The same analysis presented for $IsdB^{N1LN2}$-COHb was performed for $IsdB^{N1LN2}$-oxyHb complex and resulted in a comparable finding, confirming that IsdB interacts with both the reduced ligated forms of Hb in a similar way.

With the aim of confirming the observed oligomeric state and stoichiometry of the IsdB-COHb complex, a sample prepared using the 1:2 stoichiometric ratio at 1 g/L concentration was analyzed in the same condition using an AKTA Pure (GE Healthcare). The sample eluted as a single peak (Figure 42), supporting the finding that ligated-Hb, that is resistant to heme extraction by IsdB, does not monomerize in solution, as observed for the metHb form. These findings are indeed essential for the planning of the cryo-EM experiment that require a monodisperse sample (vide infra).

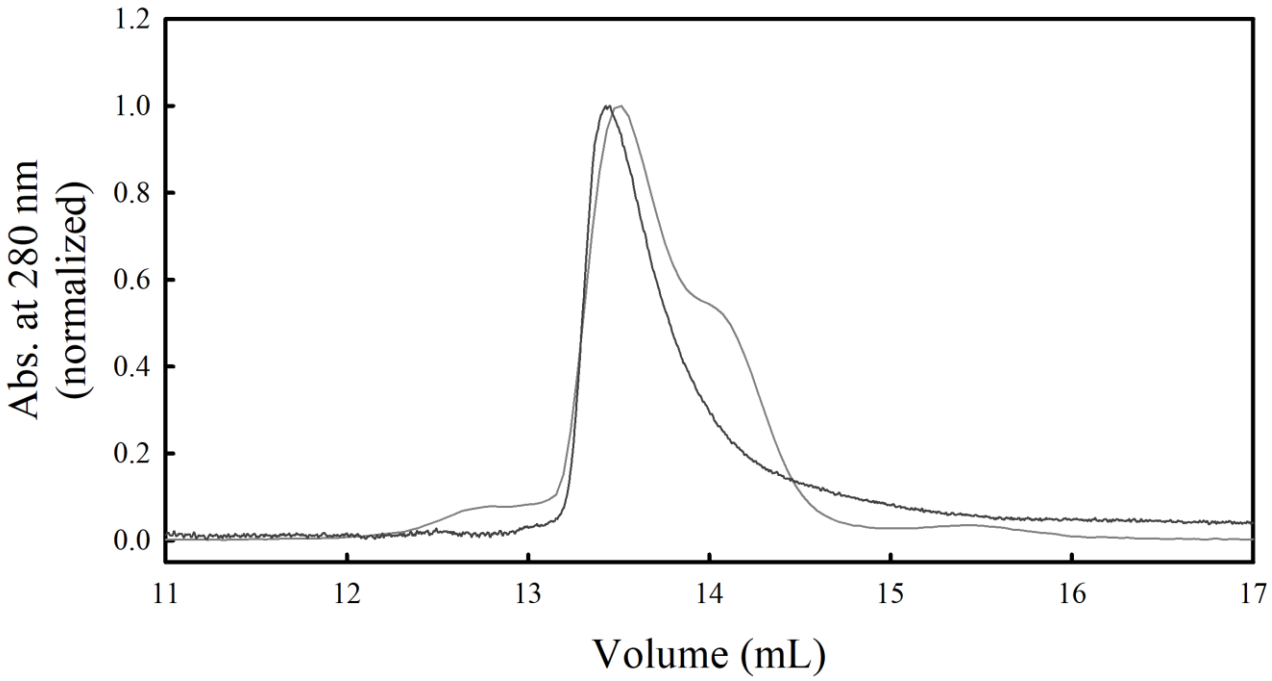

Figure 42: SEC elution profiles of IsdB^{N1LN2}-COHb complexes in either 1:1 (dark grey) or 1:2 (light grey) stoichiometric ratios.

Notably, the results of this section suggest that IsdB^{N1LN2}-metHb complex is present in solution as a single Hb chain bound to IsdB, while one molecule of the hemophore binds an Hb dimer when the latter is in the reduced, ligated form. However, structural techniques (e.g., SAXS and cryo-EM) determined that the prevalent oligomeric state of IsdB-metHb complex is a dimeric metHb bound by two hemophores, while a tetrameric Hb is bound two hemophores in IsdB^{N1LN2}-COHb complex (see paragraph 3.2). Since the concentration of the proteins used for SEC-MALS experiments was at least ten times lower than that used for SAXS or cryo-EM, the different observed oligomeric state could be simply due to protein dilution.

3.2 Structural insight on the IsdB-Hb complex

3.2.1 X-ray scattering of IsdB^{N1LN2} and metHb

IsdB^{N1LN2} and metHb were separately studied before the SAXS analysis of their complex was performed. In fact, structural information of IsdB isolated in the complex has never been published before, and the technique has made it possible to obtain the first low-resolution model of the hemophore in solution. Both isolated proteins gave good quality datasets, which clearly indicates homogeneous solutions. Principal data extrapolated from the analysis are reported in Table 12.

Table 12: Summary of molecular parameters of IsdB^{N1LN2} and metHb from SAXS.

IsdB^{N1LN2}			
	Sample 1	Sample 2	Sample3
Sample concentration (g/L)	12.53	5.93	2.93
R_g (Å) (P(r) analysis)	33.92	33.89	33.35
R_g (Å) (Guinier analysis)	33.95	33.91	33.33
D_{max} (Å)	107	105	101
Hb			
	Sample 1	Sample 2	
Sample concentration (g/L)	12.30	6.30	
R_g (Å) (P(r) analysis)	23.91	24.16	
R_g (Å) (Guinier analysis)	23.92	24.17	
D_{max} (Å)	70	73	

The SAXS intensity of different dilutions of IsdB^{N1LN2} resulted highly comparable when scaled for concentration (Figure 43C), confirming the reliability of the signal observed. For further analysis, the scattering profile of the more diluted sample was used. The linearity in the region of Guinier analysis (Figure 43A) allowed to extrapolate the first structural information and to exclude the presence of inter-particle interaction or aggregation. IsdB^{N1LN2} has a bimodal P(r) (Figure 43B), indicating a compact bi-lobed shape in good agreement with high-resolution structure of the hemophore bound to Hb in the published 3D-structure (PDB 5VMM [224]).

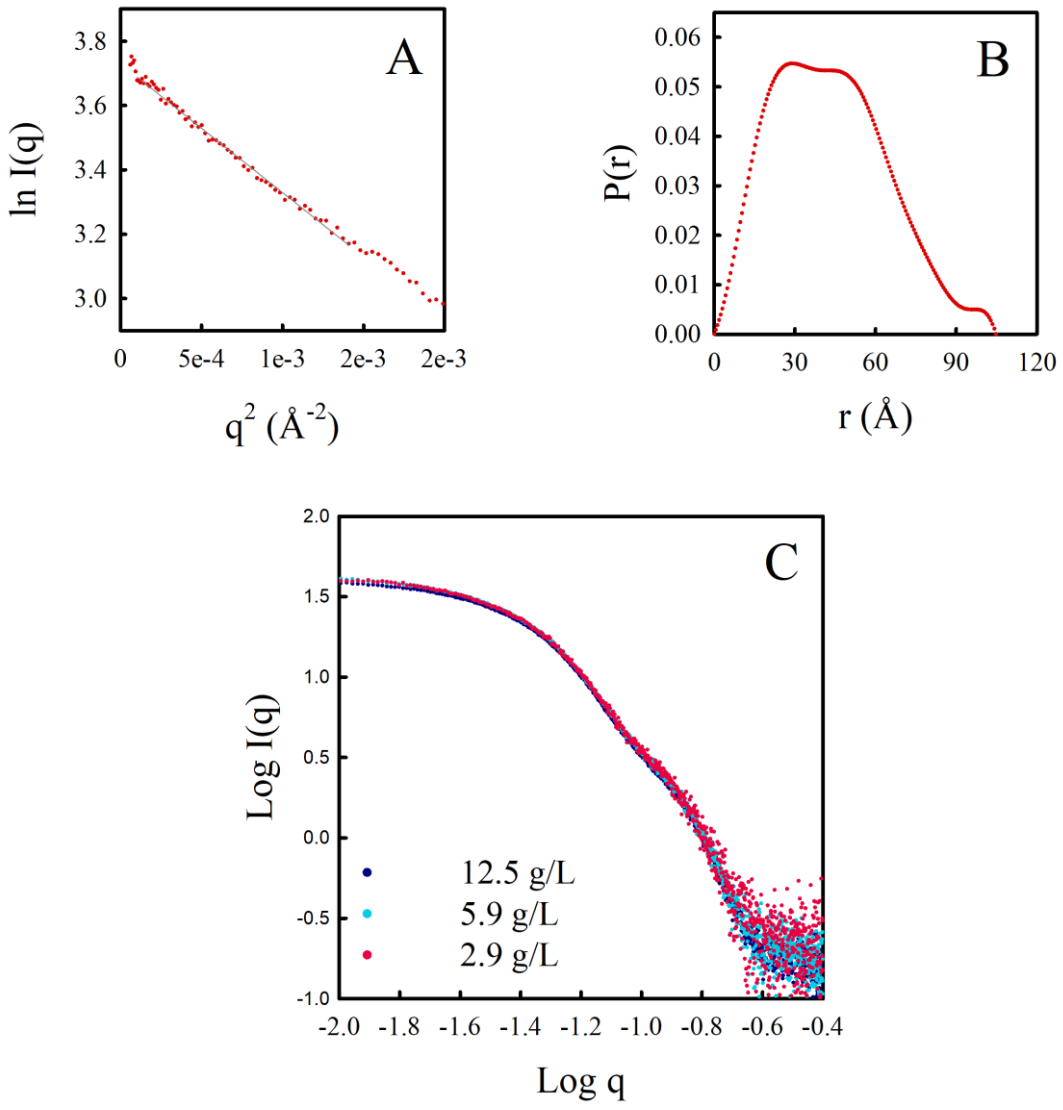

Figure 43: SAXS analysis of IsdB^{N1LN2}. (A) Guinier plot of data at lower concentration (2.9 g/L). Experimental values are red, while fitting line is grey. (B) P(r) function of IsdB^{N1LN2} sample at 2.9 g/L. (C) SAXS intensity (normalized by concentration) of three different dilutions of IsdB^{N1LN2} in the Log I(q) – Log q representation.

The molecular details obtained from the analysis for IsdB^{N1LN2} (Table 12) revealed a good agreement between the `reciprocal space' and `real space' R_g values, which was a further indicator for a well measured dataset [367]. R_g values resulted lower than 34 Å for all the hemophore concentrations, which was 5 Å bigger than the value calculated for the high-resolution structure of IsdB^{N1LN2} in the crystal. However, this 3D structure was extrapolated from the PDB structure of IsdB-Hb complex and might not perfectly describe the protein free in solution. With the aim of finding more structural information on the conformation of the hemophore in solution, the P(r) function corresponding to the sample at lower concentration was used to obtain the *ab initio* shape of IsdB^{N1LN2} (Figure 44). With this aim, DAMMIF was

used to generate 20 independent shapes, and then DAMAVER suite was employed to align created model, remove outliers, average the according shapes, and finally filter the results to identify the most probable shape. With this method, eleven shapes (with normalized spatial discrepancy of 0.915) were processed to obtain the probable low-resolution model.

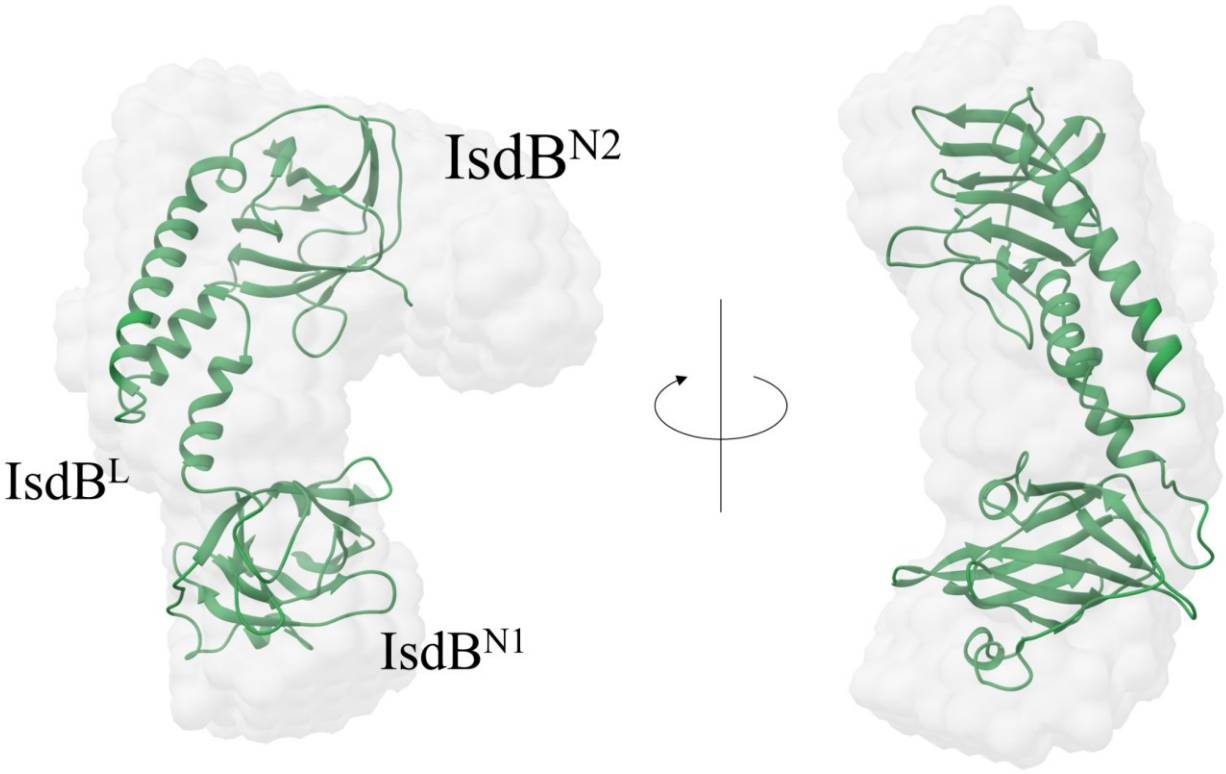

Figure 44: Front (left) and side (right) views of IsdB high-resolution structure, extracted from 5VMM, fitted inside the ab initio shape from SAXS.

The 3D structure of IsdB extrapolated from 5VMM PDB structure was in good agreement with the *ab initio* shape (Figure 44), confirming that free hemophore in solution assumes a conformation similar to the one observed when it is binding Hb, as already suggested for IsdH [237]. However, two structural differences became visible from the comparison of 3D structure and the shape. First, the shape has an empty volume close to NEAT2, the C-terminal domain of the hemophore. This region could accommodate the StrepTag®II that is fused to the protein at the C-terminus, which is not present in the 3D model of the hemophore extracted from 5VMM PDB structure. Moreover, the global shape suggests that the hemophore can adopt a

more extended conformation when it is free in solution, in fact the shape appears slightly longer than the high-resolution structure.

Guinier and model free analysis of Hb scattering data excluded protein aggregation and inter-particle interaction (Figure 45). The calculated R_g of 23.9 Å was in good agreement with the theoretical R_g of tetrameric Hb, and the P(r) function described a single bell curve consistent with a globular protein. The sample at lower concentration was used for further analysis.

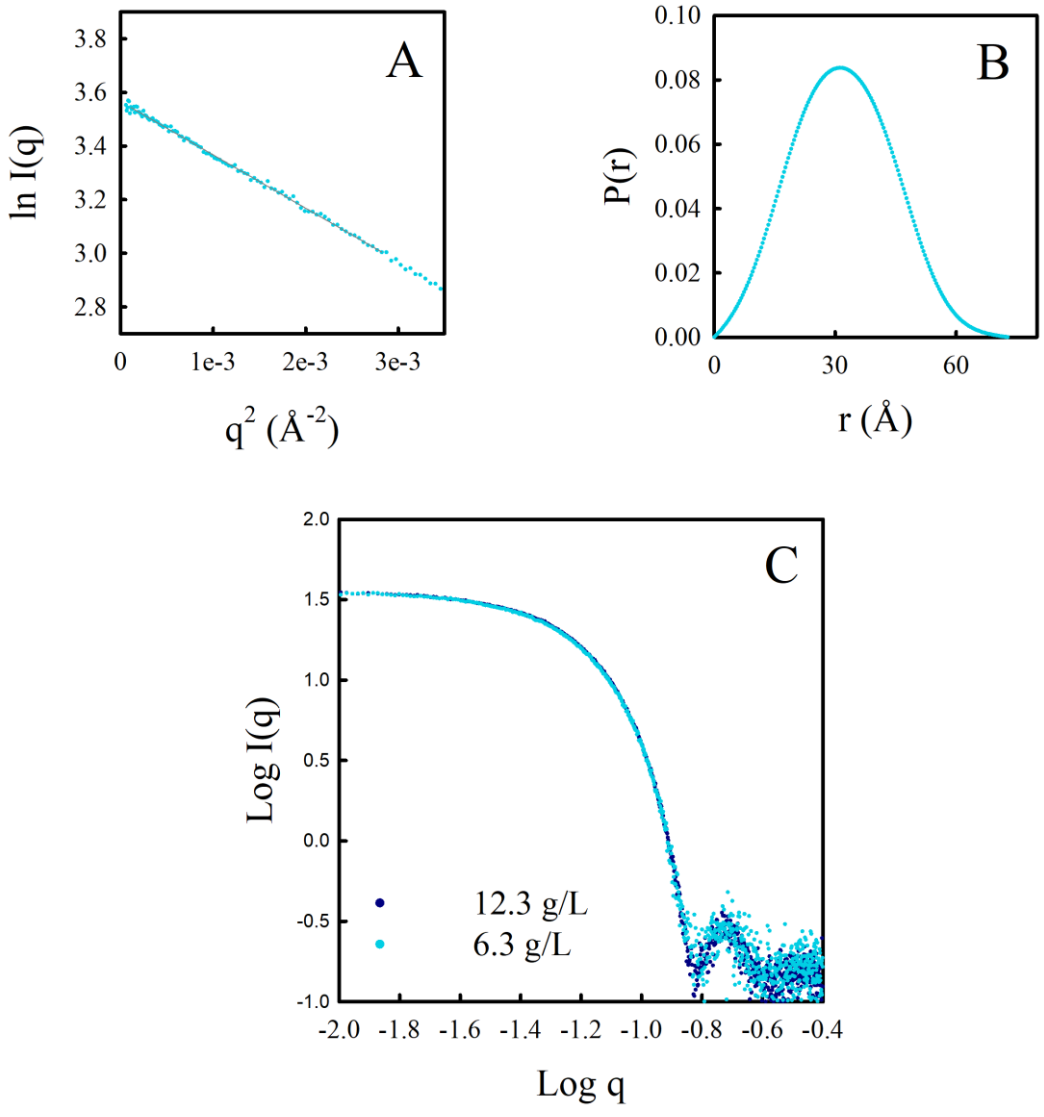

Figure 45: SAXS analysis of metHb. (A) Guinier plot of data at lower concentration (6.3 g/L). Experimental values are light blue, while fitting lines is grey. (B) P(r) function of metHb sample at 6.3 g/L. (C) SAXS intensity (normalized by concentration) of two different dilutions of metHb in the Log I(q) – Log q representation.

Also in the case of metHb, DAMMIF was used for the generation of an *ab initio* shape. Twenty independent models were elaborated using the DAMAVER suite to isolate possible outliers. The analysis gathered 13 shapes (with a normalized spatial discrepancy of 0.813). These shapes were averaged and then filtered to finally identify the most highly occupied area (Figure 46). The refined shape perfectly describes the metHb tetramer.

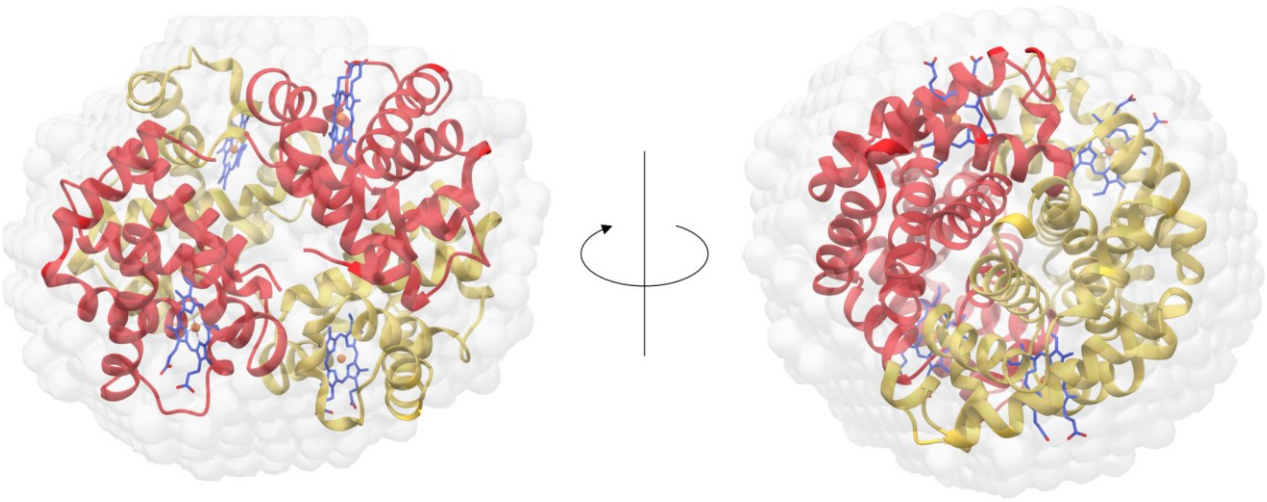

Figure 46: Front (left) and side (right) views of metHb high-resolution structure (PDB 3P5Q) fitted inside the ab initio shape. α-Hb chains are depicted in red, while β-Hb chains are yellow, and heme is blue.

3.2.2 X-Ray scattering of IsdB^{N1LN2}-metHb complex

When IsdB^{N1LN2} and Hb were mixed in a 1:1 stoichiometric ratio (i.e., one Hb subunit for each hemophore) the solution looked monodispersed (Figure 47), indicating that all the proteins in solution were forming complexes. Principal extrapolated data are summarized in Table 13.

Table 13: Summary of molecular parameters of IsdB^{N1LN2}-metHb complex from SAXS.

IsdB^{N1LN2}-metHb complex			
	Sample 1	Sample 2	Sample 3
Sample concentration (g/L)	12.88	6.74	3.05
R_g (Å) (P(r) analysis)	44.01	43.00	41.88
R_g (Å) (Guinier analysis)	43.83	42.74	41.70
D_{max} (Å)	156	156	155

The result confirmed the stoichiometric ratio used and allowed a straightforward analysis. SAXS data collected at different protein concentrations indicated that the sample behaves in a similar way from 3 to 13 g/L, therefore the lowest concentration was used for further analysis. Calculated R_g resulted within the 10% of the theoretical R_g (based on the model created *ad hoc* that represents the complex formed with an Hb dimer and two IsdB molecules) even at the higher concentration. This last finding implies that the complex where Hb is in the tetrameric state does not form even at significantly high concentration. The deviation from a single bell curve of the P(r) function was attributed to small flexible parts of the structure, most likely the StrepTag®II fused to IsdB^{N1LN2}.

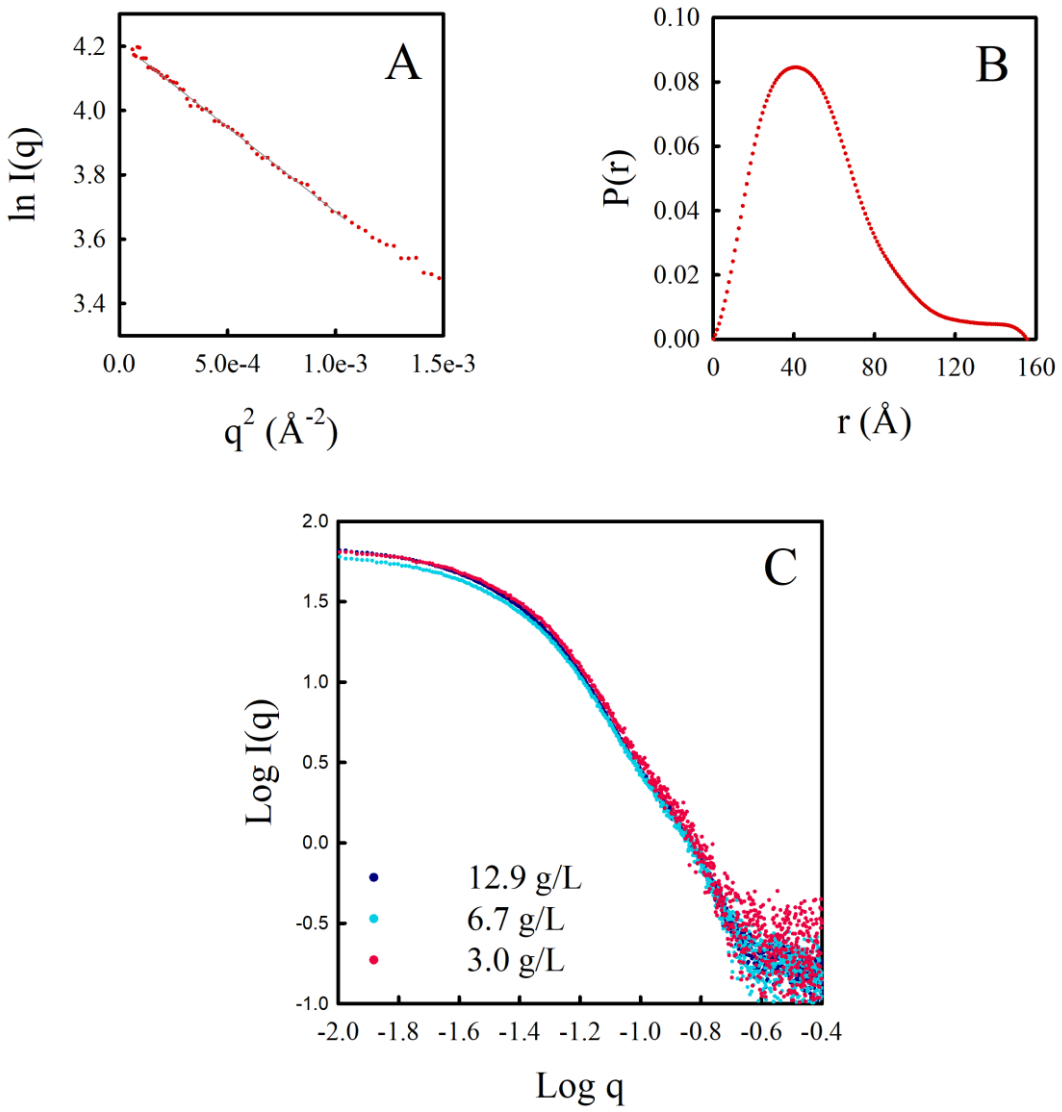

Figure 47: SAXS analysis of IsdBN1LN2-metHb complex. (A) Guinier plot of data at lower concentration (3.0 g/L). Experimental values are red, while fitting lines is grey. (B) P(r) function of the sample at 3.0 g/L. (C) SAXS intensity (normalized by concentration) of three different dilutions of the sample in the Log I(q) – Log q representation.

Ab initio shape reconstruction was carried out using the calculated P(r) function for the sample at lower concentration and the program DAMMIF (Figure 48). Twenty independent models were generated and analyzed using DAMAVER suite. 12 shapes (with a normalized spatial discrepancy of 0.950) were selected, averaged and filtered as already described for $IsdB^{N1LN2}$ and metHb samples.

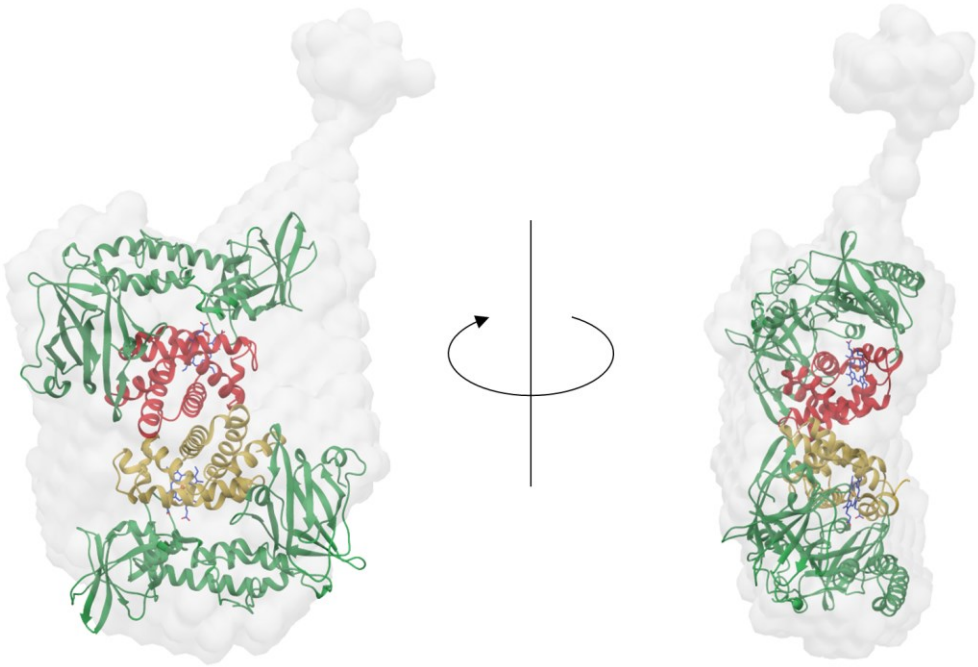

Figure 48: Front (left) and side (right) views of IsdB^{N1LN2}-metHb complex ad hoc model fitted inside the ab initio shape. α-Hb chain is depicted in red, while β-Hb chain is yellow, heme is blue, and IsdB is green.

The core of the shape described well the high-resolution model confirming the stoichiometric ratio and the oligomeric state of the complex in solution (Figure 48). The empty volume density of the shape, which significantly extrudes from the core, was probably generated based on the small shoulder present in the P(r) function and it is likely due to the StrepTag®II fused to IsdB^{N1LN2}. Since it was not possible to easily fit the affinity tag inside the shape, further data processing is probably needed. The complex structure suggested by the *ab initio* shape is very valuable to identify the prevalent oligomeric state of the complex in solution. This information was used as a starting point for setting-up the cryo-EM analysis on the same sample (vide infra). Notably, the model obtained by cryo-EM SPA confirmed the prior information from SAXS (vide infra), pointing out the good agreement between the two techniques.

3.2.3 Three-dimensional structure of IsdB^{N1LN2}-COHb complex obtained by cryo-EM

With the aim to obtain structural insight on the IsdB-Hb complex two different complexes were analyzed using cryo-EM. The IsdB-COHb complex was intended to represent a snapshot of the simple interaction between the two proteins, while the IsdB-metHb complex was expected to give fundamental information on the complex after heme extraction.

The high-resolution reconstruction through cryo-EM clearly shows that the IsdB^{N1LN2}-COHb complex (Figure 49) is formed by two IsdB^{N1LN2} molecules binding the βHb subunits of a Hb tetramer. This model is the first high-resolution structure of a WT hemophore interacting with a plasma purified Hb. In fact, the only IsdB-Hb complex deposited (PDB: 5VMM) includes two proteolyzed hemophores and some missing helices in Hb, whereas all the IsdH-Hb complexes were prepared with an heme extraction deficient hemophore (PDB 4XS0 and 6TB2), which was also modified to selectively bind α-Hb chains (PDB 4IJ2).

The stoichiometric ratio used to prepare the cryo-EM specimen was guided by results of other biochemical techniques (vide infra), and freezing the sample while in a diluted solution might have prevented the stabilization of artefactual interactions between the proteins. Therefore, the presence of IsdB only bound to β-Hb chains might be due to an intrinsic molecular property of the PPI (vide infra).

The main interface between the β-Hb chain and the hemophore measures 1170 Å^2. IsdB also interacts with the prosthetic group bound to the β-Hb subunit (56 Å^2) and with the α-Hb chains of the opposite αβ dimer (94 Å^2). A detailed analysis of the complex reveals four different interaction areas, summarised in Table 14 and shown in Figure 50.

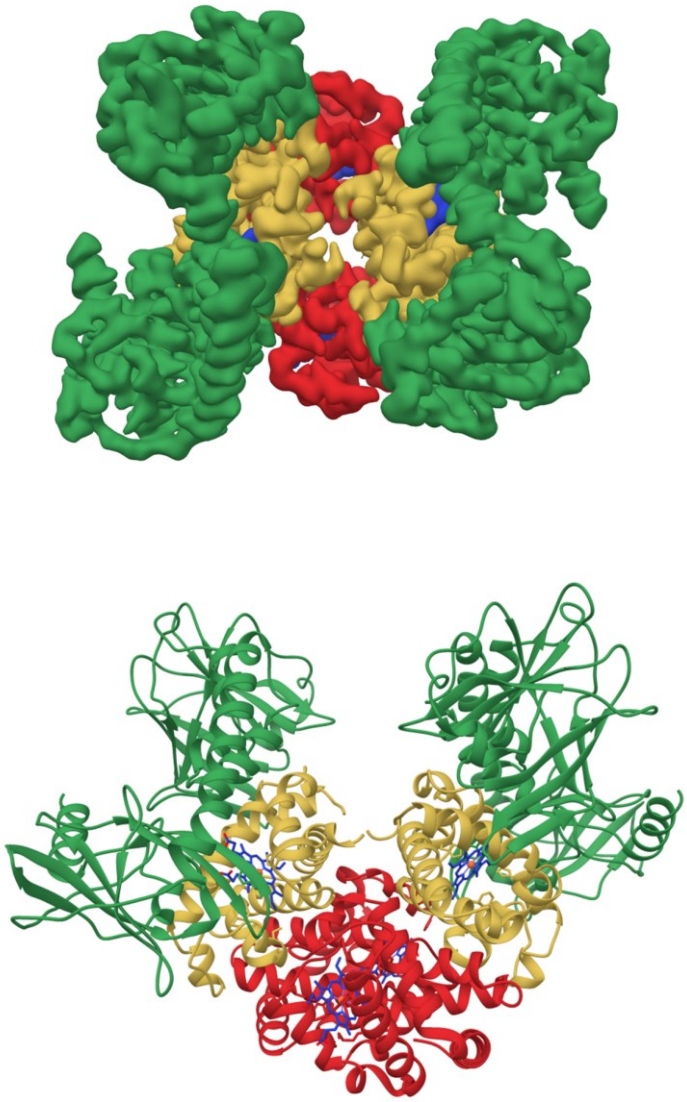

Figure 49: Three-dimensional representation of the IsdB^{N1LN2}-COHb complex. On the top, the top view of the 2.86 Å cryo-EM map. On the bottom, cartoon representation of the derived atomic model. Heme is coloured in blue, α-Hb chains in red, β-Hb chains in yellow, and IsdB molecules in green.

Table 14: List of interactions between IsdB and Hb. Contacts analysis have been derived from analysis of isolated COHb (PDB 2DN3) and the structure solved here, and are grouped according to the expected function. A single interaction could have more than one effect because several Hb residues are multifunctional within the Hb tetramer. The code in brackets indicates the Hb traditional naming scheme, whereas (H) means that a H-bond is formed between the two residues, whilst (HS) means that both H-bond and salt bridge are formed. The zone of each interaction in Figure 50 is listed in the right column.

Formation of IsdB-NEAT1 Loop2	
β-S(A6)_IsdB-Y165 (H)	A
β-T(A9)_IsdB-F164	A
β-T(A9)_IsdB-Y165	A
β-A(A10)_IsdB-Y165	A
β-W(A12)_IsdB-F164	A
β-G(A13)_IsdB-F164	A
β-S(E16)_IsdB-F164	A
β-L(E19)_IsdB-F164	A
β-A(EF1)_IsdB-Y167	A
β-A(EF1)_IsdB-A168	A
Interference with Hb hydrophobic cage	
β-T(F3)_IsdB-R290* (H)	C
β-T(F3)_IsdB-Y293* (H)	C
β-T(F3)_IsdB-Y297* (H)	C
β-E(F6)_IsdB-Y293* (H)	C
β-E(F6)_IsdB-K297* (HS)	C
β-K(FG2)_IsdB- D439*	B
β-K(FG2)_IsdB- Y440*	B
β-L(FG3)_IsdB-I438	D
β-H(FG4)_IsdB-D439* (HS)	B
F helix unfolding	
β-R(C6)_IsdB-T437 (H)	D
β-R(C6)_IsdB-I438	D
β-F(C7)_IsdB-I438	B
β-T(F3)_IsdB-R290 (H)	C
β-T(F3)_IsdB-Y293 (H)	C
β-T(F3)_IsdB-Y297 (H)	C
β-E(F6)_IsdB-Y293 (H)	C
β-E(F6)_IsdB-K297 (HS)	C
β-K(FG2)_IsdB-Y440	B
β-K(FG2)_IsdB-D439	B
β-L(FG3)_IsdB-I438	D
β-H(FG4)_IsdB-D439 (HS)	D

Destabilization of Hb-heme interaction	
β-E(CD1)_IsdB-T437 (H)	B
β-S(CD3)_IsdB-M362	B
β-K(E3)_IsdB-D364 (HS)	B
β-K(E10)_IsdB-E354 (HS)	B
β-A(EF1)_IsdB-Y167	A
β-A(EF1)_IsdB-A168	A
β-K(FG2)_IsdB-D439	B
β-K(FG2)_IsdB-Y440	B
Disruption of Hb tetramer	
α-T(C6)_IsdB-D439	D
β-P(A2)_IsdB-F194	A
β-E(A3)_IsdB-F194	A
β-R(C6)_IsdB-T437 (H)	D
β-R(C6)_IsdB-I438	D
β-E(CD1)_IsdB-T437 (H)	B
β-K(FG2)_IsdB-D439	B
β-K(FG2)_IsdB-Y440	B
β-L(FG3)_IsdB-I438	D
β-H(FG4)_IsdB-D439 (HS)	D
Disruption of Hb dimer	
β-E(GH4)_IsdB-N243 (H)	A
Complex formation	
β-K(A5)_IsdB-Q190 (H)	A
β-A(A7)_IsdB-F242	A
β-L(A11)_IsdB-F242	A
B-K(A15)_IsdB-E247 (HS)	A
Heme binding	
HEM_IsdB-M362	B
HEM_IsdB-Y440	B
HEM_IsdB-Y444	B

* The interaction is expected to disrupt the hydrophobic cage because the residue involved is next to the one that blocks the water entrance.

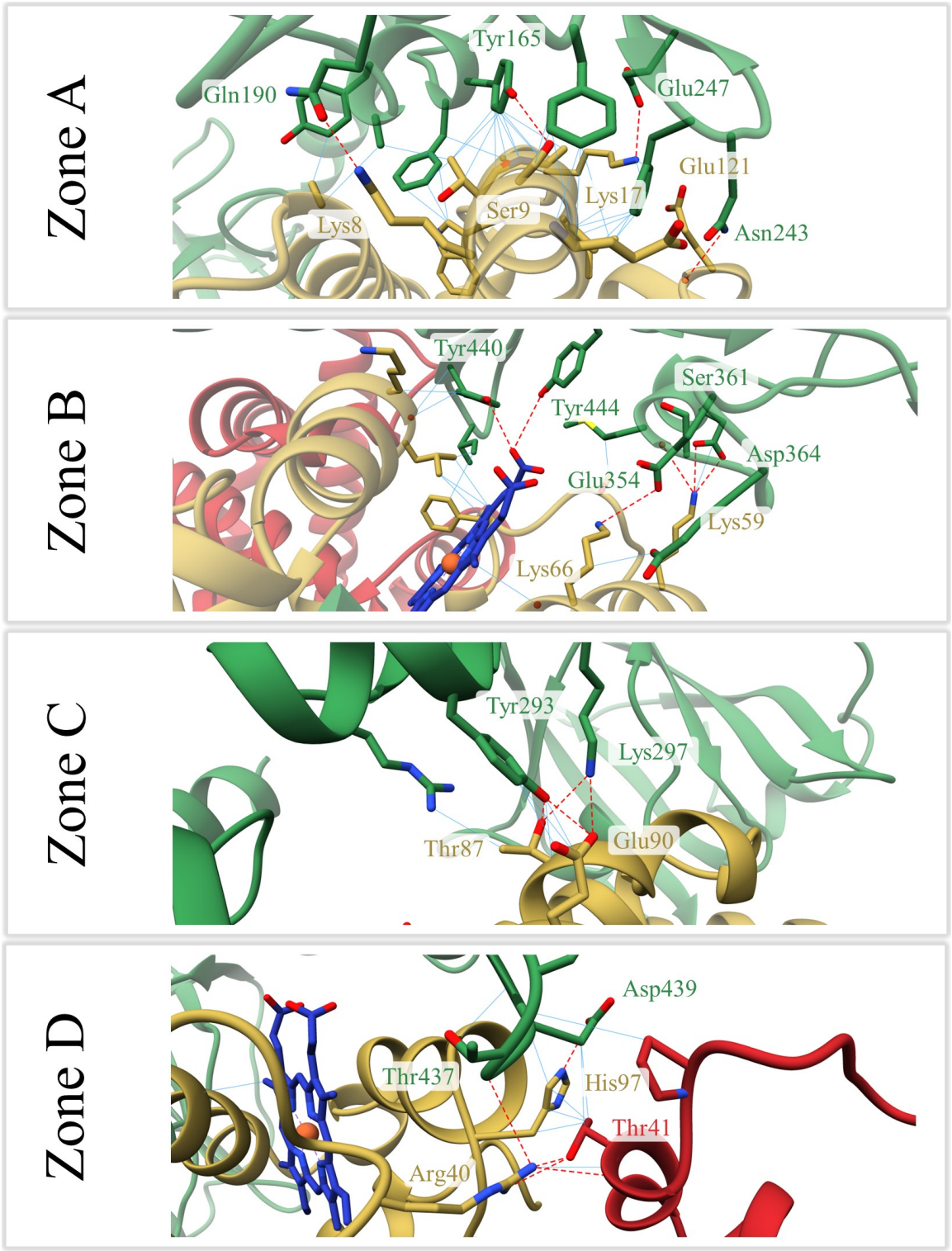

Figure 50: Principal interacting areas of IsdB-Hb in the cryo-EM atomic model. (Zone A) Molecular contacts that are expected to promote complex formation and to destabilize the α1β1 interface. The colour coding is the same as used in Figure 49. (Zone B) Network of interactions between the hemophore and the heme binding pocket of the Hb. (Zone C) Contacts of IsdB-linker with F helix. (Zone D) IsdB interactions that possibly destabilize Hb tetramer. Red dashed lines represent polar contacts, while non-polar contacts are depicted in blue.

The first interaction network (Figure 50-zoneA) comprises Hb residues that form A and H helices and the EF loop, while F164-A168, Q190, F194, F242 and N243 are the IsdB residues that populate this interfacing area. Notably, the IsdB region spanning residues F164-A168, which is usually indicated as loop 2 (Table 14), is usually identified as the Hb binding motif and it folds in an α-helix upon binding Hb [233,236]. The cryo-EM based model corroborates this function.

The second extensive contact area includes the NEAT2 heme binding domain of the hemophore with the entrance to the heme-binding pocket (Figure 50-zoneB). Hb residues interacting with IsdB are on helices E and F and the intrahelical CE loop, while in IsdB residues are from sheet β7 and the 3_{10}-helix including M362. In this interacting area, M362, Y440, and Y444 directly contact the same heme propionates, whereas D439 is contacting the proximal histidine.

Finally, only a few contacts are forming the third and fourth areas under investigation (Figure 50 zoneC and D). First of the two includes contacts between IsdB linker and F helix of Hb, whereas $IsdB^{N2}$ gets between CD and FG loops of the bound β-Hb chain and the C helix of the α-Hb chain of the opposite αβ-Hb dimer, possibly destabilizing this heterodimeric interaction, and thus the Hb tetramer.

Furthermore, even if a few contacts between IsdB and α-Hb chains are formed within the complex, several regions of the α-Hb subunits undergo a backbone movement because of the PPI formation. There are tertiary structural changes of the alpha-subunit through large backbone movements of Nterm-A, AB, CE, EF, GH, and H-Cterm loops and the E helix.

Interestingly, the hemes remain in their natural position within the complex, confirming the well-known inability of the hemophore to extract the porphyrin when its iron is in the ligated form. Even if the extraction step seems to be hindered, IsdB folds with its characteristic dumbbell structure, setting the extracting NEAT domain ($IsdB^{N2}$) against the heme binding pocket. Surprisingly, density is absent for the carbon monoxide molecule bound to the four prosthetic groups (Figure 51), and the heme retains the planar configuration typically found when a ligand occupies the axial position. The lack of ligand is difficult to explain because the visible absorbance spectrum of COHb mixed with IsdB does not change, suggesting that in solution the complex formation with hemophore is not causing the ligand loss. This puzzling result is discussed further below.

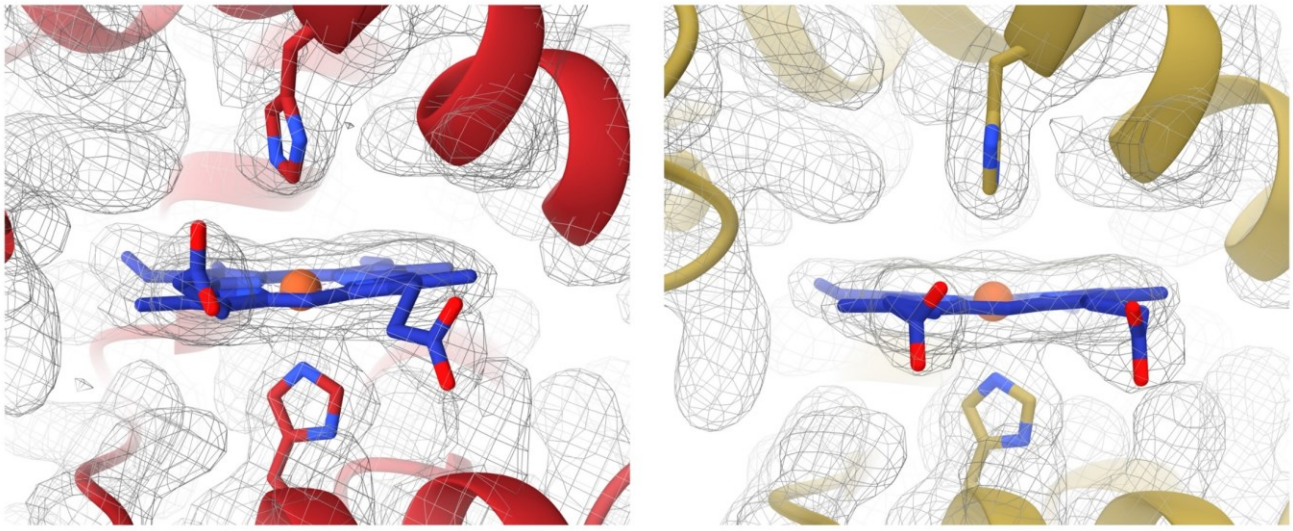

Figure 51: Atomic models and density maps of heme bound to α-Hb chain (on the left in red) and β-Hb chain (on the right in yellow) within the IsdB-COHb complex.

3.2.3.1 Effects of IsdB binding on Hb

To better analyse the effect of the hemophore binding, a detailed comparison was carried out of the Hb within the complex and a deposited COHb structure (PDB 2DN3) (Figure 52). Superimposition of separated α- and β-Hb chains of the complexed Hb with the PDB structure resulted in a very low r.m.s.d (0.49 and 0.44 Å, respectively), whilst the equivalent alignment of αβ dimer and the entire tetramer gave an increase of this parameter (0.52 Å for the dimer and 0.66 Å for the tetramer). This suggests a possible effect of the hemophore binding in quaternary structure destabilization.

Data in Table 15 confirm this observation, in fact it is possible to detect a significant reduction of the area at the α1α2 and β1β2 interfaces, which could be viewed as a Hb tetramer destabilization. It is interesting to notice that this effect is mostly pronounced on α-Hb chains, unraveling a possible allosteric effect of the PPI.

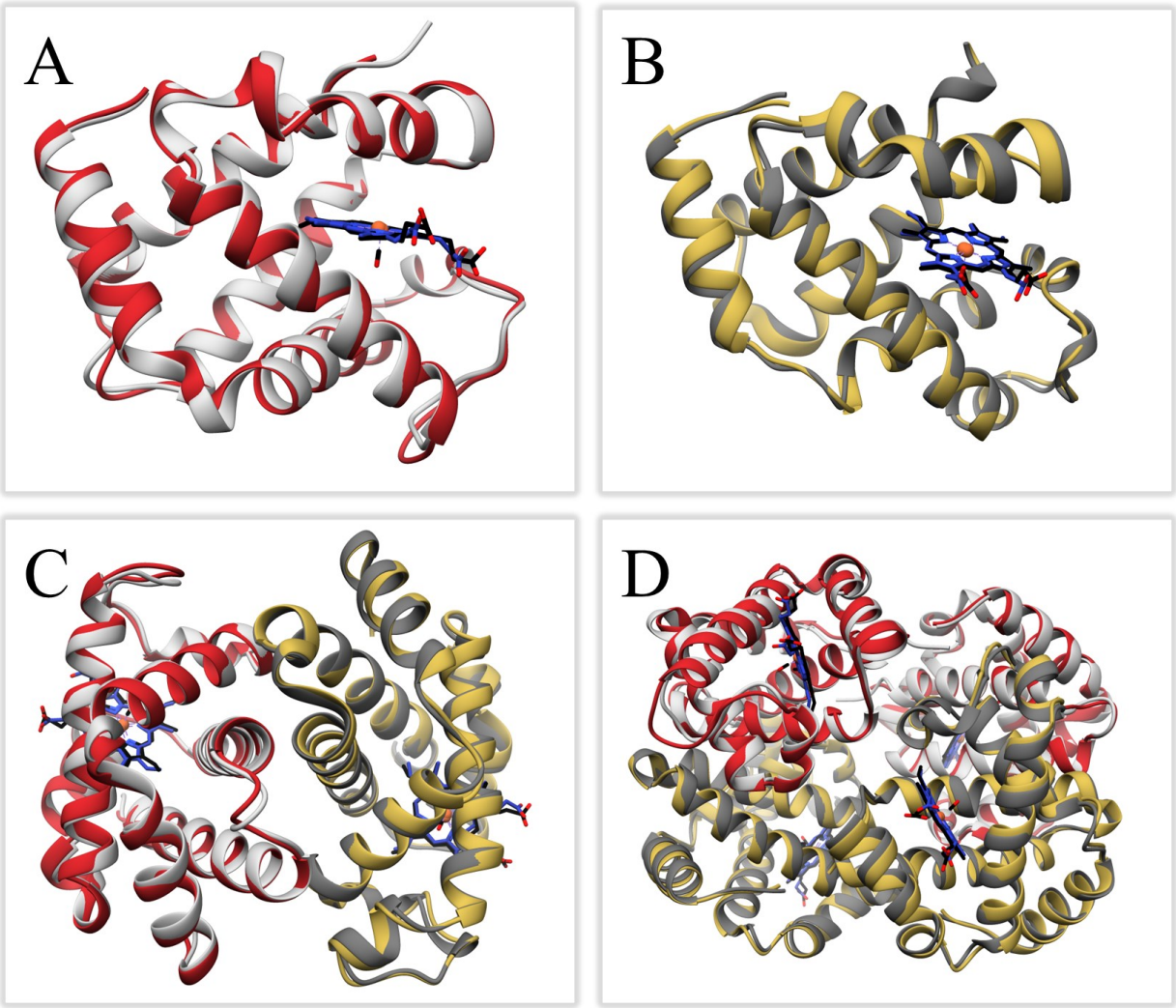

Figure 52: Alignment of COHb molecule extrapolated from cryo-EM atomic model (α-Hb chains in red, β-Hb chains in yellow, and heme in blue) and Hb structure (PDB 2DN3 – α-Hb chains in grey, β-Hb chains in dark grey, and heme in black). (A) and (B) represent the alignment of single Hb subunits, while (C) and (D) depict the superimposition of Hb dimer and tetramer.

Table 15: Computational estimation of interface area between major components of the complex, and their comparison with COHb structural model (PDB 2DN3).

	Cryo-EM map (Å^2)	2DN3 model (tetramer) (Å^2)
Hb intradimer ($\alpha_1\beta_1$)	863	913
Hb interdimer ($\alpha_1\beta_2$)	451	525
αHb chain – heme	565	584
βHb chain – heme	528	536
$\alpha_1\alpha_2$ chains	62	260
$\beta_1\beta_2$ chains	173	243

IsdB is known to selectively bind and extracts heme from metHb, so the IsdB-COHb complex is intended to be a snapshot of the single bimolecular interaction between the two proteins. As it will be shown afterwards, the stable complex between IsdB and metHb is composed of an Hb dimer bound by IsdB on both its α- and β-chains. In this scenario, the $IsdB^{N1LN2}$-COHb complex structure can give insights into the molecular process of activating the Hb for the heme extraction.

It is well known that free Hb tetramer disruption increases the hemic-iron autoxidation and the rate of cofactor release [123,368–372], at the same time, heme oxidation promotes tetramer disassembly [370,371]. The principal cause of heme oxidation is the entrance of water inside the heme pocket [373], which has been shown to promote the loss of the heme ligand first, and then disruption of the His(F8)-Fe coordination [372].

Water access to the heme binding pocket is restricted by the hydrophobic character of the heme cage. The specific residues composing the hydrophobic cage in both α and β subunits are L(F4), L(F7), L(FG3), V(FG5), F(G5), and L(αH19/βH20) [241,374]. At this level, atomic model of $IsdB^{N1LN2}$-COHb revealed interaction of IsdB with T(F3), E(F6), K(FG2), L(FG3), and H(FG4), indicating a possible direct activity of the hemophore in the enhancement of water entrance in heme-binding pocket.

Moreover, the exit of the oxidised heme from the heme-binding pocket caused by IsdB has been directly correlated to the loss of α-helical content along the F helix of Hb, where the breaking of coordination between the proximal His and hemic-iron was seen to determine the formation of a novel bis-His intermediate (e.g., H(FG1) replaces H(F8) to form a stable interaction with the cofactor) [375]. The same type of coordination has been reported for the IsdB-Hb structure by Bowden and co-workers [224], confirming the existence of this unstable reaction intermediate in the heme pathway toward the exit from its cavity and proposing the same as a key step for IsdB heme acquisition. Within the atomic model of $IsdB^{N1LN2}$-COHb complex, heme is still bound inside the heme-binding pocket, but (1) IsdB-D439 is interacting with the proximal His, likely destabilizing its coordination with heme, (2) M362, Y440 and Y444 are directly binding the cofactor and (3) the hemophore linker forms multiple contacts with the F helix. These interactions could make IsdB ready to start heme extraction, but the high stability of F helix in the Hb tetramer [373] possibly prevents the progress of the reaction.

Together with the former interactions, the cryo-EM atomic model identified other contacts that may promote heme extraction. These include the interactions between the hemophore and, in Hb, the CD loop and three lysines (K(E3), K(E10), and K(FG2)). The CD loop is necessary for distal histidine stabilization [323,376], whereas the three lysines were reported to form electrostatic interactions that stabilize the heme molecule [375].

In addition to directly promoting heme extraction, the interactions seen in the IsdB^{N1LN2}-COHb atomic model appear to destabilize the Hb oligomeric state. The movements of the CD loop and F helix are likely to also disrupt the Hb tetramer. Beside these movements, the contacts with FG loop and A helix could have an additional destabilizing effect since the FG loop is involved in forming the α1β2 interface and part of the A helix constitutes one of the β1β2 connections.

In terms of Hb disassembly, the hemophore effects on the α-Hb chains are noteworthy, as they cause significant backbone rearrangements. Deformation of the CE loop and E helix are expected to destabilize the interaction between Hb and the cofactor, whereas rearrangement of Nterm-A and H-Cterm loops can cause the weakening of tetramer interconnections at α1α2 and α1β2 interface. Finally, structural variation of AB, EF, and GH can have an impact on α1β1 stability.

Altogether, the IsdB^{N1LN2}-COHb atomic model revealed the interactions at several points that are anticipated to drive conformation changes in the globin that facilitate heme extraction. However, some force present in the COHb molecule blocks the hemophore mechanism, locking the PPI to the simple bimolecular contact. Anyway, IsdB binding to the β-chains of an Hb tetramer seems to be enough for destabilizing its quaternary organization and predisposing the heme cavity for the transfer of the prosthetic group. This result is in contrast with earlier models where Hb dimerization is induced through the steric repulsion caused by the simultaneous binding of four hemophores on the Hb tetramer [197]. Given the strength of the Hb tetramer, the earlier model requires a very strong hemophore interaction. Coming back to the puzzling finding that CO ligand is apparently absent in the hemophore-COHb complex, it may be that tetramer destabilization and the interaction with key residues forming the heme cavity might have destabilized the CO interaction with Hb. The spatial configuration of the distal histidine in the cryo-EM atomic model resembles most closely that of metHb (Figure 53B and D), or at least is not compatible with the presence of CO (Figure 53A and C). Plunge

freezing, which is known to cause mechanical stress could have determined the ligand loss and maybe the heme oxidation. However, even if the metHb was formed during sample vitrification, the kinetics of heme extraction is significantly slower than the sample freezing, thus the extraction steps, that are presented in the following paragraphs, are not expected to take place. Radiation damage is another possible mechanism for loss of the CO ligand.

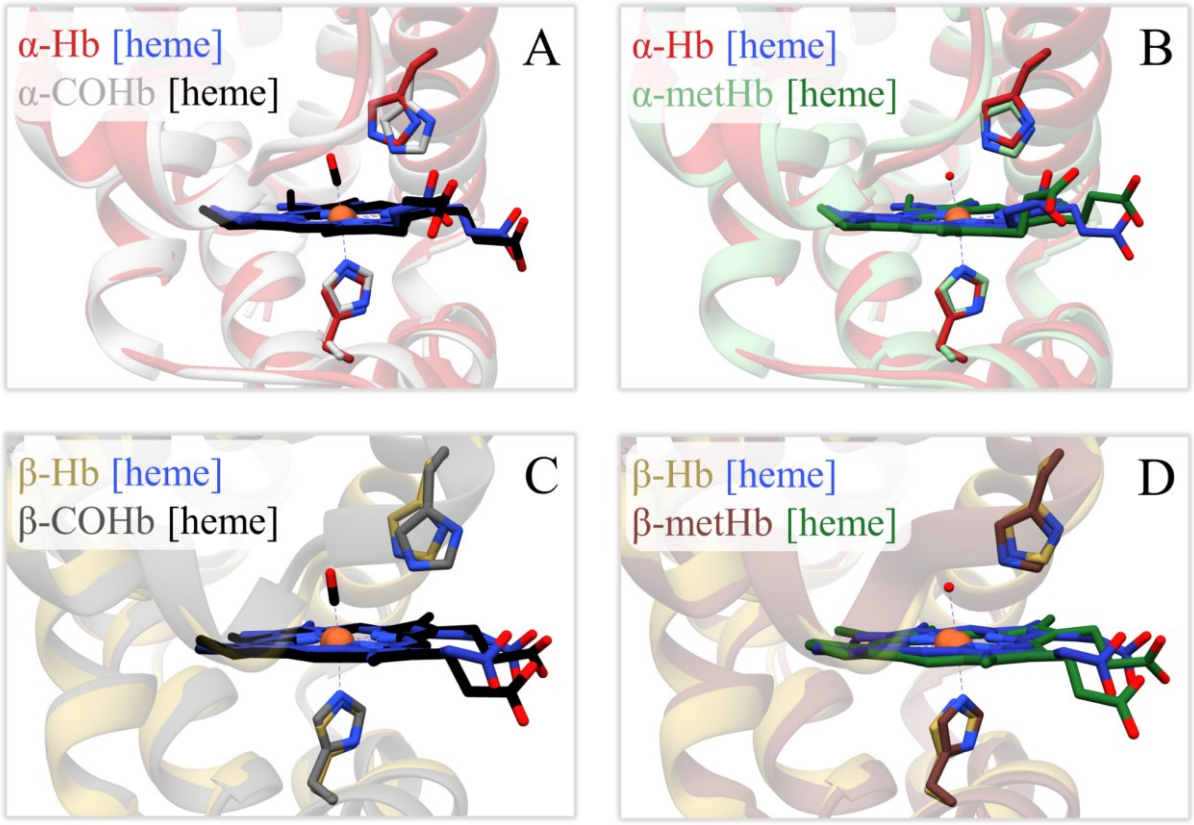

Figure 53: Spatial configuration of proximal and distal histidines. Comparison between cryo-EM atomic model (α-chain in red, β- chain in yellow, and heme in blue) and COHb (PDB 2DN3 – panel A, and C - α-chain in grey, β- chain in dark grey, and heme in black) or metHb (3P5Q - panel B, and D - α-chain in light green, β- chain in brown, and heme in green) high-resolution structures.

Finally, the IsdB binding to the β-Hb chains could derive from the higher degree of flexibility on the F helix of this globin chain compared to the α-subunits [371,375,377,378], which might ease the interaction of the hemophore linker to this Hb helix, as already suggested by Mikkelsen and co-workers [243]. Once the tight complex between IsdB and the β-Hb chains is formed, some structural rearrangements, possibly including the tetramer disruption, are needed to enable the following binding of the hemophore to the α-Hb chains, leading to the formation of the complex detected for the IsdB reaction with metHb.

3.2.4 Cryo-EM model of IsdB^{N1LN2}-metHb complex

The IsdB-metHb complex represented by the cryo-EM density map is formed by two IsdB^{N1LN2} molecules binding an Hb dimer, and this is the first time that this oligomeric state has been observed. The preparation of the specimen in its solution state, not packed in an ordered crystal, allowed visualisation of the complex form under conditions that more closely mimic those in solution. The stoichiometric ratio observed in the cryo-EM reconstructions is consistent with that determined by solution biophysical techniques (see sections 3.1.2 and 3.1.4). Considering the protein concentration used for cryo-EM experiments and the dimer-tetramer dissociation constant in the sub-μM range [see sections 3.9], the tetrameric state of Hb is expected to be the most represented form, pointing out the direct effect of IsdB binding on the Hb dimerization.
The resolution of the map (Figure 54) did not allow to precisely define the position of the amino acid residues of the proteins within the complex. However, the *ad hoc* model (which represents the complex formed by an Hb dimer with two IsdB molecules, one for each Hb subunit), refined with the program Namdinator, fits well the volume density except for the F helix of both Hb chains. The derived atomic model has the potential to elucidate many structural insights on the IsdB-metHb complex: (1) the oligomerization state of the complex in solution, (2) many conserved interactions between the complexes of the hemophore with both COHb and metHb, (3) the different positioning of IsdB on α- and β-Hb chains, and (4) the effective heme transfer from Hb to IsdB.

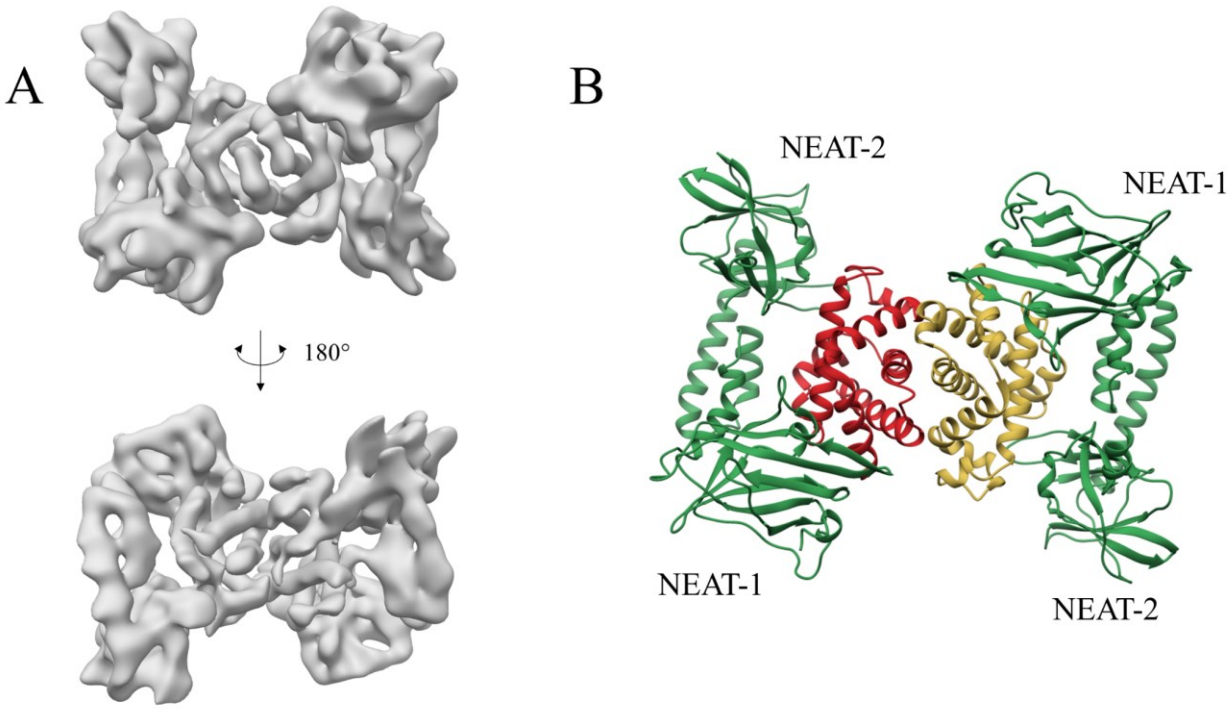

Figure 54: Cryo-EM reconstruction of IsdB^{N1LN2}-metHb complex. (A) Two different views the 5.8 Å cryo-EM map. (B) Atomic model of IsdB^{N1LN2}-metHb complex refined through Namdinator. α-Hb chain is red, β-Hb chain is yellow, and IsdB green. The colour-code is identical to the one used for IsdB^{N1LN2}-COHb complex.

Comparing IsdB^{N1LN2}-COHb and IsdB^{N1LN2}-metHb atomic models, it appears clear that interactions between IsdB^{N1} and β-Hb are conserved, and similar interactions are formed with α-Hb chain. As already mentioned, these interactions are expected to stabilize the IsdB-Hb complex but also to stress interdimer interactions, possibly inducing Hb dimerization.

Conversely, IsdB linker interactions with F helix seem to occur only between hemophore and β-Hb chains, confirming the similarity with IsdB^{N1LN2}-COHb cryo-EM model, but pointing out the first difference on the IsdB binding to the different Hb chains. Moreover, the density of the F helix is present at the α-Hb chain, whereas the density of the corresponding helix in the β-chain is almost lost. Finally, IsdB^{N2} is not forming apparent interactions with the α-Hb chain, whereas the hemophore is still interacting with the β-Hb chain.

Due to the low resolution of the model, the heme position could not be defined. Therefore, the position of the cofactor in the complex was inferred by comparison with 3RTL, the structure of the heme-bound NEAT2 domain of IsdB. The structure has been aligned to the cryo-EM model of either the hemophore bound to the α-chains or the one bound to the β-chains of Hb,

resulting in a r.m.s.d. of 1.14 Å and 1.07 Å, respectively (Figure 55). The analysis of the alignment revealed the presence of a volume density in the position occupied by heme in holo-IsdB^{N2}, suggesting that heme extraction has taken place.

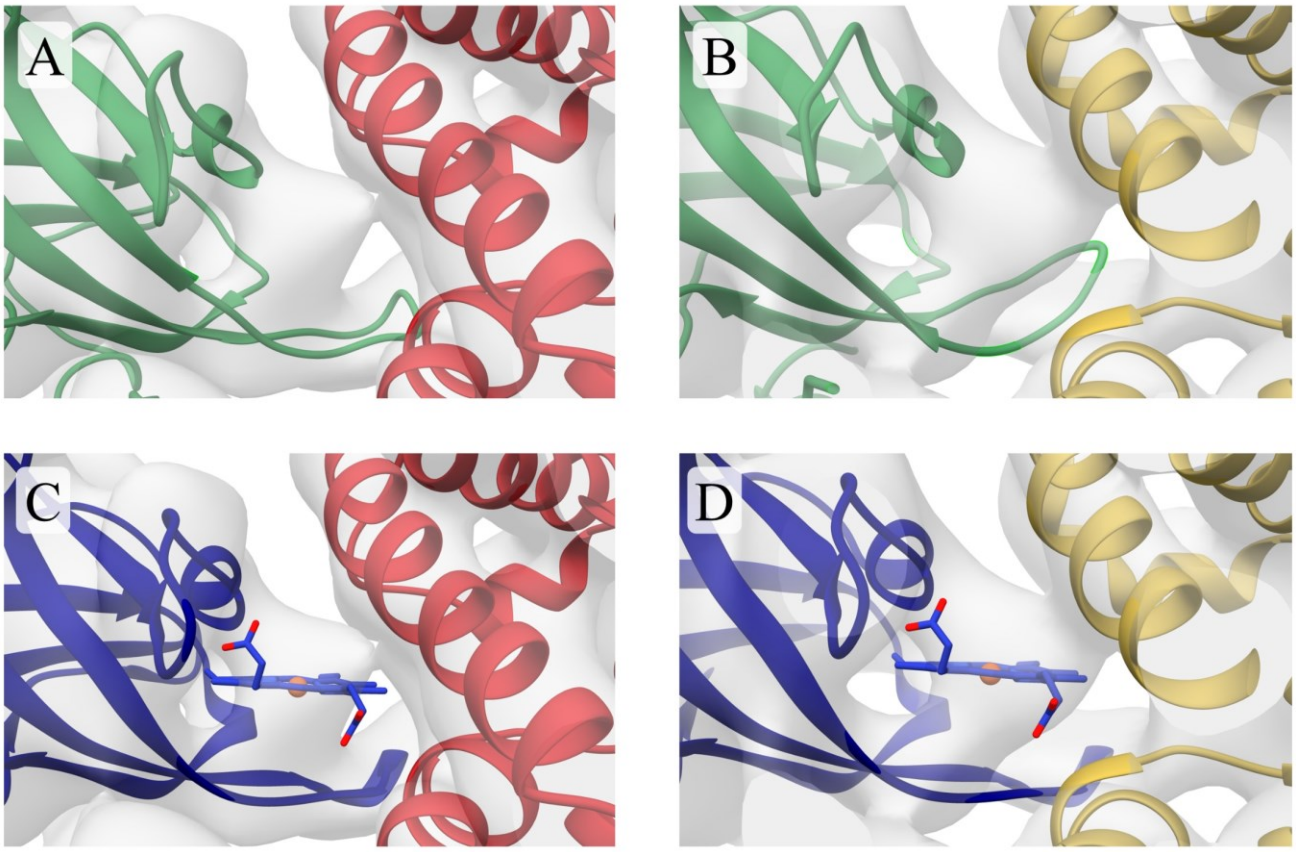

Figure 55: Cryo-EM atomic model and 3RTL fitted inside density map at the interface between Hb heme cavity and IsdB^{N2}. (A) and (B) represent the refined model of IsdB^{N1LN2}-metHb complex at the interface of α- and β-Hb subunits. In (C) and (D) holo-IsdB^{N2} (3RTL – dark blue) replaces apo-IsdB present in the cryo-EM refined model. α- and β-Hb chains representation is kept comparable in (A) and (C), and (B) and (D): α-chain is red, β chain is yellow, and heme is blue.

The consistency of the structural model built into the cryo-EM density was further assessed using published structure in PDB. The only complex formed by two hemophores (namely IsdH) and an Hb dimer was published in 2019 (PDB 6TB2) [243], but the presence of Hp in this structure might have favoured the Hb dimerization. The fitting of 6TB2 in the cryo-EM map indicated a very good agreement between the model and the map, except for the NEAT3 domains (Figure 56). Indeed, these two domains, which are responsible for heme extraction in IsdH, were reported by Mikkelsen and co-workers to have higher B-factor compared to the rest of the hemophore molecules and to be positioned a little far from the Hb heme cavity.

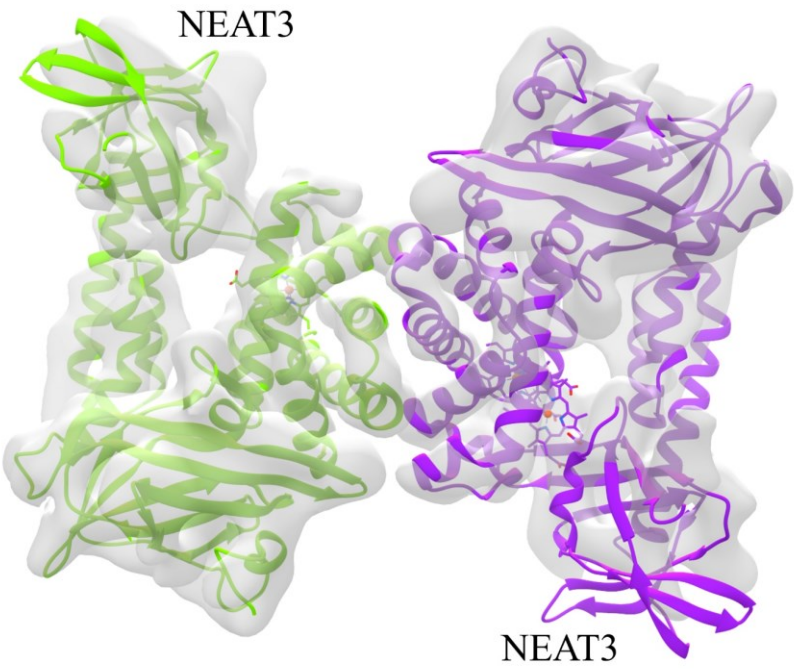

Figure 56: Fitting of 6TB2 model (where β-chain of Hp has been removed) inside cryo-EM density map. α-Hb chain and IsdH bound to it are green, whereas β-Hb chain and the bound IsdH are purple.

The authors of the 6TB2 structure speculated that Hp-stabilized F helices played a key role in limiting the IsdH-metHb complex formation and thus the heme extraction, principally being responsible for the incorrect NEAT3 positioning. Indeed, F helix disruption was indicated as a key step by Bowden and co-workers in 2018 [224]. Taken together, these evidences make it clear that readaptation of Hb structure is needed to fully accommodate hemophore binding and to allow the following extraction.

Structural insights on F helix were difficult to obtain from the cryo-EM derived atomic model. In fact, the model was refined starting from an *ad hoc* model where both the F helices were in their normal position because they were derived from a high-resolution structure of an uncomplexed metHb. Moreover, the cryo-EM volume density was not completely defined in the region corresponding to F helices, impeding Namdinator to precisely refine the atomic model used as input.

Therefore, three-dimensional structure of IsdB bound to Hb (5VMM) [224] has been considered, principally because it is the only structure where heme is removed from the Hb binding pocket and F helices appear severed.

5VMM presents one Hb tetramer bound by two IsdB molecules on the α-Hb chains and two proteolyzed IsdB molecules bound to the β-Hb subunits. Comparison of fitted model is reported in Figure 57 and F helix has been highlighted for better visualization.

The α-Hb chain of the cryo-EM model fits sufficiently well the density map and only a small final part of the helix appears unfolded in the volume density. On the contrary, F helix of α-Hb inside the 5VMM model is completely unfolded and thus it does not describe the map well. Looking at the β-Hb chains, the lack of density near to the F helix in the cryo-EM map is consistent with the crystallographic lack observed by Bowden and co-workers, thus it is possible to speculate that this Hb portion is highly flexible or completely unstructured when the hemophore interacts with it.

The cryo-EM model represents the complex where the hemophore efficiently extracts the heme, the same situation is possibly represented by β-chain part of 5VMM structure, in fact the authors were not able to find electron density of the heme in the crystal and they speculated that IsdB extracted the cofactor and then it underwent proteolysis. Differently the heme extraction is not terminated on the α-Hb chain of the 5VMM structure. On one hand, it is possible to speculate that the β-chain F helix unfolds during the heme extraction and remains unfolded after the process. On the other hand, data suggests that the α-Hb chain can lose its α-helical content during the extraction process, but it folds again when the heme is completely transferred.

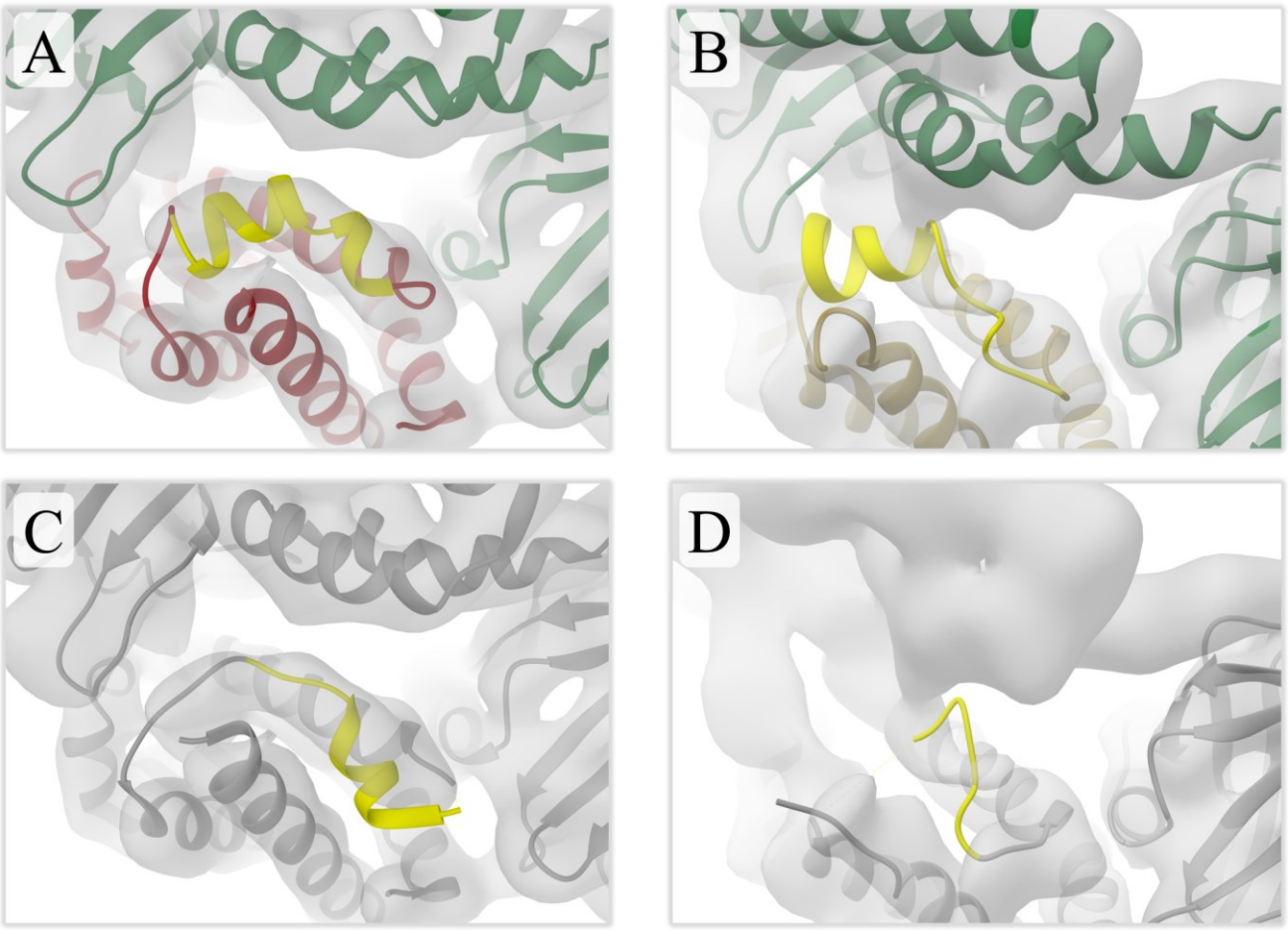

Figure 57: Fitting of cryo-EM atomic model adapted from Figure 54 (A and B) and IsdB-Hb complex structure (PDB 5VMM – C and D) inside the density map. Linker and NEAT2 domains are not present in (D) because they were not defined by 5VMM structure. IsdB binds α-Hb chains in (A) and (C) panels, whereas it binds β-Hb chains in (B) and (D) panels. F helix is highlighted in yellow in all four panels.

3.2.4.1 Heme transfer

A predicted model for the heme transfer was already proposed by Bowden and co-workers in 2018 [224], however they used the unbound structure of oxyHb (2DN1) as a starting point and assumed that 3RTL PDB (namely the holo-form of $IsdB^{N2}$ free in solution) represented the final step of the extraction. The solution of the atomic model of $IsdB^{N1LN2}$-COHb complex allowed us to have the snapshot of the first step of IsdB-Hb interaction. Moreover, the good agreement of $IsdB^{N1LN2}$-metHb complex map and 3RTL structure confirmed that the latter represents the final step of the process, when the extraction is concluded. Therefore, $IsdB^{N1LN2}$-COHb model and 3RTL structure have been exploited to reconstruct the heme transfer process. The bis-His intermediate (i.e., heme is coordinated by H(FG1) and H(E7)), present in 5VMM structure, has been used as a transition point within the heme transfer process (Figure 58B).

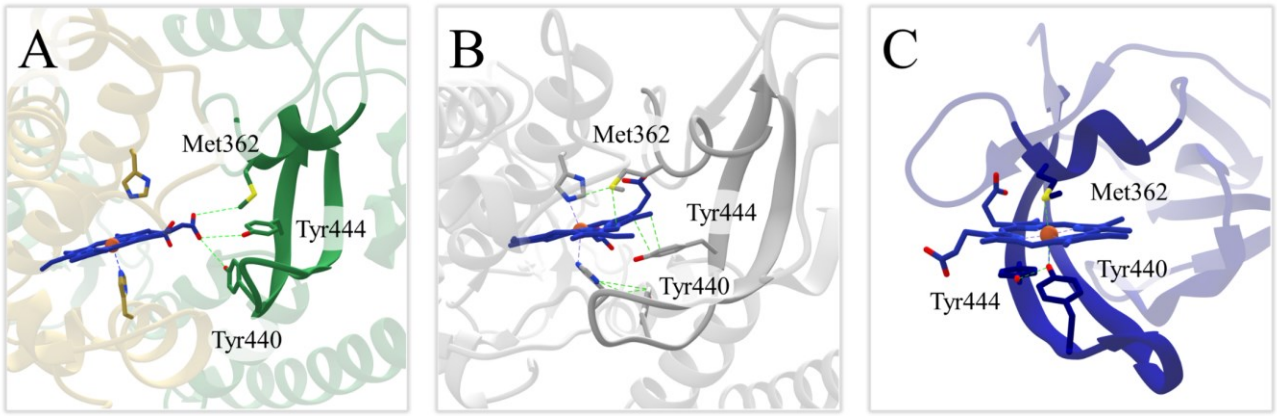

Figure 58: Model of heme extraction process. Three consecutive steps of heme transfer are depicted by (A) the cryo-EM refined model, where Hb is yellow and IsdB is green, (B) IsdB-Hb complex in 5VMM, where both Hb and IsdB are grey, and (C) holo-IsdB^{N2}, where IsdB is dark blue. Heme molecule is coloured blue within all three panels and its position is based on the alignment of IsdB^{N2} of the three models. Three IsdB key residues (M362, Y440, and Y444) are shown and labelled.

In the picture, the heme moves from the Hb binding pocket to IsdB binding pocket, and in the first stage heme propionates are located outside the Hb heme cavity, then they started to rotate (intermediate stage), and the final heme position ends with propionates looking outside of the IsdB heme pocket. To drive the heme transition M362, Y440 and Y444 directly interact with one heme propionate with the possible role of pulling the cofactor and starting to rotate it. In the second step M362 starts to pull the heme, whereas Y440 directly interacts with distal His. In fact, once the bis-His intermediate is formed, the limiting step may be the disruption of H(E7) interaction with the cofactor [375]. Finally, in the third step the heme is bound to IsdB. Notably the secondary structures shown in the lower part of Figure 58 undergo various changes. In the first stage the α-helix of IsdB is folded, it partially unfolds in the intermediate step, and it is reformed at the end. Conversely, the loop between the beta-strands stretches from the first to the second stage of heme transfer, but, when the IsdB-heme interaction is formed, it becomes totally rigid. This structural rearrangement signals the hemophore readaptation to accommodate heme transfer.

3.3 Investigation on the dimeric form of IsdB^{N1LN2}

During expression and purification of IsdB^{N1LN2}, the dimeric form of the hemophore was found to be part of the protein pool. Since the presence of the dimeric form of IsdB has never been reported in the literature, we began an investigation on its molecular properties. The first observation after the protein purification was that dimer is significantly more soluble, reaching concentrations higher than 1 mM while the monomer starts to precipitate at around 500 µM.

When analyzed through SDS-PAGE, monomer and dimer of IsdB^{N1LN2} have the same electrophoretic mobility, which is not affected by removal of β-mercaptoethanol from the sample buffer suggesting that the monomers were not covalently bound to each other within the dimer. Dimers were also found to bind a lower amount of heme after the purification.

The presence of an equilibrium between the two oligomerization states was investigated using the SEC column packed with BioSepra Ultrogel AcA on an AKTA Prime system (GE Healthcare). The same monomer-dimer mixture (40% of dimer and 60% of monomer) was incubated overnight at two different concentrations (20 and 200 µM) before loading them onto the column. The protein was diluted about 10-fold during the chromatographic run. Although the significantly different concentration and the long incubation were expected to lead to a different relative composition of monomer and dimer in the two solutions, the elution profiles of the samples were comparable (Figure 59A) suggesting that monomer and dimer were not equilibrating during the incubation.

Since monomeric IsdB^{N1LN2} binds a relatively higher heme fraction the effect of the cofactor on protein monomerization was investigated by incubating the purified dimer in the presence or in the absence of an equimolar concentration of heme overnight at 4 °C on the rotary mixer. After the incubation, the UV-visible absorption spectra of the sample incubated with heme presented a strong absorption band at 404 nm, the typical Soret band of heme-binding proteins, indicating that dimeric IsdB^{N1LN2} efficiently binds heme. Based on the molar extinction coefficient calculated for monomeric IsdB^{N1LN2}, 80% of the sample was saturated with heme. The samples were analyzed by SEC as previously described. In Figure 59B, the chromatogram indicates that heme binding to the hemophore did not favour protein monomerization.

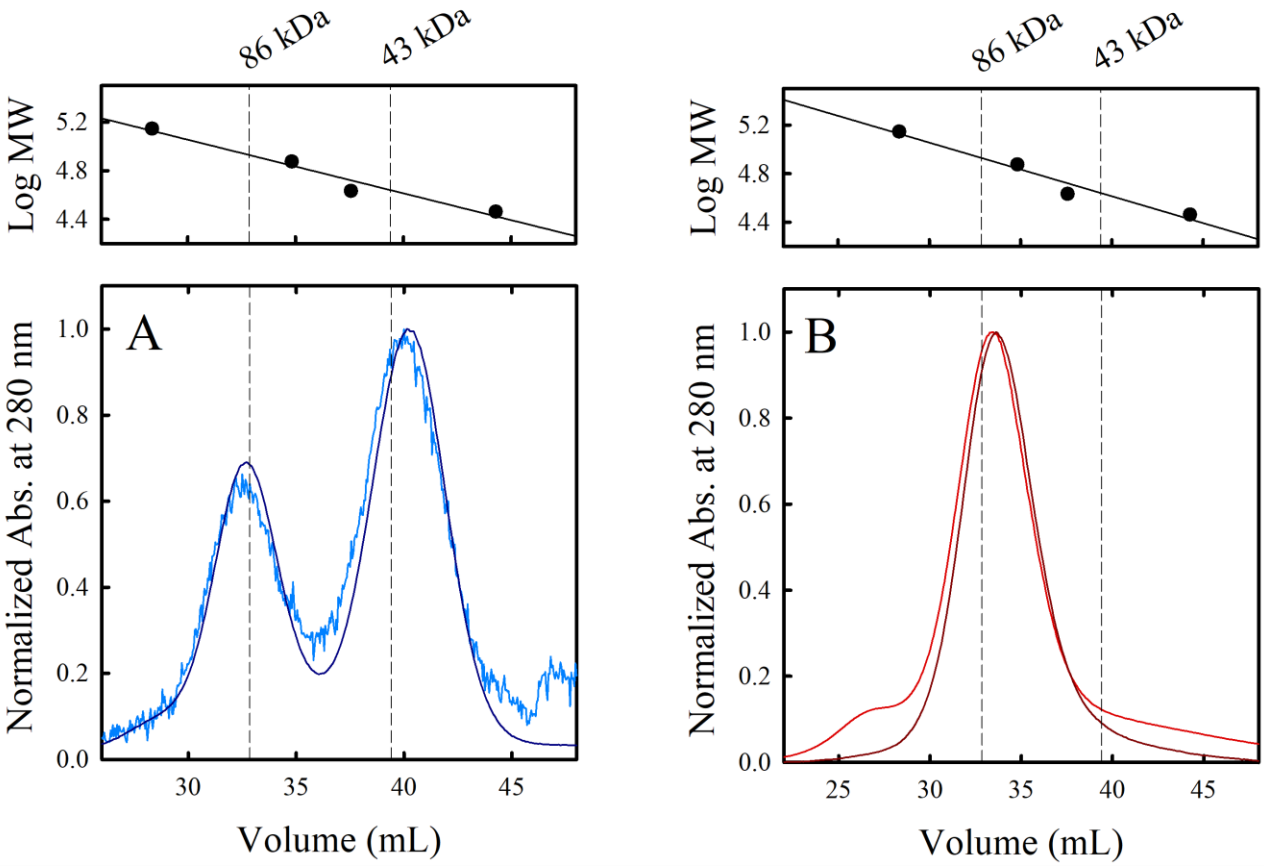

Figure 59: SEC analysis of mixtures of monomeric and dimeric IsdB^{N1LN2} at different concentrations. (A) Elution profile of monomer-dimer mixture at 20 µM (light blue) or at 200 µM (dark blue). (B) Elution profile of purified dimeric IsdB^{N1LN2} incubated overnight in the presence (red) or in the absence (dark red) of heme. Dashed line represents the theoretical retention volume of monomeric (43kDa) and dimeric (86 kDa) IsdB^{N1LN2}, which is estimated on the basis of the calibration curve (top panel).

Despite the amount of heme extracted from Hb is the same for the monomeric and dimeric forms of IsdB^{N1LN2} (data not shown), the kinetic analysis (Table 16), revealed that IsdB^{N1LN2} dimer extracts heme with an extremely lower rate with respect to the monomer.

Table 16: Comparison of observed rate constants of monomeric and dimeric IsdB^{N1LN2} obtained by fitting single-wavelength UV-visible kinetics with the modified bi-exponential equation.

	$k_{1,obs}$ (s^{-1})	$k_{2,obs}$ (s^{-1})
IsdB^{N1LN2} monomer	0.169 ± 0.001	0.0221 ± 0.0008
IsdB^{N1LN2} dimer	0.0201 ± 0.0001	0.0097 ±0.0001

To get structural insights on dimeric IsdB^{N1LN2}, its X-ray scattering profile was analyzed (Figure 60). SAXS profiles of different dilutions of the sample resulted comparable when normalized for the concentration of the protein, confirming the optimal subtraction of the baseline and the good quality of experimental data itself.

However, significant aggregation or sample heterogeneity were detected in:

(1) Log-Log plot: where SAXS intensity continued to increase even at very low angle, when it is expected to reach a plateau,

(2) Guinier analysis: where data resulted in a clear upturn at low q^2 values.

Unfortunately, the reported problems did not allow to obtain further molecular information on IsdB^{N1LN2} dimers. Since previous trials revealed that dimeric IsdB^{N1LN2} is soluble at the concentration and in the buffer used for SAXS experiments, the observed behaviour should not be attributed to extensive aggregation, but rather to a heterogeneity of species with relatively low molecular masses (monomers, dimers, and trimers, which can form at the high concentration used for X-ray scattering experiment).

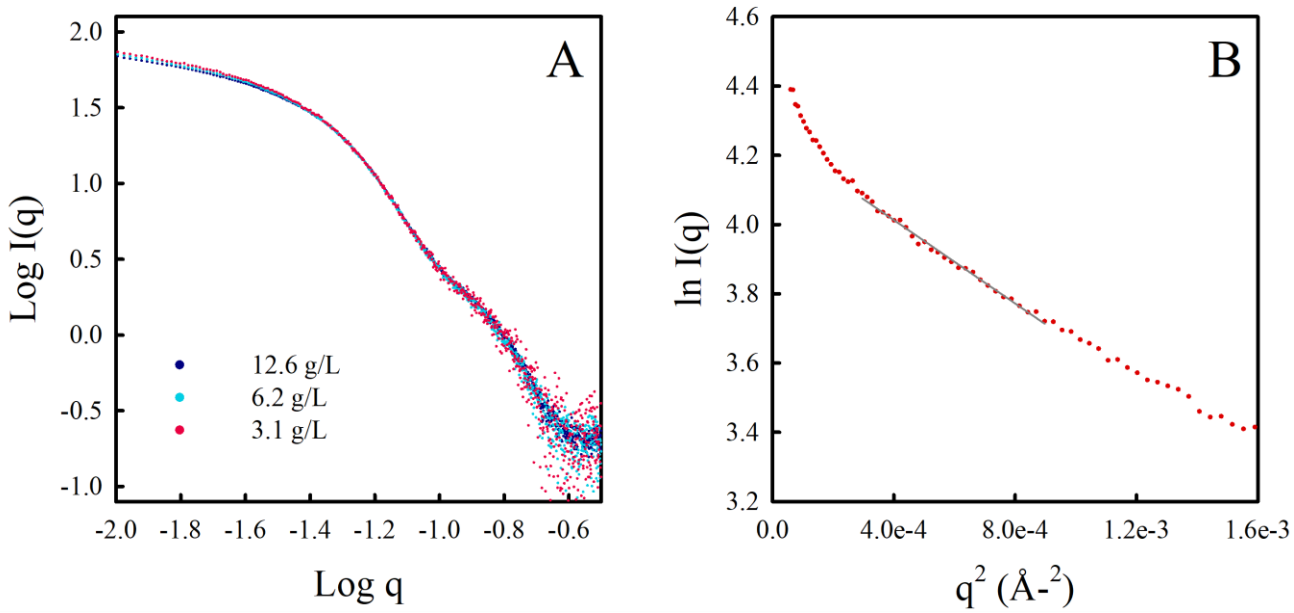

Figure 60: SAXS analysis of dimeric IsdB^{N1LN2}. (A) SAXS intensity (normalized by concentration) of different dilution of dimer IsdB^{N1LN2} samples in the Log I(q) – Log q representation. (B) Guinier plot of data at lower concentration (3.1 g/L). Experimental values are red, and fitting is grey.

Since the monomerization of the dimer was only observed during SDS-PAGE, i.e., under denaturing conditions, chemical denaturation with GndHCl was performed. After denaturation, the GndHCl removal was expected to lead to protein refolding. The main aim of the experiment

was to understand if the denatured IsdB^{N1LN2} dimer was refolding as a dimer again or as a monomer. To easily assess the presence of monomeric or dimeric IsdB^{N1LN2} in solution, the samples were analyzed by native PAGE in HEPES-imidazole buffer (see Chapter I). Denaturation and refolding of both IsdB^{N1LN2} monomer and dimer was performed. The monomer was used as a positive control, to assess if the hemophore was effectively refolding after denaturation. Three different concentrations of GndHCl were initially tested (1.4 M, 2.5 M and 5.5 M), but the lowest one was found to be enough to complete the denaturation. Fluorescence emission of Trp residues was exploited to follow denaturation and to assess the reaction completion after a 1- or 2-hours incubation. The emission spectra of IsdB^{N1LN2} in the absence or in the presence of 1.4 M GndHCl are reported in Figure 61A. The emission spectrum after one hour was comparable with the one after 2 hours, indicating that the denaturing reaction was already finished after the first time delay. With the aim to apply the gentler approach possible, 1-hour incubation was selected as the best condition. The optimized reaction was carried out on both monomeric and dimeric IsdB^{N1LN2}, the results in Figure 61B indicates that after the unfolding, both IsdB^{N1LN2} monomer and dimer refold into monomers.

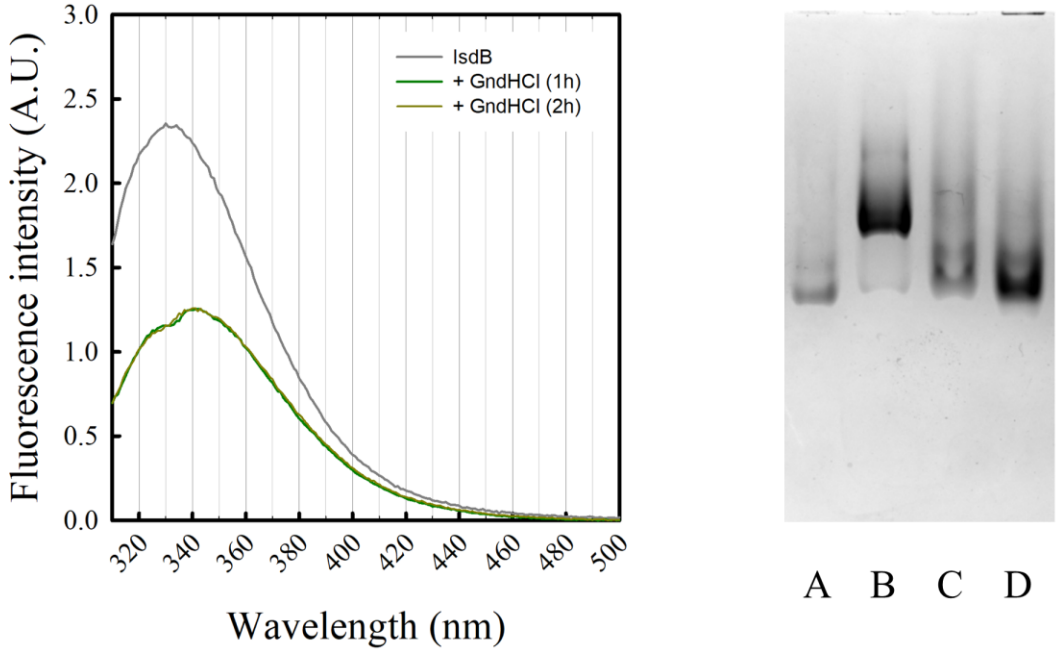

Figure 61: Chemical denaturation of IsdB^{N1LN2} with GndHCl. (A) Emission spectra for excitation at 298 nm of dimeric IsdB^{N1LN2} alone (dark grey), after one-hour incubation with 1.4 M GndHCl (dark green) and after two-hours incubation with the same denaturing agent (dark yellow). (B) Native PAGE to test IsdB^{N1LN2} unfolding or refolding. Lane 1 - monomer before the reaction, lane 2 - dimer before reaction, lane 3 - monomer after reaction, and lane 4 - dimer after reaction.

To summarize, $IsdB^{N1LN2}$ dimer is stable in solution, does not interconvert with the monomeric species down to 20 μM concentration and is not monomerizing unless upon denaturation and refolding. It is more soluble than the monomer, but it captures heme from Hb at a slower rate. A similar behaviour was reported for the *Serratia marcescens* HasA, which is a secreted hemophore that was found to form swapped domains dimers [379]. The monomer of HasA is formed by a single domain which shows an original α+β fold. The α-helices constitutes an atypical subdomain which sits in front of a subdomain formed by β-strands. The heme pocket is formed by two loops at the interface of the α- and β-parts of the molecule. Although both HasA and IsdB are hemophores, their tertiary structural rearrangement is completely different. Baiesi and co-workers defined swapped domains as "a mechanism through which two or more protein molecules form a dimer or higher oligomer by exchanging an identical structural element" [380]. HasA is a protein that acquires free or hemoprotein-bound heme and its swapped dimer has a lower affinity for heme, but it binds the right amount of cofactor. It is not able to pass the heme to following proteins in the pathway of bacterial heme acquisition, and thus is expected to have a heme reservoir function. The dimer is produced in different amounts depending on yet undefined bacterial culture conditions. Monomerization of swapped domain dimer is achieved with thermal or chemical denaturation. Most of the properties of dimeric HasA were also observed for dimeric $IsdB^{N1LN2}$, therefore a more detailed analysis of the latter is needed to confirm that IsdB can form swapped domain dimers and which is, if any, their physiological function. Swapped domains have been deeply studied in recent years as the multimerization of bacterial protein has been proposed to be favoured during protein evolution, giving structural and functional advantages, such as improved stability and control over the accessibility and specificity of colonization sites [381]. The structure, function and physiological relevance of this dimeric form will be the object of future investigations.

We planned to further investigate this aspect using FL-IsdB, which more closely represents the native protein. In case the formation of a dimeric IsdB is also confirmed with the full-length protein, we will undertake its structural and functional characterization to gain insight into the molecular and functional details of this assembly.

Chapter III – Optimization of a screening platform for the identification of PPI inhibitors of IsdB-Hb complex

1 Objectives

The previous chapter was focused on the biochemical and biophysical characterization of the complex between hHb and $IsdB^{N1LN2}$. In this chapter an optimized ELISA is presented as a screening platform for molecules aimed to interfere with complex formation.
In fact, IsdB has been indicated by various *in vivo* studies to be essential for staphylococcal pathogenesis, and its PPI with hHb enables iron acquisition, which is fundamental for bacterial proliferation. These experimental evidences and the MRSA threat make IsdB a suitable target to develop new antimicrobial agents.

The *in silico* screening campaign to select molecules tested through the optimized ELISA was performed by the research group of Prof.ssa Francesca Spyrakis (Università di Torino). Precise *ad hoc* molecular descriptors were used to pick molecules for their capacity to remain in the blood vessels and not pass cell membranes. The final goal was to select molecules that bind free Hb in the plasma, in order (1) not to interfere with Hb function inside the RBCs and (2) to avoid being scavenged by the intracellular Hb. Then, structure-based virtual screening and molecular docking were used to predict the binding to Hb on a surface cavity that is involved in complex formation (Figure 62), indeed molecules were intended to compete directly with hemophores binding to Hb.

The identified PPI inhibitors might in principle find application as first-in-class antimicrobials, cutting down the iron supply. Moreover, binding to Hb will make bacterial target mutations less relevant for development of resistance and will possibly interfere with the interaction of several hemophore systems, starting with IsdB and IsdH.
Notably, the functional and/or regulatory differences between IsdB and IsdH are still not fully understood, but their mechanism of heme acquisition from Hb seems comparable. Therefore, the presented screening platform could be easily adapted for assessing the effect of selected molecules on IsdH-Hb complex formation, with the aim of finding promising compounds active on both *S. aureus* Hb receptors.

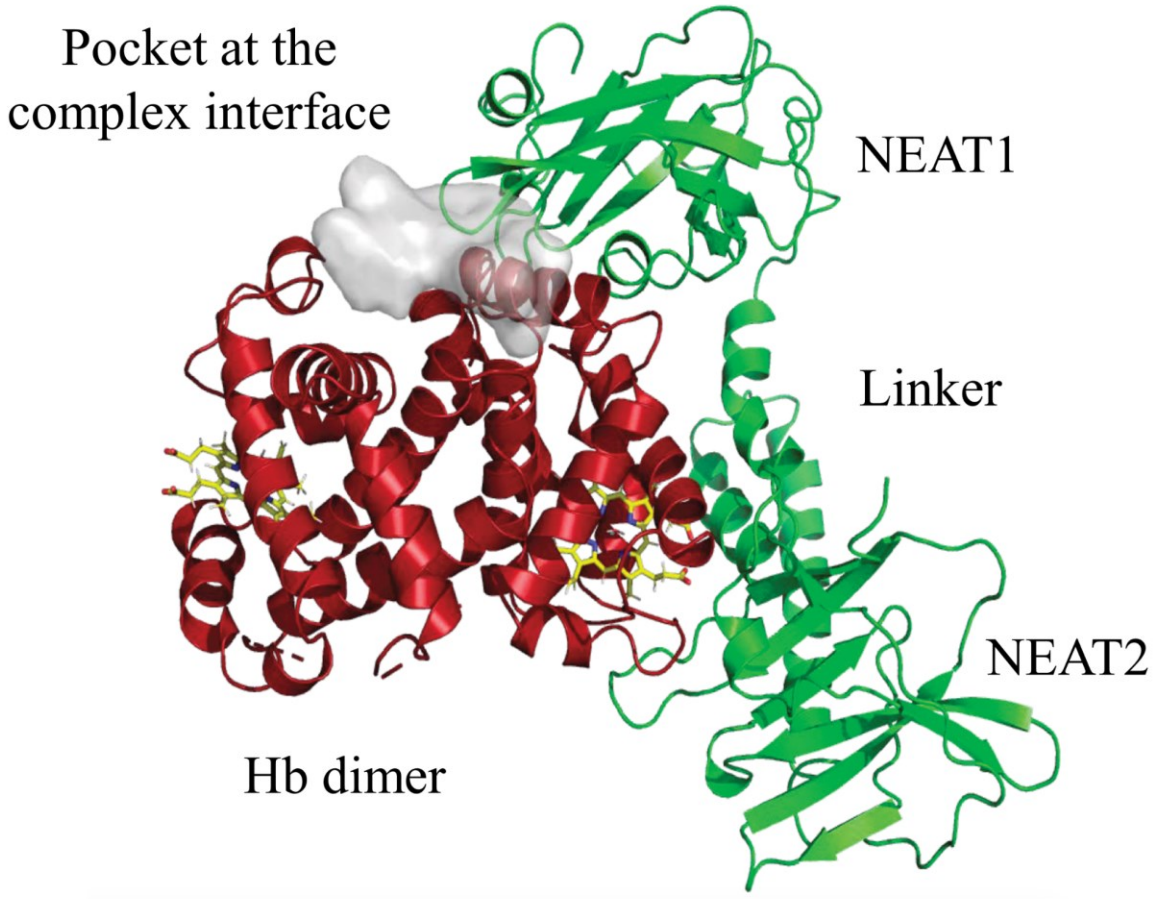

Figure 62: Representation of the pocket selected for inhibitors identification at the IsdB-Hb complex interface (courtesy of Prof.ssa Spyrakis, Università di Torino).

2 Materials and Methods

All reagents, if not otherwise specified, were obtained from Sigma Aldrich (St. Louis, MO, USA) at the best commercial quality available, and used as-received.

2.1 Samples preparation and compounds solubilization

IsdB^{N1LN2} and its variants, Hb, and semiHbs samples were prepared as described in chapter I, whereas small molecules under investigation were purchased from commercial suppliers (Enamine Ltd., Specs, and Vitas-M Laboratory, Ltd.) or synthesized by Prof.ssa Loretta Lazzarato, Università di Torino. The compounds were solubilized in aqueous solutions, taking advantage of the pH- and concentration-solubility profile estimated by Chemicalize (https://chemicalize.com/ developed by ChemAxon (http://www.chemaxon.com)), and DMSO was used only when needed (vide infra). Absorption spectra of solubilized compounds alone or in the presence of oxyHb were recorded with a microplate reader (TECAN Spark® 10M) in a 384-well, UV-transparent microplate (Greiner UV-STAR® plate – 781801). The spectra of oxyHb in the presence of purchased compounds were exploited to assess the potential oxidizing activity of small molecules on the protein. In fact, Hb Q bands are highly sensitive to the redox state of the heme bound to Hb (Figure 63) therefore, they were selected as a marker of the Hb oxidation, and the peak at 640 nm, which is characteristic for the oxidized form of Hb, was principally used for the analysis.

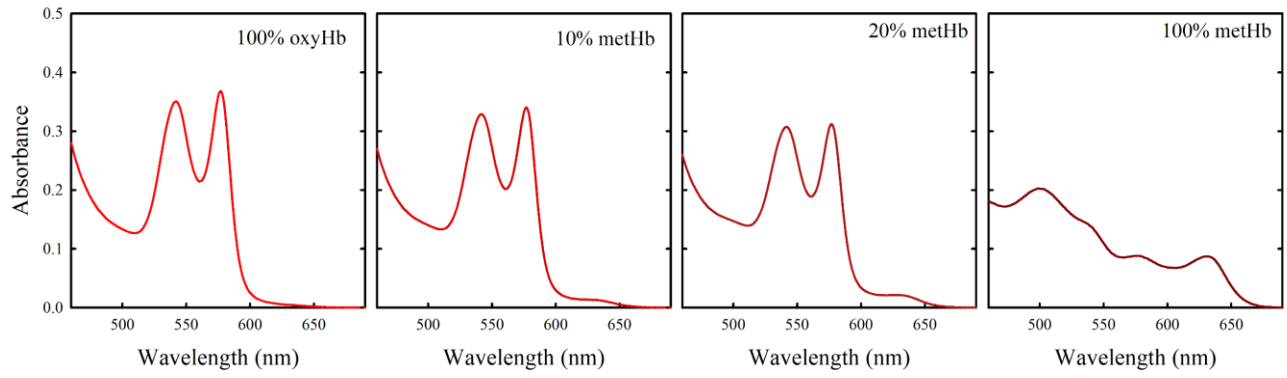

Figure 63: Spectroscopic analysis of Hb. Q-bands of pure oxyHb or metHb, and linear combinations of spectra corresponding to the two forms (e.g., 10% of metHb and 90% of oxyHb, or 20% of metHb and 80% of oxyHb).

2.2 ELISA setup optimization

Since IsdB efficiently binds oxyHb, but it is not able to extract the cofactor from it, this reduced and ligated form of Hb was selected as a starting point for the ELISA optimization to directly evaluate complex formation without artefacts coming from heme extraction that could eventually lead to complex dissociation. OxyHb will be generally indicated as Hb in this chapter, whereas metHb will be made explicit when necessary.

$IsdB^{N1LN2}$ or its variants are bound to the bottom of a 96-well plate and Hb binding is detected by a horseradish peroxidase (HRP)-coupled anti-Hb polyclonal antibody (Ab, Abcam ab19362) (Figure 64).

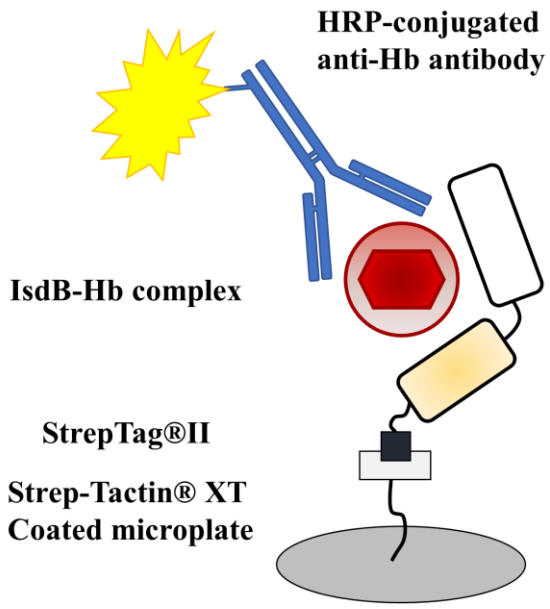

Figure 64: Schematic representation of the ELISA set-up.

The hemophore was immobilized on commercial Strep-Tactin® XT coated microplates (IBA Lifesciences) exploiting the C-terminal StrepTag®II. The binding buffer (EDTA 2 mM, NaCl 140 mM, and Tris/HCl 25 mM pH 7.6) was used throughout all the assay as suggested by the microplate manufacturer, whereas 3,3′,5,5′-tetramethylbenzidine (TMB, Acros Organics 328051000) was the substrate for the HRP reaction. This enzyme catalyses the conversion of TMB into a coloured, soluble product. To achieve a standardized result, the reaction was stopped after a defined time delay with 1 N H_2SO_4 solution. Absorption of HRP reaction product was recorded at 450 nm with a microplate reader (Dynamica Halo LED 96), and background values from TMB solutions were subtracted from each reading.

The protocol was optimized following the manufacturer's instructions.

(1) plate incubation with 200 µL of StrepTag®II-IsdB^{N1LN2} solution (or its variants solution),
(2) plate washing with 200 µL of washing buffer solution (0.05% Tween-20 in binding buffer) – repeated 3 times,
(3) plate incubation with 200 µL of Hb solution,
(4) plate washing – repeated 3 times,
(5) incubation with 200 µL of the HRP-conjugated anti-Hb Ab solution,
(6) plate washing – repeated 3 times,
(7) addition of 100 µL of TMB followed by 1-minute incubation,
(8) quenching of the HRP reaction with 100 µL of H_2SO_4 solution,
(9) reading of the absorbance intensity at 450 nm.

Since the timing for the method was not indicated, overnight incubation for StrepTag®II-IsdB variants (WT or the mutants) was selected as it is a highly diluted solution [382], while one-hour incubation was chosen for intermediate incubation of Hb and Ab [383]. Therefore, short time incubation was chosen to avoid the undesired Hb oxidation, which is relatively fast when the protein is diluted in solution. This time schedule was used throughout all the reported experiments. All the incubation steps were performed at 4 °C in the dark, and the development of the HRP reaction was carried out at 4 °C, to slow down the reaction and avoid signal saturation.

2.3 High throughput screening of potential inhibitors of IsdB-Hb PPI

Since IsdB^{N1LN2} was confirmed to bind Hb with an extremely high affinity (vide infra), the binding deficient mutant, IsdB^{Y165A}, was used to increase the sensitivity of the screening towards the first batch of potential inhibitors identified that are likely to be weak and unable to dissociate the IsdB^{N1LN2}-Hb complex. The IsdB^{Y165A} binding to Hb was assessed in the presence or the absence of the investigated molecules, and the presence of a potential inhibitor was expected to reduce the amount of bound Hb, basically increasing the dissociation constant of the complex. Commercial compounds were tested at 1 mM concentration, whereas Hb was kept at 30 µM, which corresponds to the dissociation constant of the complex between

IsdB^{Y165A} mutant and Hb. Working close to the K_D of the complex was assumed to maximize the absorbance at 450 nm variation in case of a molecule was interfering with the PPI. Since investigated molecules were expected to bind Hb, the solutions containing Hb and each potential inhibitor were incubated one hour before assessing the IsdB^{Y165A} biding through the optimized ELISA.

The protocol for the PPI inhibitors screening was:

(1) over-night incubation of 2 pmol IsdB^{Y165A} (200 µL/well),
(2) three steps of microplate washing with 200 µL/well of washing buffer,
(3) 1-hour incubation of 200 µL/well Hb-potential inhibitor solution:
    a. Hb was pre-incubated with the potential inhibitor for 1 hour at 4 °C in the dark before addition to the well
(4) three steps of microplate washing with 200 µL/well of washing buffer,
(5) 1-hour incubation of anti-Hb Ab at 1:1,000 dilution (200 µL/well),
(6) three steps of microplate washing with 200 µL/well of washing buffer,
(7) development of HRP reaction with 100 µL/well TMB solution for 1 minute at 4 °C, and quenching with 100µL/well of 1N H_2SO_4 solution,
(8) reading of the absorbance intensity at 450 nm.

3 Results and Discussion

3.1 Validation of the method

The optimization of the ELISA was aimed to obtain a platform for the high-throughput screening of small molecules that target IsdB-Hb complex formation. Firstly, the concentration of IsdB^{N1LN2}, Hb and Ab were optimized to have a high but not saturating signal. Then, the dissociation constants for IsdB-Hb complexes obtained using different variants of Hb and IsdB^{N1LN2} were calculated. Finally, the *in silico* identified PPIs inhibitors were tested for their ability to interfere with the complex formation.

The development of a specific signal that reports of IsdB^{N1LN2}-Hb complex formation was assessed on wells incubated with 8 pmol IsdB^{N1LN2} (4-fold excess of the indicated binding limit of the microplate's well). 50 nM Hb was added (which is the reported K_D from the literature

[245]) and a 1:10,000 diluted Ab solution was used for detection (the lower concentration suggested by the seller) (Figure 65). An absorbance signal developed that was specific for $IsdB^{N1LN2}$-Hb complex and did not develop in the absence of either $IsdB^{N1LN2}$ or $IsdB^{N1LN2}$ and Hb. This result also confirmed the absence of any non-specific binding of either Hb or Ab to the plate.

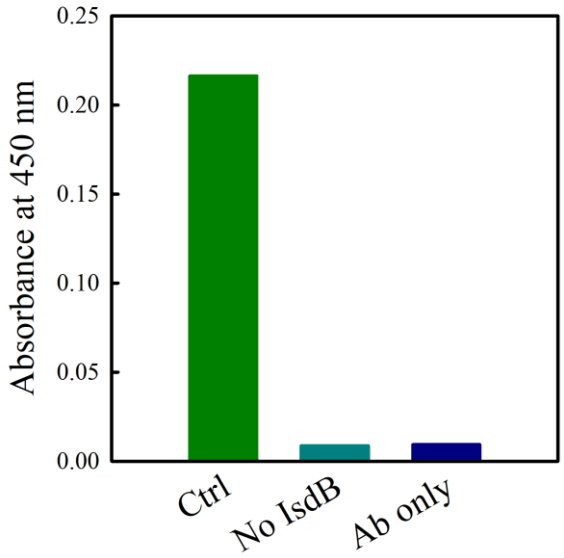

Figure 65: Assessment of non-specific binding during ELISA validation. The positive control contains all the reagents ($IsdB^{N1LN2}$, Hb and Ab); the negative control does not contain $IsdB^{N1LN2}$ (No IsdB). Ab does not bind aspecifically to the plate as demonstrated by the well where both $IsdB^{N1LN2}$ and Hb were omitted from the assay (Ab only).

Once confirmed that single reagents did not produce non-specific signals, the effect of increasing concentration of $IsdB^{N1LN2}$ and Ab was tested (Figure 66). To test increasing concentrations of the hemophore, Hb was kept at 50 nM concentration and Ab was diluted 1:10,000. The result indicated that 8 pmol of $IsdB^{N1LN2}$ was not enough to entirely cover all the binding sites of the well, and a 4-fold increase of the signal was obtained by increasing the concentration of the hemophore from 8 to 80 pmol.

The dependence of the absorbance at 450 nm on $IsdB^{N1LN2}$ concentration was a useful indication in case there was a need of increasing the limit of detection of the assay, but it was not expected to change the global result of the analysis. Conversely, it was necessary to confirm that Ab was enough to detect all the bound Hb otherwise, the absorbance at 450 nm would not be representative of the amount of complex formed inside the well. To increase as much as possible the complex attached to the microplate, 80 pmol of $IsdB^{N1LN2}$ were immobilized on

the microplate, and, in the next step, 1 µM Hb solution was incubated to saturate all IsdB^{N1LN2} present on the bottom of the well. This concentration was proved to be saturating when the dissociation constant for IsdB^{N1LN2}-Hb complex was calculated (vide infra). Ab dilutions ranging from 1:5,000 to 1:500 resulted in comparable signals, whereas the 1:10,000 dilution underestimated the amount of bound Hb. Therefore the 1:1,000 dilution was chosen for the following experiments.

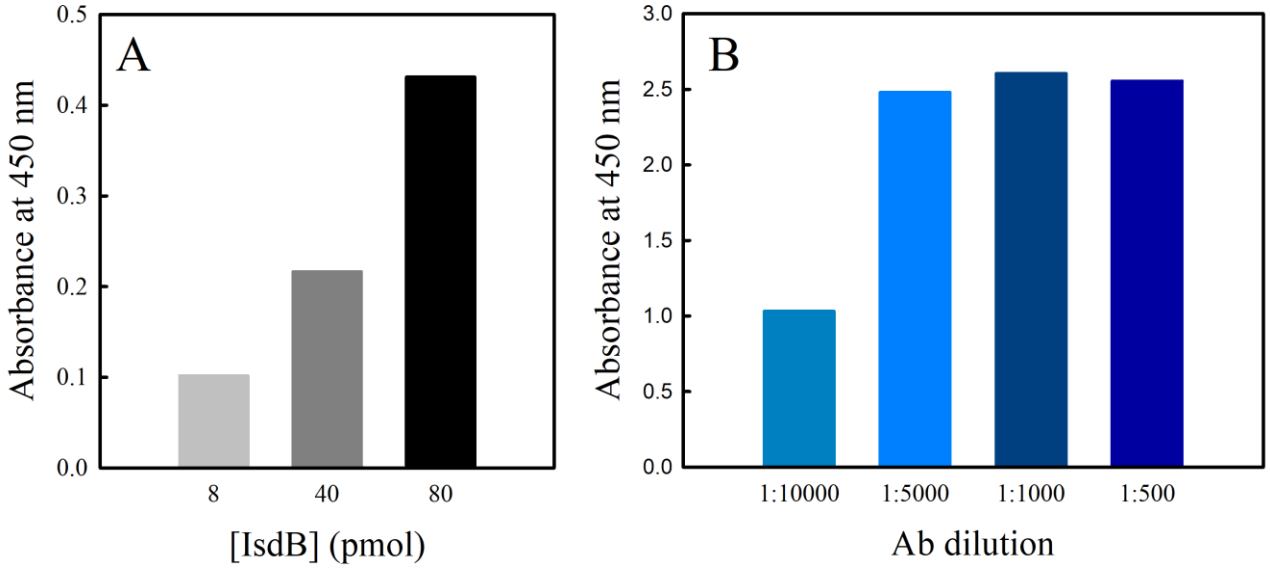

Figure 66: Absorbance at 450 nm plotted (A) as a function of IsdB^{N1LN2} quantity, and (B) as a function of Ab dilution.

Finally, to prove the reproducibility of the assay, a technical triplicate was performed together with the analysis of the effect of a different number of plate washing (Figure 67). Ideally, increasing the number of washing steps will help in removing non-specific binder, but if one of the reagents is not tightly bound to the system, it will be washed-out. For this analysis, 100 nM Hb was incubated on a plate functionalized with 80 pmol of IsdB^{N1LN2}. The complex detection was then carried out with 1:1,000 dilution of Ab. The three replicates clearly indicated a good reproducibility, with a standard deviation smaller than 5%.

To test the effect of the washing four experiments were conducted:

(1) washing the microplate six times after IsdB^{N1LN2} incubation, and three times after the other incubations,

(2) washing the microplate six times after Hb incubation, and three times after the other incubations,

(3) washing the microplate six times after Ab incubation, and three times after the other incubations,

(4) washing the microplate six times after every step of the assay.

From this last set of experiments, it resulted that increasing the washing steps did not greatly reduce the signal, which was expected if non-specific binders were still contaminating the microplate. It rather appeared that the binding of each reagent was mildly affected by the increased number of washing steps. Therefore, it was confirmed that three washing steps were the optimal solutions for thoroughly cleaning the well and not washing out reagents.

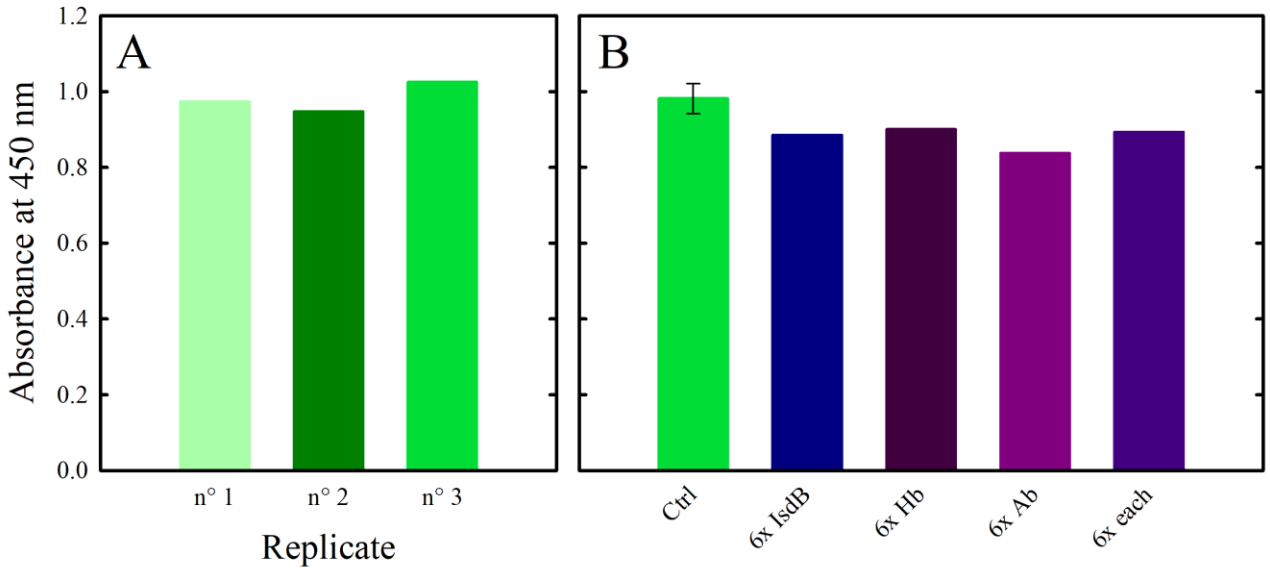

Figure 67: (A) Absorbance at 450 nm of three technical replicates. (B) Absorption signal at 450 nm of different assays where the number of washing steps was changed as described in the main text. "Ctrl" is the averaged value of the three technical replicates shown in (A).

Comparison of data reported in Figure 66B and 67A, where the same amount of IsdB^{N1LN2} and Ab were used while Hb concentration varied 10-fold indicates that signal saturates at 2.5 OD thus in the following experiments, the amount of IsdB^{N1LN2} bound to the well was reduced to avoid signal saturation.

3.2 Characterization of the IsdB-Hb complex

The complex formation between IsdB and Hb was characterized by exploiting the developed ELISA (Figure 68). Increasing concentrations of either Hb or metHb were analyzed on microplates systematically functionalized with 2 pmol of the hemophore.

The concentration of the incubated hemophore was ultimately chosen since it ensured the best dynamic range of the absorption signal at 450 nm, enabling to detect the complex formation when Hb solution was extremely diluted (nM range) and avoiding the saturation of the absorbance detector when Hb was at the highest concentration (mM range). Ab was always kept at 1:1,000 dilution, which was demonstrated to be ideal to detect the whole amount of formed $IsdB^{N1LN2}$-Hb complex, even when $IsdB^{N1LN2}$ was incubated at 400 nM concentration. For each Hb concentration, duplicate measurements were performed, and the resulting binding curves were fitted with a one-site binding isotherm:

$$S = \frac{S_{max} \times [Hb]}{K_D + [Hb]}$$

where S is the absorbance at 450 nm, S_{max} is the maximum signal that corresponds to the saturation of available hemophore immobilized to the well, [Hb] is the total concentration of Hb, and K_D is the dissociation constant for IsdB-Hb complex.

For the characterization of IsdB-Hb PPI several variants of both proteins were used, but the complex between $IsdB^{N1LN2}$ and Hb (meaning reduced oxygenated Hb) was used as a reference. Other than Hb, the ELISA was also exploited to evaluate the interaction between $IsdB^{N1LN2}$ with metHb, and semiHbs (both semi(α) and semi(β)). The interaction between $IsdB^{N1LN2}$ and metHb was expected to be potentially complicated to analyse, due to the irreversible heme extraction step. Moreover, structural analysis of $IsdB^{N1LN2}$-metHb complex (SAXS and cryo-EM) clearly indicated that metHb dimerizes within the complex, and this structural rearrangement might lead to a non-specific loss of Hb during the ELISA execution. In addition to $IsdB^{N1LN2}$-Hb complex, also the complexes with semiHbs and Y165A/Y440A variants were investigated to further validate the assay and to explore the range of its potential applications.

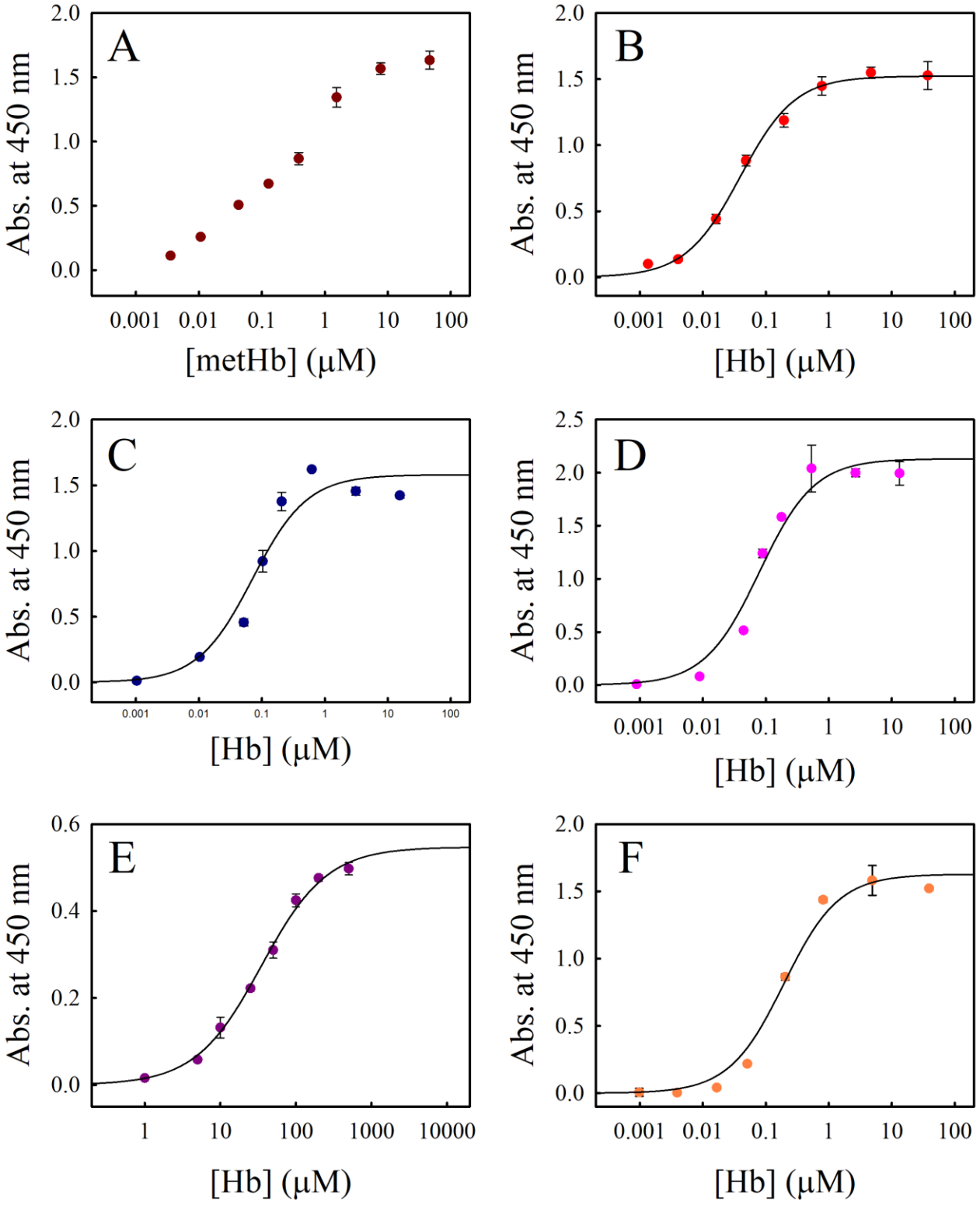

Figure 68: Dependence of the absorbance at 450 nm on Hb concentration. The first four plots represent the complex formation between IsdB^{N1LN2} and (A) metHb, (B) Hb (C) semi(α)Hb, and (D) semi(β)Hb. The analysis of the complex formation between IsdB^{Y165A} or IsdB^{Y440A} and Hb are reported in plots E and F, respectively. Dots are experimental data (error bars are frequently very low and appear smaller than data points). The black lines are the fitting with the isothermal equation.

For most of the analysis, the concentration-dependence of the signal was well fitted by the isothermal equation, and thus the K_Ds were calculated (Table 17). However, the signal registered when increasing concentration of metHb was used did not follow the expected hyperbolic trend, and thus it was not possible to calculate the dissociation constants. As expected, the ability of IsdB in extracting heme from metHb and subsequent formation of apo-Hb may have led to an increased complexity of the system and to artefacts that appear particularly relevant for low Hb concentrations. .

Table 17: Summary of dissociation constants calculated by the ELISA, and the comparison of the latter with the results from SPR (presented in Chapter II).

	ELISA K_D (SPR K_D) (nM)
$IsdB^{N1LN2}$-oxyHb	39±4 (102±3)
$IsdB^{N1LN2}$-semi(α)oxyHb	71±22 (44±2)
$IsdB^{N1LN2}$-semi(β)oxyHb	79±18 (26±1)
$IsdB^{Y165A}$-oxyHb	34.8 $x10^3$±2.9 $x10^3$
$IsdB^{Y440A}$-oxyHb	193±40 (124±10)

The overall good agreement between ELISA and SPR, albeit with some discrepancies that might originate from the different methods used, validate the optimized method. Moreover, the analysis of the calculated dissociation constants reveals a loss in affinity of the two $IsdB^{N1LN2}$ mutants. The comparable K_Ds for $IsdB^{N1LN2}$ binding to both Hb and semiHbs confirmed once again the ability of IsdB in interacting with α- and β-chains of Hb (as already indicated by SPR, SAXS and cryo-EM results).

Moreover, a 1,000-fold increase in the dissociation constant of $IsdB^{Y165A}$ mutant was calculated and it confirmed the essentiality of the mutated tyrosine residue for the complex formation, which was proposed by Pishchany and co-workers [238,294]. The calculated K_D clearly quantifies this loss in affinity for the first time, which is quite large for a single-point mutation. However, in addition to the energetic contribution of non-covalent interactions established between Tyr165 and Hb residues (e.g., one hydrogen bond, one polar contact, one π-stacking and several hydrophobic interactions - calculated through mCSM-PPI2 online platform [384]), which ideally accounts for most of the loss in affinity due to the mutation, the

role played by the residue in forming an α-helical turn upon binding Hb (Figure 69) might contribute to the free energy of binding. Taken together, the effect of the single-point mutation on direct binding, and the supposed detrimental effect of the mutation on the α-helix turn formation might explain the observed loss in affinity.

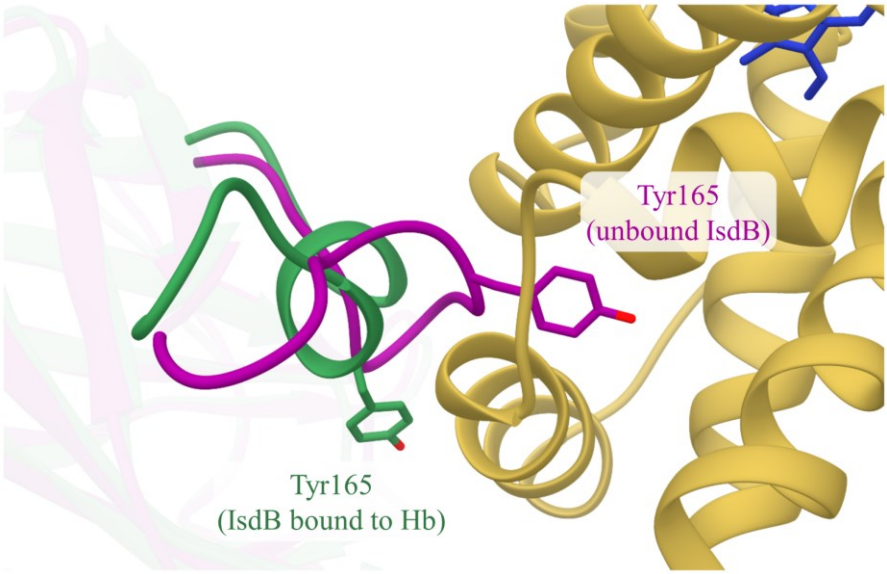

Figure 69: IsdB^{N1} folding upon binding. In the picture, β-Hb (yellow) and IsdB^{N1LN2} (green) were extracted from cryo-EM structure presented in the thesis, while isolated IsdB^{N1} (purple) was taken from the published NMR structure (PDB 2MOQ). Entire structure of Hb-bound or isolated hemophore are semi-transparent, while the region involved in folding upon binding is fully visible, together with Hb molecule. In the picture, Y165 residues are shown.

Since the amounts of IsdB, Hb and Ab selected to evaluate the dissociation constant for various IsdB-Hb resulted sensitive to the amount of formed, the validated method was considered suitable for the planned screening of potential PPI inhibitors.

3.3 Screening of potential inhibitors

The optimized ELISA was used to test the inhibitory activity towards the IsdB-Hb complex formation of the fifty-five small molecules identify by Spyrakis' group (Università di Torino). The molecules were purchased from commercial suppliers as a lyophilized powder, thus their solubilization and spectroscopical characterization were performed before testing their ability in interfering with the PPI. The fifty-five compounds were delivered and analyzed in two tranches. Therefore, the analysis of the second batch was also optimized based on technical

indications derived from the analysis of the first batch. Compounds belonging to the first batch were purchased from two commercial suppliers, Specs, and Vitas-M Laboratory, Ltd, and a serial number was assigned to them to protect the intellectual property behind their discovery. Molecules were solubilized in Milli-Q water to reach a 50 mM concentration. When the molecules resulted partially or completely insoluble after the addition of the solvent, the pH was adjusted based on their estimated pH-solubility profiles; DMSO was added only when needed. Table 18 presents the properties of the molecules and the final concentration of their stock solutions.

*Table 18: First batch of tested compounds. * DMSO at a final concentration of 50% was used to obtain complete solubilization.*

ID	MW (Da)	LogP	[stock] (mM)	ID	MW (Da)	LogP	[stock] (mM)
C01	212	0.04	50	C16	244	-0.97	50
C02	338	-2.17	19	C17	294	-1.394	25*
C03	286	-1.39	50	C18	518	2.273	25*
C04	246	-1	50	C19	303	1.42	50
C05	236	1.29	50	C20	402	0.239	50
C06	441	-2	49.5	C21	480	-0.094	50
C07	277	-1.39	50	C22	480	0.166	50
C08	426	0.01	50	C23	390	1.209	50
C09	344	-1.38	50	C24	463	0.17	50
C10	316	0.01	50	C25	470	-1.035	50
C11	281	-0.35	50	C26	331	1.696	51
C12	479	-1.55	50	C27	273	-1.387	50
C13	488	3.55	50	C28	649	0.691	25*
C14	357	0.82	50	C29	344	2.522	50
C15	268	-0.02	50	C30	403	1.088	50

The stock solution of each compound was diluted in binding buffer to reach a final concentration of 1 mM, used for the screening. It was checked and confirmed that the presence of the compound did not change the pH at the screening concentration, moreover, diluted solutions were used to spectroscopically characterize the solubilized molecules (Figure 70).

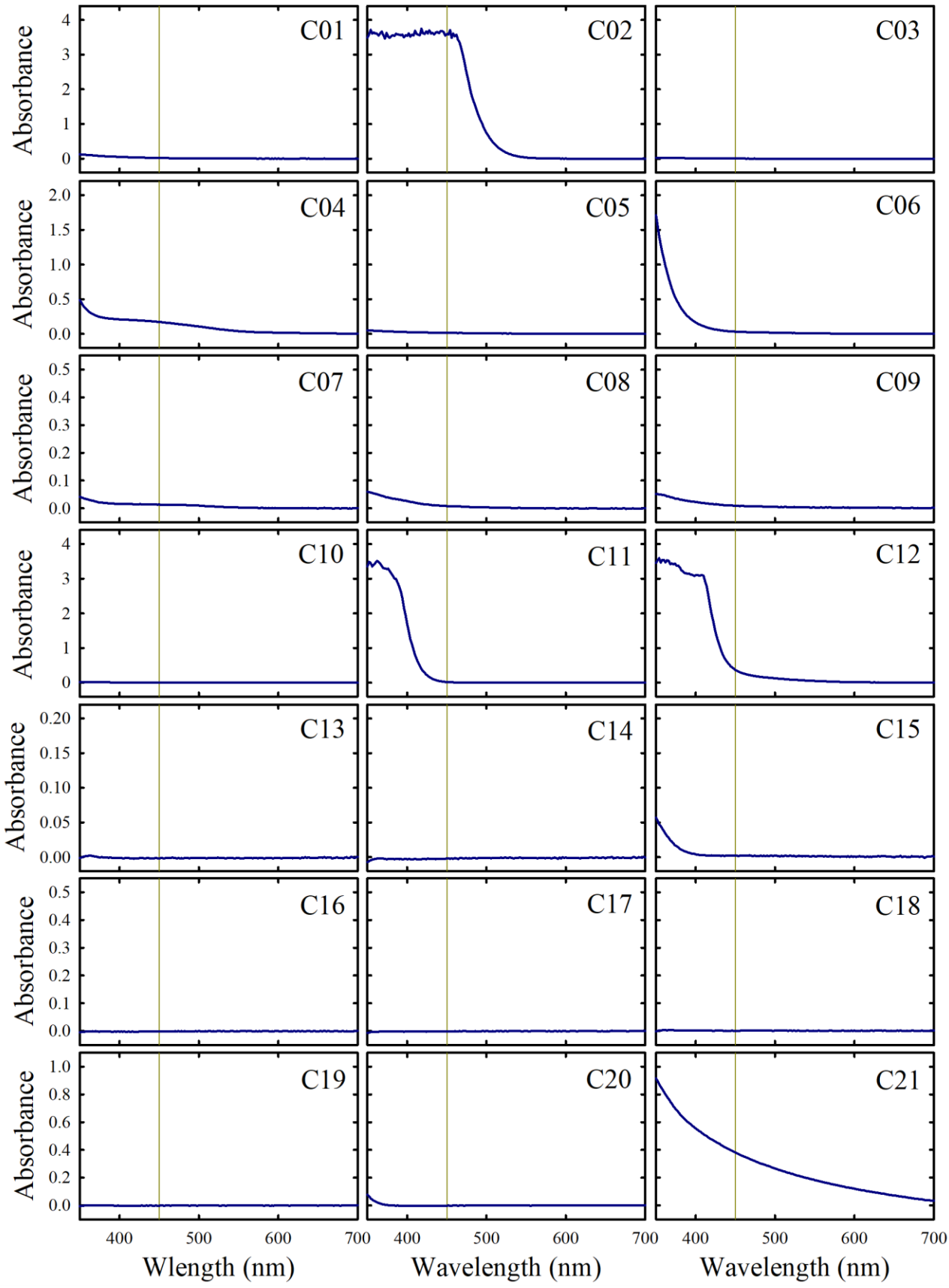
C01
C02
C03
C04
C05
C06
C07
C08
C09
C10
C11
C12
C13
C14
C15
C16
C17
C18
C19
C20
C21
Absorbance
Wlength (nm)
Wavelength (nm)
Wavelength (nm)

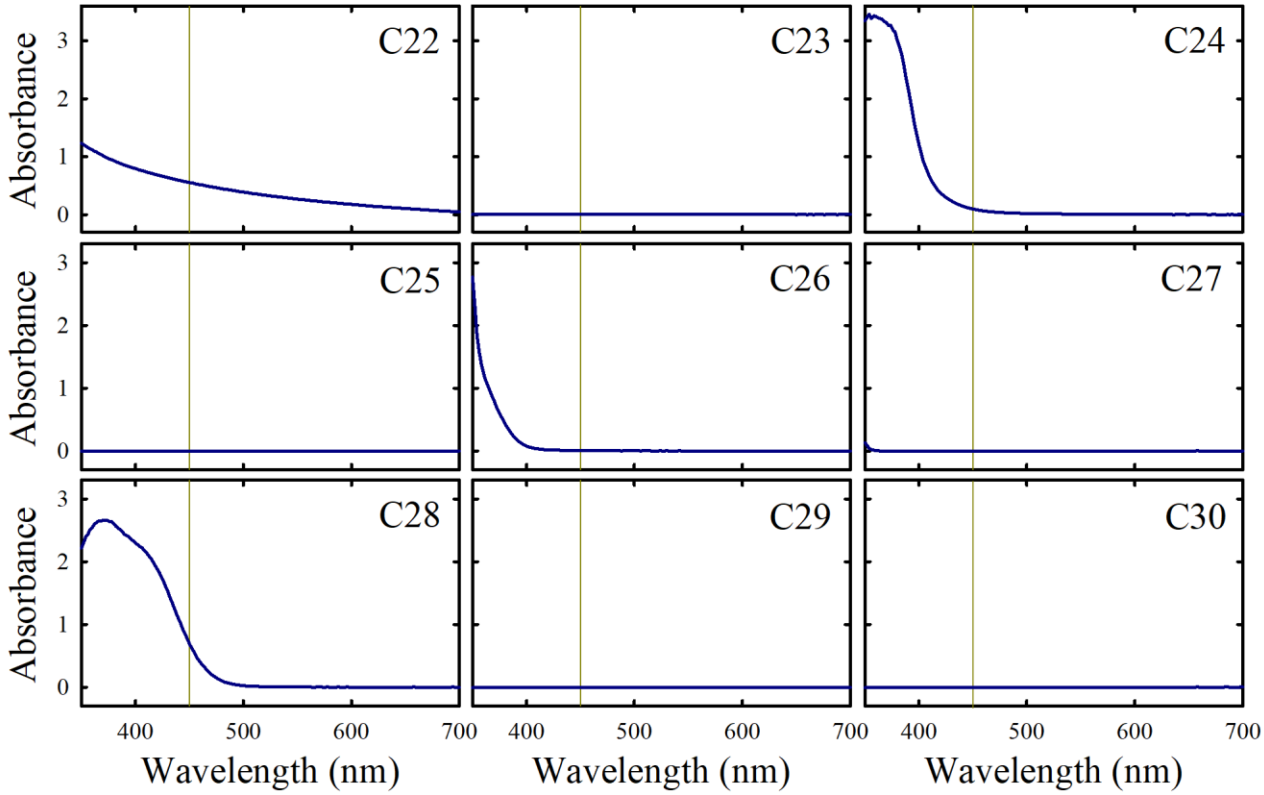

Figure 70: Visible spectra of the first batch of compounds at 1 mM concentration. The yellow line is a reference at 450 nm.

The spectroscopic analysis revealed that three compounds (namely C02, C04, and C28) significantly absorbed light at 450 nm, and thus could interfere with the analysis of ELISA results if they are not completely washed away from the microplate before the final measurement. Moreover, C20 and C21 are not completely soluble in binding buffer at 1 mM concentration. Particular attention has been paid to these compounds during the screening to avoid an incorrect evaluation of their activity.

Since the purchased compounds were supposed to bind Hb, but their reactivity with the protein was not known, the stability of Hb in the presence of each potential inhibitor was assessed through a spectroscopic analysis. OxyHb, the Hb used for the screening, is known to be prone to auto-oxidation leading to the formation of metHb, which reacts differently with IsdB. To verify if auto-oxidation was caused by the presence of the potential inhibitors, the Q bands in the absorption spectra of Hb were examined before and two hours after that each compound at 1 mM concentration was added to the protein. The time delay was chosen to be comparable with the whole duration of the assay, including the preliminary incubation of the compound

with Hb. The spectra in the Q band region are shown in Figure 71. Spectra were subtracted by the contribution of the blank and of the compound. Although most of the subtraction resulted in a reasonable spectrum, the strong absorbance of C02, C04, C12, and the scattering caused by C22 have undermined the analysis of their effect on Hb.

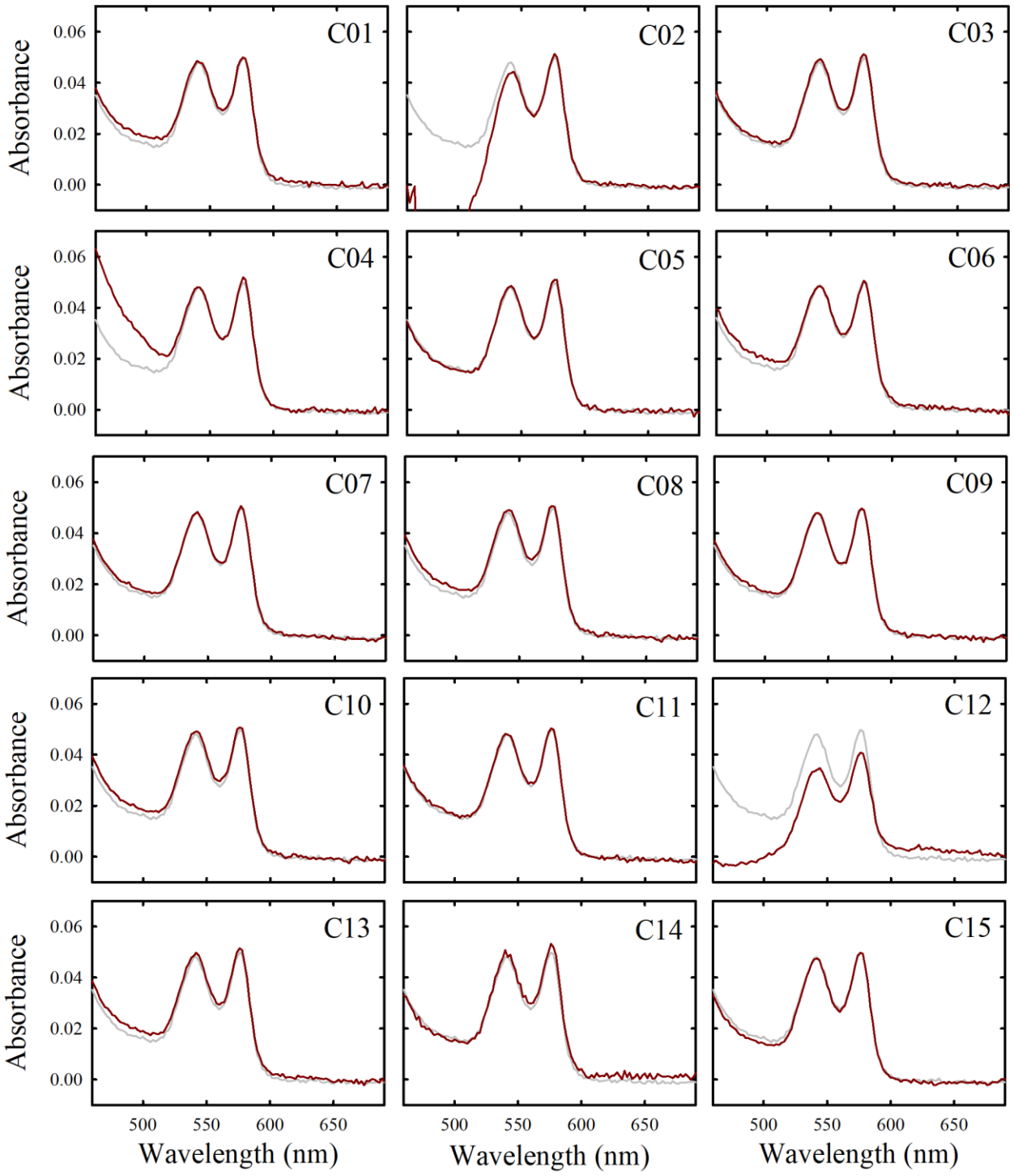

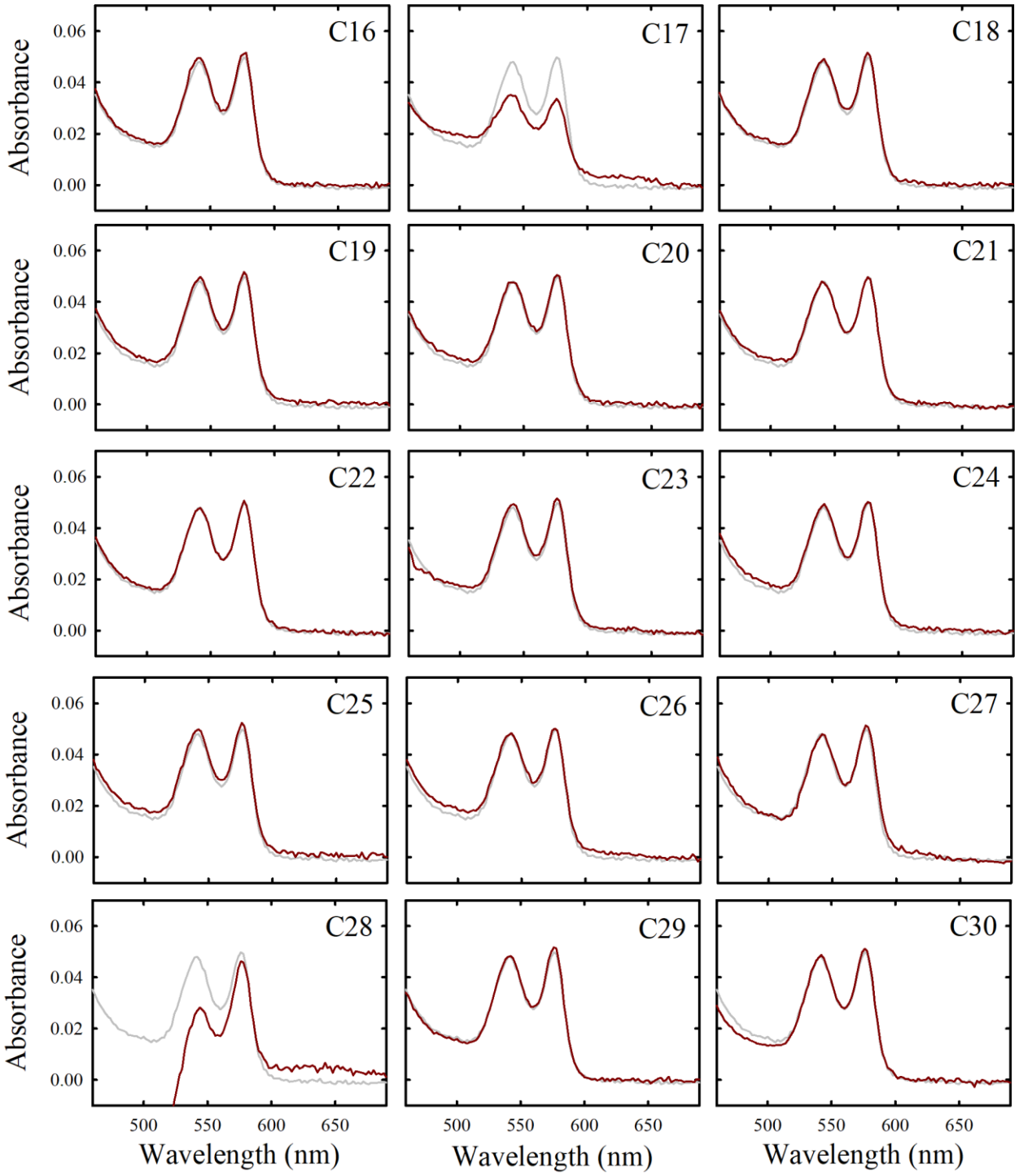

Figure 71: Spectral comparison of Hb Q band before (grey lines) and after (red lines) incubation with compounds. The spectra of Hb after incubation were subtracted by the signal of the compound alone in solution.

Most of the compounds proved to be inert, while C17 clearly caused Hb oxidation. Also, C12 and C22 caused an increase in the absorbance of Hb at around 640 nm, but the difficult subtraction of the contribution of the blank from the spectra did not allow to unequivocally

define their effect. Finally, the non-specific binding of the small molecules to the ELISA plate or to IsdB^{Y165A} was excluded by performing an ELISA in the absence of Hb (data not shown). The screening was performed on all thirty compounds in duplicate (Figure 72).

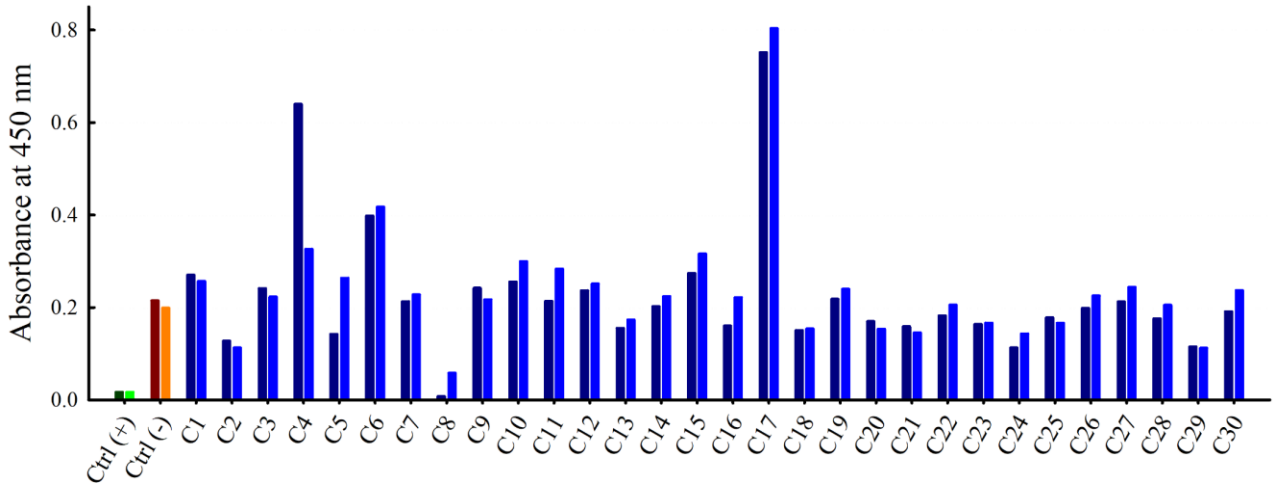

Figure 72: Results of the ELISA screening of the first batch of potential inhibitors, in duplicate. In green the signals in the absence of Hb, in brown and orange the signals in the absence of potential inhibitors, in blue the results of the screening.

The results of the screening confirmed the robustness of the method, in fact, signal corresponding to the same sample (namely the technical duplicates) resulted comparable in most of the cases. The positive control corresponds to the assay in the absence of any added inhibitor and the recorded absorbance is thus the maximum signal that can be registered. In the negative control Hb was omitted and thus the recorded absorbance is the signal expected in the presence of full inhibition of the PPI. The difference in the signal of the positive and negative controls defines the dynamic range of the assay, and half of this value was used as a threshold for the identification of positive hits. The average and the standard deviation of the results in duplicate were calculated, and the result is reported in Figure 73. Notably, the presence of C17 gave a signal higher than the positive control. Since this compound was found to oxidize the Hb, the obtained result cannot be considered reliable, in fact metHb was demonstrated to give misleading results when analyzed by the ELISA. C4 and C5 did not result in a reproducible value, whereas C6 reproducibly showed an HRP signal that was 2-fold the positive control. These four compounds were excluded from the final analysis of the screening results.

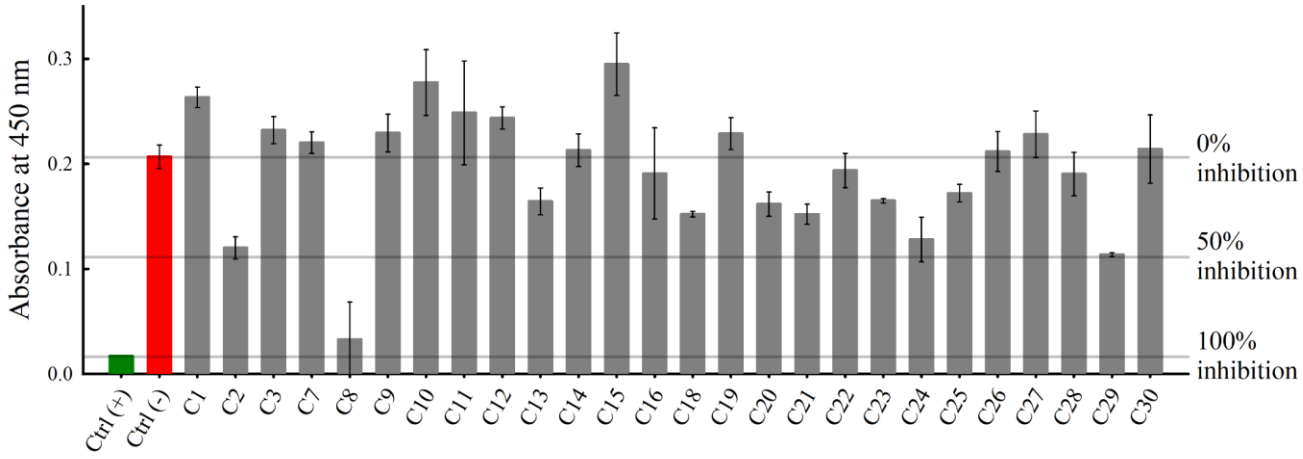

Figure 73: Averaged results of the ELISA screening with relative error bars. 0% inhibition corresponds to the negative control, 100% inhibition corresponds to the positive control, and 50% inhibition was the threshold for identifying promising compounds.

After the screening of the first batch of compounds, C8 was considered the most promising inhibitor. To confirm its ability in inhibiting the complex formation between IsdB and Hb, the entire Hb binding curve was repeated in duplicate in the presence of 1 mM concentration of this compound. Since 50% DMSO was used to solubilize the identified molecule, resulting in a 2% DMSO concentration in the screening assay, the Hb binding curve in the presence of 2% DMSO was performed to exclude any effect of the organic solvent on the complex formation (Figure 74). The presence of C8 in solution, significantly right-shifted the Hb binding curve, leading to an increased dissociation constant for the IsdB^{Y165A}-Hb complex (Table 19), thus confirming its ability in interfering with the PPI.

Table 19: Dissociation constants calculated through the ELISA for IsdB^{Y165A}-Hb complex in the absence and the presence of C8, and in the presence of DMSO as internal control to exclude any interference on the interaction due to the solvent.

	ELISA K_D (μM)
IsdB^{Y165A}-oxyHb	34.84 ± 2.92
IsdB^{Y165A}-oxyHb (+ 1 mM C8)	96.10 ± 32.61
IsdB^{Y165A}-oxyHb (+ 2% DMSO)	32.51 ± 7.70

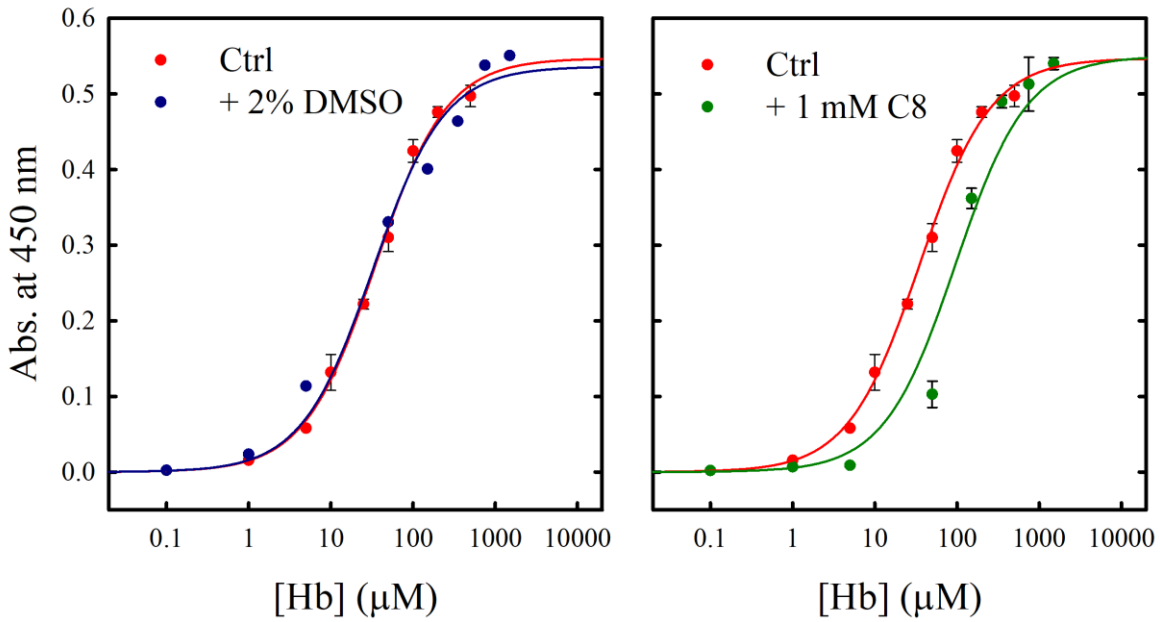

Figure 74: Absorbance at 450 nm plotted as a function of Hb concentration alone (red), in the presence of 2% of DMSO (dark blue), or in the presence of 1 mM of C8 (green).

C8 was synthesized by Prof.ssa Loretta Lazzaratto to confirm the specificity of the observed inhibition. Indeed, it is well known that commercial compounds, especially those coming from screening libraries, might contain trace impurities that can affect analysis. The synthesized C8 was solubilized in 50% DMSO and the stability of Hb in the presence of the compound was confirmed spectroscopically by evaluating the Hb Q band (data not shown). The inhibitory activity of the compound was tested at four Hb concentrations in duplicate (Figure 75), but no inhibition of complex formation was observed. The result suggested that the molecule was not effectively interfering with complex formation, thus the observed effect in the screening assay was probably due to some contaminants in solution.

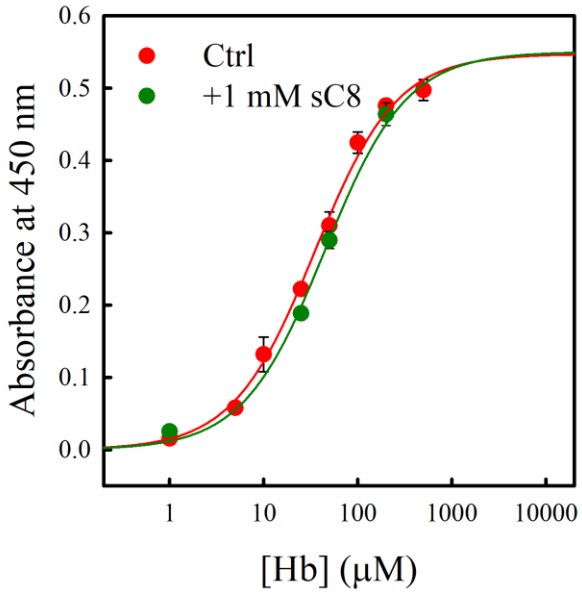

Figure 75: Absorbance at 450 nm plotted as a function of Hb concentration, in the absence (red) or in the presence of the synthesized C8 (sC8 - green) at 1 mM concentration.

The second batch of tested inhibitors was composed of molecules purchased from Enamine Ltd, which were solubilized in the same way as the ones belonging to the first batch (Table 20 summarises the principal properties of this new set of compounds and the stock concentration).

*Table 20: Second batch of tested compounds. * DMSO at a final concentration of 50% was used to obtain complete solubilization; ** 20% DMSO was used to obtain complete solubilization.*

ID	MW (Da)	LogP	[stock] (mM)
C31	373	2	50
C32	334	0.5	50
C33	330	-1.48	50**
C34	281	-1.52	33*
C35	394	2.3	50
C36	302	1.36	50
C37	355	-1.01	50
C38	305	0.16	50
C39	323	0.61	50
C40	382	1.44	50**
C41	301	0.25	50
C42	301	0.29	50
C43	340	-0.97	50

ID	MW (Da)	LogP	[stock] (mM)
C44	261	-0.45	44*
C45	350	1.31	50
C46	222	-0.19	50
C47	302	0.36	50
C48	339	1.45	50
C49	384	1.03	50
C50	375	1.44	50
C51	342	-0.36	50
C52	323	-0.71	50
C53	306	0	50
C54	263	-0.26	50**
C55	341	0.45	50

After the solubilization, the stock solutions were diluted in binding buffer at 1 mM final concentration to confirm that the compounds were not changing the pH of the solution and to spectroscopically characterize the solubilized molecules (Figure 76).

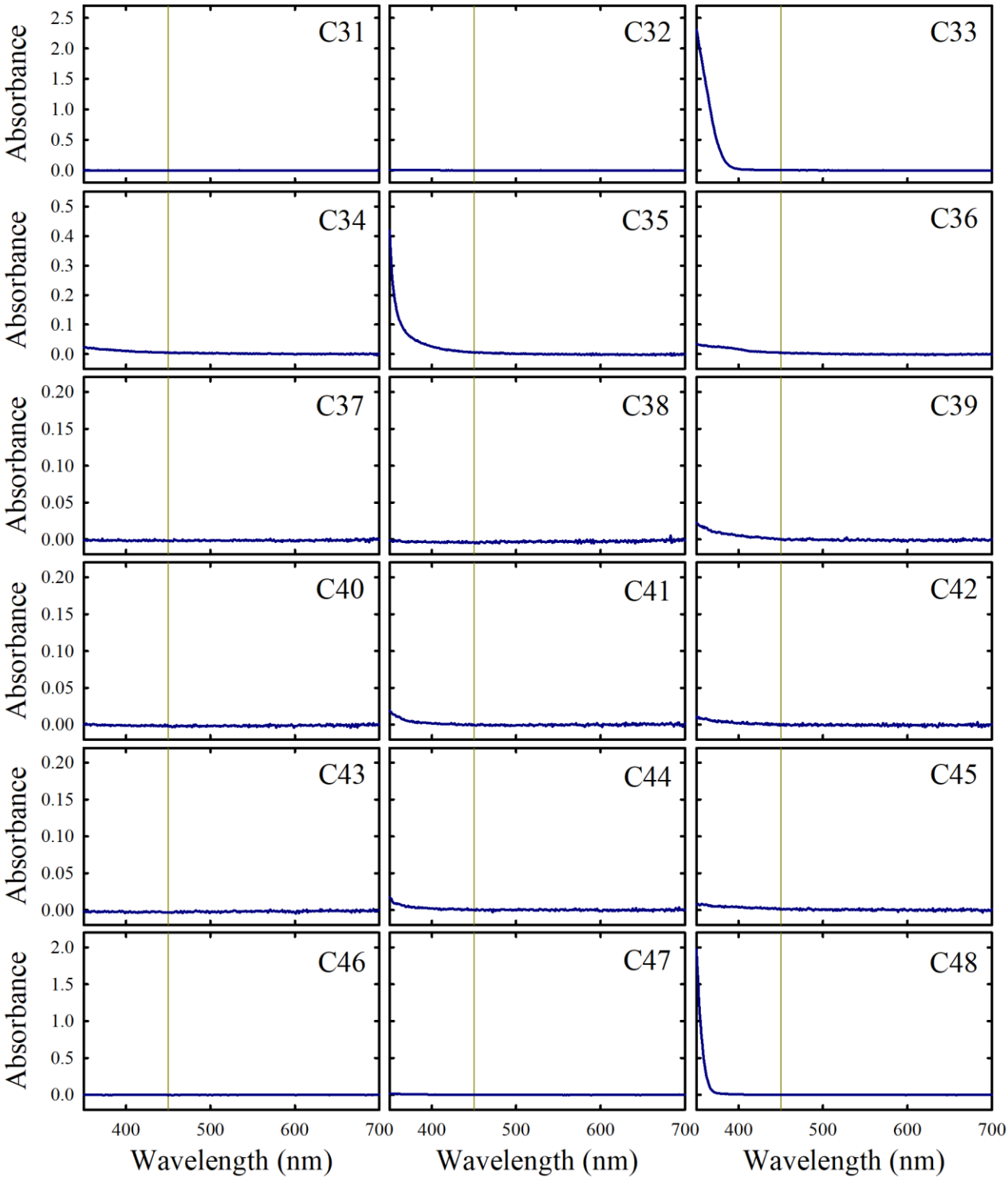

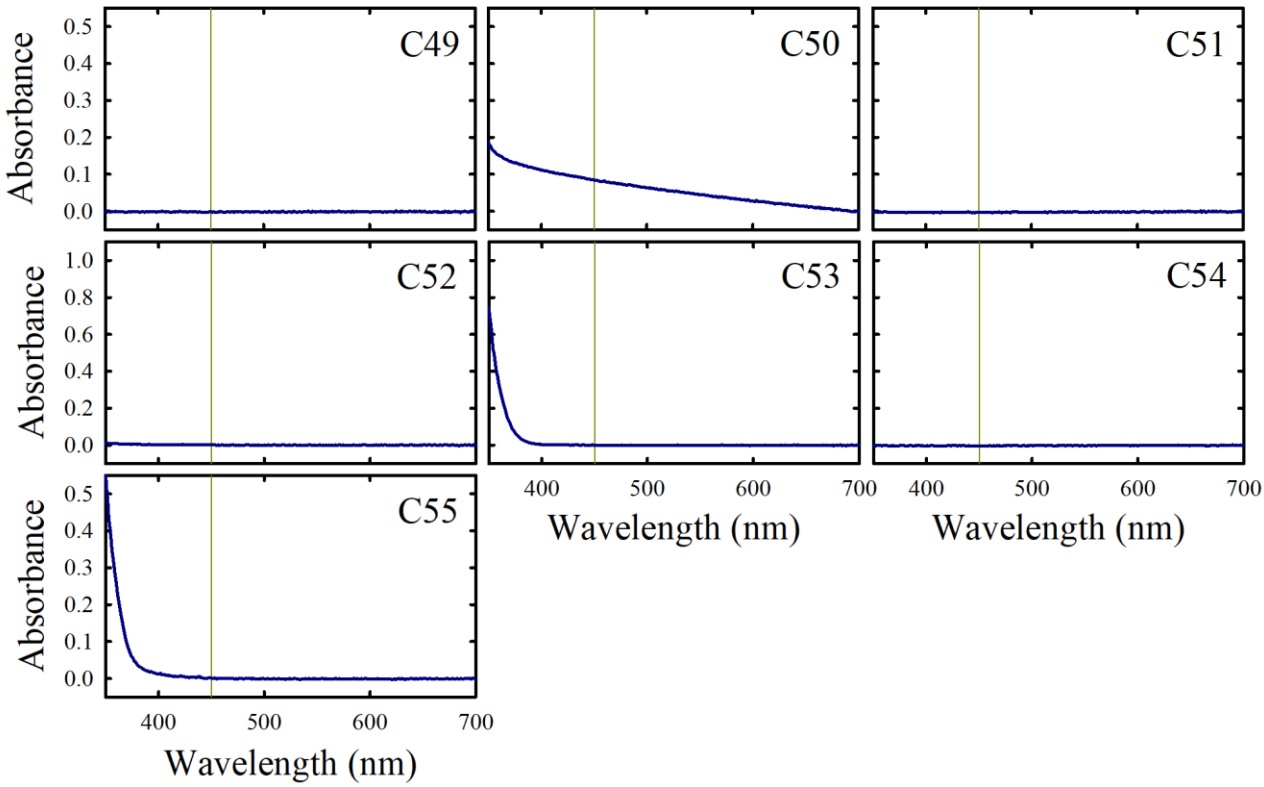

Figure 76: Visible spectra of the second batch of compounds at 1 mM concentration. The yellow line is a reference at 450 nm.

None of the molecules significantly absorbed light at 450 nm, and they appeared soluble in binding buffer at the concentration needed for the screening. The Hb stability in the presence of the molecules was assessed as described above by evaluating the characteristic Q band of the protein (Figure 77).

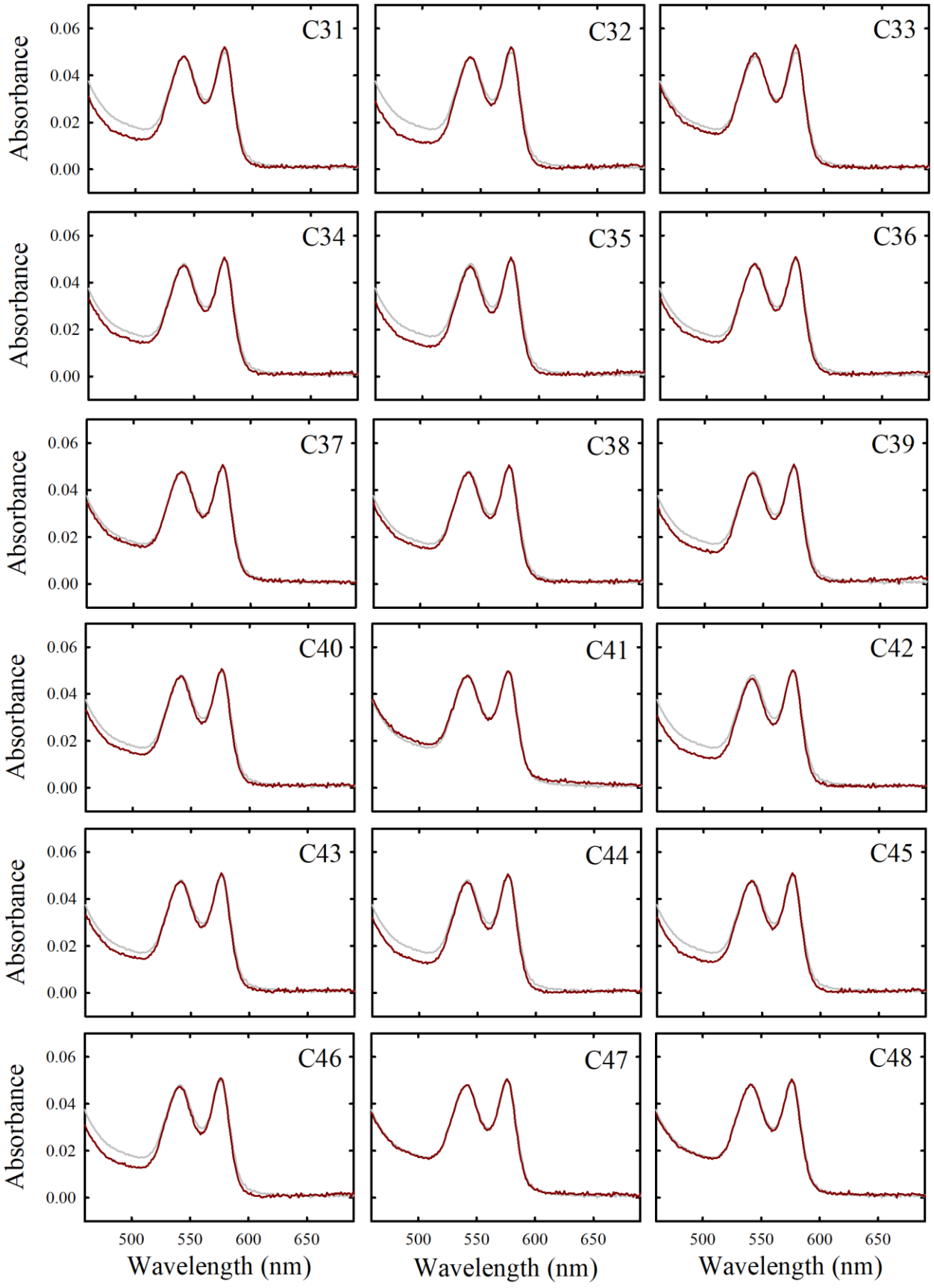
C31
C32
C33
C34
C35
C36
C37
C38
C39
C40
C41
C42
C43
C44
C45
C46
C47
C48
Absorbance
0.06
0.04
0.02
0.00
500
550
600
650
Wavelength (nm)

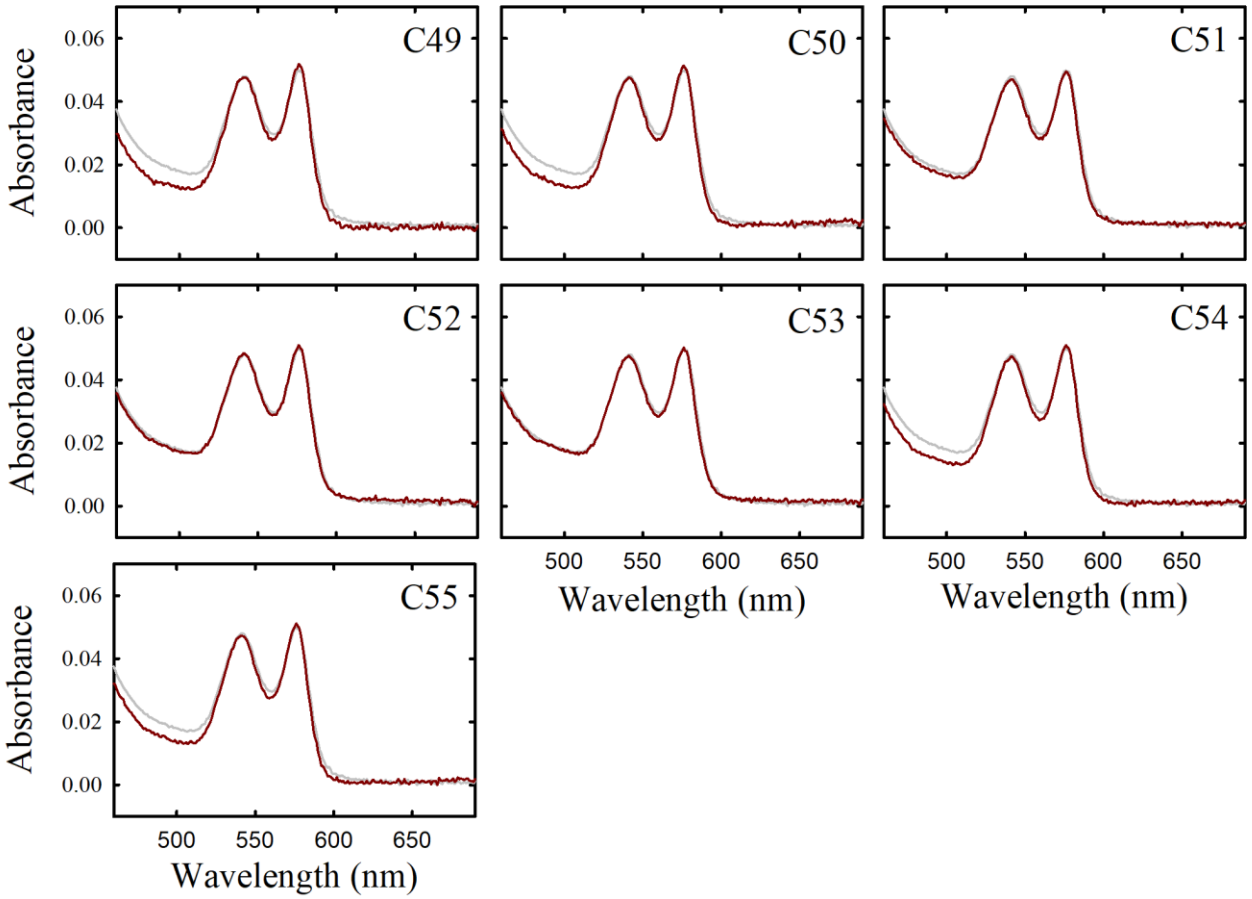

Figure 77: Spectral comparison of Hb Q band before (grey lines) and after (red lines) incubation with each screened compound. The spectra of Hb after incubation was prepared by subtracting the signal related to the compound alone in solution.

The molecules belonging to the second batch did not cause any changes on Hb absorbance spectrum and thus it was confirmed that they were not causing Hb oxidation. Finally, the non-specific binding to the ELISA microplate or to IsdB^{Y165A} was excluded by performing the ELISA screening assay in the absence of Hb (data not shown). The screening of the second batch of potential inhibitors was performed in triplicate (Figure 78). Performing the screening in triplicate allowed to easily identify outliers, that might be due to inhomogeneous wells or incorrect reagents washing and removal which were removed. In particular, the first replicate of C35 (which shows an absorbance three-folds larger than the negative control) or the first of C36, C37 and C45 (which were significantly different from of the other results obtained for the same molecules) were removed.

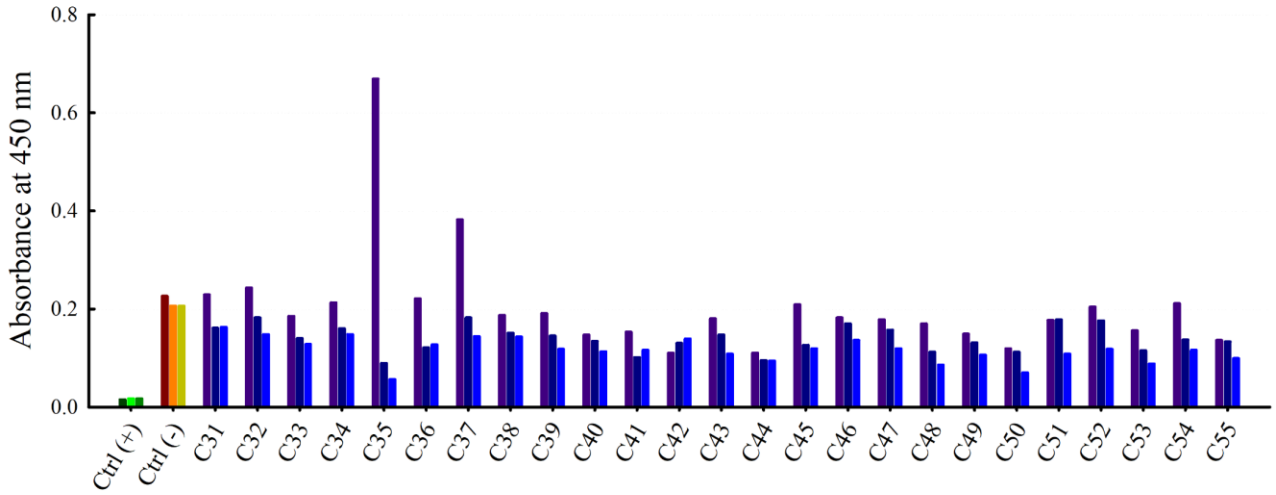

Figure 78: Results of the ELISA for the screening of the second batch of potential inhibitors, in triplicate. In green the signals in the absence of Hb, in brown and orange the signals in the absence of potential inhibitors, in blue the results of the screening.

The average and standard deviation were calculated for the remaining values and reported in a new bar chart (Figure 79). Promising inhibitors were selected for the ability in reducing the HRP signal by more than 50%, just like the first batch that was analyzed.

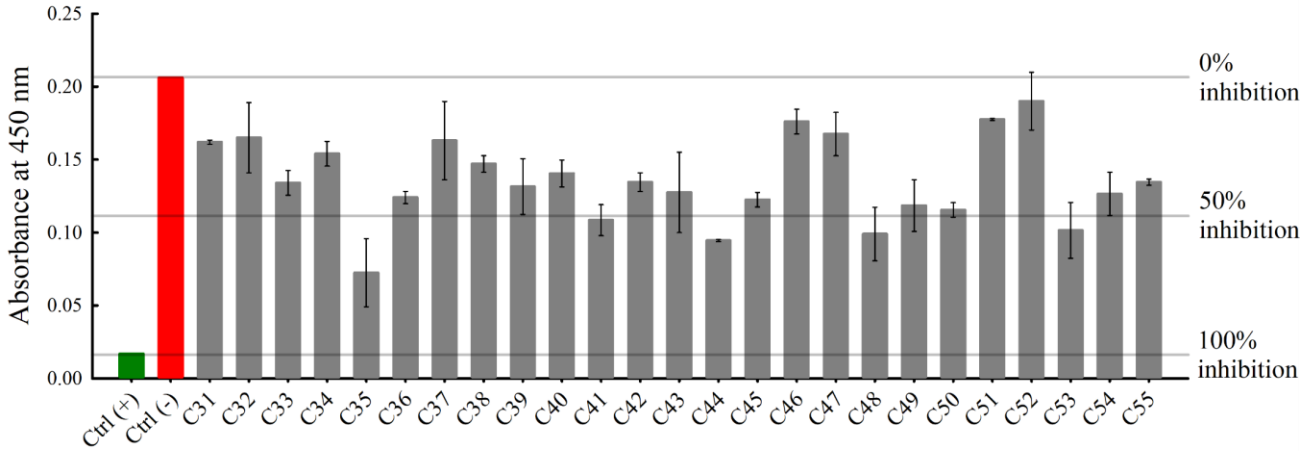

Figure 79: Averaged results of the ELISA screening with relative error bars. 0% inhibition corresponds to the negative control, 100% inhibition corresponds to the positive control, and 50% inhibition was the threshold for identifying promising compounds.

The screening of the second batch of compounds identified eight potential inhibitors (C35, C41, C42, C44, C48, C50, C53, and C55), and Saturation-Transfer Difference NMR (STD-NMR) was used to confirm the specific binding of molecules to Hb and to identify the structural epitopes that mostly contribute to binding.
The analysis was performed by Prof.ssa Serena Faggiano, Università di Parma. C44 and C55 did not demonstrate any binding to Hb, whereas C41, C42, C48, and C53 resulted in weak difference spectra, which did not allow a confident identification of molecular epitopes. Notably, C35 and C50 were found to effectively bind Hb, and the binding epitopes identified were in very good agreement with the initial molecular docking binding poses. These two last compounds have been synthesized by Prof.ssa Lazzarato, Università di Torino for further testing. If their activity will be confirmed, they will be modified to increase their potency in order to be able to test them as inhibitors of *S. aureus* growth on Hb as the sole iron source.

Anyway, STD-NMR results confirmed the reliability of the optimized ELISA for the identification of potential inhibitors of the IsdB-Hb PPI, making this method a valuable technique for cost-effective high-throughput screening of the new generation of compounds that will be possibly produced hereafter.

Conclusions

The project of the thesis aimed at the biochemical/biophysical characterization of the IsdB-Hb complex, and the identification of inhibitors of this PPI. Indeed, IsdB is one of the most important virulence factors of *S. aureus,* and its complex with Hb aims at acquiring iron, an essential micronutrient for the bacterium. *In vivo*, staphylococcal mutants lacking IsdB display reduced virulence in a mouse model, making IsdB a suitable target to develop new antimicrobial agents. The characterization of IsdB-Hb complex was intended to gain more structural and mechanistic insights on this PPI. The following screening of the first batch of *in silico* selected compounds allowed to identify hit compounds that will be used as starting points for the development of more potent molecules to be tested for the efficacy in the inhibition of bacterial growth.

Biochemical/biophysical characterization of the IsdB-Hb complex. The reconstruction of a high-resolution model of IsdB-COHb complex allowed to obtain, for the first time, structural insights on the complex formed by WT IsdB and Hb in the absence of artifacts. The analysed complex, formed by the hemophore and the reduced, ligated form of Hb, was intended to represent a snapshot of the PPI interaction preceding the heme transfer, in fact IsdB is not able to extract heme from COHb. In these conditions, the complex is formed by two IsdB molecules binding an Hb tetramer (namely, a 1:2 stoichiometric ratio), suggesting that four hemophores cannot bind a tetramer, possibly because of a steric hindrance (as already speculated in two different studies [224,239]). In this context, a dense network of contacts between Hb and all IsdB domains (including NEAT1, linker, and NEAT2) was found to force a clear structural rearrangement of Hb that has been supposed to prepare for the protein dimerization. None of the techniques utilized throughout the thesis allowed to identify the IsdB-metHb complex in a 1:2 stoichiometric ratio, indeed the structure solved by cryo-EM shows a stable complex formed by two IsdB molecules bound to an Hb dimer. These findings suggest that Hb dimerization might be an intermediate step of the process that leads to heme extraction.

SemiHbs turned out to be an invaluable tool for assessing the interaction of the hemophore with the two different Hb chains. The heme extraction rates from either semi(α) or semi(β)metHb chains were found to be comparable. Moreover, the kinetic data on the IsdB interaction with (semi)metHb and (semi)oxyHb revealed that IsdB similarly interacts with both α- and β-Hb chains, irrespective of the ligation state of Hb (oxidized or reduced, ligated Hb). Altogether, these evidences pointed out that the hemophore efficiently binds and extracts heme

from either α- and β-Hb chains. Moreover, the stoichiometry of IsdB-metHb complex was determined with two independent techniques and was proved to be 1:1, further supporting the IsdB binding to both α- and β-chains within the complex.

The cryo-EM reconstruction of the IsdB-metHb complex model achieved a mid-range resolution, and it was not possible to identify the key residues for the PPI. However, it was clarified that in solution the complex is formed by two IsdB molecules bound to an Hb dimer which is in good agreement with the calculated stoichiometric ratio. Moreover, the cryo-EM map clearly indicates that heme is in the hemophore binding pocket, supporting the completion of heme transfer. Notably, the complex formed by two IsdB molecules bound to an Hb dimer was found at very high concentration (up to 200 μM), when the Hb tetramer is expected to be highly stable. This evidence supports the hypothesis that IsdB binding causes Hb dimerization, and this last effect is needed to proceed to heme extraction. At the same time, in very diluted solution the complex is formed by one IsdB molecule bound to an Hb chain (either α or β) suggesting that heme extraction can cause a decrease of Hb dimer stability, leading to Hb monomerization.

Kinetic data calculated for IsdB-metHb complex formation were fitted to a two-step model, where the irreversible heme extraction leads to the formation of holo-IsdB-apo-Hb complex, that only slowly dissociates in the absence of a heme acceptor. The obtained kinetic constants were combined with the heme extraction rate, calculated with an independent method, to define for the first time the kinetic model for IsdB-metHb complex formation and heme extraction. Notably, dissociation of apo-Hb from holo-IsdB resulted to limit the overall process and highlights the importance of heme transfer to IsdA to increase the turnover of heme extraction.

The role of Tyr440 in heme extraction, that was already partially described by Bowden and co-workers [224], was further clarified by structural insight from cryo-EM. Published studies suggested that the residue interacts with proximal His of Hb during the exit path of the cofactor, and coordinates the hemic-iron in holo-IsdB. In the cryo-EM model of IsdB-COHb complex, when heme is still bound to Hb, this residue was observed to directly interact with one heme propionate in concert with Met362 and Tyr444, indicating that it also acts in this first step of the process. Microscopic and macroscopic kinetic constants for the binding step of Y440A mutant resulted roughly comparable with WT hemophore, however the heme transfer analysis suggested that this mutant is not able to complete the extraction of the cofactor.

An unexpected IsdB dimer was identified during the purification of IsdB that has never been reported in literature. The dimer is not in equilibrium with the monomeric form and further investigations are planned to assess if the hemophore can form a swapped domain dimer.

Identification of inhibitors of IsdB-Hb complex formation. With the aim of assessing the inhibitory activity of *in silico* selected molecules, an ELISA was validated as a screening platform. The sensitivity of the assay was increased using the $IsdB^{Y165A}$ variant that has already been reported in literature to have a reduced affinity for Hb but has never been investigated in detail. Indeed, Tyr165 was found to strongly interact with COHb in the high-resolution structure of the complex. The substitution of this residue with an alanine leads to a 3-order magnitude reduction of the hemophore affinity for Hb and 5-fold decrease in heme extraction rate. The two findings are possibly related, with the heme extraction rate highly affected by the decrease in affinity. Fifty-five molecules purchased by commercial suppliers were tested by ELISA, eight hit compounds were identified and two of them were confirmed to bind to Hb by STD-NMR. These two compounds were synthetized, and further tests are currently ongoing to further investigate their inhibitory activity. If their effect will be confirmed, these two compounds can become a starting point for a structure-activity relationship (SAR) study that will guide synthesis of new potential antimicrobial agents, the first-in-class in hemophore inhibition. Notably the tested molecules were selected to bind free Hb in the bloodstream, and thus have two principal characteristics that make them very promising: the expected lower rate of resistance and the potential to be effective against different bacteria. Indeed, the molecules bind Hb and are thus expected to be less affected by bacterial mutations and thus to be linked to a lower rate of insurgence of resistance. Moreover, since many bacterial hemophores retrieve heme from Hb, a molecule binding to Hb might interfere not only with both IsdB and IsdH, but also with the function of other hemophores. Finally, the availability of the high-resolution structure of IsdB-COHb obtained by cryo-EM will be fundamental for further *in silico* screening campaigns. In fact, the only crystallographic structure deposited so far has a lower resolution (3.6 Å) and presents several crystallographic artifacts. Therefore, the model obtained within this thesis will allow to carry out additional virtual screening and molecular docking studies with the aim to increase the number and the molecular diversity of the potential inhibitors.

References

1. Ogston, A. Report upon Micro-Organisms in Surgical Diseases. *BMJ* **1881**, *1*, 369–375. doi: 10.1136/bmj.1.1054.369.
2. Ogston, A. Micrococcus Poisoning. *J. Anat. Physiol.* **1882**, *17*, 24–58.
3. Somerville, G.A.; Proctor, R.A. The Biology of Staphylococci. In *Staphylococci in Human Disease*; Wiley-Blackwell: Oxford, UK; pp. 1–18. doi: 10.1002/9781444308464.ch1.
4. Cowan, S.T.; Shaw, C.; Williams, R.E.O. Type Strain for Staphylococcus aureus Rosenbach. *J. Gen. Microbiol.* **1954**, *10*, 174–176. doi: 10.1099/00221287-10-1-174.
5. Liu, G.Y.; Essex, A.; Buchanan, J.T.; Datta, V.; Hoffman, H.M.; Bastian, J.F.; Fierer, J.; Nizet, V. Staphylococcus aureus golden pigment impairs neutrophil killing and promotes virulence through its antioxidant activity. *J. Exp. Med.* **2005**, *202*, 209–215. doi: 10.1084/jem.20050846.
6. Loeb, L. The Influence of certain Bacteria on the Coagulation of the Blood. *J. Med. Res.* **1903**, *10*, 407–419.
7. Hobbs, B.C. A study of the serological type differentiation of Staphylococcus pyogenes. *J. Hyg. (Lond).* **1948**, *46*, 222–238. doi: 10.1017/S0022172400036329.
8. Bonar, E.; Międzobrodzki, J.; Władyka, B. The Staphylococcal Coagulases. In *Pet-To-Man Travelling Staphylococci*; Elsevier, 2018; pp. 95–102. doi: 10.1016/B978-0-12-813547-1.00007-8.
9. Kluytmans, J.; van Belkum, A.; Verbrugh, H. Nasal carriage of Staphylococcus aureus: epidemiology, underlying mechanisms, and associated risks. *Clin. Microbiol. Rev.* **1997**, *10*, 505–520. doi: 10.1128/CMR.10.3.505.
10. Wertheim, H.F.L.; Melles, D.C.; Vos, M.C.; van Leeuwen, W.; van Belkum, A.; Verbrugh, H.A.; Nouwen, J.L. The role of nasal carriage in Staphylococcus aureus infections. *Lancet Infect. Dis.* **2005**, *5*, 751–762. doi: 10.1016/S1473-3099(05)70295-4.
11. Tong, S.Y.C.; Davis, J.S.; Eichenberger, E.; Holland, T.L.; Fowler, V.G. Staphylococcus aureus Infections: Epidemiology, Pathophysiology, Clinical Manifestations, and Management. *Clin. Microbiol. Rev.* **2015**, *28*, 603–661. doi: 10.1128/CMR.00134-14.
12. Lowy, F.D. Staphylococcus aureus Infections. *N. Engl. J. Med.* **1998**, *339*, 520–532. doi: 10.1056/NEJM199808203390806.

13. Foster, T.J.; Geoghegan, J.A. Staphylococcus aureus. In *Molecular Medical Microbiology*; Elsevier, 2015; Vol. 2–3, pp. 655–674 ISBN 9780123971692. doi: 10.1016/B978-0-12-397169-2.00037-8.
14. Cheung, A.L.; Bayer, A.S.; Zhang, G.; Gresham, H.; Xiong, Y.-Q. Regulation of virulence determinants in vitro and in vivo in Staphylococcus aureus. *FEMS Immunol. Med. Microbiol.* **2004**, *40*, 1–9. doi: 10.1016/S0928-8244(03)00309-2.
15. Patti, J.M.; Allen, B.L.; McGavin, M.J.; Hook, M. MSCRAMM-Mediated Adherence of Microorganisms to Host Tissues. *Annu. Rev. Microbiol.* **1994**, *48*, 585–617. doi: 10.1146/annurev.mi.48.100194.003101.
16. Foster, T.J.; Geoghegan, J.A.; Ganesh, V.K.; Höök, M. Adhesion, invasion and evasion: the many functions of the surface proteins of Staphylococcus aureus. *Nat. Rev. Microbiol.* **2014**, *12*, 49–62. doi: 10.1038/nrmicro3161.
17. Foster, T.J. The MSCRAMM Family of Cell-Wall-Anchored Surface Proteins of Gram-Positive Cocci. *Trends Microbiol.* **2019**, *27*, 927–941. doi: 10.1016/j.tim.2019.06.007.
18. Zecconi, A.; Scali, F. Staphylococcus aureus virulence factors in evasion from innate immune defenses in human and animal diseases. *Immunol. Lett.* **2013**, *150*, 12–22. doi: 10.1016/j.imlet.2013.01.004.
19. Maresso, A.W.; Schneewind, O. Iron Acquisition and Transport in Staphylococcus aureus. *BioMetals* **2006**, *19*, 193–203. doi: 10.1007/s10534-005-4863-7.
20. Hammer, N.D.; Skaar, E.P. Molecular Mechanisms of Staphylococcus aureus Iron Acquisition. *Annu. Rev. Microbiol.* **2011**, *65*, 129–147. doi: 10.1146/annurev-micro-090110-102851.
21. Marchetti, M.; De Bei, O.; Bettati, S.; Campanini, B.; Kovachka, S.; Gianquinto, E.; Spyrakis, F.; Ronda, L. Iron Metabolism at the Interface between Host and Pathogen: From Nutritional Immunity to Antibacterial Development. *Int. J. Mol. Sci.* **2020**, *21*, 2145. doi: 10.3390/ijms21062145.
22. Weinberg, E.D. Nutritional Immunity. *JAMA* **1975**, *231*, 39. doi: 10.1001/jama.1975.03240130021018.
23. Ganz, T. Iron in innate immunity: starve the invaders. *Curr. Opin. Immunol.* **2009**, *21*, 63–67. doi: 10.1016/j.coi.2009.01.011.

24. Lindsay, J.A.; Riley, T. V. Staphylococcal iron requirements, siderophore production, and iron-regulated protein expression. *Infect. Immun.* **1994**, *62*, 2309–2314. doi: 10.1128/IAI.62.6.2309-2314.1994.
25. Mazmanian, S.K.; Ton-That, H.; Su, K.; Schneewind, O. An iron-regulated sortase anchors a class of surface protein during Staphylococcus aureus pathogenesis. *Proc. Natl. Acad. Sci.* **2002**, *99*, 2293–2298. doi: 10.1073/pnas.032523999.
26. Mazmanian, S.K. Passage of heme-iron across the envelope of Staphylococcus aureus. *Science* **2003**, *299*, 906–909. doi: 10.1126/science.1081147.
27. Bhakdil, S.; Tranum-Jensen, J. Alpha-toxin of Staphylococcus aureus. *Microbiol. Rev.* **1991**, *55*, 733–751.
28. Babior, B.M. Phagocytes and oxidative stress. *Am. J. Med.* **2000**, *109*, 33–44. doi: 10.1016/S0002-9343(00)00481-2.
29. Trivier, D. Iron depletion and virulence in Staphylococcus aureus. *FEMS Microbiol. Lett.* **1996**, *141*, 117–127. doi: 10.1016/0378-1097(96)00233-9.
30. Cassat, J.E.; Skaar, E.P. Metal ion acquisition in Staphylococcus aureus: overcoming nutritional immunity. *Semin. Immunopathol.* **2012**, *34*, 215–235. doi: 10.1007/s00281-011-0294-4.
31. Kobayashi, S.D.; DeLeo, F.R. Staphylococcus aureus Protein A Promotes Immune Suppression. *MBio* **2013**, *4*, 4–6. doi: 10.1128/mBio.00764-13.
32. Prévost, G.; Cribier, B.; Couppié, P.; Petiau, P.; Supersac, G.; Finck-Barbançon, V.; Monteil, H.; Piemont, Y. Panton-Valentine leucocidin and gamma-hemolysin from Staphylococcus aureus ATCC 49775 are encoded by distinct genetic loci and have different biological activities. *Infect. Immun.* **1995**, *63*, 4121–4129. doi: 10.1128/IAI.63.10.4121-4129.1995.
33. de Haas, C.J.C.; Veldkamp, K.E.; Peschel, A.; Weerkamp, F.; Van Wamel, W.J.B.; Heezius, E.C.J.M.; Poppelier, M.J.J.G.; Van Kessel, K.P.M.; van Strijp, J.A.G. Chemotaxis Inhibitory Protein of Staphylococcus aureus, a Bacterial Antiinflammatory Agent. *J. Exp. Med.* **2004**, *199*, 687–695. doi: 10.1084/jem.20031636.
34. Skinner, D.; Keefer, C. Significance of Bacteremia Caused By Staphylococcus Aureus. *Arch. Intern. Med.* **1941**, *68*, 851.

35. Chambers, H.F.; DeLeo, F.R. Waves of resistance: Staphylococcus aureus in the antibiotic era. *Nat. Rev. Microbiol.* **2009**, *7*, 629–641. doi: 10.1038/nrmicro2200.
36. McCarthy, A.J.; Lindsay, J.A. Genetic variation in Staphylococcus aureus surface and immune evasion genes is lineage associated: implications for vaccine design and host-pathogen interactions. *BMC Microbiol.* **2010**, *10*, 173. doi: 10.1186/1471-2180-10-173.
37. Rammelkamp, C.H.; Maxon, T. Resistance of Staphylococcus aureus to the Action of Penicillin. *Exp. Biol. Med.* **1942**, *51*, 386–389. doi: 10.3181/00379727-51-13986.
38. Kirby, W.M.M. Extraction of a highly potent penicillin inactivator from penicillin resistant staphylococci. *Science* **1944**, *99*, 452–453. doi: 10.1126/science.99.2579.452.
39. Bondi, A.; Dietz, C.C. Penicillin Resistant Staphylococci. *Exp. Biol. Med.* **1945**, *60*, 55–58. doi: 10.3181/00379727-60-15089.
40. Rutenburg, A.M.; Greenberg, H.L.; Schweinburg, F.B. Clinical Experiences with 2, 6-Dimethoxyphenyl Penicillin Monohydrate in Staphylococcal Infections. *N. Engl. J. Med.* **1960**, *263*, 1174–1178. doi: 10.1056/NEJM196012082632305.
41. Jevons, M.P. "Celbenin" - resistant Staphylococci. *BMJ* **1961**, *1*, 124–125. doi: 10.1136/bmj.1.5219.124-a.
42. Lakhundi, S.; Zhang, K. Methicillin-Resistant Staphylococcus aureus : Molecular Characterization, Evolution, and Epidemiology. *Clin. Microbiol. Rev.* **2018**, *31*, 1–103. doi: 10.1128/CMR.00020-18.
43. Turner, G.C. Newly Recognised Strains of *Staphylococcus aureus* Associated with Hospital Staphylococci. *Lancet* **1963**, *281*, 1156. doi: 10.1016/S0140-6736(63)91824-5.
44. Udo, E. Genetic analysis of community isolates of methicillin-resistant Staphylococcus aureus in Western Australia. *J. Hosp. Infect.* **1993**, *25*, 97–108. doi: 10.1016/0195-6701(93)90100-E.
45. Kourtis, A.P.; Hatfield, K.; Baggs, J.; Mu, Y.; See, I.; Epson, E.; Nadle, J.; Kainer, M.A.; Dumyati, G.; Petit, S.; et al. Vital Signs: Epidemiology and Recent Trends in Methicillin-Resistant and in Methicillin-Susceptible Staphylococcus aureus Bloodstream Infections — United States. *MMWR. Morb. Mortal. Wkly. Rep.* **2019**, *68*, 214–219. doi: 10.15585/mmwr.mm6809e1.

46. O'Neill, J. Tackling Drug-Resistant Infections Globally: Final Report and Recommendations. *Rev. Antimicrob. Resist.* **2016**, 1–80.
47. Rice, L.B. Federal Funding for the Study of Antimicrobial Resistance in Nosocomial Pathogens: No ESKAPE. *J. Infect. Dis.* **2008**, *197*, 1079–1081. doi: 10.1086/533452.
48. Ventola CL The antibiotic resistance crisis: part 1: causes and threats. *P T J.* **2015**, *40*, 277–283.
49. Tacconelli, E.; Magrini, N. *Global priority list of antibiotic-resistant bacteria to guide research, discovery, and development of new antibiotics*; 2017;
50. Hoebe, K.; Janssen, E.; Beutler, B. The interface between innate and adaptive immunity. *Nat. Immunol.* **2004**, *5*, 971–974. doi: 10.1038/ni1004-971.
51. Proctor, R. Recent developments for Staphylococcus aureus vaccines: clinical and basic science challenges. *Eur. Cells Mater.* **2015**, *30*, 315–326. doi: 10.22203/eCM.v030a22.
52. Turvey, S.E.; Broide, D.H. Innate immunity. *J. Allergy Clin. Immunol.* **2010**, *125*, S24–S32. doi: 10.1016/j.jaci.2009.07.016.
53. Brandt, S.L.; Putnam, N.E.; Cassat, J.E.; Serezani, C.H. Innate Immunity to Staphylococcus aureus : Evolving Paradigms in Soft Tissue and Invasive Infections. *J. Immunol.* **2018**, *200*, 3871–3880. doi: 10.4049/jimmunol.1701574.
54. Bekeredjian-Ding, I.; Stein, C.; Uebele, J. The Innate Immune Response Against Staphylococcus aureus. In; 2015; pp. 385–418. doi: 10.1007/82_2015_5004.
55. Janeway, C.A.; Medzhitov, R. Innate Immune Recognition. *Annu. Rev. Immunol.* **2002**, *20*, 197–216. doi: 10.1146/annurev.immunol.20.083001.084359.
56. Williams, R.J.P. Iron in evolution. *FEBS Lett.* **2012**, *586*, 479–484. doi: 10.1016/j.febslet.2011.05.068.
57. Lindley, P.F. Iron in biology: a structural viewpoint. *Reports Prog. Phys.* **1996**, *59*, 867–933. doi: 10.1088/0034-4885/59/7/002.
58. Hood, M.I.; Skaar, E.P. Nutritional immunity: transition metals at the pathogen–host interface. *Nat. Rev. Microbiol.* **2012**, *10*, 525–537. doi: 10.1038/nrmicro2836.
59. Py, B.; Barras, F. Building Fe–S proteins: bacterial strategies. *Nat. Rev. Microbiol.* **2010**, *8*, 436–446. doi: 10.1038/nrmicro2356.

60. Johnson, D.C.; Dean, D.R.; Smith, A.D.; Johnson, M.K. Structure, Function, and Formation of Biological Iron-Sulfur Clusters. *Annu. Rev. Biochem.* **2005**, *74*, 247–281. doi: 10.1146/annurev.biochem.74.082803.133518.

61. Dhungana, S.; Crumbliss, A.L. Coordination Chemistry and Redox Processes in Siderophore-Mediated Iron Transport. *Geomicrobiol. J.* **2005**, *22*, 87–98. doi: 10.1080/01490450590945870.

62. Wu, L.-F.; Meng, S.; Tang, G.-L. Ferrous iron and α-ketoglutarate-dependent dioxygenases in the biosynthesis of microbial natural products. *Biochim. Biophys. Acta - Proteins Proteomics* **2016**, *1864*, 453–470. doi: 10.1016/j.bbapap.2016.01.012.

63. McDonough, M.A.; Loenarz, C.; Chowdhury, R.; Clifton, I.J.; Schofield, C.J. Structural studies on human 2-oxoglutarate dependent oxygenases. *Curr. Opin. Struct. Biol.* **2010**, *20*, 659–672. doi: 10.1016/j.sbi.2010.08.006.

64. Yamamoto, I.; Saiki, T.; Shiu Mei Liu; Ljungdahl, L.G. Purification and properties of NADP-dependent formate dehydrogenase from Clostridium thermoaceticum, a tungsten-selenium-iron protein. *J. Biol. Chem.* **1983**, *258*, 1826–1832.

65. Chong, G.W.; Karbelkar, A.A.; El-Naggar, M.Y. Nature's conductors: what can microbial multi-heme cytochromes teach us about electron transport and biological energy conversion? *Curr. Opin. Chem. Biol.* **2018**, *47*, 7–17. doi: 10.1016/j.cbpa.2018.06.007.

66. Comer, J.; Zhang, L. Experimental Methods for Studying Cellular Heme Signaling. *Cells* **2018**, *7*, 47. doi: 10.3390/cells7060047.

67. Wolf, G.; Strahl, A.; Meisel, J.; Hammes, W.P. Heme-dependent catalase activity of lactobacilli. *Int. J. Food Microbiol.* **1991**, *12*, 133–140. doi: 10.1016/0168-1605(91)90062-T.

68. Forstermann, U.; Sessa, W.C. Nitric oxide synthases: regulation and function. *Eur. Heart J.* **2012**, *33*, 829–837. doi: 10.1093/eurheartj/ehr304.

69. Shelver, D.; Kerby, R.L.; He, Y.; Roberts, G.P. CooA, a CO-sensing transcription factor from Rhodospirillum rubrum, is a CO-binding heme protein. *Proc. Natl. Acad. Sci.* **1997**, *94*, 11216–11220. doi: 10.1073/pnas.94.21.11216.

70. Faller, M.; Matsunaga, M.; Yin, S.; Loo, J.A.; Guo, F. Heme is involved in microRNA processing. *Nat. Struct. Mol. Biol.* **2007**, *14*, 23–29. doi: 10.1038/nsmb1182.

71. Chen, J.-J.; London, I.M. Hemin enhances the differentiation of mouse 3T3 cells to adipocytes. *Cell* **1981**, *26*, 117–122. doi: 10.1016/0092-8674(81)90039-8.
72. Itano, H.A. The Human Hemoglobins: Their Properties and Genetic Control. In *Biology of Perceptual Systems*; Elsevier, 1957; pp. 215–268. doi: 10.1016/S0065-3233(08)60117-5.
73. Venkataraman, D.; Du, Y.; Wilson, S.R.; Hirsch, K.A.; Zhang, P.; Moore, J.S. A Coordination Geometry Table of the d-Block Elements and Their Ions. *J. Chem. Educ.* **1997**, *74*, 915. doi: 10.1021/ed074p915.
74. Berg, J.; Tymoczko, J.; Gatto, G.J.J.; Stryer, L. *Biochemistry*; 8th editio.; New York: W H Freeman, 2015; ISBN 1-4641-2610-0.
75. Sassa, S. Why Heme Needs to Be Degraded to Iron, Biliverdin IXα, and Carbon Monoxide? *Antioxid. Redox Signal.* **2004**, *6*, 819–824. doi: 10.1089/ars.2004.6.819.
76. Fenton, H.J.H. LXXIII.—Oxidation of tartaric acid in presence of iron. *J. Chem. Soc., Trans.* **1894**, *65*, 899–910. doi: 10.1039/CT8946500899.
77. Rigo, A.; Stevanato, R.; Finazzi-Agro, A.; Rotilio, G. An attempt to evaluate the rate of the haber-weiss reaction by using ·OH radical scavengers. *FEBS Lett.* **1977**, *80*, 130–132. doi: 10.1016/0014-5793(77)80422-5.
78. Lieu, P.T.; Heiskala, M.; Peterson, P.A.; Yang, Y. The roles of iron in health and disease. *Mol. Aspects Med.* **2001**, *22*, 1–87. doi: 10.1016/S0098-2997(00)00006-6.
79. Brieger, K.; Schiavone, S.; Miller, J.; Krause, K. Reactive oxygen species: from health to disease. *Swiss Med. Wkly.* **2012**, *142*, 1–14. doi: 10.4414/smw.2012.13659.
80. Niedzielska, E.; Smaga, I.; Gawlik, M.; Moniczewski, A.; Stankowicz, P.; Pera, J.; Filip, M. Oxidative Stress in Neurodegenerative Diseases. *Mol. Neurobiol.* **2016**, *53*, 4094–4125. doi: 10.1007/s12035-015-9337-5.
81. Simcox, J.A.; McClain, D.A. Iron and Diabetes Risk. *Cell Metab.* **2013**, *17*, 329–341. doi: 10.1016/j.cmet.2013.02.007.
82. Halliwell, B.; Gutteridge, J.M.C. Lipid Peroxidation in Brain Homogenates: The Role of Iron and Hydroxyl Radicals. *J. Neurochem.* **2002**, *69*, 1330–1330. doi: 10.1046/j.1471-4159.1997.69031330.x.
83. Pantopoulos, K.; Porwal, S.K.; Tartakoff, A.; Devireddy, L. Mechanisms of Mammalian Iron Homeostasis. *Biochemistry* **2012**, *51*, 5705–5724. doi: 10.1021/bi300752r.

84. Hentze, M.W.; Muckenthaler, M.U.; Galy, B.; Camaschella, C. Two to Tango: Regulation of Mammalian Iron Metabolism. *Cell* **2010**, *142*, 24–38. doi: 10.1016/j.cell.2010.06.028.
85. Ganz, T.; Nemeth, E. Regulation of iron acquisition and iron distribution in mammals. *Biochim. Biophys. Acta - Mol. Cell Res.* **2006**, *1763*, 690–699. doi: 10.1016/j.bbamcr.2006.03.014.
86. Abbaspour, N.; Hurrell, R.; Kelishadi, R. Review on iron and its importance for human health. *J. Res. Med. Sci.* **2014**, *19*, 164–174.
87. Andrews, N.C. Iron homeostasis: insights from genetics and animal models. *Nat. Rev. Genet.* **2000**, *1*, 208–217. doi: 10.1038/35042073.
88. Sjodt, M. Investigating Hemoglobin Capture and Heme Acquisition by the Pathogen Staphylococcus aureus, University of California, 2016.
89. Aisen, P.; Leibman, A.; Zweier, J. Stoichiometric and site characteristics of the binding of iron to human transferrin. *J. Biol. Chem.* **1978**, *253*, 1930–1937.
90. Raymond, K.N.; Dertz, E.A.; Kim, S.S. Enterobactin: An archetype for microbial iron transport. *Proc. Natl. Acad. Sci.* **2003**, *100*, 3584–3588. doi: 10.1073/pnas.0630018100.
91. Granick, S. FERRITIN. *J. Biol. Chem.* **1943**, *149*, 157–167.
92. Koechlin, B.A. Preparation and Properties of Serum and Plasma Proteins. XXVIII. The β 1 -Metal-combining Protein of Human Plasma 1a, b. *J. Am. Chem. Soc.* **1952**, *74*, 2649–2653. doi: 10.1021/ja01130a054.
93. Montreuil, J.; Tonnelat, J.; Mullet, S. Préparation et propriétés de la lactosidérophiline (lactotransferrine) du lait de femme. *Biochim. Biophys. Acta* **1960**, *45*, 413–421. doi: 10.1016/0006-3002(60)91478-5.
94. Oliveira, F.; Rocha, S.; Fernandes, R. Iron Metabolism: From Health to Disease. *J. Clin. Lab. Anal.* **2014**, *28*, 210–218. doi: 10.1002/jcla.21668.
95. Andrews, N.C. Disorders of Iron Metabolism. *N. Engl. J. Med.* **1999**, *341*, 1986–1995. doi: 10.1056/NEJM199912233412607.
96. Harrison, P.M.; Arosio, P. The ferritins: molecular properties, iron storage function and cellular regulation. *Biochim. Biophys. Acta - Bioenerg.* **1996**, *1275*, 161–203. doi: 10.1016/0005-2728(96)00022-9.

97. Linder, M. Mobilization of Stored Iron in Mammals: A Review. *Nutrients* **2013**, *5*, 4022–4050. doi: 10.3390/nu5104022.
98. Gunshin, H.; Mackenzie, B.; Berger, U. V.; Gunshin, Y.; Romero, M.F.; Boron, W.F.; Nussberger, S.; Gollan, J.L.; Hediger, M.A. Cloning and characterization of a mammalian proton-coupled metal-ion transporter. *Nature* **1997**, *388*, 482–488. doi: 10.1038/41343.
99. Fleet, J.C. Identification of Nramp2 as an Iron Transport Protein: Another Piece of the Intestinal Iron Absorption Puzzle. *Nutr. Rev.* **1998**, *56*, 88–89. doi: 10.1111/j.1753-4887.1998.tb01701.x.
100. Canonne-Hergaux, F.; Zhang, A.-S.; Ponka, P.; Gros, P. Characterization of the iron transporter DMT1 (NRAMP2/DCT1) in red blood cells of normal and anemic mk/mkmice. *Blood* **2001**, *98*, 3823–3830. doi: 10.1182/blood.V98.13.3823.
101. Sun, H.; Li, H.; Sadler, P.J. Transferrin as a Metal Ion Mediator. *Chem. Rev.* **1999**, *99*, 2817–2842. doi: 10.1021/cr980430w.
102. Abboud, S.; Haile, D.J. A Novel Mammalian Iron-regulated Protein Involved in Intracellular Iron Metabolism. *J. Biol. Chem.* **2000**, *275*, 19906–19912. doi: 10.1074/jbc.M000713200.
103. Ramey, G.; Deschemin, J.-C.; Durel, B.; Canonne-Hergaux, F.; Nicolas, G.; Vaulont, S. Hepcidin targets ferroportin for degradation in hepatocytes. *Haematologica* **2010**, *95*, 501–504. doi: 10.3324/haematol.2009.014399.
104. Pakdaman, R.; Petitjean, M.; El Hage Chahine, J.-M. Transferrins. A mechanism for iron uptake by lactoferrin. *Eur. J. Biochem.* **1998**, *254*, 144–153. doi: 10.1046/j.1432-1327.1998.2540144.x.
105. Baker, E.N.; Baker, H.M.; Kidd, R.D. Lactoferrin and transferrin: Functional variations on a common structural framework. *Biochem. Cell Biol.* **2002**, *80*, 27–34. doi: 10.1139/o01-153.
106. Bullen, J.J.; Rogers, H.J.; Griffiths, E. Role of Iron in Bacterial Infection. In *Current Topics in Microbiology and Immunology*; 1978; Vol. 80, pp. 1–35. doi: 10.1007/978-3-642-66956-9_1.

107. Andrews, N.C. Forging a field: the golden age of iron biology. *Blood* **2008**, *112*, 219–230. doi: 10.1182/blood-2007-12-077388.
108. Cheng, Y.; Zak, O.; Aisen, P.; Harrison, S.C.; Walz, T. Structure of the Human Transferrin Receptor-Transferrin Complex. *Cell* **2004**, *116*, 565–576. doi: 10.1016/S0092-8674(04)00130-8.
109. Rosa, L.; Cutone, A.; Lepanto, M.; Paesano, R.; Valenti, P. Lactoferrin: A Natural Glycoprotein Involved in Iron and Inflammatory Homeostasis. *Int. J. Mol. Sci.* **2017**, *18*, 1985. doi: 10.3390/ijms18091985.
110. Friedman, D.B.; Stauff, D.L.; Pishchany, G.; Whitwell, C.W.; Torres, V.J.; Skaar, E.P. Staphylococcus aureus Redirects Central Metabolism to Increase Iron Availability. *PLoS Pathog.* **2006**, *2*, e87. doi: 10.1371/journal.ppat.0020087.
111. Clarke, S.R.; Foster, S.J. IsdA Protects Staphylococcus aureus against the Bactericidal Protease Activity of Apolactoferrin. *Infect. Immun.* **2008**, *76*, 1518–1526. doi: 10.1128/IAI.01530-07.
112. Gruys, E.; Toussaint, M.J.M.; Niewold, T.A.; Koopmans, S.J. Acute phase reaction and acute phase proteins. *J. Zhejiang Univ. Sci.* **2005**, *6B*, 1045–1056. doi: 10.1631/jzus.2005.B1045.
113. Holmes, M.A.; Paulsene, W.; Jide, X.; Ratledge, C.; Strong, R.K. Siderocalin (Lcn 2) Also Binds Carboxymycobactins, Potentially Defending against Mycobacterial Infections through Iron Sequestration. *Structure* **2005**, *13*, 29–41. doi: 10.1016/j.str.2004.10.009.
114. Borregaard, N.; Cowland, J.B. Neutrophil Gelatinase-associated Lipocalin, a Siderophore-binding Eukaryotic Protein. *BioMetals* **2006**, *19*, 211–215. doi: 10.1007/s10534-005-3251-7.
115. De Domenico, I.; Ward, D.M.; Kaplan, J. Hepcidin regulation: ironing out the details. *J. Clin. Invest.* **2007**, *117*, 1755–1758. doi: 10.1172/JCI32701.
116. Rishi, G.; Wallace, D.F.; Subramaniam, V.N. Hepcidin: regulation of the master iron regulator. *Biosci. Rep.* **2015**, *35*, 1–12. doi: 10.1042/BSR20150014.
117. Kohgo, Y.; Ikuta, K.; Ohtake, T.; Torimoto, Y.; Kato, J. Body iron metabolism and pathophysiology of iron overload. *Int. J. Hematol.* **2008**, *88*, 7–15. doi: 10.1007/s12185-008-0120-5.

118. Haley, K.P.; Skaar, E.P. A battle for iron: host sequestration and Staphylococcus aureus acquisition. *Microbes Infect.* **2012**, *14*, 217–227. doi: 10.1016/j.micinf.2011.11.001.
119. Laurell, C.-B. Determination of the Haptoglobin Group. *Scand. J. Clin. Lab. Invest.* **1959**, *11*, 18–19. doi: 10.3109/00365515909060402.
120. Muller-Eberhard, U. Hemopexin. *N. Engl. J. Med.* **1970**, *283*, 1090–1094. doi: 10.1056/NEJM197011122832007.
121. Smith, A.; McCulloh, R.J. Hemopexin and haptoglobin: allies against heme toxicity from hemoglobin not contenders. *Front. Physiol.* **2015**, *6*. doi: 10.3389/fphys.2015.00187.
122. Schaer, D.J.; Buehler, P.W.; Alayash, A.I.; Belcher, J.D.; Vercellotti, G.M. Hemolysis and free hemoglobin revisited: exploring hemoglobin and hemin scavengers as a novel class of therapeutic proteins. *Blood* **2013**, *121*, 1276–1284. doi: 10.1182/blood-2012-11-451229.
123. Mollan, T.L.; Jia, Y.; Banerjee, S.; Wu, G.; Timothy Kreulen, R.; Tsai, A.-L.; Olson, J.S.; Crumbliss, A.L.; Alayash, A.I. Redox properties of human hemoglobin in complex with fractionated dimeric and polymeric human haptoglobin. *Free Radic. Biol. Med.* **2014**, *69*, 265–277. doi: 10.1016/j.freeradbiomed.2014.01.030.
124. Núñez, G.; Sakamoto, K.; Soares, M.P. Innate Nutritional Immunity. *J. Immunol.* **2018**, *201*, 11–18. doi: 10.4049/jimmunol.1800325.
125. Andersen, C.B.F.; Stødkilde, K.; Sæderup, K.L.; Kuhlee, A.; Raunser, S.; Graversen, J.H.; Moestrup, S.K. Haptoglobin. *Antioxid. Redox Signal.* **2017**, *26*, 814–831. doi: 10.1089/ars.2016.6793.
126. Kristiansen, M.; Graversen, J.H.; Jacobsen, C.; Sonne, O.; Hoffman, H.-J.; Law, S.K.A.; Moestrup, S.K. Identification of the haemoglobin scavenger receptor. *Nature* **2001**, *409*, 198–201. doi: 10.1038/35051594.
127. Etzerodt, A.; Moestrup, S.K. CD163 and Inflammation: Biological, Diagnostic, and Therapeutic Aspects. *Antioxid. Redox Signal.* **2013**, *18*, 2352–2363. doi: 10.1089/ars.2012.4834.

128. Raynes, J.G.; Eagling, S.; McAdam, K.P.W.J. Acute-phase protein synthesis in human hepatoma cells: differential regulation of serum amyloid A (SAA) and haptoglobin by interleukin-1 and interleukin-6. *Clin. Exp. Immunol.* **1991**, *83*, 488–491. doi: 10.1111/j.1365-2249.1991.tb05666.x.

129. Buechler, C.; Ritter, M.; Orsó, E.; Langmann, T.; Klucken, J.; Schmitz, G. Regulation of scavenger receptor CD163 expression in human monocytes and macrophages by pro- and antiinflammatory stimuli. *J. Leukoc. Biol.* **2000**, *67*, 97–103. doi: 10.1002/jlb.67.1.97.

130. Mitani, K.; Fujita, H.; Kappas, A.; Sassa, S. Heme oxygenase is a positive acute-phase reactant in human Hep3B hepatoma cells. *Blood* **1992**, *79*, 1255–1259.

131. Delanghe, J.; Allcock, K.; Langlois, M.; Claeys, L.; De Buyzere, M. Fast determination of haptoglobin phenotype and calculation of hemoglobin binding capacity using high pressure gel permeation chromatography. *Clin. Chim. Acta* **2000**, *291*, 43–51. doi: 10.1016/S0009-8981(99)00194-1.

132. Van Vlierberghe, H.; Langlois, M.; Delanghe, J. Haptoglobin polymorphisms and iron homeostasis in health and in disease. *Clin. Chim. Acta* **2004**, *345*, 35–42. doi: 10.1016/j.cccn.2004.03.016.

133. Tolosano, E.; Altruda, F. Hemopexin: Structure, Function, and Regulation. *DNA Cell Biol.* **2002**, *21*, 297–306. doi: 10.1089/104454902753759717.

134. Rolla, S.; Ingoglia, G.; Bardina, V.; Silengo, L.; Altruda, F.; Novelli, F.; Tolosano, E. Acute-Phase Protein Hemopexin Is a Negative Regulator of Th17 Response and Experimental Autoimmune Encephalomyelitis Development. *J. Immunol.* **2013**, *191*, 5451–5459. doi: 10.4049/jimmunol.1203076.

135. Tolosano, E.; Fagoonee, S.; Morello, N.; Vinchi, F.; Fiorito, V. Heme Scavenging and the Other Facets of Hemopexin. *Antioxid. Redox Signal.* **2010**, *12*, 305–320. doi: 10.1089/ars.2009.2787.

136. Hvidberg, V.; Maniecki, M.B.; Jacobsen, C.; Højrup, P.; Møller, H.J.; Moestrup, S.K. Identification of the receptor scavenging hemopexin-heme complexes. *Blood* **2005**, *106*, 2572–2579. doi: 10.1182/blood-2005-03-1185.

137. Cheng, A.G.; DeDent, A.C.; Schneewind, O.; Missiakas, D. A play in four acts: Staphylococcus aureus abscess formation. *Trends Microbiol.* **2011**, *19*, 225–232. doi: 10.1016/j.tim.2011.01.007.

138. Troxell, B.; Hassan, H.M. Transcriptional regulation by Ferric Uptake Regulator (Fur) in pathogenic bacteria. *Front. Cell. Infect. Microbiol.* **2013**, *3*, 1–13. doi: 10.3389/fcimb.2013.00059.

139. Mazmanian, S.K.; Ton-That, H.; Su, K.; Schneewind, O. An iron-regulated sortase anchors a class of surface protein during Staphylococcus aureus pathogenesis. *Proc. Natl. Acad. Sci.* **2002**, *99*, 2293–2298. doi: 10.1073/pnas.032523999.

140. Dale, S.E.; Doherty-Kirby, A.; Lajoie, G.; Heinrichs, D.E. Role of Siderophore Biosynthesis in Virulence of Staphylococcus aureus: Identification and Characterization of Genes Involved in Production of a Siderophore. *Infect. Immun.* **2004**, *72*, 29–37. doi: 10.1128/IAI.72.1.29-37.2004.

141. Marraffini, L.A.; Schneewind, O. Anchor Structure of Staphylococcal Surface Proteins. *J. Biol. Chem.* **2005**, *280*, 16263–16271. doi: 10.1074/jbc.M500071200.

142. Allard, M.; Moisan, H.; Brouillette, É.; Gervais, A.L.; Jacques, M.; Lacasse, P.; Diarra, M.S.; Malouin, F. Transcriptional modulation of some Staphylococcus aureus iron-regulated genes during growth in vitro and in a tissue cage model in vivo. *Microbes Infect.* **2006**, *8*, 1679–1690. doi: 10.1016/j.micinf.2006.01.022.

143. Biswas, L.; Biswas, R.; Nerz, C.; Ohlsen, K.; Schlag, M.; Schäfer, T.; Lamkemeyer, T.; Ziebandt, A.-K.; Hantke, K.; Rosenstein, R.; et al. Role of the Twin-Arginine Translocation Pathway in Staphylococcus. *J. Bacteriol.* **2009**, *191*, 5921–5929. doi: 10.1128/JB.00642-09.

144. Lojek, L.J.; Farrand, A.J.; Weiss, A.; Skaar, E.P. Fur regulation of Staphylococcus aureus heme oxygenases is required for heme homeostasis. *Int. J. Med. Microbiol.* **2018**, *308*, 582–589. doi: 10.1016/j.ijmm.2018.01.009.

145. Chen, F.; Liu, B.; Wang, D.; Wang, L.; Deng, X.; Bi, C.; Xiong, Y.; Wu, Q.; Cui, Y.; Zhang, Y.; et al. Role of sortase A in the pathogenesis of Staphylococcus aureus-induced mastitis in mice. *FEMS Microbiol. Lett.* **2014**, *351*, 95–103. doi: 10.1111/1574-6968.12354.

146. Torres, V.J.; Attia, A.S.; Mason, W.J.; Hood, M.I.; Corbin, B.D.; Beasley, F.C.; Anderson, K.L.; Stauff, D.L.; McDonald, W.H.; Zimmerman, L.J.; et al. Staphylococcus aureus Fur Regulates the Expression of Virulence Factors That Contribute to the Pathogenesis of Pneumonia. *Infect. Immun.* **2010**, *78*, 1618–1628. doi: 10.1128/IAI.01423-09.

147. Johnson, M.; Sengupta, M.; Purves, J.; Tarrant, E.; Williams, P.H.; Cockayne, A.; Muthaiyan, A.; Stephenson, R.; Ledala, N.; Wilkinson, B.J. Fur is required for the activation of virulence gene expression through the induction of the sae regulatory system in Staphylococcus aureus. *Int. J. Med. Microbiol.* **2011**, *301*, 44–52. doi: 10.1016/j.ijmm.2010.05.003.

148. Horsburgh, M.J.; Ingham, E.; Foster, S.J. In Staphylococcus aureus, Fur Is an Interactive Regulator with PerR, Contributes to Virulence, and Is Necessary for Oxidative Stress Resistance through Positive Regulation of Catalase and Iron Homeostasis. *J. Bacteriol.* **2001**, *183*, 468–475. doi: 10.1128/JB.183.2.468-475.2001.

149. Johnson, M.; Cockayne, A.; Morrissey, J.A. Iron-Regulated Biofilm Formation in Staphylococcus aureus Newman Requires ica and the Secreted Protein Emp. *Infect. Immun.* **2008**, *76*, 1756–1765. doi: 10.1128/IAI.01635-07.

150. Mäder, U.; Nicolas, P.; Depke, M.; Pané-Farré, J.; Debarbouille, M.; van der Kooi-Pol, M.M.; Guérin, C.; Dérozier, S.; Hiron, A.; Jarmer, H.; et al. Staphylococcus aureus Transcriptome Architecture: From Laboratory to Infection-Mimicking Conditions. *PLOS Genet.* **2016**, *12*, e1005962. doi: 10.1371/journal.pgen.1005962.

151. Liu, W.; Rochat, T.; Toffano-Nioche, C.; Le Lam, T.N.; Bouloc, P.; Morvan, C. Assessment of Bona Fide sRNAs in Staphylococcus aureus. *Front. Microbiol.* **2018**, *9*, 1–13. doi: 10.3389/fmicb.2018.00228.

152. Gaballa, A.; Antelmann, H.; Aguilar, C.; Khakh, S.K.; Song, K.-B.; Smaldone, G.T.; Helmann, J.D. The Bacillus subtilis iron-sparing response is mediated by a Fur-regulated small RNA and three small, basic proteins. *Proc. Natl. Acad. Sci.* **2008**, *105*, 11927–11932. doi: 10.1073/pnas.0711752105.

153. Janagama, H.K.; Senthilkumar; Bannantine, J.P.; Kugadas, A.; Jagtap, P.; Higgins, L.; Witthuhn, B.A.; Sreevatsan, S. Iron-sparing Response of Mycobacterium avium subsp. paratuberculosis is strain dependent. *BMC Microbiol.* **2010**, *10*, 268. doi: 10.1186/1471-2180-10-268.
154. Smaldone, G.T.; Revelles, O.; Gaballa, A.; Sauer, U.; Antelmann, H.; Helmann, J.D. A Global Investigation of the Bacillus subtilis Iron-Sparing Response Identifies Major Changes in Metabolism. *J. Bacteriol.* **2012**, *194*, 2594–2605. doi: 10.1128/JB.05990-11.
155. Oglesby-Sherrouse, A.G.; Murphy, E.R. Iron-responsive bacterial small RNAs: variations on a theme. *Metallomics* **2013**, *5*, 276. doi: 10.1039/c3mt20224k.
156. Zheng, T.; Nolan, E.M. Siderophore-based detection of Fe(iii) and microbial pathogens. *Metallomics* **2012**, *4*, 866. doi: 10.1039/c2mt20082a.
157. Hider, R.C.; Kong, X. Chemistry and biology of siderophores. *Nat. Prod. Rep.* **2010**, *27*, 637. doi: 10.1039/b906679a.
158. Carrano, C.J.; Raymond, K.N. Ferric ion sequestering agents. 2. Kinetics and mechanism of iron removal from transferrin by enterobactin and synthetic tricatechols. *J. Am. Chem. Soc.* **1979**, *101*, 5401–5404. doi: 10.1021/ja00512a047.
159. Crumbliss, A.L.; Harrington, J.M. Iron sequestration by small molecules: Thermodynamic and kinetic studies of natural siderophores and synthetic model compounds. In *Advances in Inorganic Chemistry*; Elsevier, 2009; Vol. 61, pp. 179–250 ISBN 9780123750334. doi: 10.1016/S0898-8838(09)00204-9.
160. Harrington, J.M.; Crumbliss, A.L. The redox hypothesis in siderophore-mediated iron uptake. *BioMetals* **2009**, *22*, 679–689. doi: 10.1007/s10534-009-9233-4.
161. Holden, V.I.; Bachman, M.A. Diverging roles of bacterial siderophores during infection. *Metallomics* **2015**, *7*, 986–995. doi: 10.1039/C4MT00333K.
162. Raisen, C. Investigation of a novel iron-uptake system and other genomic features in mecC Staphylococcus aureus, University of Cambridge, 2019.
163. KONETSCHNY-RAPP, S.; JUNG, G.; MEIWES, J.; ZAHNER, H. Staphyloferrin A: a structurally new siderophore from staphylococci. *Eur. J. Biochem.* **1990**, *191*, 65–74. doi: 10.1111/j.1432-1033.1990.tb19094.x.

164. Meiwes, J. Isolation and characterization of staphyloferrin A, a compound with siderophore activity from Staphylococcus hyicus DSM 20459. *FEMS Microbiol. Lett.* **1990**, *67*, 201–205. doi: 10.1016/0378-1097(90)90195-V.

165. Drechsel, H.; Freund, S.; Nicholson, G.; Haag, H.; Jung, O.; ZAHNER, H.; Jung, G. Purification and chemical characterization of staphyloferrin B, a hydrophilic siderophore from staphylococci. *Biometals* **1993**, *6*, 185–192. doi: 10.1007/BF00205858.

166. Haag, H.; Fiedler, H.-P.; Meiwes, J.; Drechsel, H.; Jung, G.; Zähner, H. Isolation and biological characterization of staphyloferrin B, a compound with siderophore activity from staphylococci. *FEMS Microbiol. Lett.* **1994**, *115*, 125–130. doi: 10.1111/j.1574-6968.1994.tb06626.x.

167. Perry, W.J.; Spraggins, J.M.; Sheldon, J.R.; Grunenwald, C.M.; Heinrichs, D.E.; Cassat, J.E.; Skaar, E.P.; Caprioli, R.M. Staphylococcus aureus exhibits heterogeneous siderophore production within the vertebrate host. *Proc. Natl. Acad. Sci.* **2019**, *116*, 21980–21982. doi: 10.1073/pnas.1913991116.

168. Verstraete, M.M.; Perez-Borrajero, C.; Brown, K.L.; Heinrichs, D.E.; Murphy, M.E.P. SbnI is a free serine kinase that generates O -phospho-l-serine for staphyloferrin B biosynthesis in Staphylococcus aureus. *J. Biol. Chem.* **2018**, *293*, 6147–6160. doi: 10.1074/jbc.RA118.001875.

169. Miethke, M.; Klotz, O.; Linne, U.; May, J.J.; Beckering, C.L.; Marahiel, M.A. Ferri-bacillibactin uptake and hydrolysis in Bacillus subtilis. *Mol. Microbiol.* **2006**, *61*, 1413–1427. doi: 10.1111/j.1365-2958.2006.05321.x.

170. Beasley, F.C.; Marolda, C.L.; Cheung, J.; Buac, S.; Heinrichs, D.E. Staphylococcus aureus Transporters Hts, Sir, and Sst Capture Iron Liberated from Human Transferrin by Staphyloferrin A, Staphyloferrin B, and Catecholamine Stress Hormones, Respectively, and Contribute to Virulence. *Infect. Immun.* **2011**, *79*, 2345–2355. doi: 10.1128/IAI.00117-11.

171. Beasley, F.C.; Vinés, E.D.; Grigg, J.C.; Zheng, Q.; Liu, S.; Lajoie, G.A.; Murphy, M.E.P.; Heinrichs, D.E. Characterization of staphyloferrin A biosynthetic and transport mutants in Staphylococcus aureus. *Mol. Microbiol.* **2009**, *72*, 947–963. doi: 10.1111/j.1365-2958.2009.06698.x.

172. Cotton, J.L.; Tao, J.; Balibar, C.J. Identification and Characterization of the Staphylococcus aureus Gene Cluster Coding for Staphyloferrin A †. *Biochemistry* **2009**, *48*, 1025–1035. doi: 10.1021/bi801844c.
173. Grigg, J.C.; Cooper, J.D.; Cheung, J.; Heinrichs, D.E.; Murphy, M.E.P. The Staphylococcus aureus Siderophore Receptor HtsA Undergoes Localized Conformational Changes to Enclose Staphyloferrin A in an Arginine-rich Binding Pocket. *J. Biol. Chem.* **2010**, *285*, 11162–11171. doi: 10.1074/jbc.M109.097865.
174. Skaar, E.P. Iron-Source Preference of Staphylococcus aureus Infections. *Science* **2004**, *305*, 1626–1628. doi: 10.1126/science.1099930.
175. Speziali, C.D.; Dale, S.E.; Henderson, J.A.; Vinés, E.D.; Heinrichs, D.E. Requirement of Staphylococcus aureus ATP-Binding Cassette-ATPase FhuC for Iron-Restricted Growth and Evidence that It Functions with More than One Iron Transporter. *J. Bacteriol.* **2006**, *188*, 2048–2055. doi: 10.1128/JB.188.6.2048-2055.2006.
176. Hannauer, M.; Arifin, A.J.; Heinrichs, D.E. Involvement of reductases IruO and NtrA in iron acquisition by Staphylococcus aureus. *Mol. Microbiol.* **2015**, *96*, 1192–1210. doi: 10.1111/mmi.13000.
177. Cheung, J.; Beasley, F.C.; Liu, S.; Lajoie, G.A.; Heinrichs, D.E. Molecular characterization of staphyloferrin B biosynthesis in Staphylococcus aureus. *Mol. Microbiol.* **2009**, *74*, 594–608. doi: 10.1111/j.1365-2958.2009.06880.x.
178. Heinrichs, J.H.; Gatlin, L.E.; Kunsch, C.; Choi, G.H.; Hanson, M.S. Identification and characterization of SirA, an iron-regulated protein from Staphylococcus aureus. *J. Bacteriol.* **1999**, *181*, 1436–1443.
179. Courcol, R.J.; Trivier, D.; Bissinger, M.C.; Martin, G.R.; Brown, M.R.W. Siderophore production by Staphylococcus aureus and identification of iron-regulated proteins. *Infect. Immun.* **1997**, *65*, 1944–1948.
180. Sebulsky, M.T.; Hohnstein, D.; Hunter, M.D.; Heinrichs, D.E. Identification and Characterization of a Membrane Permease Involved in Iron-Hydroxamate Transport inStaphylococcus aureus. *J. Bacteriol.* **2000**, *182*, 4394–4400. doi: 10.1128/JB.182.16.4394-4400.2000.

181. Torres, V.J.; Pishchany, G.; Humayun, M.; Schneewind, O.; Skaar, E.P. Staphylococcus aureus IsdB Is a Hemoglobin Receptor Required for Heme Iron Utilization. *J. Bacteriol.* **2006**, *188*, 8421–8429. doi: 10.1128/JB.01335-06.
182. Pishchany, G.; Dickey, S.E.; Skaar, E.P. Subcellular Localization of the Staphylococcus aureus Heme Iron Transport Components IsdA and IsdB. *Infect. Immun.* **2009**, *77*, 2624–2634. doi: 10.1128/IAI.01531-08.
183. Farrand, A.J.; Reniere, M.L.; Ingmer, H.; Frees, D.; Skaar, E.P. Regulation of Host Hemoglobin Binding by the Staphylococcus aureus Clp Proteolytic System. *J. Bacteriol.* **2013**, *195*, 5041–5050. doi: 10.1128/JB.00505-13.
184. Reniere, M.L.; Torres, V.J.; Skaar, E.P. Intracellular metalloporphyrin metabolism in Staphylococcus aureus. *BioMetals* **2007**, *20*, 333–345. doi: 10.1007/s10534-006-9032-0.
185. Kramer, J.; Özkaya, Ö.; Kümmerli, R. Bacterial siderophores in community and host interactions. *Nat. Rev. Microbiol.* **2020**, *18*, 152–163. doi: 10.1038/s41579-019-0284-4.
186. Patel, T.A.; Belcher, E.; Warner, T.D.; Harding, S.E.; Mitchell, J.A. Identification and Characterization of a Dysfunctional Cardiac Myocyte Phenotype: Role of Bacteria, Toll-like Receptors, and Endothelin. *Shock* **2007**, *28*, 434–440. doi: 10.1097/shk.0b013e31804a55a7.
187. Torres, V.J.; Stauff, D.L.; Pishchany, G.; Bezbradica, J.S.; Gordy, L.E.; Iturregui, J.; Anderson, K.L.; Dunman, P.M.; Joyce, S.; Skaar, E.P. A Staphylococcus aureus Regulatory System that Responds to Host Heme and Modulates Virulence. *Cell Host Microbe* **2007**, *1*, 109–119. doi: 10.1016/j.chom.2007.03.001.
188. Stauff, D.L.; Torres, V.J.; Skaar, E.P. Signaling and DNA-binding Activities of the Staphylococcus aureus HssR-HssS Two-component System Required for Heme Sensing. *J. Biol. Chem.* **2007**, *282*, 26111–26121. doi: 10.1074/jbc.M703797200.
189. Wakeman, C.A.; Stauff, D.L.; Zhang, Y.; Skaar, E.P. Differential Activation of Staphylococcus aureus Heme Detoxification Machinery by Heme Analogues. *J. Bacteriol.* **2014**, *196*, 1335–1342. doi: 10.1128/JB.01067-13.
190. Surdel, M.C.; Dutter, B.F.; Sulikowski, G.A.; Skaar, E.P. Bacterial Nitric Oxide Synthase Is Required for the Staphylococcus aureus Response to Heme Stress. *ACS Infect. Dis.* **2016**, *2*, 572–578. doi: 10.1021/acsinfecdis.6b00081.

191. Turlin, E.; Débarbouillé, M.; Augustyniak, K.; Gilles, A.-M.; Wandersman, C. Staphylococcus aureus FepA and FepB Proteins Drive Heme Iron Utilization in Escherichia coli. *PLoS One* **2013**, *8*, e56529. doi: 10.1371/journal.pone.0056529.
192. Laakso, H.A.; Marolda, C.L.; Pinter, T.B.; Stillman, M.J.; Heinrichs, D.E. A Heme-responsive Regulator Controls Synthesis of Staphyloferrin B in Staphylococcus aureus. *J. Biol. Chem.* **2016**, *291*, 29–40. doi: 10.1074/jbc.M115.696625.
193. Verstraete, M.M.; Morales, L.D.; Kobylarz, M.J.; Loutet, S.A.; Laakso, H.A.; Pinter, T.B.; Stillman, M.J.; Heinrichs, D.E.; Murphy, M.E.P. The heme-sensitive regulator SbnI has a bifunctional role in staphyloferrin B production by Staphylococcus aureus. *J. Biol. Chem.* **2019**, *294*, 11622–11636. doi: 10.1074/jbc.RA119.007757.
194. Horsburgh, M.J.; Clements, M.O.; Crossley, H.; Ingham, E.; Foster, S.J. PerR Controls Oxidative Stress Resistance and Iron Storage Proteins and Is Required for Virulence in Staphylococcus aureus. *Infect. Immun.* **2001**, *69*, 3744–3754. doi: 10.1128/IAI.69.6.3744-3754.2001.
195. Morrissey, J.A.; Cockayne, A.; Brummell, K.; Williams, P. The Staphylococcal Ferritins Are Differentially Regulated in Response to Iron and Manganese and via PerR and Fur. *Infect. Immun.* **2004**, *72*, 972–979. doi: 10.1128/IAI.72.2.972-979.2004.
196. Morikawa, K.; Ushijima, Y.; Ohniwa, R.L.; Miyakoshi, M.; Takeyasu, K. What Happens in the Staphylococcal Nucleoid under Oxidative Stress? *Microorganisms* **2019**, *7*, 631. doi: 10.3390/microorganisms7120631.
197. Spirig, T.; Malmirchegini, G.R.; Zhang, J.; Robson, S.A.; Sjodt, M.; Liu, M.; Krishna Kumar, K.; Dickson, C.F.; Gell, D.A.; Lei, B.; et al. Staphylococcus aureus Uses a Novel Multidomain Receptor to Break Apart Human Hemoglobin and Steal Its Heme. *J. Biol. Chem.* **2013**, *288*, 1065–1078. doi: 10.1074/jbc.M112.419119.
198. Bowden, C.F.M.; Verstraete, M.M.; Eltis, L.D.; Murphy, M.E.P. Hemoglobin Binding and Catalytic Heme Extraction by IsdB Near Iron Transporter Domains. *Biochemistry* **2014**, *53*, 2286–2294. doi: 10.1021/bi500230f.
199. Moriwaki, Y.; Terada, T.; Tsumoto, K.; Shimizu, K. Rapid Heme Transfer Reactions between NEAr Transporter Domains of Staphylococcus aureus: A Theoretical Study Using QM/MM and MD Simulations. *PLoS One* **2015**, *10*, e0145125. doi: 10.1371/journal.pone.0145125.

200. Sjodt, M.; Macdonald, R.; Spirig, T.; Chan, A.H.; Dickson, C.F.; Fabian, M.; Olson, J.S.; Gell, D.A.; Clubb, R.T. The PRE-Derived NMR Model of the 38.8-kDa Tri-Domain IsdH Protein from Staphylococcus aureus Suggests That It Adaptively Recognizes Human Hemoglobin. *J. Mol. Biol.* **2016**, *428*, 1107–1129. doi: 10.1016/j.jmb.2015.02.008.

201. Choby, J.E.; Skaar, E.P. Heme Synthesis and Acquisition in Bacterial Pathogens. *J. Mol. Biol.* **2016**, *428*, 3408–3428. doi: 10.1016/j.jmb.2016.03.018.

202. Mazmanian, S.K. Passage of Heme-Iron Across the Envelope of Staphylococcus aureus. *Science* **2003**, *299*, 906–909. doi: 10.1126/science.1081147.

203. Muryoi, N.; Tiedemann, M.T.; Pluym, M.; Cheung, J.; Heinrichs, D.E.; Stillman, M.J. Demonstration of the Iron-regulated Surface Determinant (Isd) Heme Transfer Pathway in Staphylococcus aureus. *J. Biol. Chem.* **2008**, *283*, 28125–28136. doi: 10.1074/jbc.M802171200.

204. Zhu, H.; Xie, G.; Liu, M.; Olson, J.S.; Fabian, M.; Dooley, D.M.; Lei, B. Pathway for Heme Uptake from Human Methemoglobin by the Iron-regulated Surface Determinants System of Staphylococcus aureus. *J. Biol. Chem.* **2008**, *283*, 18450–18460. doi: 10.1074/jbc.M801466200.

205. Villareal, V.A.; Spirig, T.; Robson, S.A.; Liu, M.; Lei, B.; Clubb, R.T. Transient Weak Protein–Protein Complexes Transfer Heme Across the Cell Wall of Staphylococcus aureus. *J. Am. Chem. Soc.* **2011**, *133*, 14176–14179. doi: 10.1021/ja203805b.

206. Tiedemann, M.T.; Stillman, M.J. Heme binding to the IsdE(M78A; H229A) double mutant: challenging unidirectional heme transfer in the iron-regulated surface determinant protein heme transfer pathway of Staphylococcus aureus. *JBIC J. Biol. Inorg. Chem.* **2012**, *17*, 995–1007. doi: 10.1007/s00775-012-0914-z.

207. Mazmanian, S.K.; Liu, G.; Jensen, E.R.; Lenoy, E.; Schneewind, O. Staphylococcus aureus sortase mutants defective in the display of surface proteins and in the pathogenesis of animal infections. *Proc. Natl. Acad. Sci.* **2000**, *97*, 5510–5515. doi: 10.1073/pnas.080520697.

208. Reniere, M.L.; Skaar, E.P. Staphylococcus aureus haem oxygenases are differentially regulated by iron and haem. *Mol. Microbiol.* **2008**, *69*, 1304–1315. doi: 10.1111/j.1365-2958.2008.06363.x.

209. Wandersman, C.; Delepelaire, P. Bacterial Iron Sources: From Siderophores to Hemophores. *Annu. Rev. Microbiol.* **2004**, *58*, 611–647. doi: 10.1146/annurev.micro.58.030603.123811.

210. Ton-That, H.; Liu, G.; Mazmanian, S.K.; Faull, K.F.; Schneewind, O. Purification and characterization of sortase, the transpeptidase that cleaves surface proteins of Staphylococcus aureus at the LPXTG motif. *Proc. Natl. Acad. Sci.* **1999**, *96*, 12424–12429. doi: 10.1073/pnas.96.22.12424.

211. DeDent, A.; Bae, T.; Missiakas, D.M.; Schneewind, O. Signal peptides direct surface proteins to two distinct envelope locations of Staphylococcus aureus. *EMBO J.* **2008**, *27*, 2656–2668. doi: 10.1038/emboj.2008.185.

212. Silhavy, T.J.; Kahne, D.; Walker, S. The Bacterial Cell Envelope. *Cold Spring Harb. Perspect. Biol.* **2010**, *2*, a000414–a000414. doi: 10.1101/cshperspect.a000414.

213. Spirig, T.; Weiner, E.M.; Clubb, R.T. Sortase enzymes in Gram-positive bacteria. *Mol. Microbiol.* **2011**, *82*, 1044–1059. doi: 10.1111/j.1365-2958.2011.07887.x.

214. Jacobitz, A.W.; Kattke, M.D.; Wereszczynski, J.; Clubb, R.T. Sortase Transpeptidases: Structural Biology and Catalytic Mechanism. In *Advances in Protein Chemistry and Structural Biology*; Elsevier Inc., 2017; Vol. 109, pp. 223–264. doi: 10.1016/bs.apcsb.2017.04.008.

215. Ton-That, H.; Marraffini, L.A.; Schneewind, O. Protein sorting to the cell wall envelope of Gram-positive bacteria. *Biochim. Biophys. Acta - Mol. Cell Res.* **2004**, *1694*, 269–278. doi: 10.1016/j.bbamcr.2004.04.014.

216. Navarre, W.W.; Schneewind, O. Surface Proteins of Gram-Positive Bacteria and Mechanisms of Their Targeting to the Cell Wall Envelope. *Microbiol. Mol. Biol. Rev.* **1999**, *63*, 174–229. doi: 10.1128/MMBR.63.1.174-229.1999.

217. Taylor, J.M.; Heinrichs, D.E. Transferrin binding in Staphylococcus aureus: involvement of a cell wall-anchored protein. *Mol. Microbiol.* **2002**, *43*, 1603–1614. doi: 10.1046/j.1365-2958.2002.02850.x.

218. Morrissey, J.A.; Cockayne, A.; Hammacott, J.; Bishop, K.; Denman-Johnson, A.; Hill, P.J.; Williams, P. Conservation, Surface Exposure, and In Vivo Expression of the Frp Family of Iron-Regulated Cell Wall Proteins in Staphylococcus aureus. *Infect. Immun.* **2002**, *70*, 2399–2407. doi: 10.1128/IAI.70.5.2399-2407.2002.

219. Dryla, A.; Gelbmann, D.; Von Gabain, A.; Nagy, E. Identification of a novel iron regulated staphylococcal surface protein with haptoglobin-haemoglobin binding activity. *Mol. Microbiol.* **2003**, *49*, 37–53. doi: 10.1046/j.1365-2958.2003.03542.x.

220. Moriwaki, Y.; Caaveiro, J.M.M.; Tanaka, Y.; Tsutsumi, H.; Hamachi, I.; Tsumoto, K. Molecular Basis of Recognition of Antibacterial Porphyrins by Heme-Transporter IsdH-NEAT3 of Staphylococcus aureus. *Biochemistry* **2011**, *50*, 7311–7320. doi: 10.1021/bi200493h.

221. Liu, M.; Tanaka, W.N.; Zhu, H.; Xie, G.; Dooley, D.M.; Lei, B. Direct Hemin Transfer from IsdA to IsdC in the Iron-regulated Surface Determinant (Isd) Heme Acquisition System of Staphylococcus aureus. *J. Biol. Chem.* **2008**, *283*, 6668–6676. doi: 10.1074/jbc.M708372200.

222. Grigg, J.C.; Mao, C.X.; Murphy, M.E.P. Iron-Coordinating Tyrosine Is a Key Determinant of NEAT Domain Heme Transfer. *J. Mol. Biol.* **2011**, *413*, 684–698. doi: 10.1016/j.jmb.2011.08.047.

223. Abe, R.; Caaveiro, J.M.M.; Kozuka-Hata, H.; Oyama, M.; Tsumoto, K. Mapping Ultra-weak Protein-Protein Interactions between Heme Transporters of Staphylococcus aureus. *J. Biol. Chem.* **2012**, *287*, 16477–16487. doi: 10.1074/jbc.M112.346700.

224. Bowden, C.F.M.; Chan, A.C.K.; Li, E.J.W.; Arrieta, A.L.; Eltis, L.D.; Murphy, M.E.P. Structure–function analyses reveal key features in Staphylococcus aureus IsdB-associated unfolding of the heme-binding pocket of human hemoglobin. *J. Biol. Chem.* **2018**, *293*, 177–190. doi: 10.1074/jbc.M117.806562.

225. Gaudin, C.F.M.; Grigg, J.C.; Arrieta, A.L.; Murphy, M.E.P. Unique Heme-Iron Coordination by the Hemoglobin Receptor IsdB of Staphylococcus aureus. *Biochemistry* **2011**, *50*, 5443–5452. doi: 10.1021/bi200369p.

226. Moriwaki, Y.; Terada, T.; Caaveiro, J.M.M.; Takaoka, Y.; Hamachi, I.; Tsumoto, K.; Shimizu, K. Heme Binding Mechanism of Structurally Similar Iron-Regulated Surface Determinant Near Transporter Domains of Staphylococcus aureus Exhibiting Different Affinities for Heme. *Biochemistry* **2013**, *52*, 8866–8877. doi: 10.1021/bi4008325.

227. Andrade, M.A.; Ciccarelli, F.D.; Perez-Iratxeta, C.; Bork, P. NEAT: a domain duplicated in genes near the components of a putative Fe3+ siderophore transporter from Gram-positive pathogenic bacteria. *Genome Biol.* **2002**, *3*, research0047.1. doi: https://doi.org/10.1186/gb-2002-3-9-research0047.

228. Sharp, K.H.; Schneider, S.; Cockayne, A.; Paoli, M. Crystal Structure of the Heme-IsdC Complex, the Central Conduit of the Isd Iron/Heme Uptake System in Staphylococcus aureus. *J. Biol. Chem.* **2007**, *282*, 10625–10631. doi: 10.1074/jbc.M700234200.

229. Watanabe, M.; Tanaka, Y.; Suenaga, A.; Kuroda, M.; Yao, M.; Watanabe, N.; Arisaka, F.; Ohta, T.; Tanaka, I.; Tsumoto, K. Structural Basis for Multimeric Heme Complexation through a Specific Protein-Heme Interaction. *J. Biol. Chem.* **2008**, *283*, 28649–28659. doi: 10.1074/jbc.M803383200.

230. Pluym, M.; Muryoi, N.; Heinrichs, D.E.; Stillman, M.J. Heme binding in the NEAT domains of IsdA and IsdC of Staphylococcus aureus. *J. Inorg. Biochem.* **2008**, *102*, 480–488. doi: 10.1016/j.jinorgbio.2007.11.011.

231. Macdonald, R.; Mahoney, B.J.; Ellis-Guardiola, K.; Maresso, A.; Clubb, R.T. NMR experiments redefine the hemoglobin binding properties of bacterial NEAr-iron Transporter domains. *Protein Sci.* **2019**, *28*, 1513–1523. doi: 10.1002/pro.3662.

232. Bateman, A. UniProt: a worldwide hub of protein knowledge. *Nucleic Acids Res.* **2019**, *47*, D506–D515. doi: 10.1093/nar/gky1049.

233. Fonner, B.A.; Tripet, B.P.; Eilers, B.J.; Stanisich, J.; Sullivan-Springhetti, R.K.; Moore, R.; Liu, M.; Lei, B.; Copié, V. Solution Structure and Molecular Determinants of Hemoglobin Binding of the First NEAT Domain of IsdB in Staphylococcus aureus. *Biochemistry* **2014**, *53*, 3922–3933. doi: 10.1021/bi5005188.

234. Pilpa, R.M.; Robson, S.A.; Villareal, V.A.; Wong, M.L.; Phillips, M.; Clubb, R.T. Functionally Distinct NEAT (NEAr Transporter) Domains within the Staphylococcus aureus IsdH/HarA Protein Extract Heme from Methemoglobin. *J. Biol. Chem.* **2009**, *284*, 1166–1176. doi: 10.1074/jbc.M806007200.

235. Sæderup, K.L.; Stødkilde, K.; Graversen, J.H.; Dickson, C.F.; Etzerodt, A.; Hansen, S.W.K.; Fago, A.; Gell, D.; Andersen, C.B.F.; Moestrup, S.K. The Staphylococcus aureus Protein IsdH Inhibits Host Hemoglobin Scavenging to Promote Heme Acquisition by the Pathogen. *J. Biol. Chem.* **2016**, *291*, 23989–23998. doi: 10.1074/jbc.M116.755934.

236. Krishna Kumar, K.; Jacques, D.A.; Pishchany, G.; Caradoc-Davies, T.; Spirig, T.; Malmirchegini, G.R.; Langley, D.B.; Dickson, C.F.; Mackay, J.P.; Clubb, R.T.; et al. Structural Basis for Hemoglobin Capture by Staphylococcus aureus Cell-surface Protein, IsdH. *J. Biol. Chem.* **2011**, *286*, 38439–38447. doi: 10.1074/jbc.M111.287300.

237. Dickson, C.F.; Kumar, K.K.; Jacques, D.A.; Malmirchegini, G.R.; Spirig, T.; Mackay, J.P.; Clubb, R.T.; Guss, J.M.; Gell, D.A. Structure of the Hemoglobin-IsdH Complex Reveals the Molecular Basis of Iron Capture by Staphylococcus aureus. *J. Biol. Chem.* **2014**, *289*, 6728–6738. doi: 10.1074/jbc.M113.545566.

238. Pishchany, G.; Sheldon, J.R.; Dickson, C.F.; Alam, M.T.; Read, T.D.; Gell, D.A.; Heinrichs, D.E.; Skaar, E.P. IsdB-dependent Hemoglobin Binding Is Required for Acquisition of Heme by Staphylococcus aureus. *J. Infect. Dis.* **2014**, *209*, 1764–1772. doi: 10.1093/infdis/jit817.

239. Dickson, C.F.; Jacques, D.A.; Clubb, R.T.; Guss, J.M.; Gell, D.A. The structure of haemoglobin bound to the haemoglobin receptor IsdH from Staphylococcus aureus shows disruption of the native α-globin haem pocket. *Acta Crystallogr. Sect. D Biol. Crystallogr.* **2015**, *71*, 1295–1306. doi: 10.1107/S1399004715005817.

240. Sjodt, M.; Macdonald, R.; Marshall, J.D.; Clayton, J.; Olson, J.S.; Phillips, M.; Gell, D.A.; Wereszczynski, J.; Clubb, R.T. Energetics underlying hemin extraction from human hemoglobin by Staphylococcus aureus. *J. Biol. Chem.* **2018**, *293*, 6942–6957. doi: 10.1074/jbc.RA117.000803.

241. Ellis-Guardiola, K.; Clayton, J.; Pham, C.; Mahoney, B.J.; Wereszczynski, J.; Clubb, R.T. The Staphylococcus aureus IsdH Receptor Forms a Dynamic Complex with Human Hemoglobin that Triggers Heme Release via Two Distinct Hot Spots. *J. Mol. Biol.* **2020**, *432*, 1064–1082. doi: 10.1016/j.jmb.2019.12.023.

242. Spirig, T.; Clubb, R.T. Backbone 1H, 13C and 15N resonance assignments of the 39 kDa staphylococcal hemoglobin receptor IsdH. *Biomol. NMR Assign.* **2012**, *6*, 169–172. doi: 10.1007/s12104-011-9348-8.

243. Mikkelsen, J.H.; Runager, K.; Andersen, C.B.F. The human protein haptoglobin inhibits IsdH-mediated heme-sequestering by Staphylococcus aureus. *J. Biol. Chem.* **2020**, *295*, 1781–1791. doi: 10.1074/jbc.RA119.011612.

244. Pilpa, R.M.; Fadeev, E.A.; Villareal, V.A.; Wong, M.L.; Phillips, M.; Clubb, R.T. Solution Structure of the NEAT (NEAr Transporter) Domain from IsdH/HarA: the Human Hemoglobin Receptor in Staphylococcus aureus. *J. Mol. Biol.* **2006**, *360*, 435–447. doi: 10.1016/j.jmb.2006.05.019.

245. Dryla, A.; Hoffmann, B.; Gelbmann, D.; Giefing, C.; Hanner, M.; Meinke, A.; Anderson, A.S.; Koppensteiner, W.; Konrat, R.; von Gabain, A.; et al. High-Affinity Binding of the Staphylococcal HarA Protein to Haptoglobin and Hemoglobin Involves a Domain with an Antiparallel Eight-Stranded β-Barrel Fold. *J. Bacteriol.* **2007**, *189*, 254–264. doi: 10.1128/JB.01366-06.

246. Honsa, E.S.; Maresso, A.W.; Highlander, S.K. Molecular and Evolutionary Analysis of NEAr-Iron Transporter (NEAT) Domains. *PLoS One* **2014**, *9*, e104794. doi: 10.1371/journal.pone.0104794.

247. Brewitz, H.H.; Hagelueken, G.; Imhof, D. Structural and functional diversity of transient heme binding to bacterial proteins. *Biochim. Biophys. Acta - Gen. Subj.* **2017**, *1861*, 683–697. doi: 10.1016/j.bbagen.2016.12.021.

248. Grigg, J.C.; Vermeiren, C.L.; Heinrichs, D.E.; Murphy, M.E.P. Haem recognition by a Staphylococcus aureus NEAT domain. *Mol. Microbiol.* **2007**, *63*, 139–149. doi: 10.1111/j.1365-2958.2006.05502.x.

249. Villareal, V.A.; Pilpa, R.M.; Robson, S.A.; Fadeev, E.A.; Clubb, R.T. The IsdC Protein from Staphylococcus aureus Uses a Flexible Binding Pocket to Capture Heme. *J. Biol. Chem.* **2008**, *283*, 31591–31600. doi: 10.1074/jbc.M801126200.

250. Sakipov, S.; Rafikova, O.; Kurnikova, M.G.; Rafikov, R. Molecular mechanisms of bio-catalysis of heme extraction from hemoglobin. *Redox Biol.* **2017**, *11*, 516–523. doi: 10.1016/j.redox.2017.01.004.

251. Grigg, J.C.; Ukpabi, G.; Gaudin, C.F.M.; Murphy, M.E.P. Structural biology of heme binding in the Staphylococcus aureus Isd system. *J. Inorg. Biochem.* **2010**, *104*, 341–348. doi: 10.1016/j.jinorgbio.2009.09.012.

252. Vermeiren, C.L.; Pluym, M.; Mack, J.; Heinrichs, D.E.; Stillman, M.J. Characterization of the Heme Binding Properties of Staphylococcus aureus IsdA †. *Biochemistry* **2006**, *45*, 12867–12875. doi: 10.1021/bi0607711.

253. Tiedemann, M.T.; Muryoi, N.; Heinrichs, D.E.; Stillman, M.J. Characterization of IsdH (NEAT domain 3) and IsdB (NEAT domain 2) in Staphylococcus aureus by magnetic circular dichroism spectroscopy and electrospray ionization mass spectrometry. *J. Porphyr. Phthalocyanines* **2009**, *13*, 1006–1016. doi: 10.1142/S1088424609001352.

254. Hempel, K.; Herbst, F.-A.; Moche, M.; Hecker, M.; Becher, D. Quantitative Proteomic View on Secreted, Cell Surface-Associated, and Cytoplasmic Proteins of the Methicillin-Resistant Human Pathogen Staphylococcus aureus under Iron-Limited Conditions. *J. Proteome Res.* **2011**, *10*, 1657–1666. doi: 10.1021/pr1009838.

255. Ho, W.W.; Li, H.; Eakanunkul, S.; Tong, Y.; Wilks, A.; Guo, M.; Poulos, T.L. Holo- and Apo-bound Structures of Bacterial Periplasmic Heme-binding Proteins. *J. Biol. Chem.* **2007**, *282*, 35796–35802. doi: 10.1074/jbc.M706761200.

256. Berntsson, R.P.A.; Smits, S.H.J.; Schmitt, L.; Slotboom, D.-J.; Poolman, B. A structural classification of substrate-binding proteins. *FEBS Lett.* **2010**, *584*, 2606–2617. doi: 10.1016/j.febslet.2010.04.043.

257. Rice, A.J.; Park, A.; Pinkett, H.W. Diversity in ABC transporters: Type I, II and III importers. *Crit. Rev. Biochem. Mol. Biol.* **2014**, *49*, 426–437. doi: 10.3109/10409238.2014.953626.

258. Mack, J.; Vermeiren, C.; Heinrichs, D.E.; Stillman, M.J. In vivo heme scavenging by Staphylococcus aureus IsdC and IsdE proteins. *Biochem. Biophys. Res. Commun.* **2004**, *320*, 781–788. doi: 10.1016/j.bbrc.2004.06.025.

259. Grigg, J.C.; Vermeiren, C.L.; Heinrichs, D.E.; Murphy, M.E.P. Heme Coordination by Staphylococcus aureus IsdE. *J. Biol. Chem.* **2007**, *282*, 28815–28822. doi: 10.1074/jbc.M704602200.

260. Tiedemann, M.T.; Pinter, T.B.J.; Stillman, M.J. Insight into blocking heme transfer by exploiting molecular interactions in the core Isd heme transporters IsdA-NEAT, IsdC-NEAT, and IsdE of Staphylococcus aureus. *Metallomics* **2012**, *4*, 751. doi: 10.1039/c2mt20067h.

261. Skaar, E.P.; Gaspar, A.H.; Schneewind, O. IsdG and IsdI, Heme-degrading Enzymes in the Cytoplasm of Staphylococcus aureus. *J. Biol. Chem.* **2004**, *279*, 436–443. doi: 10.1074/jbc.M307952200.

262. Reniere, M.L.; Ukpabi, G.N.; Harry, S.R.; Stec, D.F.; Krull, R.; Wright, D.W.; Bachmann, B.O.; Murphy, M.E.; Skaar, E.P. The IsdG-family of haem oxygenases degrades haem to a novel chromophore. *Mol. Microbiol.* **2010**, *75*, 1529–1538. doi: 10.1111/j.1365-2958.2010.07076.x.

263. Matsui, T.; Nambu, S.; Ono, Y.; Goulding, C.W.; Tsumoto, K.; Ikeda-Saito, M. Heme Degradation by Staphylococcus aureus IsdG and IsdI Liberates Formaldehyde Rather Than Carbon Monoxide. *Biochemistry* **2013**, *52*, 3025–3027. doi: 10.1021/bi400382p.

264. Wu, R.; Skaar, E.P.; Zhang, R.; Joachimiak, G.; Gornicki, P.; Schneewind, O.; Joachimiak, A. Staphylococcus aureus IsdG and IsdI, Heme-degrading Enzymes with Structural Similarity to Monooxygenases. *J. Biol. Chem.* **2005**, *280*, 2840–2846. doi: 10.1074/jbc.M409526200.

265. Lee, W.C.; Reniere, M.L.; Skaar, E.P.; Murphy, M.E.P. Ruffling of Metalloporphyrins Bound to IsdG and IsdI, Two Heme-degrading Enzymes in Staphylococcus aureus. *J. Biol. Chem.* **2008**, *283*, 30957–30963. doi: 10.1074/jbc.M709486200.

266. Haley, K.P.; Janson, E.M.; Heilbronner, S.; Foster, T.J.; Skaar, E.P. Staphylococcus lugdunensis IsdG Liberates Iron from Host Heme. *J. Bacteriol.* **2011**, *193*, 4749–4757. doi: 10.1128/JB.00436-11.

267. Wilks, A.; Heinzl, G. Heme oxygenation and the widening paradigm of heme degradation. *Arch. Biochem. Biophys.* **2014**, *544*, 87–95. doi: 10.1016/j.abb.2013.10.013.

268. Loutet, S.A.; Kobylarz, M.J.; Chau, C.H.T.; Murphy, M.E.P. IruO Is a Reductase for Heme Degradation by IsdI and IsdG Proteins in Staphylococcus aureus. *J. Biol. Chem.* **2013**, *288*, 25749–25759. doi: 10.1074/jbc.M113.470518.

269. Surmann, K.; Simon, M.; Hildebrandt, P.; Pförtner, H.; Michalik, S.; Stentzel, S.; Steil, L.; Dhople, V.M.; Bernhardt, J.; Schlüter, R.; et al. A proteomic perspective of the interplay of Staphylococcus aureus and human alveolar epithelial cells during infection. *J. Proteomics* **2015**, *128*, 203–217. doi: 10.1016/j.jprot.2015.07.034.

270. Sibbald, M.J.J.B.; Ziebandt, A.K.; Engelmann, S.; Hecker, M.; de Jong, A.; Harmsen, H.J.M.; Raangs, G.C.; Stokroos, I.; Arends, J.P.; Dubois, J.Y.F.; et al. Mapping the Pathways to StaphylococcalPathogenesis by Comparative Secretomics. *Microbiol. Mol. Biol. Rev.* **2006**, *70*, 755–788. doi: 10.1128/MMBR.00008-06.

271. Foster, T.J. Surface Proteins of Staphylococcus aureus. *Microbiol. Spectr.* **2019**, *7*. doi: 10.1128/microbiolspec.GPP3-0046-2018.

272. Clarke, S.R.; Wiltshire, M.D.; Foster, S.J. IsdA of Staphylococcus aureus is a broad spectrum, iron-regulated adhesin. *Mol. Microbiol.* **2004**, *51*, 1509–1519. doi: 10.1111/j.1365-2958.2003.03938.x.

273. Clarke, S.R.; Foster, S.J. Surface Adhesins of Staphylococcus aureus. In *Advances in Microbial Physiology*; 2006; Vol. 51, pp. 187–224 ISBN 0120277514. doi: 10.1016/S0065-2911(06)51004-5.

274. Clarke, S.R.; Andre, G.; Walsh, E.J.; Dufrêne, Y.F.; Foster, T.J.; Foster, S.J. Iron-Regulated Surface Determinant Protein A Mediates Adhesion of Staphylococcus aureus to Human Corneocyte Envelope Proteins. *Infect. Immun.* **2009**, *77*, 2408–2416. doi: 10.1128/IAI.01304-08.

275. Corrigan, R.M.; Miajlovic, H.; Foster, T.J. Surface proteins that promote adherence of Staphylococcus aureus to human desquamated nasal epithelial cells. *BMC Microbiol.* **2009**, *9*, 22. doi: 10.1186/1471-2180-9-22.

276. Krismer, B.; Weidenmaier, C.; Zipperer, A.; Peschel, A. The commensal lifestyle of Staphylococcus aureus and its interactions with the nasal microbiota. *Nat. Rev. Microbiol.* **2017**, *15*, 675–687. doi: 10.1038/nrmicro.2017.104.

277. Palazzolo-Ballance, A.M.; Reniere, M.L.; Braughton, K.R.; Sturdevant, D.E.; Otto, M.; Kreiswirth, B.N.; Skaar, E.P.; DeLeo, F.R. Neutrophil Microbicides Induce a Pathogen Survival Response in Community-Associated Methicillin-Resistant Staphylococcus aureus. *J. Immunol.* **2008**, *180*, 500–509. doi: 10.4049/jimmunol.180.1.500.

278. Miajlovic, H.; Zapotoczna, M.; Geoghegan, J.A.; Kerrigan, S.W.; Speziale, P.; Foster, T.J. Direct interaction of iron-regulated surface determinant IsdB of Staphylococcus aureus with the GPIIb/IIIa receptor on platelets. *Microbiology* **2010**, *156*, 920–928. doi: 10.1099/mic.0.036673-0.

279. Zapotoczna, M.; Jevnikar, Z.; Miajlovic, H.; Kos, J.; Foster, T.J. Iron-regulated surface determinant B (IsdB) promotes Staphylococcus aureus adherence to and internalization by non-phagocytic human cells. *Cell. Microbiol.* **2013**, *15*, 1026–1041. doi: 10.1111/cmi.12097.

280. Alva-Murillo, N.; López-Meza, J.E.; Ochoa-Zarzosa, A. Nonprofessional Phagocytic Cell Receptors Involved in Staphylococcus aureus Internalization. *Biomed Res. Int.* **2014**, *2014*, 1–9. doi: 10.1155/2014/538546.

281. Hamzeh-Cognasse, H.; Damien, P.; Chabert, A.; Pozzetto, B.; Cognasse, F.; Garraud, O. Platelets and Infections â€“ Complex Interactions with Bacteria. *Front. Immunol.* **2015**, *6*, 1–18. doi: 10.3389/fimmu.2015.00082.

282. Pietrocola, G.; Pellegrini, A.; Alfeo, M.J.; Marchese, L.; Foster, T.J.; Speziale, P. The iron-regulated surface determinant B (IsdB) protein from Staphylococcus aureus acts as a receptor for the host protein vitronectin. *J. Biol. Chem.* **2020**, *295*, 10008–10022. doi: 10.1074/jbc.RA120.013510.

283. Visai, L.; Yanagisawa, N.; Josefsson, E.; Tarkowski, A.; Pezzali, I.; Rooijakkers, S.H.M.; Foster, T.J.; Speziale, P. Immune evasion by Staphylococcus aureus conferred by iron-regulated surface determinant protein IsdH. *Microbiology* **2009**, *155*, 667–679. doi: 10.1099/mic.0.025684-0.

284. Verkaik, N.J.; van Wamel, W.J.; van Belkum, A. Immunotherapeutic approaches against Staphylococcus aureus. *Immunotherapy* **2011**, *3*, 1063–1073. doi: 10.2217/imt.11.84.

285. Foster, C.E.; Kok, M.; Flores, A.R.; Minard, C.G.; Luna, R.A.; Lamberth, L.B.; Kaplan, S.L.; Hulten, K.G. Adhesin genes and biofilm formation among pediatric Staphylococcus aureus isolates from implant-associated infections. *PLoS One* **2020**, *15*, e0235115. doi: 10.1371/journal.pone.0235115.

286. Schneewind, O.; Missiakas, D. Sortases, Surface Proteins, and Their Roles in Staphylococcus aureus Disease and Vaccine Development. In *Protein Secretion in Bacteria*; American Society of Microbiology, 2019; pp. 173–188. doi: 10.1128/microbiolspec.PSIB-0004-2018.

287. Cheng, A.G.; Kim, H.K.; Burts, M.L.; Krausz, T.; Schneewind, O.; Missiakas, D.M. Genetic requirements for Staphylococcus aureus abscess formation and persistence in host tissues. *FASEB J.* **2009**, *23*, 3393–3404. doi: 10.1096/fj.09-135467.

288. Diep, B.A.; Phung, Q.; Date, S.; Arnott, D.; Bakalarski, C.; Xu, M.; Nakamura, G.; Swem, D.L.; Alexander, M.K.; Le, H.N.; et al. Identifying Potential Therapeutic Targets of Methicillin-resistant Staphylococcus aureus Through in Vivo Proteomic Analysis. *J. Infect. Dis.* **2014**, *209*, 1533–1541. doi: 10.1093/infdis/jit662.

289. Thomsen, I.P.; Liu, G.Y. Targeting fundamental pathways to disrupt Staphylococcus aureus survival: clinical implications of recent discoveries. *JCI Insight* **2018**, *3*. doi: 10.1172/jci.insight.98216.

290. Mazmanian, S.K.; Ton-That, H.; Schneewind, O. Sortase-catalysed anchoring of surface proteins to the cell wall of Staphylococcus aureus. *Mol. Microbiol.* **2001**, *40*, 1049–1057. doi: 10.1046/j.1365-2958.2001.02411.x.

291. Jonsson, I.; Mazmanian, S.K.; Schneewind, O.; Verdrengh, M.; Bremell, T.; Tarkowski, A. On the Role of Staphylococcus aureus Sortase and Sortase-Catalyzed Surface Protein Anchoring in Murine Septic Arthritis. *J. Infect. Dis.* **2002**, *185*, 1417–1424. doi: 10.1086/340503.

292. Jonsson, I.-M.; Mazmanian, S.K.; Schneewind, O.; Bremell, T.; Tarkowski, A. The role of Staphylococcus aureus sortase A and sortase B in murine arthritis. *Microbes Infect.* **2003**, *5*, 775–780. doi: 10.1016/S1286-4579(03)00143-6.

293. Kim, H.K.; DeDent, A.; Cheng, A.G.; McAdow, M.; Bagnoli, F.; Missiakas, D.M.; Schneewind, O. IsdA and IsdB antibodies protect mice against Staphylococcus aureus abscess formation and lethal challenge. *Vaccine* **2010**, *28*, 6382–6392. doi: 10.1016/j.vaccine.2010.02.097.

294. Pishchany, G.; McCoy, A.L.; Torres, V.J.; Krause, J.C.; Crowe, J.E.; Fabry, M.E.; Skaar, E.P. Specificity for Human Hemoglobin Enhances Staphylococcus aureus Infection. *Cell Host Microbe* **2010**, *8*, 544–550. doi: 10.1016/j.chom.2010.11.002.

295. Conger, M.A.; Pokhrel, D.; Liptak, M.D. Tight binding of heme to Staphylococcus aureus IsdG and IsdI precludes design of a competitive inhibitor. *Metallomics* **2017**, *9*, 556–563. doi: 10.1039/C7MT00035A.

296. Mozzi, A.; Forni, D.; Clerici, M.; Cagliani, R.; Sironi, M. The Diversity of Mammalian Hemoproteins and Microbial Heme Scavengers Is Shaped by an Arms Race for Iron Piracy. *Front. Immunol.* **2018**, *9*, 2086. doi: 10.3389/fimmu.2018.02086.

297. Ster, C.; Beaudoin, F.; Diarra, M.S.; Jacques, M.; Malouin, F.; Lacasse, P. Evaluation of some Staphylococcus aureus iron-regulated proteins as vaccine targets. *Vet. Immunol. Immunopathol.* **2010**, *136*, 311–318. doi: 10.1016/j.vetimm.2010.03.010.

298. Kim, H.K.; Missiakas, D.; Schneewind, O. Mouse models for infectious diseases caused by Staphylococcus aureus. *J. Immunol. Methods* **2014**, *410*, 88–99. doi: 10.1016/j.jim.2014.04.007.

299. Nishitani, K.; Beck, C.A.; Rosenberg, A.F.; Kates, S.L.; Schwarz, E.M.; Daiss, J.L. A Diagnostic Serum Antibody Test for Patients With Staphylococcus aureus Osteomyelitis. *Clin. Orthop. Relat. Res.* **2015**, *473*, 2735–2749. doi: 10.1007/s11999-015-4354-2.

300. Pancari, G.; Fan, H.; Smith, S.; Joshi, A.; Haimbach, R.; Clark, D.; Li, Y.; Hua, J.; McKelvey, T.; Ou, Y.; et al. Characterization of the mechanism of protection mediated by CS-D7, a monoclonal antibody to Staphylococcus aureus iron regulated surface determinant B (IsdB). *Front. Cell. Infect. Microbiol.* **2012**, *2*, 36. doi: 10.3389/fcimb.2012.00036.

301. Jansen, K.U.; Girgenti, D.Q.; Scully, I.L.; Anderson, A.S. Vaccine review: "Staphyloccocus aureus vaccines: Problems and prospects." *Vaccine* **2013**, *31*, 2723–2730. doi: 10.1016/j.vaccine.2013.04.002.

302. Fowler, V.G.; Allen, K.B.; Moreira, E.D.; Moustafa, M.; Isgro, F.; Boucher, H.W.; Corey, G.R.; Carmeli, Y.; Betts, R.; Hartzel, J.S.; et al. Effect of an Investigational Vaccine for Preventing Staphylococcus aureus Infections After Cardiothoracic Surgery. *JAMA* **2013**, *309*, 1368. doi: 10.1001/jama.2013.3010.

303. McNeely, T.B.; Shah, N.A.; Fridman, A.; Joshi, A.; Hartzel, J.S.; Keshari, R.S.; Lupu, F.; DiNubile, M.J. Mortality among recipients of the Merck V710 Staphylococcus aureus vaccine after postoperative S. aureus infections: An analysis of possible contributing host factors. *Hum. Vaccin. Immunother.* **2014**, *10*, 3513–3516. doi: 10.4161/hv.34407.

304. Nishitani, K.; Ishikawa, M.; Morita, Y.; Yokogawa, N.; Xie, C.; de Mesy Bentley, K.L.; Ito, H.; Kates, S.L.; Daiss, J.L.; Schwarz, E.M. IsdB antibody–mediated sepsis following S. aureus surgical site infection. *JCI Insight* **2020**, *5*. doi: 10.1172/jci.insight.141164.

305. Proctor, R.A. Is there a future for a Staphylococcus aureus vaccine? *Vaccine* **2012**, *30*, 2921–2927. doi: 10.1016/j.vaccine.2011.11.006.

306. Fowler, V.G.; Proctor, R.A. Where does a Staphylococcus aureus vaccine stand? *Clin. Microbiol. Infect.* **2014**, *20*, 66–75. doi: 10.1111/1469-0691.12570.

307. Vuong, C.; Yeh, A.J.; Cheung, G.Y.C.; Otto, M. Investigational drugs to treat methicillin-resistant Staphylococcus aureus. *Expert Opin. Investig. Drugs* **2016**, *25*, 73–93. doi: 10.1517/13543784.2016.1109077.

308. Speziale, P.; Rindi, S.; Pietrocola, G. Antibody-Based Agents in the Management of Antibiotic-Resistant Staphylococcus aureus Diseases. *Microorganisms* **2018**, *6*, 25. doi: 10.3390/microorganisms6010025.

309. Tsai, C.-M.; Soper, N.; Bennett, M.; Fallon, J.K.; Michell, A.R.; Alter, G.; Liu, G.Y.; Thomsen, I. Adoptive Transfer of Serum Samples From Children With Invasive Staphylococcal Infection and Protection Against Staphylococcus aureus Sepsis. *J. Infect. Dis.* **2020**, *2581*, 1–10. doi: 10.1093/infdis/jiaa482.

310. Clarke, S.R.; Brummell, K.J.; Horsburgh, M.J.; McDowell, P.W.; Mohamad, S.A.S.; Stapleton, M.R.; Acevedo, J.; Read, R.C.; Day, N.P.J.; Peacock, S.J.; et al. Identification of In vivo–expressed antigens of Staphylococcus aureus and their use in vaccinations for protection against nasal carriage. *J. Infect. Dis.* **2006**, *193*, 1098–1108. doi: 10.1086/501471.

311. Kuklin, N.A.; Clark, D.J.; Secore, S.; Cook, J.; Cope, L.D.; McNeely, T.; Noble, L.; Brown, M.J.; Zorman, J.K.; Wang, X.M.; et al. A Novel Staphylococcus aureus Vaccine: Iron Surface Determinant B Induces Rapid Antibody Responses in Rhesus Macaques and Specific Increased Survival in a Murine S. aureus Sepsis Model. *Infect. Immun.* **2006**, *74*, 2215–2223. doi: 10.1128/IAI.74.4.2215-2223.2006.

312. Harro, C.; Betts, R.; Orenstein, W.; Kwak, E.-J.; Greenberg, H.E.; Onorato, M.T.; Hartzel, J.; Lipka, J.; DiNubile, M.J.; Kartsonis, N. Safety and Immunogenicity of a Novel Staphylococcus aureus Vaccine: Results from the First Study of the Vaccine Dose Range in Humans. *Clin. Vaccine Immunol.* **2010**, *17*, 1868–1874. doi: 10.1128/CVI.00356-10.

313. Stranger-Jones, Y.K.; Bae, T.; Schneewind, O. Vaccine assembly from surface proteins of Staphylococcus aureus. *Proc. Natl. Acad. Sci.* **2006**, *103*, 16942–16947. doi: 10.1073/pnas.0606863103.

314. Delfani, S.; Imani Fooladi, A.A.; Mobarez, A.M.; Emaneini, M.; Amani, J.; Sedighian, H. In silico analysis for identifying potential vaccine candidates against Staphylococcus aureus. *Clin. Exp. Vaccine Res.* **2015**, *4*, 99. doi: 10.7774/cevr.2015.4.1.99.

315. Delfani, S.; Mohabati Mobarez, A.; Imani Fooladi, A.A.; Amani, J.; Emaneini, M. Protection of mice against Staphylococcus aureus infection by a recombinant protein ClfA–IsdB–Hlg as a vaccine candidate. *Med. Microbiol. Immunol.* **2016**, *205*, 47–55. doi: 10.1007/s00430-015-0425-y.

316. Zeng, H.; Yang, F.; Feng, Q.; Zhang, J.; Gu, J.; Jing, H.; Cai, C.; Xu, L.; Yang, X.; Xia, X.; et al. Rapid and Broad Immune Efficacy of a Recombinant Five-Antigen Vaccine against Staphylococcus aureus Infection in Animal Models. *Vaccines* **2020**, *8*, 134. doi: 10.3390/vaccines8010134.

317. Brown, M.; Kowalski, R.; Zorman, J.; Wang, X.; Towne, V.; Zhao, Q.; Secore, S.; Finnefrock, A.C.; Ebert, T.; Pancari, G.; et al. Selection and Characterization of Murine Monoclonal Antibodies to Staphylococcus aureus Iron-Regulated Surface Determinant B with Functional Activity In Vitro and In Vivo. *Clin. Vaccine Immunol.* **2009**, *16*, 1095–1104. doi: 10.1128/CVI.00085-09.

318. Ebert, T.; Smith, S.; Pancari, G.; Clark, D.; Hampton, R.; Secore, S.; Towne, V.; Fan, H.; Wang, X.-M.; Wu, X.; et al. A fully human monoclonal antibody to Staphylococcus aureus iron regulated surface determinant B (IsdB) with functional activity in vitro and in vivo. *Hum. Antibodies* **2010**, *19*, 113–128. doi: 10.3233/HAB-2010-0235.

319. Yeung, Y.A.; Foletti, D.; Deng, X.; Abdiche, Y.; Strop, P.; Glanville, J.; Pitts, S.; Lindquist, K.; Sundar, P.D.; Sirota, M.; et al. Germline-encoded neutralization of a Staphylococcus aureus virulence factor by the human antibody repertoire. *Nat. Commun.* **2016**, *7*, 13376. doi: 10.1038/ncomms13376.

320. Bennett, M.R.; Dong, J.; Bombardi, R.G.; Soto, C.; Parrington, H.M.; Nargi, R.S.; Schoeder, C.T.; Nagel, M.B.; Schey, K.L.; Meiler, J.; et al. Human V H 1-69 Gene-Encoded Human Monoclonal Antibodies against Staphylococcus aureus IsdB Use at Least Three Distinct Modes of Binding To Inhibit Bacterial Growth and Pathogenesis. *MBio* **2019**, *10*, 1–14. doi: 10.1128/mBio.02473-19.

321. Jenkins, A.; Diep, B.A.; Mai, T.T.; Vo, N.H.; Warrener, P.; Suzich, J.; Stover, C.K.; Sellman, B.R. Differential Expression and Roles of Staphylococcus aureus Virulence Determinants during Colonization and Disease. *MBio* **2015**, *6*, 1–10. doi: 10.1128/mBio.02272-14.

322. Ghasemzadeh-Moghaddam, H.; van Wamel, W.; van Belkum, A.; Hamat, R.A.; Tavakol, M.; Neela, V.K. Humoral immune consequences of Staphylococcus aureus ST239-associated bacteremia. *Eur. J. Clin. Microbiol. Infect. Dis.* **2018**, *37*, 255–263. doi: 10.1007/s10096-017-3124-3.

323. Perutz, M.F. The Croonian Lecture, 1968 - The haemoglobin molecule. *Proc. R. Soc. London. Ser. B. Biol. Sci.* **1969**, *173*, 113–140. doi: 10.1098/rspb.1969.0043.

324. Cassat, J.E.; Skaar, E.P. Iron in Infection and Immunity. *Cell Host Microbe* **2013**, *13*, 509–519. doi: 10.1016/j.chom.2013.04.010.

325. Ip, S.H.C.; Ackers, G.K. Thermodynamic Studies on Subunit Assembly in Human Hemoglobin. *J. Biol. Chem.* **1977**, *252*, 82–87.

326. Manning, L.R.; Jenkins, W.T.; Hess, J.R.; Vandegriff, K.; Winslow, R.M.; Manning, J.M. Subunit dissociations in natural and recombinant hemoglobins. *Protein Sci.* **1996**, *5*, 775–781. doi: 10.1002/pro.5560050423.

327. Wiseman, G.M. The hemolysins of Staphylococcus aureus. *Bacteriol. Rev.* **1975**, *39*, 317–44.

328. Umbreit, J. Methemoglobin—It's not just blue: A concise review. *Am. J. Hematol.* **2007**, *82*, 134–144. doi: 10.1002/ajh.20738.

329. Choby, J.E.; Buechi, H.B.; Farrand, A.J.; Skaar, E.P.; Barber, M.F. Molecular Basis for the Evolution of Species-Specific Hemoglobin Capture by Staphylococcus aureus. *MBio* **2018**, *9*, 1–15. doi: 10.1128/mBio.01524-18.

330. Andersen, C.B.F.; Torvund-Jensen, M.; Nielsen, M.J.; de Oliveira, C.L.P.; Hersleth, H.-P.; Andersen, N.H.; Pedersen, J.S.; Andersen, G.R.; Moestrup, S.K. Structure of the haptoglobin–haemoglobin complex. *Nature* **2012**, *489*, 456–459. doi: 10.1038/nature11369.

331. Dickson, C.F.; Rich, A.M.; D'Avigdor, W.M.H.; Collins, D.A.T.; Lowry, J.A.; Mollan, T.L.; Khandros, E.; Olson, J.S.; Weiss, M.J.; Mackay, J.P.; et al. α-Hemoglobin-stabilizing Protein (AHSP) Perturbs the Proximal Heme Pocket of Oxy-α-hemoglobin and Weakens the Iron-Oxygen Bond. *J. Biol. Chem.* **2013**, *288*, 19986–20001. doi: 10.1074/jbc.M112.437509.

332. Zhu, H.; Li, D.; Liu, M.; Copié, V.; Lei, B. Non-Heme-Binding Domains and Segments of the Staphylococcus aureus IsdB Protein Critically Contribute to the Kinetics and Equilibrium of Heme Acquisition from Methemoglobin. *PLoS One* **2014**, *9*, e100744. doi: 10.1371/journal.pone.0100744.

333. Vu, N.T.; Moriwaki, Y.; Caaveiro, J.M.M.; Terada, T.; Tsutsumi, H.; Hamachi, I.; Shimizu, K.; Tsumoto, K. Selective binding of antimicrobial porphyrins to the heme-receptor IsdH-NEAT3 of Staphylococcus aureus. *Protein Sci.* **2013**, *22*, 942–953. doi: 10.1002/pro.2276.

334. Krishna Kumar, K.; Jacques, D.A.; Guss, J.M.; Gell, D.A. The structure of α-haemoglobin in complex with a haemoglobin-binding domain from Staphylococcus aureus reveals the elusive α-haemoglobin dimerization interface. *Acta Crystallogr. Sect. F Struct. Biol. Commun.* **2014**, *70*, 1032–1037. doi: 10.1107/S2053230X14012175.

335. Stødkilde, K.; Torvund-Jensen, M.; Moestrup, S.K.; Andersen, C.B.F. Structural basis for trypanosomal haem acquisition and susceptibility to the host innate immune system. *Nat. Commun.* **2014**, *5*, 5487. doi: 10.1038/ncomms6487.

336. Eliezer, D.; Wright, P.E. Is Apomyoglobin a Molten Globule? Structural Characterization by NMR. *J. Mol. Biol.* **1996**, *263*, 531–538. doi: 10.1006/jmbi.1996.0596.

337. Krishna Kumar, K.; Dickson, C.F.; Weiss, M.J.; Mackay, J.P.; Gell, D.A. AHSP (α-haemoglobin-stabilizing protein) stabilizes apo-α-haemoglobin in a partially folded state. *Biochem. J.* **2010**, *432*, 275–282. doi: 10.1042/BJ20100642.

338. Gianquinto, E.; Moscetti, I.; De Bei, O.; Campanini, B.; Marchetti, M.; Luque, F.J.; Cannistraro, S.; Ronda, L.; Bizzarri, A.R.; Spyrakis, F.; et al. Interaction of human hemoglobin and semi-hemoglobins with the Staphylococcus aureus hemophore IsdB: a kinetic and mechanistic insight. *Sci. Rep.* **2019**, *9*, 18629. doi: 10.1038/s41598-019-54970-w.

339. Cassoly, R.; Banerjee, R. Structure and Function of Human Semihemoglobins alpha and beta. *Eur. J. Biochem.* **1971**, *19*, 514–522. doi: 10.1111/j.1432-1033.1971.tb01343.x.

340. Liu, H.; Naismith, J.H. An efficient one-step site-directed deletion, insertion, single and multiple-site plasmid mutagenesis protocol. *BMC Biotechnol.* **2008**, *8*, 91. doi: 10.1186/1472-6750-8-91.

341. Fuhr, J.E.; Medici, P. An in vitro effect of thyroid hormone upon bone marrow synthesis of hemoglobin. *FEBS Lett.* **1970**, *11*, 20–22. doi: 10.1016/0014-5793(70)80481-1.

342. Viappiani, C.; Abbruzzetti, S.; Ronda, L.; Bettati, S.; Henry, E.R.; Mozzarelli, A.; Eaton, W.A. Experimental basis for a new allosteric model for multisubunit proteins. *Proc. Natl. Acad. Sci.* **2014**, *111*, 12758–12763. doi: 10.1073/pnas.1413566111.

343. Antonini, E.; Brunori, M. *Hemoglobin and myoglobin in their reactions with ligands*; Amsterdam : North-Holland, 1971; ISBN 0720471214.

344. Ascoli, F.; Rossi Fanelli, M.R.; Antonini, E. [5] Preparation and properties of apohemoglobin and reconstituted hemoglobins. In; 1981; Vol. 76, pp. 72–87 ISBN 0121819760. doi: 10.1016/0076-6879(81)76115-9.

345. Bucci, E.; Fronticelli, C. A New Method For The Preparation Of Alpha And Beta Subunits Of Human Hemoglobin. *J. Biol. Chem.* **1965**, *240*, PC551-2.

346. Wojdyr, M. Fityk : a general-purpose peak fitting program. *J. Appl. Crystallogr.* **2010**, *43*, 1126–1128. doi: 10.1107/S0021889810030499.

347. Barr, I.; Guo, F. Pyridine Hemochromagen Assay for Determining the Concentration of Heme in Purified Protein Solutions. *BIO-PROTOCOL* **2015**, *5*, 1–8. doi: 10.21769/BioProtoc.1594.

348. McLellan, T. Electrophoresis buffers for polyacrylamide gels at various pH. *Anal. Biochem.* **1982**, *126*, 94–99. doi: 10.1016/0003-2697(82)90113-0.

349. Kristinsson, H.G.; Mony, S.S.; Petty, H.T. Properties of Tilapia Carboxy- and Oxyhemoglobin at Postmortem pH. *J. Agric. Food Chem.* **2005**, *53*, 3643–3649. doi: 10.1021/jf048107j.

350. Ronda, L.; Bruno, S.; Viappiani, C.; Abbruzzetti, S.; Mozzarelli, A.; Lowe, K.C.; Bettati, S. Circular dichroism spectroscopy of tertiary and quaternary conformations of human hemoglobin entrapped in wet silica gels. *Protein Sci.* **2006**, *15*, 1961–1967. doi: 10.1110/ps.062272306.

351. Yip, Y.K.; Waks, M.; Beychok, S. Reconstitution of native human hemoglobin from separated globin chains and alloplex intermediates. *Proc. Natl. Acad. Sci.* **1977**, *74*, 64–68. doi: 10.1073/pnas.74.1.64.

352. Cassoly, R. [10] Preparation of globin-hemoglobin hybrids: Artificially prepared and naturally occurring semihemoglobins. In; 1981; Vol. 76, pp. 121–125 ISBN 0121819760. doi: 10.1016/0076-6879(81)76120-2.

353. Girod, S.; Baldet-Dupy, P.; Maillols, H.; Devoisselle, J.-M. On-line direct determination of the second virial coefficient of a natural polysaccharide using size-exclusion chromatography and multi-angle laser light scattering. *J. Chromatogr. A* **2002**, *943*, 147–152. doi: 10.1016/S0021-9673(01)01415-7.

354. Konarev, P. V.; Volkov, V. V.; Sokolova, A. V.; Koch, M.H.J.; Svergun, D.I. PRIMUS : a Windows PC-based system for small-angle scattering data analysis. *J. Appl. Crystallogr.* **2003**, *36*, 1277–1282. doi: 10.1107/S0021889803012779.

355. Franke, D.; Svergun, D.I. DAMMIF , a program for rapid ab-initio shape determination in small-angle scattering. *J. Appl. Crystallogr.* **2009**, *42*, 342–346. doi: 10.1107/S0021889809000338.
356. Volkov, V. V.; Svergun, D.I. Uniqueness of ab initio shape determination in small-angle scattering. *J. Appl. Crystallogr.* **2003**, *36*, 860–864. doi: 10.1107/S0021889803000268.
357. Pettersen, E.F.; Goddard, T.D.; Huang, C.C.; Couch, G.S.; Greenblatt, D.M.; Meng, E.C.; Ferrin, T.E. UCSF Chimera?A visualization system for exploratory research and analysis. *J. Comput. Chem.* **2004**, *25*, 1605–1612. doi: 10.1002/jcc.20084.
358. Tegunov, D.; Cramer, P. Real-time cryo-electron microscopy data preprocessing with Warp. *Nat. Methods* **2019**, *16*, 1146–1152. doi: 10.1038/s41592-019-0580-y.
359. Punjani, A.; Rubinstein, J.L.; Fleet, D.J.; Brubaker, M.A. cryoSPARC: algorithms for rapid unsupervised cryo-EM structure determination. *Nat. Methods* **2017**, *14*, 290–296. doi: 10.1038/nmeth.4169.
360. Liebschner, D.; Afonine, P. V.; Baker, M.L.; Bunkóczi, G.; Chen, V.B.; Croll, T.I.; Hintze, B.; Hung, L.-W.; Jain, S.; McCoy, A.J.; et al. Macromolecular structure determination using X-rays, neutrons and electrons: recent developments in Phenix. *Acta Crystallogr. Sect. D Struct. Biol.* **2019**, *75*, 861–877. doi: 10.1107/S2059798319011471.
361. Scheres, S.H.W. RELION: Implementation of a Bayesian approach to cryo-EM structure determination. *J. Struct. Biol.* **2012**, *180*, 519–530. doi: 10.1016/j.jsb.2012.09.006.
362. Zhang, K. Gctf: Real-time CTF determination and correction. *J. Struct. Biol.* **2016**, *193*, 1–12. doi: 10.1016/j.jsb.2015.11.003.
363. Emsley, P.; Lohkamp, B.; Scott, W.G.; Cowtan, K. Features and development of Coot. *Acta Crystallogr. Sect. D Biol. Crystallogr.* **2010**, *66*, 486–501. doi: 10.1107/S0907444910007493.
364. Kidmose, R.T.; Juhl, J.; Nissen, P.; Boesen, T.; Karlsen, J.L.; Pedersen, B.P. Namdinator – automatic molecular dynamics flexible fitting of structural models into cryo-EM and crystallography experimental maps. *IUCrJ* **2019**, *6*, 526–531. doi: 10.1107/S2052252519007619.
365. Krissinel, E.; Henrick, K. Inference of Macromolecular Assemblies from Crystalline State. *J. Mol. Biol.* **2007**, *372*, 774–797. doi: 10.1016/j.jmb.2007.05.022.

366. Shaeffer, J.R.; McDonald, M.J.; Turcit, S.M.; Dinda, D.M.; Bunn, H.F. Dimer-Monomer Dissociation of Human Hemoglobin A. *J. Biol. Chem.* **1984**, *259*, 14544–14547.
367. Putnam, C.D. Guinier peak analysis for visual and automated inspection of small-angle X-ray scattering data. *J. Appl. Crystallogr.* **2016**, *49*, 1412–1419. doi: 10.1107/S1600576716010906.
368. Benesch, R.E. [31] The stability of the heme-globin linkage: Measurement of heme exchange. In *Journal of Biological Chemistry*; 1994; Vol. 265, pp. 496–502. doi: 10.1016/0076-6879(94)31033-5.
369. Zhang, L.; Levy, A.; Rifkind, J.M. Autoxidation of hemoglobin enhanced by dissociation into dimers. *J. Biol. Chem.* **1991**, *266*, 24698–24701. doi: 10.1016/S0021-9258(18)54286-1.
370. Hargrove, M.S.; Barrick, D.; Olson, J.S. The Association Rate Constant for Heme Binding to Globin Is Independent of Protein Structure †. *Biochemistry* **1996**, *35*, 11293–11299. doi: 10.1021/bi9603711.
371. Hargrove, M.S.; Whitaker, T.; Olson, J.S.; Vali, R.J.; Mathews, A.J. Quaternary Structure Regulates Hemin Dissociation from Human Hemoglobin. *J. Biol. Chem.* **1997**, *272*, 17385–17389. doi: 10.1074/jbc.272.28.17385.
372. Liong, E.C.; Dou, Y.; Scott, E.E.; Olson, J.S.; Phillips, G.N. Waterproofing the Heme Pocket. *J. Biol. Chem.* **2001**, *276*, 9093–9100. doi: 10.1074/jbc.M008593200.
373. Samuel, P.P.; Ou, W.C.; Phillips, G.N.; Olson, J.S. Mechanism of Human Apohemoglobin Unfolding. *Biochemistry* **2017**, *56*, 1444–1459. doi: 10.1021/acs.biochem.6b01235.
374. Gelin, B.R.; Karplus, M. Mechanism of tertiary structural change in hemoglobin. *Proc. Natl. Acad. Sci.* **1977**, *74*, 801–805. doi: 10.1073/pnas.74.3.801.
375. Samuel, P.P.; Case, D.A. Atomistic Simulations of Heme Dissociation Pathways in Human Methemoglobins Reveal Hidden Intermediates. *Biochemistry* **2020**, *59*, 4093–4107. doi: 10.1021/acs.biochem.0c00607.
376. Gell, D.A. Structure and function of haemoglobins. *Blood Cells, Mol. Dis.* **2018**, *70*, 13–42. doi: 10.1016/j.bcmd.2017.10.006.

377. Perutz, M.F. Stereochemistry of Cooperative Effects in Haemoglobin: Haem–Haem Interaction and the Problem of Allostery. *Nature* **1970**, *228*, 726–734. doi: 10.1038/228726a0.

378. Perutz, M.F. Hemoglobin Structure and Respiratory Transport. *Sci. Am.* **1978**, *239*, 92–125. doi: 10.1038/scientificamerican1278-92.

379. Czjzek, M.; Létoffé, S.; Wandersman, C.; Delepierre, M.; Lecroisey, A.; Izadi-Pruneyre, N. The Crystal Structure of the Secreted Dimeric Form of the Hemophore HasA Reveals a Domain Swapping with an Exchanged Heme Ligand. *J. Mol. Biol.* **2007**, *365*, 1176–1186. doi: 10.1016/j.jmb.2006.10.063.

380. Baiesi, M.; Orlandini, E.; Trovato, A.; Seno, F. Linking in domain-swapped protein dimers. *Sci. Rep.* **2016**, *6*, 33872. doi: 10.1038/srep33872.

381. Harmer, J. *Encyclopedia of Biophysics*; Roberts, G.C.K., Ed.; Springer Berlin Heidelberg: Berlin, Heidelberg, 2013; ISBN 978-3-642-16711-9. doi: 10.1007/978-3-642-16712-6.

382. Crowther, J.R. *The ELISA Guidebook*; Methods in Molecular Biology; Humana Press: Totowa, NJ, 2009; Vol. 516; ISBN 978-1-60327-253-7. doi: 10.1007/978-1-60327-254-4.

383. *ELISA*; Hnasko, R., Ed.; Methods in Molecular Biology; Springer New York: New York, NY, 2015; Vol. 1318; ISBN 978-1-4939-2741-8. doi: 10.1007/978-1-4939-2742-5.

384. Rodrigues, C.H.M.; Myung, Y.; Pires, D.E. V; Ascher, D.B. mCSM-PPI2: predicting the effects of mutations on protein–protein interactions. *Nucleic Acids Res.* **2019**, *47*, W338–W344. doi: 10.1093/nar/gkz383.